FLOW CHARACTERISTICS OF TWO-DIMENSIONAL SPOUTED AND SPOUT-FLUIDIZED BEDS OF PARTICLES

by

Maria Laura de Azevedo Passos ©

A Thesis submitted to the Faculty of Graduate Studies and Research in Partial Fulfillment of the Requirements for the Degree of Doctor of Philosophy

Department of Chemical Engineering
McGill University
Montreal, Canada

November 1990

It is a poem
with numbers...
equations...

solving with passion...
feelings...
love.

To my parents,

my friend Odette,

to Fehri.

ABSTRACT

The flow characteristics of two dimensional spouted beds (2DSBs) were studied experimentally for various bed heights in a variety of air-particle systems. The effects of fluid-solid system properties, fluid flow rates, vessel dimensions, bed height, etc. on both fluid and solids flow characteristics were examined.

A new approach to analyze the fluid-solid-wall interaction forces in packed and spouted beds was developed; it is based on the elastic-plastic deformations of the porous medium at failure.

Equations for the design and simulation of the overall fluid-particle flow in a 2DSB were obtained on the basis of a solid stress analysis of the spout-annulus interface region. These include: (a) a correlation for the maximum spoutable bed height; (b) equations for the minimum spouting pressure drop and the minimum spouting velocity; and (c) an equation for the solids circulation rates near minimum spouting. These equations were verified by the experimental results obtained in this study as well as those from published literature.

The effect of introduction of additional air in the annular region of a 2DSB on the bed aerodynamics and solids circulation rates was also examined. Fluid flow regimes were mapped as functions of the spouting flow rate, the annular flow rate and the bed height. A preliminary comparison between a two dimensional spouted bed and a two dimensional spout-fluidized beds was made on the basis of the results obtained.

RESUME

Les caractéristiques de l'écoulement d'un lit à deux dimensions "spouté" son etudiées expérimentalement pour différentes hauteurs de lit avec une variéte de systèmes air-particules. Les effets des propriétés des systèmes fluides-solides, les débits des fluides, les dimensions du récipient et la hauteur du lit sur les caractéristiques de l'écoulement du fluide et des matières solides sont examinés.

Une nouvelle approche est développée pour analyser les interactions entre le fluide, les matières solides et la paroi dans un lit garni et "spouté"; elle est basée sur les déformations élastiques-plastiques du milieu poreux à la rupture.

Les équations de la conception et de la simulation du débit global du fluide et des matières solides dans un lit à deux dimensions au "spouting" minimal, sont obtenues sur la base d'une analyse de contraintes d'un solide dans la region annulaire. Ces équations incluent: (a) la corrélation pour la hauteur maximale de jaillissement ("spouting"); (b) les équations pour une chute de pression au "spouting" minimal et une vitesse au "spouting" minimal; (c) l'équation pour le taux de circulation des matières solides près de "spouting" minimal. Ces équations sont vérifiées par des résultats expérimentaux obtenus dans cette étude et aussi dans la litérature publiée.

L'effet de l'introduction de l'air additional dans la region annulaire sur l'áerodynamique du lit et sur le taux de circulation des matières solides est aussi examiné. Les régimes d'écoulement du fluide

sont indiqués dans des diagrammes de phase, sont des fonctions du débit du "spout", du débit annulaire et de la hauteur du lit. Une comparaison préliminaire entre un lit à deux dimensions "spouté" et un lit à deux dimensions "spouté" et fluidizé est faîte sur la base des résultats obtenus.

ACKNOWLEDGMENTS

I wish to express my gratitude to Dr. Arun S. Mujumdar for the guidance, attention and encouragement received under his supervision. I would also like to thank Dr. G. S. V. Raghavan for his support during the experimental work.

I wish to acknowledge: (i) World University Service of Canada (Canadian Government) and Conselho Nacional de Desenvolvimento Cientifico e Tecnologico (Brazilian Government) for the scholarship; (ii) Quebec Ministry of Education for the FCAR grant.

I am grateful to the professors and secretaries of the Chemical Engineering Department of Federal University of Minas Gerais for the support given to me during my years in Canada. Many thanks to all my students who honored me during this period - it was one of the best supports that I received.

I want to thank a special friend, Roberto Szente, who encouraged my ideas, who helped me in the preparation of this thesis. "Obrigada por tudo!"

Finally, I want to thank my family, specially Fehri, for their care, love and confidence.

TABLE OF CONTENTS

LIST OF FIGURES

Page

CHAPTER 4 PARTICLE CHARACTERIZATION

CHAPTER 5 FLOW MODEL FOR TWO DIMENSIONAL BEDS OF COARSE PARTICLES

LIST OF TABLES

Page

Page

Page

CHAPTER 1

INTRODUCTION

In a spouted bed (SB), a central jet of fluid is forced vertically upward through a mass of solid particles. As shown in Figure 1.1, when a jet breaks the top surface of the bed, three different regions are formed: the annulus region, where the particles move downwards and inwards in contact with the upward fluid flow; the spout region, where the particles are carried upward by the spouting fluid; and the fountain region, in which the particles change the direction of their motion and fall back into the annulus. This cyclic solids motion results in effective contact between the solid-particles and the spouting fluid.

Spouted beds have been used for drying coarse particles such as grains. Higher inlet air temperature can be used for drying grains without thermal damage of the product due to the short residence time of particles in the spout region. SBs are also suitable for drying sticky materials such as slurries and pastes if the spouting material comprises inert particles.

Although this work was motivated by potential applications in drying, SBs can also be used in any process which requires good particle-fluid contact e.g. heating or cooling of solids, particle coating, granulation, solids blending, gas cleaning, coal carbonization or gasification, shale pyrolysis, ore reduction, gas combustion, etc. (Mathur and Epstein, 1974).

Conventional spouted beds, CSBs (conical-cylindrical vessel geometry), present a serious limitation on processing capacity per unit

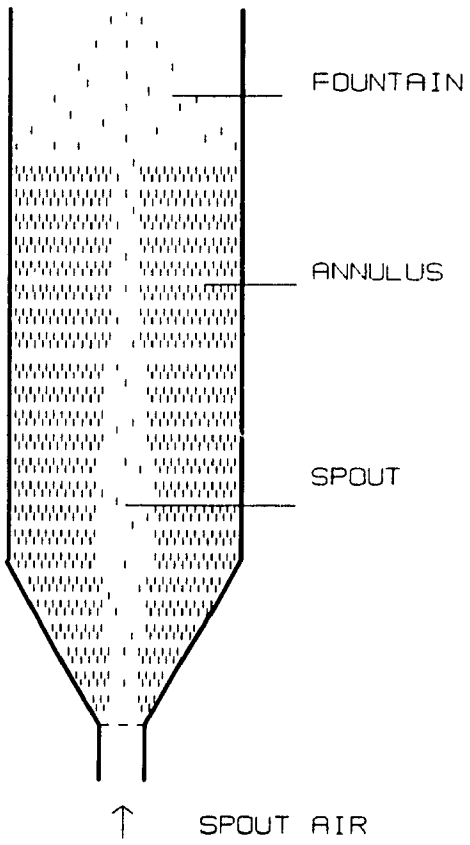

FIGURE 1.1 - Schematic Diagram of a Conventional Spouted Bed (Conical-cylindrical bed geometry).

floor space. Stable spouting operation, characterized by a regular cyclic solids motion, is restricted to a narrow range of vessel dimensions. Modification of the basic CSB design is necessary to overcome this and other limitations. Mujumdar (1984) and Passos et al. (1987b) have summarized some of the useful modifications of the spouted bed configuration.

A spout-fluid bed (SFB) combines some of the advantages of both spouted and fluidized beds. In SFBs, additional fluid is introduced in the annular region through a distributor plate. The cyclic solids movement pattern is maintained as in pure spouting while the solid-fluid contact is enhanced in the annulus region. Moreover, a SFB presents more flexibility in operation since different flow regimes can be achieved by independently varying the spout and the annulus flow rates. The annular flow is generally held lower than or equal to the minimum fluidization flow rate.

This flexibility of SFBs can be advantageous in drying wet particulate materials. Since the annular flow can fluidize the particles in the annulus, the gas-solid heat transfer coefficient in this region can be increased significantly over values obtained in CSBs.

For drying materials characterized by the falling drying rate period e. g. grains, the SFB should improve the drying performance as shown by Passos et al. (1989). The annular gas flow rate must then be low enough to aerate the annulus without fluidizing it. A reduction of the minimum spouting flow rate enables the SFB dryer to use different air inlet temperatures for improving the drying efficiency. Our preliminary results show that CSBs with annular aeration can increase the grain drying

efficiency at high grain feed rates and at low bed temperatures as shown in Figure 1.2.

The 2D bed geometry can increase the bed capacity per unit floor space and also simplify scale-up as pointed out by Mujumdar (1984). As seen in Figure 1.3, the bed capacity is easily increased by extending the length dimension, L_2. In addition, in a 2D vessel design, supplementary heat can be supplied directly into the bed by heating the flat side walls. This indirect heating can increase the thermal efficiency of drying.

Although the 2D bed geometry seems very attractive for easy scale-up, caution is needed in developing the scale-up criteria. The front and back vessel walls play an important role in spout formation in 2DSBs. Table 1.1 shows the bed dimensions for three 2D-slot-SBs (2D-slot-SBs can be viewed as half 2DSB columns). For Anderson et al.'s (1984) bed design, channels or multi-spouts developed along the L_2 direction. For Verlaan's (1984), and Ojalvo's (1989) designs, the stable spouting regime (similar to that in CSBs of coarse particles) could be achieved. A comparison between these data shows that an increase in the inlet nozzle area (by increasing L_N for a same range of d_p) can lead to different mechanisms of spout formation. Ojalvo (1989) obtained different spouting regimes by changing the included angle and the nozzle width. His data shows the flexibility of operation of a 2D geometry. However, for scale-up, it is necessary to obtain dimensionless parameters which describe the effect of vessel wall, nozzle dimensions and particle properties on spout formation in 2DSBs. Research in 2DSBs has just begun and no data exist in

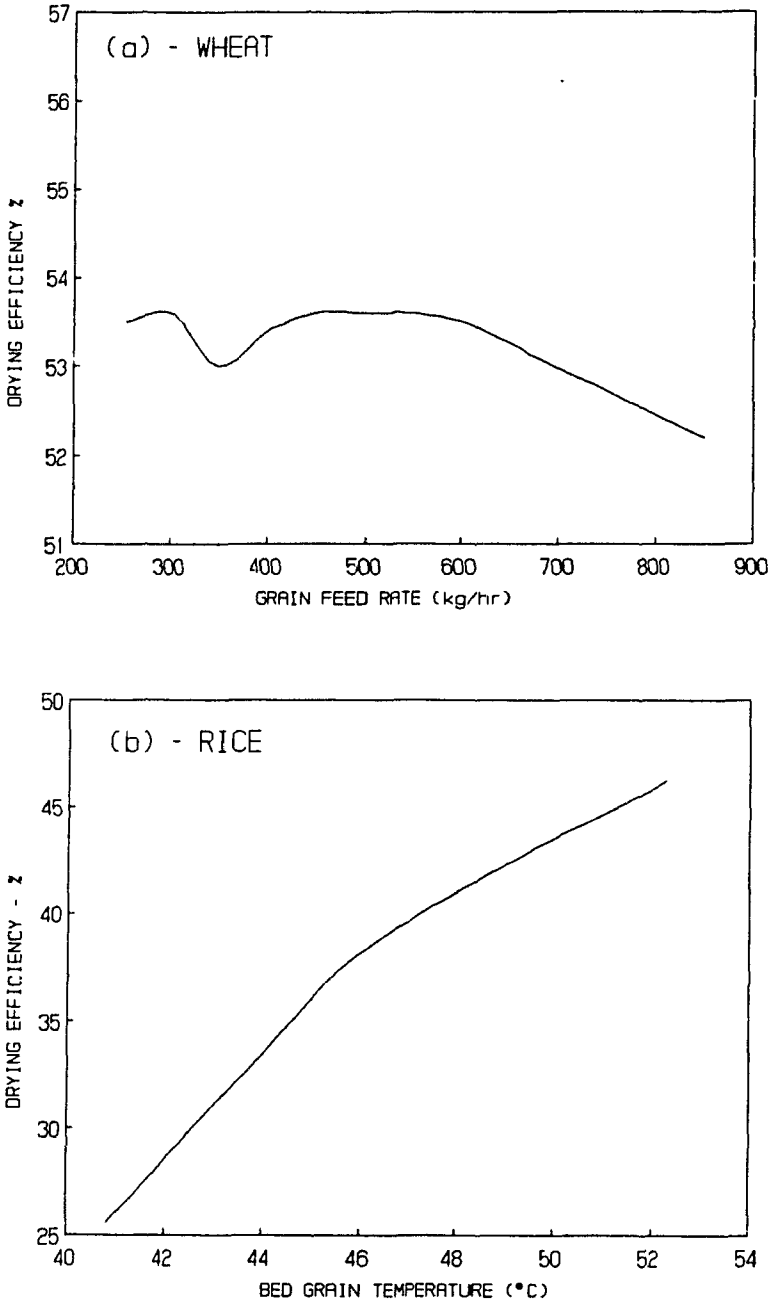

FIGURE 1.2 - Grain Drying Efficiency in Conventional Spouted and Spout-Fluid Bed Dryers as a function of: (a) Feed Rates and (b) Bed Temperature.
Full lines: drying efficiency curves in CSBs. Dashed lines: drying efficiency curves in CSFBs.
Drying conditions for wheat: inlet and outlet moisture contents = 0.22 and 0.16 dry basis, bed temperature = 56°C.
Drying conditions for rice: inlet and outlet moisture contents = 0.20 and 0.16 dry basis, grain feed rate = 250 kg/hr.
Simulations from Passos et al. (1989).

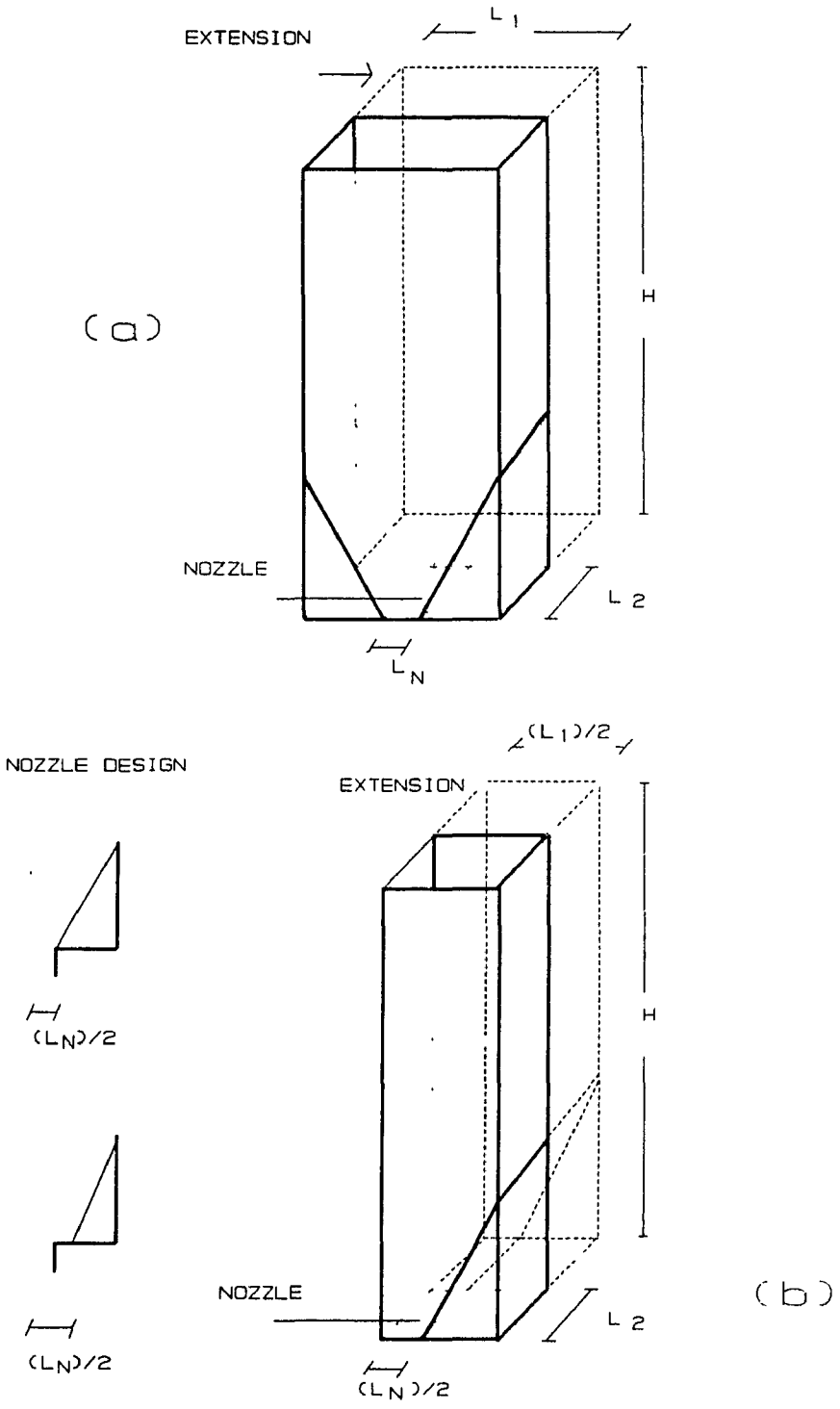

FIGURE 1.3 - Schematic Diagram of a Two Dimensional Spouted Bed: (a) Full Column, (b) Half Column.

TABLE 1.1

BED DIMENSIONS AND SPOUT CHARACTERISTICS IN TWO DIMENSIONAL SLOT SPOUTED BEDS

(2D HALF COLUMN)

L_1 (m)	L_2 (m)	L_N (m)	H (m)	d_p (mm)	SPOUT CONDITION	REFERENCE
2x0.05	0.50	2x0.01	0.10 - 0.30	4 - 8	channeling	Anderson et al. (1984)
2x0.20	0.20	2x0.02 (*)	0.15 - 0.55	4 - 8	true spout	Verlaan (1984)
2x0.50 2x0.10	0.20	2x0.013 2x0.001 (**)	0.15 - 0.30	6	true spout	Ojalvo (1989)

(*) The inlet duct width is 2x0.001 m. The nozzle width, L_N, includes the inlet duct width and the distance from the duct to the slant base (see Fig. 1.3).

(**) The nozzle and the inlet duct widths were varied in the range presented. The nozzle width is defined as in (*) (see Fig. 1.3).

The half included bed angle is equal to 45 degrees for Anderson et al.'s and Verlaan's data. Ojalvo varied this angle from 30 to 45 degrees.

the literature to describe the spouting mechanism in a 2DSB.

The basic objectives of this work are:

(i) to obtain the relevant dimensionless parameters and correlations for scale-up of 2DSBs;

(ii) to analyze and describe the overall flow characteristics in two dimensional spouted and spout-fluidized beds of coarse particles.

The dynamics of spouted and spout- fluidized beds are reviewed in Chapter 2. The similarity between a CSB and a 2DSB is developed based on the dimensionless parameters which characterize the spout formation and bed dynamics. Chapter 3 describes the experimental equipments and procedures used. Chapter 4 presents the experimental results for characterization of minimum fluidization in 2D packed beds of coarse particles. Chapter 5 uses the results of Chap. 4 to develop a general model to describe the effect of particle-wall interactions on the aerodynamics of packed beds. This model is used to obtain practical equations to predict the overall flow characteristics in two dimensional packed-spouted beds. The mechanisms of the spout termination in a two dimensional geometry are analyzed in Chapter 6. Chapter 7 is concerned with the fluid and solids dynamics in 2DSBs. This chapter includes experimental results and modeling equations to characterize the minimum spouting conditions and the solids circulation rates in a 2DSB. The flow characteristics in 2DSFBs are compared with those in 2DSBs in Chapter 8. The general conclusions, contributions to existing knowledge as well suggestions for further work are presented in Chapter 9. A list of the nomenclature used is given at the end of the thesis.

CHAPTER 2

LITERATURE REVIEW

Becker (1961) has postulated the following similarity principle for scaling-up SBs: "SBs of a given fluid-solid system in geometrically similar columns behave similarly when the reduced bed heights H/H_{max} are the same". Based on this principle, the design and scale-up of any SB require two major steps: the identification of the spout termination mechanism for prediction of H_{max} ; and the description of the bed dynamics as a function of the geometric parameters, particle and fluid properties.

2.1 Mechanisms of Spout Instability

Mathur and Epstein (1974) have pointed out three distinct mechanisms which cause spout termination in bed heights higher than H_{max} :

(i) fluidization of the annulus top;

(ii) choking of the spout;

(iii) growth of instability.

They have shown that, for a CSB of a given fluid-solid system, H_{max} increases initially with the particle diameter, goes through a maximum and then decreases. The fluidization of the annulus top is characterized by the decrease of H_{max} with increasing d_p. The choking of the spout is characterized by the increase of H_{max} with increasing d_p. The growth of instability is not well defined as a mechanism of spout termination.

2.1.1 Fluidization of the annulus top:

The fluidization of the annulus top has been reported in CSBs of coarse particles (d_p > 1 mm) spouted by air at ambient temperature. Based on experimental results, Littman et al. (1979, 1988), Morgan and Littman (1982) have described this mechanism by the following boundary conditions:

(1) the fluid velocity at the top of the annulus is equal to the minimum fluidization velocity;

(2) the inlet spout fluid velocity is greater than or, at least, equal to the terminal particle velocity;

(3) the ratio between the spout pressure drop and the minimum fluidization pressure drop is a constant value for a given fluid-solid system in a given SB column.

The dimensionless groups proposed by Littman et al. (1979, 1988) for the aerodynamics in CSBs are presented in Table 2.1. Equation (2.1) is the criterion of spoutability for CSBs where the fluidization of the annulus top is the mechanism of spout termination. Eq. (2.1) establishes a maximum value of D_i for a given column, above which the spout terminates. For beds in which $D_i < D_{i(max)}$, the minimum fluidization velocity is reached at the top before the terminal velocity is achieved at the inlet spout nozzle. Such beds will not spout in the traditional way (Littman and Morgan, 1986). For large spherical particles, $(D_c/D_i)_{min}$ becomes only a function of the minimum fluidization bed porosity (e. g. for ϵ_{mf} = 0.42, D_c/D_i > 2.90).

Equation (2.2) defines the basic parameters for the maximum spoutable bed height. Parameter A, as specified in Table 2.1, determines the minimum inlet energy required to sustain the spout to the minimum

frictional energy lost across the spout at $H_{ms} = H_{max}$. Eq. (2.2) has been obtained assuming a proportionality between the frictional energy lost across the spout and the kinetic energy carried by the inlet jet. Appendix A presents more details about this assumption.

Based on experimental data available in CSB literature, Morgan and Littman (1982) have reported a minimum value of A (=0.02 for spherical particles and =0.014 for non-spherical particles) for which a change in the spout termination mechanism occurs. This means that there is a maximum value of D_i/d_p which characterizes the fluidization of the annulus top mechanism. For large spherical particles, $(D_i/d_p)_{max}$ depends on the minimum fluidization bed porosity. For large non-spherical particles, this value depends on the particle sphericity as well.

McNab and Bridgwater (see Epstein and Grace, 1984) have developed a semi-theoretical equation for H_{max} in CSBs of coarse non-spherical particles. Epstein and Grace (1984) have shown that this equation can be applied for the following conditions:

(1) $Re_{ms} = 1.11\ Re_{mf}$ at h=1;

(2) $\epsilon_{mf} = 0.47$ and $\phi = 0.67$.

Although the condition (2) is a restriction, the McNab and Bridgwater equation predicts well H_{max} for non-spherical particles at low value of A (close to the transition). Appendix A compares the McNab and Bridgwater equation with the Littman et al. equation.

As shown in Appendix A, the McNab and Bridgwater equation can be written as a function of the dimensionless parameter A as follows:

$$H_{max} D_i / D_c^2 = f(D_i/d_p, D_c/D_i)\ A \qquad (2.5).$$

TABLE 2.1

BASIC DIMENSIONLESS PARAMETERS FOR SCALE-UP CHARACTERIZATION IN CSBs OF COARSE PARTICLES

(following Littman and Morgan, 1988)

1- Limit Boundary for Stable Spouting:

$$(D_c/D_i)_{min} = (V_T/V_{mf})^{1/2}, \text{ at } h \lesssim 1 \qquad (2.1)$$

$$h = H_{ms}/H_{max}$$

$$H_{max}\, D_i/D_c^2 = f(A) \qquad (2.2)$$

$$A = Re_{mf}\, Re_T\, (d_p/D_i)/Ar$$

$A > 0.02$ (for spherical particles),

$A > 0.014$ (for non-spherical particles).

2- Aerodynamic Parameters at the minimum spouting:

$$\Delta P_{ms}/\Delta P_{mf} = f(H/D_c, [A - D_i/D_c]) \qquad (2.3)$$

$$V_{ms}/V_{mf} = f(Re_{mf}, Ar, \epsilon_{aH}, \phi C^*) \qquad (2.4)$$

$$C^* = f(H/D_c, A, D_i/D_c)$$

It is an important result because A can be assumed to be the basic parameter to predict H_{max} in a CSB of coarse particles.

It is suggested in this work that eqs. (2.1) and (2.2) can be used for a two dimensional bed geometry, as follows:

$$(L_1/L_N)_{min} = V_T/V_{mf} \text{ , at } h \lesssim 1 \qquad (2.6),$$

$$H_{max}/ L_1 = f(A_{2D}, L_1/L_N, L_2/L_N) \qquad (2.7),$$

with $A_{2D} = Re_{mf} Re_T (d_p/L_N)/Ar$.

Eq. (2.6) should represent the spoutability criterion for a 2DSB of coarse particles where the fluidization of the annulus top is the spout termination mechanism. Eq. (2.7) establishes the possible dimensionless parameters for prediction of H_{max} in a 2DSB.

However, it is important to note that for a 2DSB, V_{mf} can be affected by wall-particle interaction. As a consequence, the Ergun equation (Ergun, 1952 - see also Appendix A) would not be used in calculation of V_{mf}

Previous works (Passos et al., 1987a, 1987c) have attempted to compare the aerodynamics in a 2DSB with those in a similar CSB by using an equivalent D_i and an equivalent D_c. However, the results obtained are specific, with different procedures to determine $D_{c(eq)}$ and $D_{i(eq)}$ depending on L_2.

2.1.2 Choking of spout:

This mechanism is characteristic of CSBs of fine or small particles

(d_p < 1 mm). In this mechanism, the internal spout cavity degenerates into bubbles which travel upwards in the annulus region.

Chandnani and Epstein (1984) and Epstein and Chandnani (1987) have studied the gas spouting characteristics of fine particles (0.17 mm < d_{ps} < 1mm). They worked in a half CSB column (D_c = 0.152 m) with 2.8 mm < D_i < 28 mm. Based on their results, the following conclusions can be drawn regarding:

1 - The boundary conditions for the choking of spout mechanism:

(i) $D_i/d_{ps} < 25$ (2.8);

(ii) $0.55 < V_{ms} / V_{mf} < 0.70$ for h = 1;

(iii) the value of the spout porosity at the inlet nozzle seems to be close to unity (based on visual observation). This result is quite different from the prediction of Morgan et al. (1985);

2 - The spouting characteristics:

(iv) five different regimes are identified: fixed bed, steady spouting, progressively incoherent spouting, bubbling and slugging. Steady spouting is characterized by a steady fountain and a spout-annulus interface. In progressively incoherent spouting, the fountain is distorted, and waves are developed along the spout-annulus interface near the bed surface. The interface sustains a rippling motion. When the amplitudes of these waves become equal to the spout radius, the so-called bubbling regime is achieved. Large bubbles with diameters equal to the bed column diameter characterize the slugging regime. The progressively incoherent spouting regime is a characteristic of fine particles spouted by gas;

(v) a large stagnant zone extends in the lower outer periphery of the annulus. The volume occupied by this stagnant zone decreases with the air flow and increases with the included angle;

(vi) the spout diameter is almost constant along the bed height;

(vii) the fountain height and the particle circulation present similar trends to those in CSBs of coarse particles;

(viii) for the spout pressure drop characteristic curves, two distinct points have been found for the spout break-up and the spout collapse. The pressure drop continues to increase with air flow rate after the minimum spouting condition. This behavior is explained by a reduction of the stagnant zone with the increase of the air flow rate (Epstein and Chandnani, 1987). As the gas flow rate increases beyond the minimum spouting value, more particles from the stagnant zone start moving. The number of particles entraining into the spout increases near the bottom, and, consequently, the spout pressure drop rises.

The basic criterion for spoutability is given by eq. (2.8). It is important to point out that d_{ps} is the mean particle size obtained by the standard sieve analysis. For angular quartz particles in the range size 105 - 600 μm and $0.64 < \phi < 0.93$, Abrahamsen and Geldart (1980) have found $d_{ps} = 1.148\ \phi\ d_p$. As a consequence of this, the criterion of spoutability proposed by eq. (2.8) is a function of the particle sphericity as well. Grace and Lim (1987) have demonstrated that eq. (2.8) can be applied for permanent jet formation in fluidized, spout-fluidized and spouted beds to predict the transition from jet to bubbles.

2.1.3 Transition between coarse and fine particles in conventional spouted beds:

Botterill et al. (1982) have shown that the increase in the bed temperature of fluidized beds of small coarse particles (d_p = 1 mm) can change progressively the pressure drop characteristics from those typical of non-Darcy flow (Geldart group D) towards ones typical of Darcy flow (Geldart group B). Wu et al. (1987) have reported that the increase in the bed temperature of CSBs of small coarse particles can change the spout termination mechanism from the fluidization of the annulus top to the choking of spout.

Basically, Botterill et al. and Wu et al. have proved that any alteration in the fluid-solid properties leads to change in the fluid-particle interaction forces. Moreover, for small coarse particles (particles close to Geldart B-D boundary), such changes can result in distinct dynamic characteristics for fluidized or spouted beds.

Changes in the spouted bed dynamics due to the alteration of the fluid properties are predicted by the parameter A. The values of A for the air-sand system used by Wu et al. (1987) are presented in Table 2.2 as a function of T_b. The parameter A was calculated based on Wu et al.'s considerations about d_p and ϕ ($d_p = d_{ps}$ and ϕ calculated by the Ergun equation). As expected, the parameter A decreases with T_b. This means that the minimum energy required to sustain the spout decreases as the bed temperature increases. For D_i = 12.7 mm, the parameter A is equal to 0.014 at T_b = 300°C; it indicates a change in the mechanism of spout termination. From an analysis of Fig. 2 of Wu et al., there is a

TABLE 2.2

SPOUTABILITY OF SAND PARTICLES

Fluid: atmospheric air at different temperatures

Based on Wu et al. (1987) (*).

d_{ps}	D_i/d_{ps}	D_c/D_i	STABLE SPOUTING			
(mm)	(-)	(-)	20°C	170°C	300°C	420°C
1.665	7.6	12.3	YES A=0.020	YES A=0.016	YES A=0.014	YES A=0.012
1.250	10.2	12.3	YES A=0.013	YES A=0.010	YES A=0.008	YES A=0.006
1.665	11.4	8.2	YES A=0.013	YES A=0.011	YES A=0.009	YES A=0.008
0.945	13.4	12.3	YES A=0.008	YES A=0.005	YES A=0.004	YES A=0.003(2)
1.250	15.2	8.2	YES A=0.009	YES A=0.006	YES A=0.005	YES A=0.004
1.665	16.0	5.8	YES A=0.010	YES A=0.008	YES A=0.006	YES A=0.006
0.945	20.2	8.2	YES A=0.005	YES A=0.004	NO A=0.002(7)	NO A=0.002
1.250	21.3	5.8	YES A=0.006	YES A=0.005	YES A=0.004	YES A=0.003
0.945	28.2	5.8	NO A=0.004	NO A=0.003	NO A=0.002	NO A=0.001

(*) data obtained in a half column with D_c = 0.156 m.

different trend in the maximum spoutable bed height versus the bed temperature curve at $T_b > 170°C$. It is a good indication of the change in the spout termination mechanism. The regime map for sand particles with $d_{ps} = 1.25$ mm spouted by ambient air confirms the presence of a progressively incoherent spouting regime characteristic of fine particles. As shown in Table 2.2, stable spouting is always achieved for $A > 0.003$ with $D_i/d_{ps} < 25$.

The parameter A seems a consistent dimensionless group for design and scale-up of CSBs of particles spouted by gas. For CSBs of coarse particles, the criterion of spoutability is given by eq. (2.1) with $A > 0.014$. For CSBs of fine particles, this criterion is given by eq. (2.8) with $A > 0.003$.

Another criterion to describe the transition between fine and coarse particles in CSBs is based on the spout porosity variation. This is proposed by Morgan et al. (1985) and Day (1986). Through a momentum balance in the spout region at the minimum condition, the following parameter is defined:

$$C_o = \int_0^1 [1 - \epsilon_s (y/H)]_{ms}/(1 - \epsilon_{mf})\, d(y/H) \qquad (2.9)$$

This parameter C_o determines the transition between fine and coarse particles. As shown in Appendix A, C_o is the sum of the spout pressure drop and the inlet jet momentum/unit area of the spout region. For $0.215 < C_o < 0.785$, the spouting regime is characteristic of coarse particles, with the inlet spout porosity equal to 1 and the outlet spout porosity equal to that for minimum fluidization. For $C_o > 0.785$, the spouting

regime is characteristic of fine particles, with the inlet spout porosity < 1.

2.1.4 Growth of instability:

Volpicelli et al. (1967) reported on instabilities in a 2DSB. They worked with a full 2D column (L_1 = 0.20 m, L_2 = 0.016 m, L_N = 4 mm) with glass beads (0.6 mm < d_p < 3 mm), ceramic chips (d_p = 0.8 mm), and plastic spheres (d_p = 3 mm), all of them spouted by air. Their basic conclusions are:

(i) two distinct mechanisms of spout instabilities characterize a 2DSB. The first one is related to the waves disturbance developed at the bottom of the spout. These waves move upwards along the spout-annulus interface like ripples. The second one is related to the oscillations of the spout around its axis;

(ii) stable spouting is achieved in a narrow range of values for the air spouting velocities;

(iii) H_{max} is much lower than that observed in CSBs (in the range of 20 to 25 cm for glass beads and 30 cm for ceramic chips);

The first mechanism of spout instability pointed out by Volpicelli et al. is similar to the progressively incoherent spout regime described by Epstein and Chandnani (1987) for fine particles. This type of instability is due to the low jet inertia characteristics which can be achieved by decreasing d_p or by increasing the inlet nozzle area.

The effects of the inlet nozzle area on the dynamics of 2DSBs of coarse particles are shown in Figs. 2.1, 2.2 and 2.3 (Anderson et al., 1984 and Ojalvo, 1989). The specific dimensionless parameters calculated

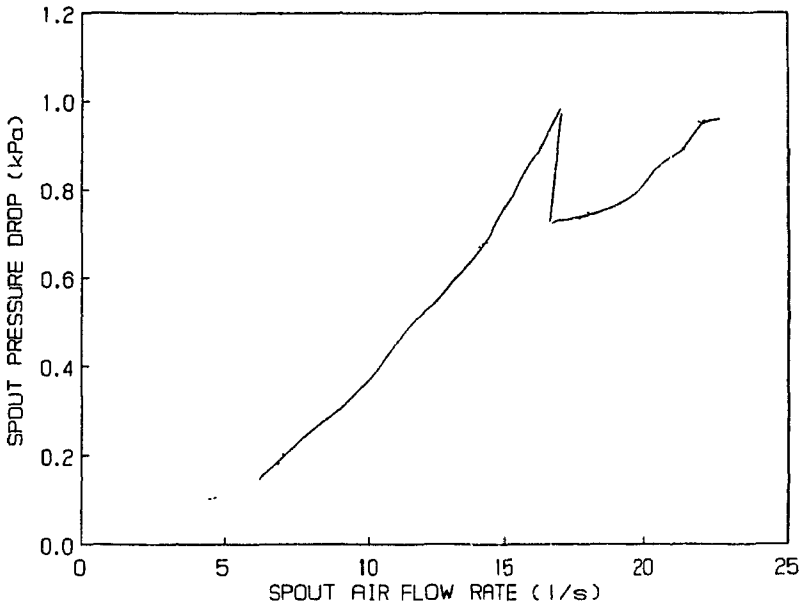

FIGURE 2.1 - Spouting Pressure Drop versus Air Flow Rate for a Half 2DSB of Oat.
Data from Anderson et al. (1984). Full line represents increasing flow. Dashed line represents decreasing flow. Fluid: ambient air.

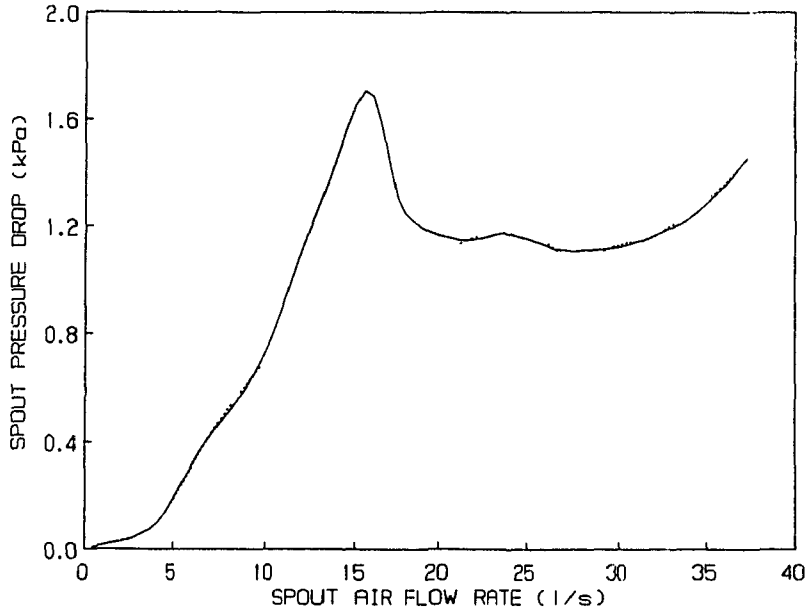

FIGURE 2.2 - Spouting Pressure Drop versus Air Flow Rate for a Half 2DSB of Soybean.
Data from Ojalvo (1989). Full line represents increasing flow, dashed line decreasing flow. Fluid: ambient air.

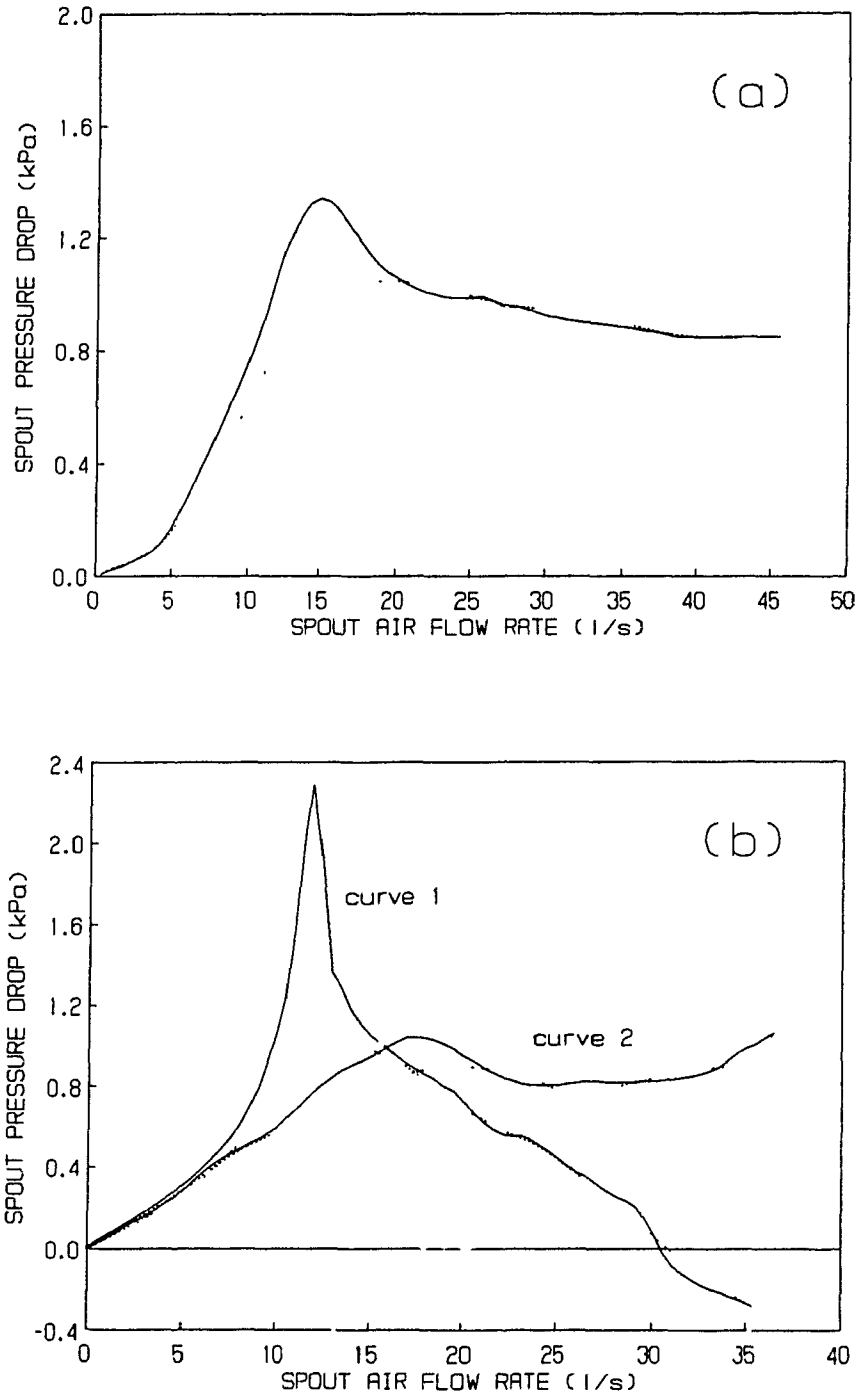

FIGURE 2.3 - Effect of Included Angle and Inlet Nozzle on Spout Pressure Drop Characteristics for a Half 2DSB of Soybean. Data from Ojalvo (1989). Data specification in Table 2.3. Full lines represent increasing flow, dashed lines decreasing flow. Fluid: ambient air.

TABLE 2.3

DIMENSIONLESS PARAMETERS OBTAINED IN A TWO DIMENSIONAL HALF SPOUTED BED

(Based on data obtained by Anderson et al., 1984 and Ojalvo, 1989)

DATA	L_1/L_N (-)	V_T/V_{mf} (-)	A_{2D} (-)	$D_{i(eq)}/d_p$ (-)	H_{ms} (m)
Fig. 2.1 θ = 90°	5.3	4	0.025	27.1	0.156
Fig. 2.2 θ = 60°	9.1	14	0.042	13.6	0.183
Fig. 2.3a θ = 60°	40.4	11	0.220	5.8	0.194
Fig. 2.3b curve 1 θ = 60°	119.4	12	0.595	3.8	0.205
curve 2 θ = 90°	165.0	9	0.825	3.8	0.164

for these figures are given in Table 2.3. A_{2D} was determined by eq. (2.6), with V_{mf} obtained from the Ergun equation (1952) and V_T calculated using the Littman et al. correlation for non-spherical particles (see Appendix A). The prediction of V_{mf} is only approximate since the vessel wall can affect the dynamics of the packed bed in a 2D column. $D_{i(eq)}$ was determined based on the inlet nozzle area of the 2DSB. L_1 was taken as equal to the bed width at the top of the cone for the experimental curves obtained by Ojalvo (1989) in a conical 2D bed configuration.

It can be seen in Figures 2.1 and 2.2 that the spout pressure drop continues to increase with increasing air flow rates beyond minimum spouting. This is the characteristic behavior of fine particles spouted by gas in a CSB. A_{2D} reaches the lowest values for these two cases as shown in Table 2.3. Based on eq. (2.8), the stable spouting regime cannot be achieved in Anderson et al.'s 2DSB ($D_{i(eq)}/d_p > 25$). This explains Anderson et al.'s results (see Table 1.1) which show channels inside the bed instead of a true spout. For Ojalvo's data in Fig. 2.2, $D_{i(eq)}/d_p < 25$, and as a result stable spouting regime can be achieved. However, $L_1/L_N < V_T / V_{mf}$ indicating that the fluidization of the annulus top is not the spout termination mechanism for such a bed.

Decreasing the inlet nozzle area, the inlet jet momentum increases, and, as a consequence, the 2DSB behavior approaches the one characteristic of coarse particles in CSBs. The curve in Fig. 2.3a shows that the spout pressure drop becomes constant with air flow beyond the the minimum spouting flow rate; A_{2D} is 0.220 in this case (Table 2.3).

Interesting results were obtained for higher values of A_{2D} with the included angle of 60° (Fig. 2.3b). The spout pressure drop decreases

rapidly with increasing air flow rates beyond the minimum spouting, reaching negative values for high air flow rates. As noted by Ojalvo (1989), the spout begins to pulsate and the particle circulation is increased. Ojalvo and Gubulin (1988) have shown that the region of negative pressure extends from the inlet nozzle to 4 or 5 cm above it. In this region, the venturi effect and the downflow of solids contribute to the backflow of air. For the same L_N, this effect diminishes as the included angle increases (as shown by curve 2 in Fig. 2.3b).

The decrease of the spout pressure drop with increasing air flow rates beyond V_{ms} was reported for a 2DSB of glass beads using a flat base column (Passos et al., 1988). Morgan et al. (1989) have noted the existence of a large negative pressure at the inlet of the spouting systems characterized by $H > H_{max}$ in a CSB with a flat base. The authors suggested that this phenomenon is due to the large fluid momentum exchange occurring in the inlet region. It is possible that the decrease of the spout pressure drop observed in 2DSBs is related to H_{max} ; however, there is no correlation or even studies to determine H_{max} for a 2DSB.

Based on these results, it can be concluded that further studies are needed to determine the mechanisms of spout termination in 2DSBs as well as to obtain a general correlation for H_{max} as a function of particle properties, the column and nozzle dimensions.

2.2 Dynamics of Spouted Beds

To describe the aerodynamics and solids flow characteristics, it is necessary first to specify the fluid-solid and solid-solid interaction

forces in the annulus and in the spout, and the boundary conditions at the spout-annulus interface.

In a CSB of coarse particles, several models have been developed to determine the minimum spouting pressure drop and velocity (see e. g. Mathur and Epstein, 1974; Epstein et al., 1978, and more recently Littman and Morgan, 1988). The most comprehensive semi-empirical model was the one presented by Morgan and Littman (1980) and Littman and Morgan (1983). In this model, the authors developed dimensionless groups with physical significance. These groups are listed in Table 2.1. The parameter A is also used to predict the minimum spouting pressure drop and the minimum spouting velocity. The dimensionless H/D_c defines the characteristics of the fluid flow (deep beds: one-dimensional fluid flow regime; shallow beds: two-dimensional fluid flow regime). The equations obtained by Littman and Morgan are given in Appendix A. The parameter C^* in eq. (2.4) (defined by eq. (A.4)) is the dimensionless pressure gradient at the annulus top, and this parameter C^* determines the fluid flow at the top of SBs.

Rovero et al. (1983) and Littman et al. (1985) assumed the particle motion to be negligible and the fluid-particle interaction forces to be described by the vector form of the Ergun equation (Stanek and Szekely, 1974) for modeling the asymmetric fluid flow distribution in the annular region of CSBs of coarse particles.

Rovero et al. (1983) used the equation derived by Epstein and Levine (see Epstein et al., 1978) for the pressure condition at the spout-annulus interface. In their model the conical region of the CSB was taken into account. Rovero et al.'s model can predict qualitatively the fluid

flow distribution in a CSB; however it fails to predict the backflow in the lowest part of the bed which is observed experimentally. As pointed out by the authors, the backflow region is associated with the motion of the solids and the venturi effect near the inlet nozzle. The inclusion of solids downflow should improve their model.

Littman et al. (1985) have used eq. (A.3) to derive the interfacial spout-annulus boundary; they used a CSB of coarse particles with flat base. Their results show the existence of the radial pressure gradient in the lowest region of the spout. Day (1986) measured the axial spout pressure profile, and found that the pressure at the spout-annulus interface becomes a little higher than the radial average pressure across the spout for $y/H < 0.4$.

In both approaches, the spout diameter was assumed constant along the bed level, and was determined by measurements or predicted by the McNab empirical correlation (McNab 1972). This assumption is not valid for the inlet nozzle region where the spout diameter may neck slightly or alternately expand.

McNab and Bridgwater (1974) have attempted to use the Mohr-Coulomb failure criterion to determine the spout dimensions as a function of the bed level. They concluded that the location of the spout-annulus interface is a function of the normal radial stress at the spout wall, the solid and solid-wall friction angles and the diameter of the column. The normal radial stress at the interface depends on the gas flowing from the spout to annulus and on the spout particles pounding the interface. Although these researchers have not obtained an analytical function for the radial normal stress at the spout-annulus interface, their results

can be used to elucidate the solids motion in the annular region. They have shown that the particle slip angle should vary along the radial coordinate. Moreover, there is a point between the spout interface and the vessel radius where the vertical effective stress becomes the principal stress for a rough vessel wall. This means that the slip particle velocity must vary with the radial coordinate.

Several models have been suggested for calculating the particle circulation rates in a CSB of coarse particles based on the dynamics of the spout region. Mathur and Epstein (1974) and Day (1986) have presented critical reviews of these models. Basically, two approaches are used to describe the spout region: one based on a force balance of individual particles and the other based on the mass and momentum balances for continuous solid and fluid phases. Both approaches require numerical solution of the respective differential equations. The difficulty encountered is to define the solid-fluid interaction force in the spout region where particle acceleration and deceleration exist together.

Day (1986) has presented an interesting numerical solution of the mass and momentum equations. In this model, the solid-fluid interaction drag coefficient is obtained naturally instead of being postulated a priori. His model is based on:

(i) the axial spout porosity distribution at minimum spouting;

(ii) the Morgan and Littman (1980) correlation for the pressure drop distribution on the spout-annulus interface at minimum spouting;

(iii) the Grbavcic et al. (1976) equation for the fluid velocity at the annulus region;

(iv) the assumption of constant spout diameter.

Day (1986) relaxed the later assumption to fit his experimental data. For practical applications, a simplified analytical solution for the particle circulation rate was also obtained as a function of C_o and the spout porosity at the top of the spout. The latter parameter is the only unknown, as seen in eq. (A.7) (Appendix A). Empirical correlations for evaluating the spout bed porosity at the top of the annulus were given by Day (1986) based on the fountain height.

It is important to note the work developed by Patrose and Caram (1984) on 2DSBs. They worked in a small 2D column, and with a very shallow bed. The spout particle velocity was measured by a fiber optics probe anemometer. Their results show a maximum for the spout particle velocity at $0.1 < z/H < 0.2$. Beyond this maximum, the particle is decelerated until it reaches the top of the spout. These experimental results are very similar to those reported by Day (1986) for a CSB with flat base. It proves that the dynamics in a 2DSB can be compared with those in a CSB, if correct dimensionless groups are used to assure dynamic similarity.

2.3 Flow Regime Maps in Spout-Fluid Beds

Nagarkatti and Chatterjee (1974), Dumitrescu (1981), Heil and Tels (1983), Vukovic et al. (1984) and Sutanto et al. (1984) have investigated the various flow regimes in SFBs using air as the spouting fluid. Although they used different distributor designs, this is not important for mapping the different flow regimes. The flow regimes have been mapped following the coordinates proposed first by Vukovic et al. (1984)

in order to observe the characteristics and similarities among these data.. In this diagram, the abscissa is the square root of the dimensionless spout inlet superficial velocity (V_s/V_{mf}); the ordinate is the square root of the dimensionless annulus inlet superficial velocity (V_a/V_{mf}). The square root is used because of $V_a + V_s = V_{mf}$ in a fluidized bed. As shown by Vukovic et al. (1984), all the flow regimes must lie inside the quarter of a circle which has a radius equal to $(V_T/V_{mf})^{1/2}$.

Some of the flow regime diagrams obtained here based on Dumitrescu's (1981), Sutanto et al.'s (1984), and Heil and Tels' (1983) data are shown in Figure 2.4. The geometric and dynamic parameters for these diagrams are given in Table 2.4. Basically, there are four flow regimes common to all maps:

(i) Fixed Bed - characterized by the formation of a spout cavity and where the particles are not in continuous motion. The upper limit curve of this regime is given for $V_s = V_{msf}$;

(ii) Spouting with aeration - characterized by aeration of the annular region but with the behavior of the bed similar to the pure spouting. In this regime $V_s > V_{msf}$ and $V_a < V_{mf}$;

(iii) Spout-Fluidization - characterized by a jet immersed in a fluidized bed but with solids circulation due to solids entrainment into the jet. The jet is generally in a pulsating motion. This type of regime was identified by Yang and Keairns (1982) as a permanent-flame-like jet regime;

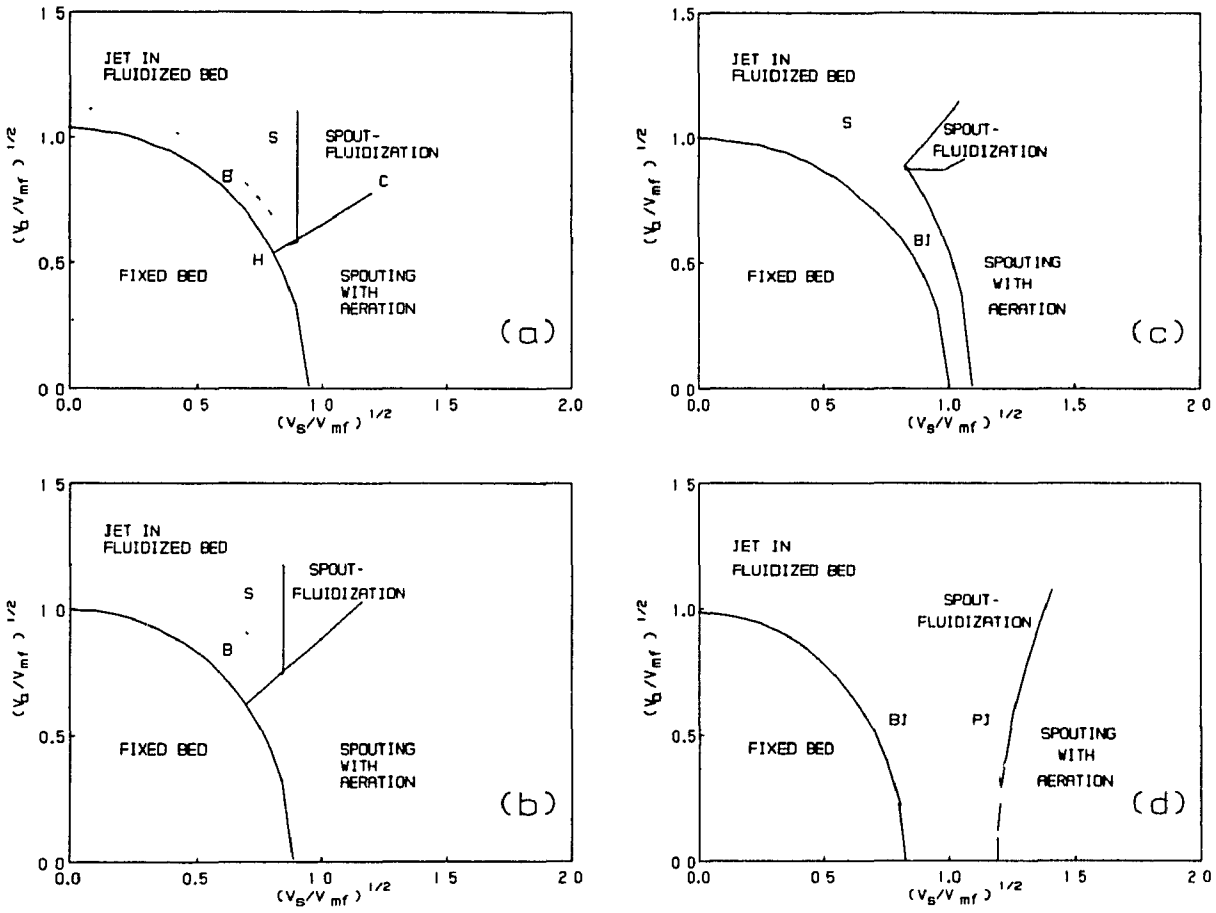

FIGURE 2.4 - Flow Regime Maps for CSFBs of Coarse and Fines Particles following Vukovic et al. (1984).
(a) and (b): Dumitrescu's (1981) data; (c): Sutanto et al.'s (1984) data; (d): Heil and Tels' (1983) data.
B - bubbling, S - slugging, BJ - bubbling jet, PJ - pulsating jet.

TABLE 2.4

GEOMETRIC AND DYNAMIC PARAMETERS FOR DATA IN FIGURE 2.4.

DATA	D_c (m)	D_c/D_i (-)	d_p (mm)	h (-)	A (-)	NOTE
(a)	0.15	9.4	3.2	0.76	0.037	non-spherical particle
(b)				0.57		
(c)	0.152	8.0	2.9	0.67	0.013	non-spherical particle
(d)	0.152	15.2	0.56	(*)	0.004	sand particles
				H=0.3m		

(*) H_{max} not available.

(iv) Jet in Fluidized Bed - characterized by a bubbling jet immersed in a fluidized bed. In this regime the jet breaks up into bubbles near the inlet nozzle. Solids mixing occurs due to the rise of these bubbles. For coarse particles, these bubbles coalesce generating slugs. As a result, bubbling and slugging regimes can occur. This regime is achieved for $V_a > V_{mf}$ and $V_a < V_{ms}$.

The effect of particle sphericity seems to be related to the slope of the line HC in diagram (a) in Fig. 2.4. The HC line is horizontal for spherical particles as shown in Fig.6 from Vukovic et al. (1984). Nagarkatti and Chatterjee's (1974) data show the same trends for spherical particles. This means that the region of spouting with aeration is reduced as the particle sphericity increases. Note that for the Vukovic et al. data, A=0.033 and h=0.52; this is in the same range for diagram (b).

The effect of bed height can be seen by comparing diagram (a) with (b). As the bed height increases, the spouting with aeration region is reduced, as predicted by Vukovic et al. (1984). At h=1 the spouting with aeration regime must disappear.

As shown in Table 2.4, the parameter A is lower for diagram (c) (A<0.014). This means that the mechanism of spout termination, diagram (c), is characteristic of low inlet jet momentum. When diagram (c) is compared with diagram (a), it can be seen that there is a transitional flow regime between fixed bed and spouting with aeration regimes for A < 0.014. This transitional flow regime is characterized by smaller bubbles reaching the bed surface (Sutanto et al. 1984). Heil and Tels worked with fine sand particles with very low values of A (see Table 2.4). Their map presents this transitional regime, which is characterized by a bubbling - pulsed jet (the spout cavity breaks into bubbles which rapidly ascend vertically to the surface; the annulus region is not fluidized as in the case of spout-fluidization and jet in a fluidized bed regimes).

The aerodynamics of SFBs have been studied by Hadzismajlovic et al.

(1983). These researchers have developed a semi-theoretical model to describe the minimum spout fluid condition in beds of coarse particles. Some of the assumptions in their model are inconsistent (see Vukovic et al., 1987); however, their empirical constants seem to correct any inconsistencies in their model. Povrenovic et al. (1987) used Hadzismajlovic et al.'s model to describe the aerodynamics in a conical spouted bed; the agreement with their experimental data is quite good. More details of the Hadzismajlovic et al. empirical model are presented in Chapter 8. Concerning the pressure drop and gas flow distribution along the annular region of the spouting with aeration bed, Heil and Tels (1983) have solved the momentum and mass balances for the fluid phase. They assumed Darcy's law for the calculation of the fluid-solid interaction forces; this assumption is valid for fine particles.

Donadono and Massimilla (1978), Massimilla et al. (1981), Yang and Keairns (1982), Filla et al. (1983), and Yang et al. (1984) presented a comparative study for the spout-fluidization and jet in fluidized bed regimes. It is not within the scope of this work to analyze the dynamics in these two regimes. This work is restricted to the aerodynamics of a 2DSFB in the spouting with aeration and the spout-fluidization regimes.

2.4 Closure

In summary, the following conclusions can be drawn from this literature review:

(a) Spout termination mechanism in Spouted Beds:

1 - The mechanism of spout termination for coarse particles is understood as being fluidization of the top layers of the annulus. Eq.

(2.1) and the dimensionless group A, defined by eq. (2.2), can be used as a criterion of spoutability with A > 0.02 (spherical particles) or A > 0.014 (non-spherical particles).

2 - Choking of spout is the mechanism of spout termination for fine particles or SBs with low value of A. The criterion of spoutability is not well defined for beds with low values of A. For gases, eq. (2.8) with A > 0.003 may be a reasonable criterion. However, more research in this area is necessary to describe this mechanism.

3 - The mechanism of spout termination in a 2DSB has not been well analyzed. The growth of instabilities described by Volpicelli et al. (1967) is not well defined as a mechanism of spout termination. The analysis developed here shows that the same bed of particles can behave similarly to a CSB of coarse particles as well to a CSB of fine particles depending on the value of L_N. A small increase in L_N can change the spout termination mechanism due to the large increase in the cross sectional inlet area. The dimensionless parameter A, proposed by Littman et al. (1988) for characterization of the spouting of CSBs of coarse particles, has been redefined here for a two dimensional geometry. However, more data are needed in order to analyze the spout formation and to predict the maximum spoutable bed height;

(b) Bed dynamics of SBs and SFBs:

4 - Theoretical models have been obtained (rather than empirical correlations) to describe the dynamics of CSBs of coarse particles. However, some aspects are yet unknown regarding the spout-annulus interface boundary.

Based on the brief review of the flow regime diagram for CSFBs, the

following conclusions may be drawn:

5 - There are basically four regimes in a SFB: fixed bed; spouting with aeration; spout-fluidization and jet in fluidized bed. An additional unstable regime was identified here for CSFBs characterized by low inlet jet momentum (low value of A);

6 - The description of the dynamics in SFBs is in developmental stage. Empirical correlations exist in the literature but they are restricted to the range of experimental parameters used to derive them.

CHAPTER 3

EXPERIMENTAL SETUP AND PROCEDURES

3.1 Spouted Bed and Spout-Fluid Bed Apparatus

A rectangular column was made of plexiglas (wall thickness 6.35 mm) to allow visual observation of particle movement. Its dimensions were: 0.20 m x 0.015 m cross sectional area and 0.5 m height. The column rested on a rectangular calming section as shown in Figure 3.1.

A perforated plate with 18% free area (1.6 mm holes on 3.60 mm triangular pitch) was used to distribute air in the "annular" region of the bed. (Note: although the word annulus is normally used for the cylindrical geometry, it is used here for a rectangular geometry to maintain the usual nomenclature of spouted beds; it refers to the downcomer section).

The inlet nozzle, inserted centrally into the calming section, was projected 7 mm above the base of the column. This design assures a more stable spouting operation as pointed out by Mathur and Epstein (1974). Two nozzles were tested: 0.015 m x 0.030 m and 0.015 m x 0.015 m. A wire screen was welded at the nozzle top to prevent the particles from falling into the plenum.

An air compressor and a centrifugal blower were used to supply air (at atmospheric conditions) to the spout and annulus lines, respectively. A by-pass valve controlled the air flow rate in each line. Figure 3.2 displays a schematic sketch of the equipment and instrumentation used for the experiments.

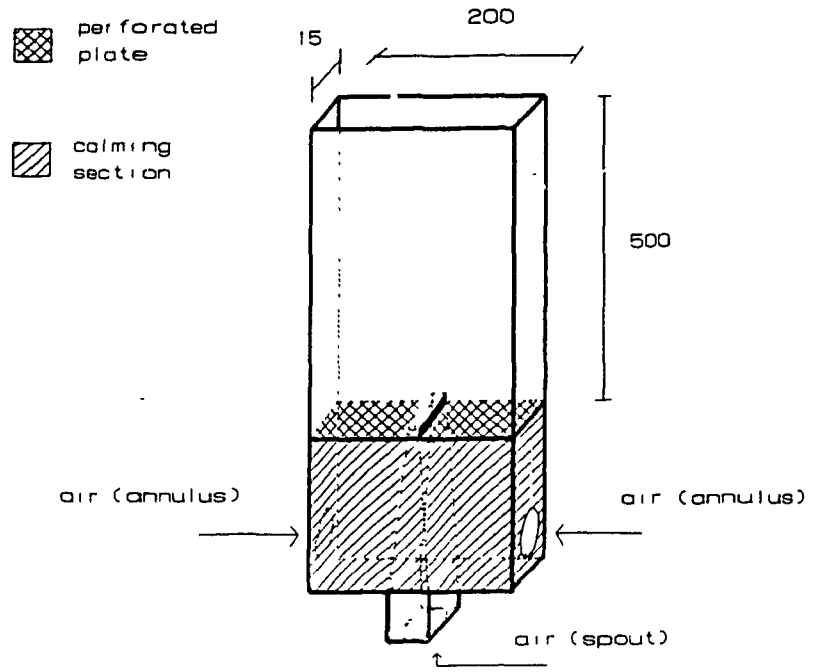

FIGURE 3.1 - Schematic Representation of the Rectangular Bed Column. (All dimensions are in mm).

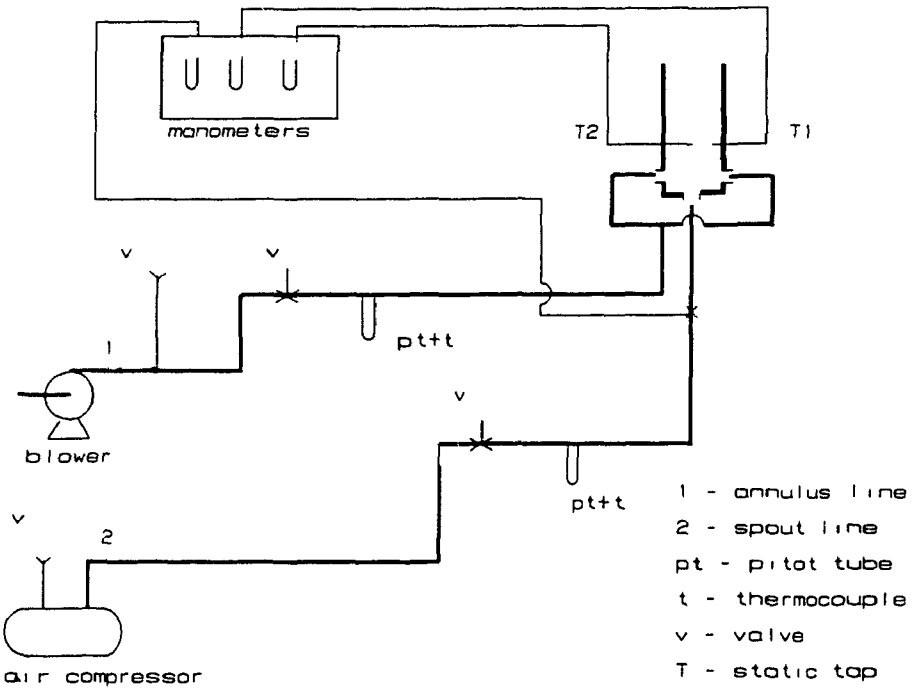

FIGURE 3.2 - Layout of Equipment.

Air flow rates were measured by calibrated pitot tubes (Dwyer model 167-6) placed on each line. Micromanometers (M/S Wilh Lambrecht AG, Göttigen) with a manometric fluid (Meriam red, specific gravity = 1.0) recorded the pressure drops to compute the inlet air velocities. Each pitot tube was calibrated in-line using a dry gas flowmeter.

The static pressure taps (2 mm I.D.) were located in the back wall face of the column 1.7 cm from the base of the column. The spout pressure tap was set centrally in the column wall; the annulus pressure tap was set midway between the nozzle and the outer edge of the bed. The openings of both taps were covered (if necessary) with a fine gauze to prevent particles entering the openings. The pressure drop was measured by U-tube manometers (Meriam red manometric fluid) with the top of the bed open to the atmosphere.

The air temperature was recorded by a digital thermometer (Omega Model 2160) using thermocouples (Omega type J) installed in each inlet line. The air humidity was obtained by local measurement of the dry-wet bulb air temperature. The mean values of air temperature and humidity obtained during each run were used to evaluate the air properties.

The bed height, spout dimensions, the extent of the dead zone and the particle displacements were measured by millimeter scale tapes affixed on the sides and center of the bed column. Photographs were also taken to verify these measurements.

3.2 Experimental Design and Procedure

The experimental program was divided into three different steps as shown in Table 3.1. The experiments were designed to meet the basic

TABLE 3.1

EXPERIMENTAL PROGRAM

STEPS	SPECIFIC OBJECTIVE (for scale-up, design)	GENERAL OBJECTIVE (for modeling)
1-Fluidization experiments	to determine the air-solid dynamic properties	to specify the air-solid interaction force
2-Spouting experiments	to define the range of stable spouting	to specify the spout instability mechanism
	to determine the solids circulation rates	to specify the solid-solid interaction forces
3-Spout-fluid experiments	to define the types of flow regimes and their operation ranges	to specify the air flow characteristics in spout and annulus

objectives of each step.

The experimental parameters for characterization of the air-solid system are shown in Table 3.2. Barley, glass beads, linseed, millet, molecular sieve, plastic pellets, rice, sesame seed and wheat were used as the model particles. The equivalent sphere diameter, d_p, was used to characterize the particle size. As noted by Clift (1987), d_p is expected to be close to Stokes' diameter for particles which do not have very "plated" or very elongated shapes.

TABLE 3.2

EXPERIMENTAL PARAMETERS FOR

CHARACTERIZATION OF THE AIR-SOLID SYSTEM

A - SOLID PHYSICAL PROPERTIES:		
1 -	solid density	ρ_s
2 -	particle shape	d_p, ϕ
3 -	bed porosity at static condition	ϵ_o
B - AIR PHYSICAL PROPERTIES:		
1 -	air density	$\rho_f(T,RH)$
2 -	air viscosity	$\mu_f(T)$

Particle sphericity, ϕ , defined as the ratio of the surface area of the equivolume sphere to the actual particle surface, characterizes the particle shape. To determine d_p and ϕ , a random sample was taken from each particle population. This sample, collected after intensive mixing, was randomly divided into sub-samples containing one hundred particles each. Two to four sub-samples were used. The particle dimensions were measured by a micrometer (with an estimated error of $\pm$ 0.017 mm in 3 consecutive measurements). The bed porosity at static condition was

determined by the solid and bulk densities. The solid density, ρ_s, was obtained by measuring the volume of liquid displaced by a known mass of particles. For grains, the liquid used was toluene, following Becker (1959). For molecular sieve, it was glycerol. A digital balance (Bosch PE620 with accuracy of $\pm$ 0.1 g) and a graduated glass container (with an estimated error of $\pm$ 0.12 ml in three consecutive measurements) were used in this procedure. Five to six replicates were performed for each material. The bulk density was determined by weighing the amount of particles necessary to fill a specific known volume in the 2D column. The air properties were obtained from correlations and charts presented in handbooks (Perry and Chilton, 1973).

The design of the fluidization experiments is presented in Table 3.3. Three different particle types (wheat, millet and linseed) were chosen in this step. The static bed height was varied in the range displayed in Table 3.3. The experiments were carried out during summer (RH = 60% $\pm$ 5% and T_b = 26°C $\pm$ 3°C) and winter (RH = 30% $\pm$ 2% and T_b = 19°C $\pm$ 1°C) seasons. The bed of particles was prepared in a standardized manner before starting each run. Particles were poured slowly inside the column until the desirable value of H_o was reached. The bed was fluidized continuously for five minutes. The air supply was then shut off, and the bed allowed to rest for one or two minutes. This standard procedure allowed good reproducibility of the measurements as shown in the next section. H represents the expanded bed height obtained after the bed preparation. H_{mf} represents the expanded bed height minus the height of the pressure static tap used in the measurements.

TABLE 3.3

DESIGN OF FLUIDIZATION EXPERIMENTS

A - DESIGN VARIABLES:	
1 - Particles:	wheat, millet, linseed (*)
2 - H_o:	0.10 m to 0.25 m
3 - RH :	2 different ranges RH= 30% and RH= 60%
4 - T_b:	19°C to 29°C
B - MEASURED VARIABLES:	
1 - ΔP, V	
2 - H, H_{mf}	
C - EXPERIMENTAL PARAMETERS AND CORRELATIONS:	
1 - $\Delta P / H_{mf} = f(Re)$	
2 - ϵ_{mf} , V_{mf} , V_{mb} , V_G	

(*) other air-solid systems were used in specific range to check the empirical correlations.

In these experiments, the spout flow valve was closed completely. Air was injected in the annular region only through the porous plate distributor. Pressure drop versus superficial velocity curves were obtained at different static bed heights. The pressure drop was measured at the center of the bed (by the spout static tap - T2) and midway of the right side of the column (by the annulus static tap - T1). Bed expansion (or contraction) were computed for each run. Qualitative observations of bubble formation and growth were made for different bed heights. Additional experiments using other particles at specific conditions were carried out to complement these data.

The design of the spouting experiments is shown in Table 3.4. The effect of nozzle dimensions on spout stability was analyzed for two types of particles (wheat and molecular sieve). Based on experimental results, L_N was selected and fixed for subsequent experiments. The static bed height was varied from 0.10 m to H_o close to H_{max}. Six different types of particles (barley, linseed, millet, molecular sieve, rice, and wheat) were used. The bed of particles was prepared in a standardized manner before starting each run. The particles were poured slowly inside the column and were spouted for five consecutive minutes. The air supply was then shut off, and the bed allowed to rest for one or two minutes. In these experiments the annulus air line was closed completely. The spout air flow rate was increased slowly until the stable spouting regime was reached. The air flow rate was then decreased slowly. For each increase (or decrease) in the air flow rate, the spout pressure drop, the bed height and the spout dimensions were recorded. The system was allowed to come to steady state before recording the pressure drops. The data were

TABLE 3.4

DESIGN OF SPOUTING EXPERIMENTS

A - DESIGN VARIABLES:	
1 - Particles:	barley, wheat, molecular sieve, rice millet, linseed
2 - H_o:	0.10 m to H_{max}
3 - RH and T_b:	30% and 19°C (mean values) 60% and 26°C (mean values)
4 - L_N:	1.5 cm and 3.0 cm
B - MEASURED VARIABLES:	
1 - ΔP_s , V_s , ΔP_a	
2 - H_{ms}	
3 - shape and dimensions of internal spout cavity	
4 - deformation of bed surface before spouting	
5 - L_s , H_f	
6 - u_y, L_{ds}, H_{ds}	
C - EXPERIMENTAL PARAMETERS AND CORRELATIONS:	
1 - $\Delta P_{ms}(H_o)$, $\epsilon_{ms}(H_o)$, $V_{ms}(H_o)$	= f(air-solid system)
2 - H_{max}	= f (geometric parameters, air-solid properties)
3 - particle slip angle and annulus porosity (at the onset of spouting)	
4 - M_p (V_s, H_o, air-solid properties)	

replicated at least twice.

The vertical particle velocity in the bed annulus was measured by timing the distance necessary for a set of colored tracer particles to travel from the top of the annulus to the lower spout interface. As the solids motion was not true plug flow, the particle velocity was measured as a function of the lateral distance, X_i, at annulus surface. Figure 3.3 summarizes the experimental procedure for the particle velocity measurements. A value averaged over two to seven replicates was used to evaluate the particle velocity at each X_i. The dead zone extent, the spout width and the fountain height were measured for each data set of particle velocity.

Photographs were taken during each run to document and complement the experimental data.

The design of the spout-fluidization experiments is presented in Table 3.5. Millet was select as the model particle. The bed of particles was prepared similarly to the spouting experiments. The annular air flow rate was maintained constant. The spout air flow was gradually increased in small steps. The spout pressure drop and the annulus pressure drop were recorded for each increase (or decrease) in the spout air flow. The procedure was similar to the one used for pure spouting. The different flow regimes obtained were mapped as functions of the annulus and spout velocities, the bed height, the spout formation, and the fountain height.

The vertical particle velocity in the annulus region was measured as described above in the spouting experiments.

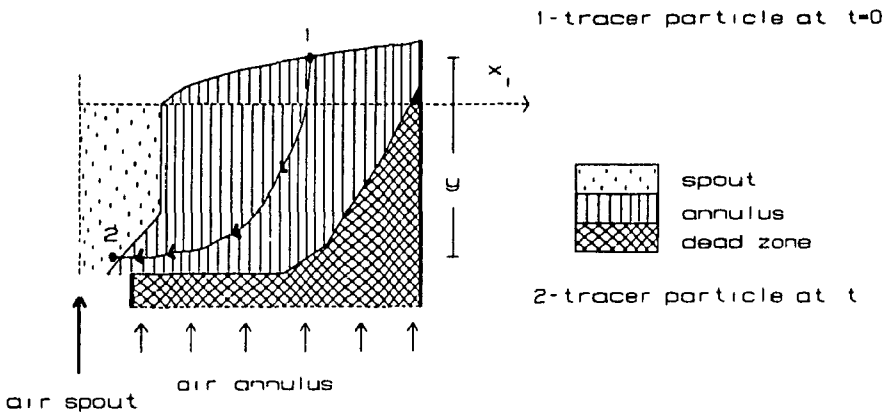

$$u_y = y/t \tag{3.1a}$$

$$\bar{u}_y = \int_{L_s/2}^{X_{iDZ}} u_y \, dX_i \Big/ \int_{L_s/2}^{X_{iDZ}} dX_i \tag{3.1b}$$

$$M_p = (1-\epsilon_a)\, \rho_s \bar{u}_y A_{aeff} \tag{3.1c}$$

FIGURE 3.3 - Schematic Representation of Vertical Particle Velocity Measurements and Correlations used for Solids Circulation Rates.

TABLE 3.5

DESIGN OF SPOUT-FLUID EXPERIMENTS

A - DESIGN VARIABLES:	
1 - Particle:	millet
2 - H_o:	0.10 m to 0.30 m
3 - RH and T_b:	30% and 19°C
4 - L_N:	1.5 cm
5 - V_a:	0 to 1.2 V_{mf}

B - MEASURED VARIABLES:
1 - ΔP_a, ΔP_s, V_s
2 - H_{msf}
3 - L_s, H_s, H_f
4 - u_y, L_{ds}, H_{ds}

C - EXPERIMENTAL PARAMETERS AND CORRELATIONS:
1 - $\Delta P_{msf}(V_a, H_o)$
2 - $V_{msf}(V_a, H_o)$
3 - $\epsilon_{msf}(V_a, H_o)$
4 - Flow regime maps
5 - annulus aeration rate = $f(V_a, V_s, H_o)$
6 - $M_p(V_s, V_a, H_o)$

3.3 Data Replication and Experimental Errors

A comparison between the instrumental error and the standard deviation based on data replications is shown in Table 3.6. The instrumental error was estimated based on the maximum error limits of each instrument used. For the superficial air velocity, it was obtained from the calibration curves of both pitot tubes.

The statistical methods presented by Himmelblau (1970) were used to evaluate the standard deviation. For a measured variable, the following relation was used:

$$SD_p = [(\Sigma \quad (p_i - \bar{p})^2)/(n-1)]^{1/2} \tag{3.2}$$

where: n is the total number of replications;

p_i is the individual measured value for the variable p;

$\bar{p}$ is the mean value of the variable;

SD_p is the standard deviation of the variable.

The pooled deviation of the data set was, then, estimated by:

$$SD = [\Sigma \quad (n_j - 1)\, SD_{pj}^2 / \quad \Sigma \quad (n_j - 1)]^{1/2} \tag{3.3}$$

where: SD is the standard deviation of the data set;

n_j is the number replication for each, j, group of data;

SD_{pj} is the standard deviation of the variable at each j.

For dependent variables represented as:

$$Y = c\, p_1^{a1} p_2^{a2} \ldots p_n^{an} \tag{3.4}$$

with: p_1, p_2 .... p_n - the independent measured variables;

TABLE 3.6

MEAN EXPERIMENTAL ERROR FOR THE MEASURED VARIABLES

VARIABLE	RANGE	INST. ERROR (*) (%)	EXP. ERROR (**) (%)
V (m/s)	0 - 0.45	5	
	0.45 - 2.50	1 - 3	
Δ P (Pa)	0 - 2000	< 1	
Δ P (Pa) versus V (m/s) curves			2 - 6
u_y (cm/s)	0 - 25	5 - 8	5 - 12
ϵ (-)	0.30 - 0.50	1	1 - 3
ϕ (-)	0.57 - 1.00		1 - 3
d_p (mm)	1.90 - 3.92	< 1	< 1
ρ_s (kg/m ^{3})	1067 - 2521	1	1

(*) instrumental error: based on the error limits of each instrument

(**) experimental error: based on data replication.

c, a_1, ... a_n - constants;

the standard deviation of Y was determined by:

$$(SD_Y / Y)^2 = a_1^2 (SD_{p1} / p_1)^2 + \ldots + a_n^2 (SD_{pn} / p_n)^2 \qquad (3.5).$$

Figure 3.4 illustrates typical data replicates for the spout pressure drop and for the packed bed pressure drop curves. The experimental standard deviation at replicated points is within the limits of the instrumental error (see also Table 3.6). It is important to emphasize that the reproducibility of these data depends upon the initial configuration of the bed.

The mean deviation of particle dimensions is 9%. This high value is due to the non-homogeneity of particle sizes. A mean standard error of 0.6% is expected for the particle diameter. The bed height, the spout and the dead zone dimensions present experimental errors in the range of 1 - 3%, depending on the particle dimensions.

For the vertical particle velocity measurements, the experimental standard deviation increases systematically as X_i decreases. For lower values of X_i (close to the spout-annulus interface) SD reaches values as high as 40%. The increase of SD is related to the spout motion. As shown in Chapter 7, the spout oscillates periodically around the central axis of the column. It produces a periodic oscillation in the annular particle velocity. When the spout moves towards the right side of the column, the vertical particle velocities reach maximum values on this side of the annular region. While, on the left side of the annulus, the vertical particle velocities reach minimum values. As the spout moves towards the left side of the column, this condition is reversed. These maximum and

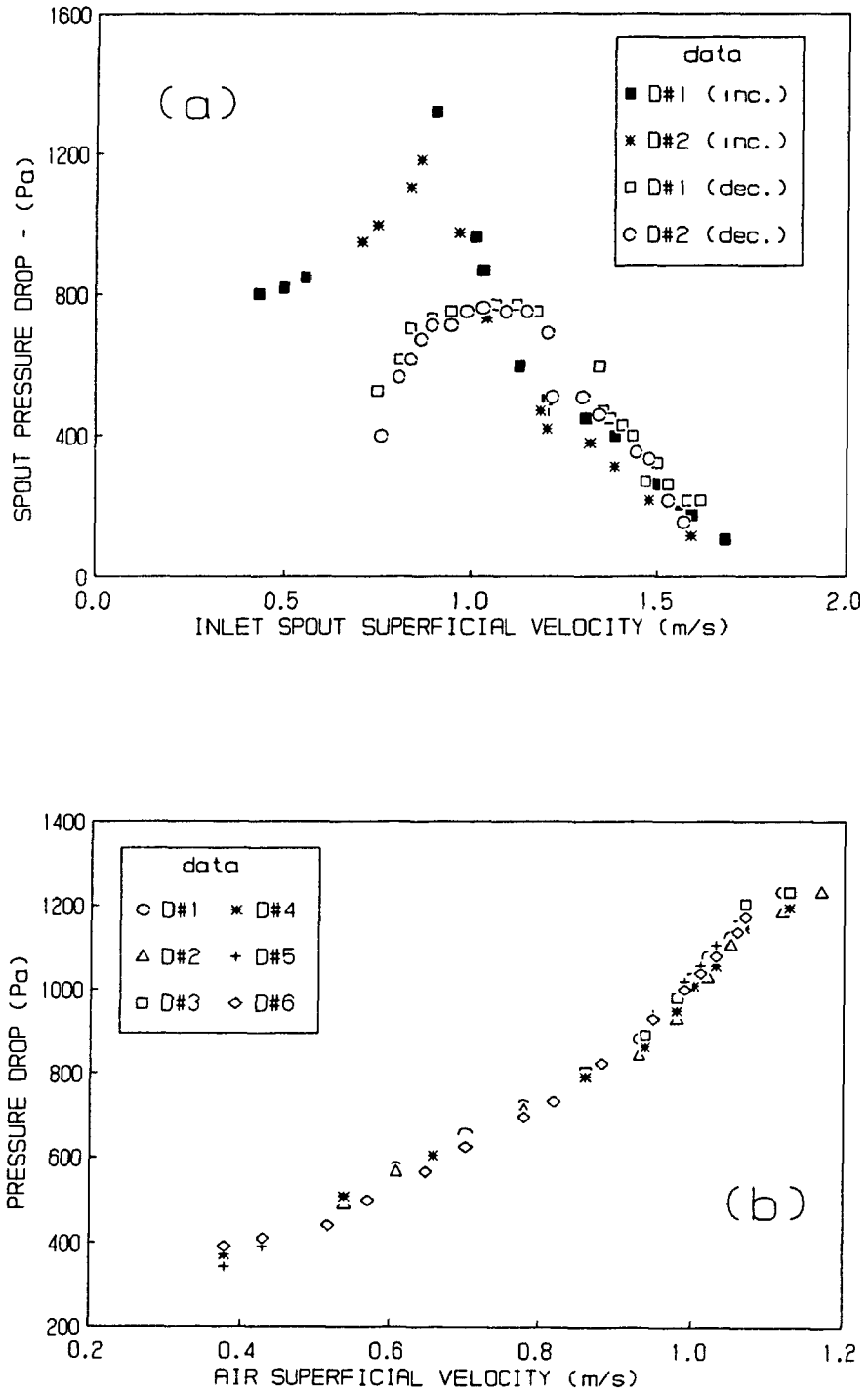

FIGURE 3.4 - Data Replication for Pressure Drop Characteristic Curves.
(a) Spout-fluidization: glass beads; H_o = 0.10 m; V_a = 0.45 m/s. (b) Packed bed: barley; H_o = 0.17 m.
D#n = data replication number n; inc. = increase of air velocity; dec. = decrease of air velocity.

minimum values of velocities obtained for the vertical particle velocity are compared in Figure 3.5. Curve 1 in Figure 3.5 represents the maximum velocity values obtained. Curve 2 represents the minimum velocity values. The mean velocity values given by curve 3 represent the data for which the spout is in the center of the column. From Figure 3.5, it can be seen that for lower values of X_1 the oscillation about the mean value is higher. This explains the high standard deviation obtained when all the points are used to calculate the mean value. However, in this case, a high standard deviation does not imply a high experimental error, but fluctuations of the particle velocity around a mean value. From Figure 3.5, the experimental error for duplicate data is about 5% to 12%. In addition, it is important to note that only the mean points (corresponding to curve 3 in Figure 3.5) were used to calculate the solids circulation rates.

Based on these results, it can be concluded that the experimental techniques and procedures are of adequate accuracy and reproducibility to provide reliable data.

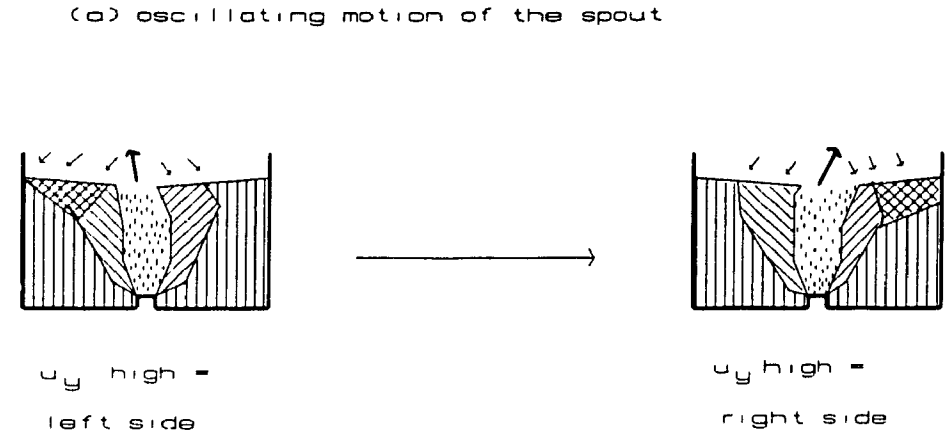

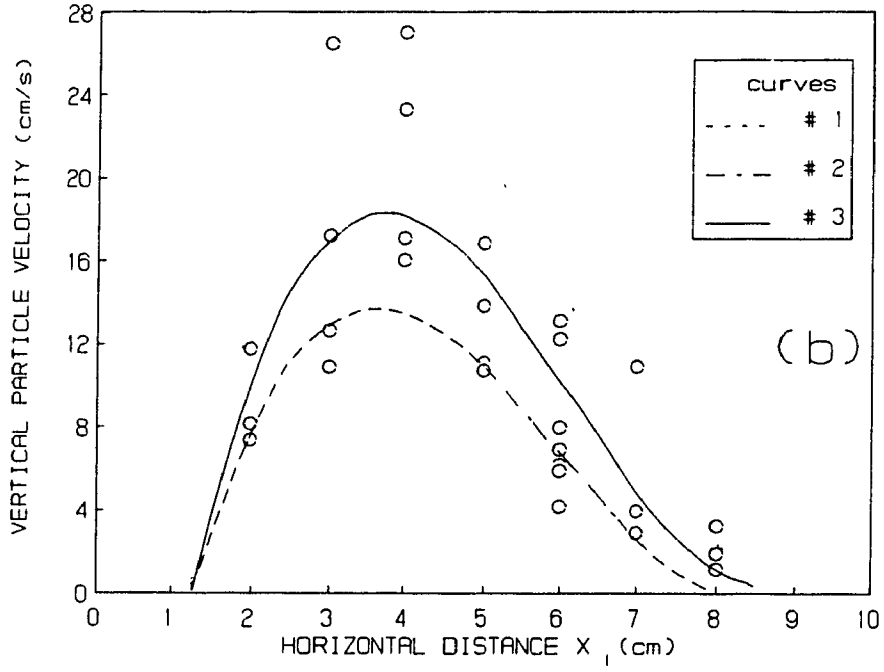

FIGURE 3.5 - Data Replication for Vertical Particle Velocity.
(a) Scheme of spout oscillations. (b) Experimental data for SB of wheat: H_o = 0.17 m; V_g = 1.65 m/s.
Curve 1 = best fit for the maximum points, curve 2 for the the minimum points, curve 3 for the mean points.

CHAPTER 4

PARTICLE CHARACTERIZATION

4.1 Physical Properties of Particles Used

For the spherical glass beads used in this study, the particle diameter, d_p, was supplied by the manufacturer, Fisher Scientific Company to be 3 mm ($\pm$ 0.01 mm). Measurements on randomly taken samples authenticated this value. Microscopic analysis of these samples confirmed the sphericity of these particles. The wheat particle dimensions were obtained from Kalwar et al. (1986), who worked with the same batch of wheat as used in this work.

For the other non-spherical particles, the average measured value for the length, width and thickness and the corresponding standard error are presented in Table 4.1. The heterogeneity in size for rice was wide because of the significant amount of broken grains.

For calculation of the particle sphericity, the shape of particles was approximated to one of the following geometries:

i) A prolate spheroid for wheat, barley and rice;

ii) An oblate spheroid for millet;

iii) A combination of ellipsoidal and cylindrical geometries for linseed and sesame seed;

iv) A parallelepiped for plastic pellets.

Table 4.2 lists the mean particle diameter, the sphericity and the dimensionless ratio $L_1/d_p\,\phi$ for the particles used.

Linseed, glass bead and plastic pellets had a smooth surface while the other particles presented some asperities in their surfaces. The

TABLE 4.1

PARTICLE DIMENSIONS FOR THE GRANULAR SOLID MATERIALS

(non-spherical particles)

MATERIAL	LENGTH (mm)	WIDTH (mm)	THICKNESS (mm)
BARLEY	4.81 (0.03)	3.21 (0.01)	2.53 (0.01)
LINSEED	4.76 (<0.01)	2.50 (<0.01)	1.31 (<0.01)
MILLET	2.44 (0.01)	2.34 (<0.01)	1.91 (<0.01)
PLASTIC PELLETS	3.15 (0.02)	2.42 (0.02)	2.10 (0.02)
RICE	6.01 (0.07)	2.21 (0.01)	1.88 (<0.01)
SESAME SEED	3.05 (0.04)	2.05 (0.03)	1.10 (0.02)
WHEAT (*)	6.59	3.09	2.95

(*) Kalwar et al. (1986).

Note: the mean standard error of each length (obtained over 400 measurements) is presented in parentheses below the corresponding variable.

TABLE 4.2

PARTICLE SIZE AND SHAPE FOR THE GRANULAR SOLID MATERIALS

MATERIAL	d_p (mm)	ϕ (-)	$L_1/d_p\phi$ (-)
SESAME SEED	1.90	0.70	150.36
LINSEED	2.50	0.57	140.35
MILLET	2.21	0.98	92.34
RICE	2.91	0.84	81.82
PLASTIC PELLETS	3.13	0.80	79.87
GLASS BEAD	3.00	1.00	66.67
BARLEY	3.39	0.95	62.10
MOLECULAR SIEVE	3.42	1.00	58.49
WHEAT	3.92	0.91	56.07

Note: the range of the experimental error for these variables is already presented in Table 3.6.

grain surface roughness increased in the following order: millet, rice, wheat, sesame seed, and barley. Molecular sieve presented a soft rough surface, causing significant dusting during the spout-fluidization experiments. Hence, molecular sieve was not used in these experiments.

The grain solid densities were measured at ambient condition with RH = 30%. To evaluate ρ_s at RH = 60%, the following correlation was used (Becker, 1959):

$$\rho_{s2} = (1 + m_2)\rho_s^* / (1 + m_2 \rho_s^* / \rho_w) \qquad (4.1)$$

with: $\rho_s^* = \rho_{s1} / (1 + m_1 (1 - \rho_{s1} / \rho_w))$;

ρ_w representing the water density;

subscripts 1 and 2 representing, respectively, RH= 30% and RH= 60%.

The equilibrium moisture contents, m_1 and m_2, were calculated based on the sorption curves reported in the literature (Baxter and Hahn, 1982). The grain bulk density was measured at RH = 30% and 60%.

The solid and bulk properties for the solid material used are shown in Table 4.3. The variation of the grain solid density with RH is negligible (less than 2%). However, the variation of the grain bulk density (or the static bed porosity) becomes significant for millet, barley and linseed. This variation is the result of the change in the particle-wall interactions, as discussed in Appendix B.

Mixtures of linseed and millet particles were used to analyze the segregation in a 2D-fluidized bed. The following mass proportions were

TABLE 4.3

SOLID AND BULK PROPERTIES FOR THE GRANULAR SOLID MATERIALS

MATERIAL	ρ_s (kg/m^3)	SE (%)	ρ_b (kg/m^3)	SE (%)	ϵ_o (-)	SE (%)	m (d.b.)	RH (%)
BARLEY	1406	1.3	838	1.3	0.404	1.6	0.085	30
	1385		873		0.370		0.128	60
GLASS BEAD	2521	0.2	1545	0.5	0.339	0.8	-	-
LINSEED	1143	0.7	703	1.7	0.385	1.5	0.055	30
	1139		731		0.358		0.079	60
MILLET	1319	2.0	799	3.0	0.394	3.5	0.100	30
	1303		834		0.360		0.144	60
MOLECULAR SIEVE	1250	1.0	778	1.7	0.378	2.0	?	30
			795		0.364			60
PLASTIC PELLETS	1217	1.0	822	1.7	0.326	2.0	-	30
RICE	1440	1.0	792	3.7	0.450	3.6	0.095	30
	1419		805		0.433		0.133	60
SESAME SEED	1067	0.4	651	0.5	0.390	0.7	?	30
WHEAT	1273	0.9	771	1.8	0.394	2.0	0.084	30
	1258		779		0.380		0.134	60

SE = standard error.
Note: the standard error for the moisture content varies from 0.007 to 0.005 d.b. The standard error for the particle properties at 60% is estimated to be 3%.

used in the experiments:

	linseed	millet
Mixture #1	67%	33%
Mixture #2	47%	53%
Mixture #3	28%	72%

The particle volume (V_p) and the particle surface area (S_p) for these mixtures were calculated, respectively, using the following equations:

$$V_p = (X_{v1}/V_{p1} + X_{v2}/V_{p2})^{-1} \tag{4.2}$$

$$S_p = X_{v1}(d_p/d_{p1})^3 S_{p1} + X_{v2}(d_p/d_{p2})^3 S_{p2} \tag{4.3}$$

where the subscripts 1 and 2 represent the first and second components of the mixture; and X_v the volumetric concentration.

The solid density was calculated through a relation similar to eq. (4.2) using mass concentration instead of volumetric concentration. Table 4.4 summarizes the results obtained for the properties of these mixtures.

4.2 Fluidization in a Two Dimensional Bed of Coarse Particles

4.2.1 Particle Classification:

Following Geldart's classification (Geldart, 1973) all the particles used in this work belong to group D, coarse or spoutable particles, as shown in Figure 4.1.

TABLE 4.4

PHYSICAL PROPERTIES FOR MIXTURES

OF LINSEED AND MILLET

(RH = 60%)

MIXTURE	ρ_s (kg/m^3)	ρ_b (kg/m^3)	ϵ_o (-)
M#1	1188	744	0.374
M#2	1221	765	0.373
M#3	1253	815	0.350

MATERIAL	d_p (mm)	ϕ (-)	$L_1/d_p\phi$ (-)
M#1	2.40	0.66	126.26
M#2	2.34	0.73	117.08
M#3	2.26	0.86	102.90

Note: the standard error estimated for the mixture properties is 3%.

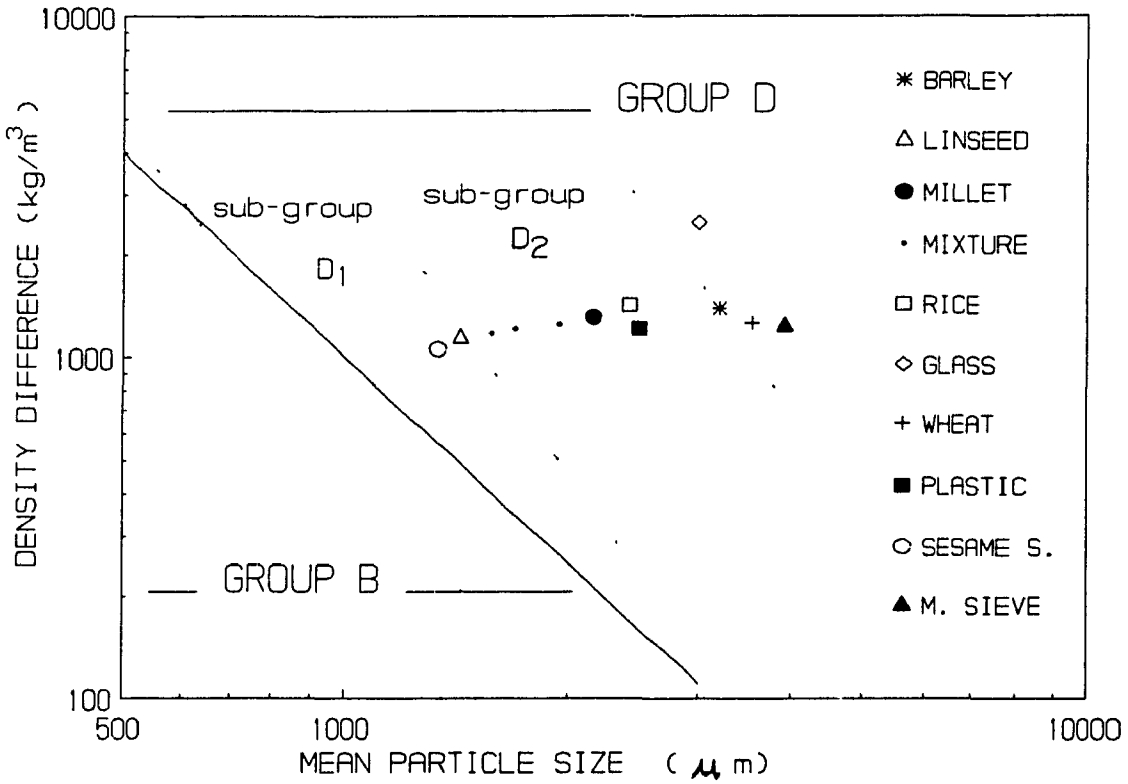

FIGURE 4.1 - Particle Classification following Geldart (1973) and Saxena and Ganzha (1984).
(Note: mean particle size = d_p ϕ).

Saxena and Ganzha (1984) complemented Geldart's classification dividing the transition region between group B and group D into two different sub-groups (see Fig. 4.1). In sub-group D_1, the viscous air-particle interaction force is more important but not dominant as it is in Geldart's group B. In sub-group D_2, the air inertial force becomes more important but not dominant as it is in the true Geldart group D.

As shown in Fig. 4.1, sesame seed and linseed belong to sub-group D_1. Millet-linseed mixtures, millet, rice and plastic pellets belong to sub-group D_2. Wheat, barley and glass beads are the truly group D particles. Linseed, millet and wheat were chosen from each sub-group to characterize the effect of bed heights, and of the air relative humidity on the particle interactions. Millet-linseed mixtures were used to analyze the effect of particle size distribution on the dynamics of 2D-fluidized beds. Data obtained for the other particles at specific conditions were used to complement this analysis.

4.2.2 Effect of Bed Height:

The minimum fluidization properties for linseed, wheat and millet as a function of bed height are presented in Tables 4.5, 4.6 and 4.7. The ambient air with relative humidity close to 60% was used to fluidize the 2D-beds of these particles. The mean inlet air temperature (T_b) was 28°C for linseed, and 24°C for millet and wheat.

The values of $\Delta P_{mf} / H_{mf}$, presented in parentheses in Tables 4.5 to 4.7, were calculated based on the weight of the bed. The value of Re_{mf} predicted by the Ergun equation (eq. A.9) is also included in these tables for comparison. The experimental error estimated for Re_{mf} was 3%.

TABLE 4.5

MINIMUM FLUIDIZATION PROPERTIES FOR LINSEED AT RH = 60%

H_0 (m)	H (m)	ϵ_{mf} (-)	Re_{mf} (-)	$\Delta P_{mf}/H_{mf}$ (Pa/m)	$Re_{mf(ERGUN)}$ (-)
0.10	0.117	0.450	72	5697 (6134)	54
0.15	0.165	0.416	47	5696 (6513)	45
0.20	0.217	0.408	54	(?) * (6602)	43

* large pressure fluctuations.

TABLE 4.6

MINIMUM FLUIDIZATION PROPERTIES FOR MILLET AT RH = 60%

H_0 (m)	H (m)	ϵ_{mf} (-)	Re_{mf} (-)	$\Delta P_{mf}/H_{mf}$ (Pa/m)	$Re_{mf(ERGUN)}$ (-)
0.10	0.110	0.422	139	7376 (7376)	114
0.17	0.179	0.393	104	7788 (7751)	99
0.20	0.205	0.375	95	8186 (7974)	90
0.25	0.260	0.385	98	8066 (7847)	95
0.30	0.315	0.390	91	7859 [a] (7783)	98

[a] large pressure fluctuations just after fluidization (see Fig. 4.5).

TABLE 4.7

MINIMUM FLUIDIZATION PROPERTIES FOR WHEAT AT RH = 60%

H_0 (m)	H (n_l)	ϵ_{mf} (-)	Re_{mf} (-)	$\Delta P_{mf}/H_{mf}$ (Pa/m)	$Re_{mf(ERGUN)}$ (-)
0.10	0.106	0.418	253	6719 (7167)	256
0.15	0.160	0.409	251	7266 (7278)	246
0.20	0.210	0.409	251	7207 (7278)	246
0.25	0.257	0.397	234	7554 [a] (7426)	234

[a] large pressure fluctuations just after fluidization.

From Tables 4.5, 4.6 and 4.7, it can be seen that:

(i) The minimum fluidization velocity, as well as the mean bed porosity, decreases with increasing bed height until reaching fairly constant values at $H_o > 0.17$ m ;

(ii) The Ergun equation (eq. A.9) can predict well (with an error of 2%) the minimum fluidization velocity for 2D beds of large particles such as wheat. However, the Ergun equation cannot predict as closely V_{mf} for 2D beds of particles of sub-groups D_1 and D_2 (such as millet and linseed);

(iii) Unstable fluidization regime with large pressure drop

fluctuations characterizes 2D fluidized beds of coarse particles at $H_o > L_1$;

(iv) The minimum fluidization pressure drop is lower than the weight of bed per cross sectional area for 2D fluidized beds of very flat particles such as linseed.

The pressure drop characteristic curves for 2D beds of millet and wheat are shown in Figures 4.2a and 4.2b. For 2D beds of wheat (large particles belong to the true Geldart group D), three different curves have been obtained as the bed height increases. These curves are strongly dependent on the bed height at low Re number while these are convergent at high Re number (see Fig. 4.2b). For 2D beds of millet (particles belong to sub-group D_2) at $H_o > 0.10$ m, the pressure drop characteristic curves are more similar in behavior as shown in Fig. 4.2a.

The experimental observations of the bubble formation and the disturbances generated inside the 2D beds of wheat, millet and linseed can be summarized as:

(i) Channels developed inside the beds of linseed at low flow rate. For $V > V_{mf}$, bubbles appeared at the bottom of the bed and coalesced vertically generating wide channels;

(ii) Disturbances in the packing structure were generated inside the 2D beds of millet and wheat a few centimeters above the bottom of the column before fluidization. These disturbances moved, like ripples, towards the lateral vessel wall. Depending on the bed height, these waves died out on the wall or were reflected towards the center of the bed. The shape of the bed surface changed before fluidization. These disturbances are shown schematically in Figure 4.3.

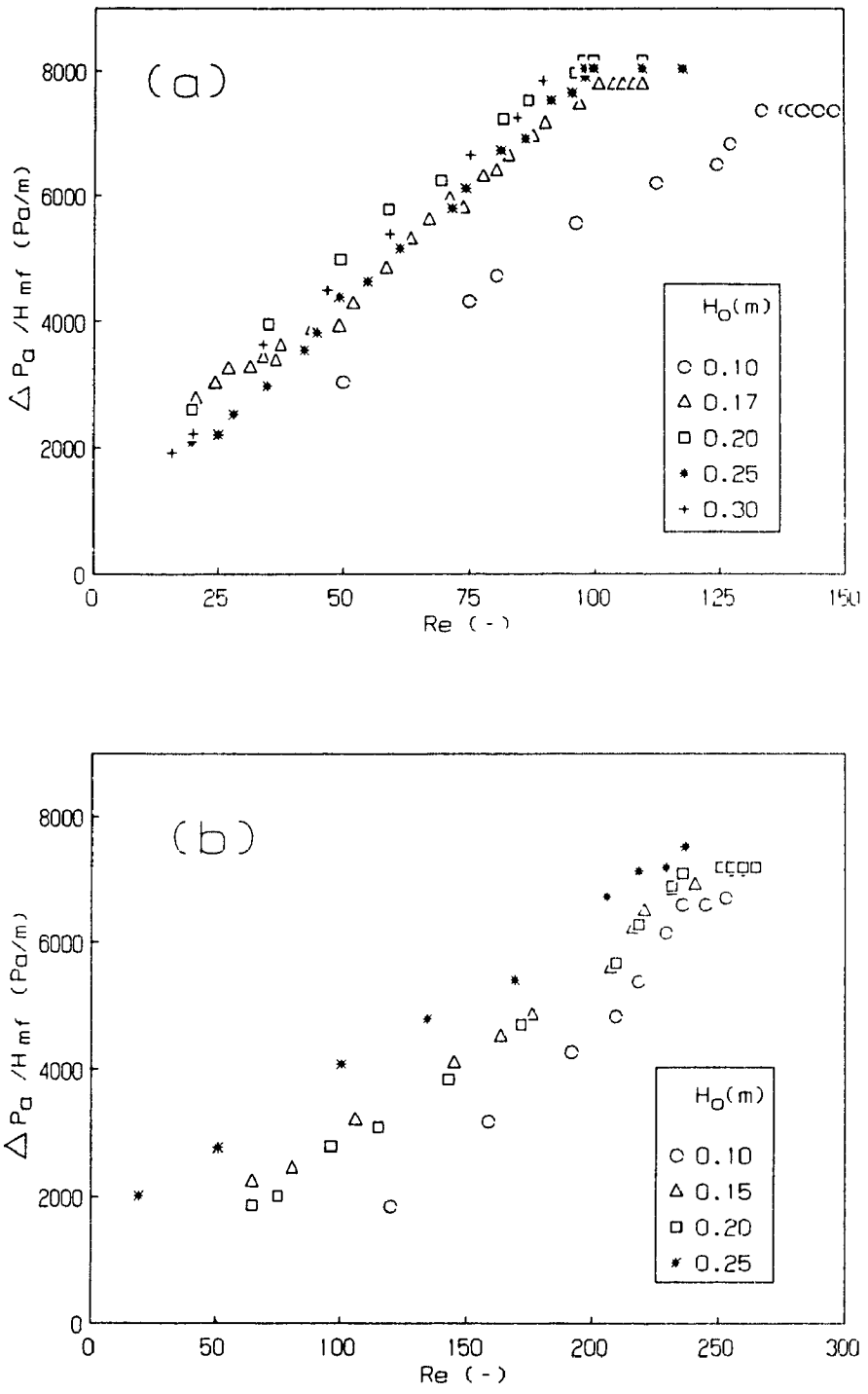

FIGURE 4.2 - Effect of Bed Heights on Pressure Drop Characteristic Curves for 2D-Packed Beds of: (a) Millet, (b) Wheat at RH = 60%. Pressure drop measured by the annulus static tap. SD = 3.3% for millet data, and 4% for wheat data.

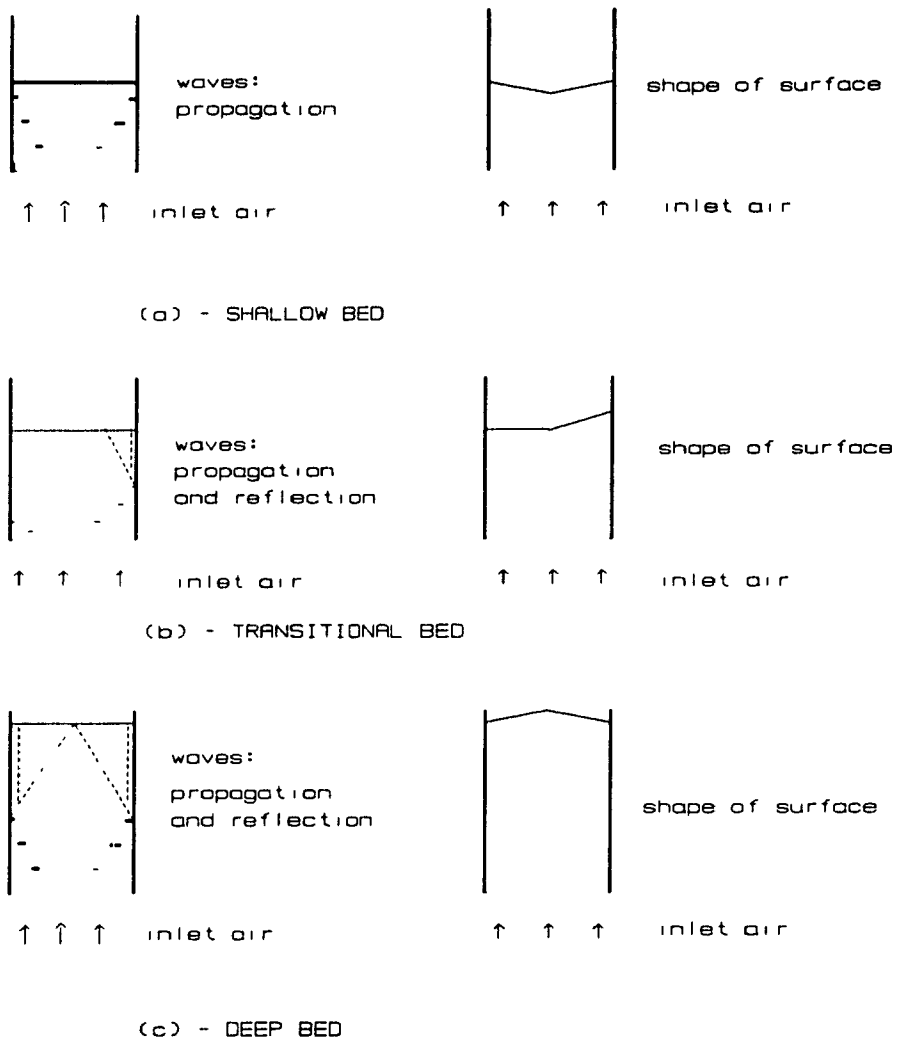

FIGURE 4.3 - Schematic Representation of Disturbances occurring in 2D-Packed Beds of Coarse Particles with RH = 60%.

The formation of channels in 2D beds of linseed explains the low value for the minimum fluidization pressure drop presented in Table 4.5. Air flows preferentially through these channels and the pressure drop becomes lower than one obtained in homogeneous fluidization.

Disturbances of the packing structure should explain the different pressure drop characteristic curves obtained in 2D beds of wheat and millet. From Fig. 4.3, it can be seen that three different shapes of bed surface are observed: (a) a parabolic concave shape characteristic of shallow beds of coarse particles (wheat and glass beads at H_o = 0.10 m); (b) a parabolic convex shape characteristic of deep beds, in which pressure fluctuations were large after the minimum fluidization (millet at H_o = 0.30 m and wheat at H_o = 0.25 m); (c) a non-symmetric shape characteristic of the transition between shallow and deep beds.

The Ergun equation (eq. A.9) predicted well the pressure drop characteristic curves for the 2D shallow beds with a standard deviation from the mean experimental data of 4% (34 Pa) and the average deviation of 3%. Note that the standard deviation based on data replication is about 5.7% for wheat and 5% for millet, as shown in Figure 4.4.

In 2D transitional beds, bubbles were developed on one side of the column a few centimeters above the distributor plate, while the other side was not fluidized at all. Specific experiments carried out in beds of millet demonstrated that small disturbances in the initial packing of particles were not damped out with the increase of the bed height, but they grew faster as the bed height increases. This behavior seems to be characteristic of the rectangular geometry. Szekely and Poveromo (1975) reported exactly opposite behavior for cylindrical beds of coarse

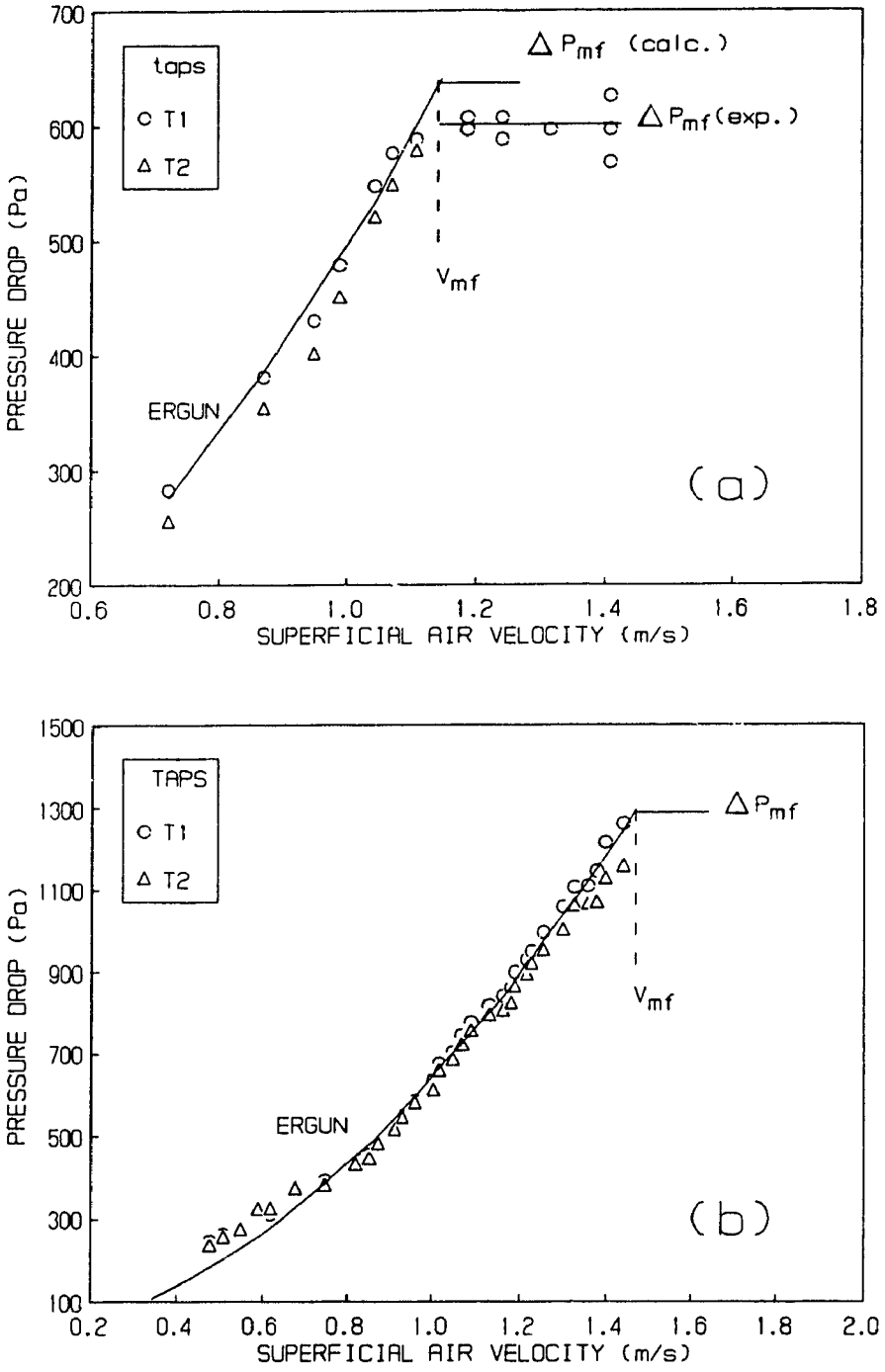

FIGURE 4.4 - Pressure Drop versus Air Superficial Velocity for Shallow 2D Packed Beds of: (a) Wheat, (b) Glass Beads at RH = 60%. H_o = 0.10 m. T1- pressure drop measured by the annulus static tap. T2 - pressure drop measured by the spout static tap.
SD (experimental) = 5.7% for wheat, and 5% for glass beads.

particles. Such results are related to the vessel wall effect on the particle packing.

Assuming no adhesion force between the particles and the wall, the wall effect can be described as follows: the first layer of particles in contact with the vessel wall is forced to be well ordered. This layer itself is less smooth than the wall, and induces a weaker order on the adjacent layer. Hence, the degree of order decreases as the distance from the vessel wall increases; this leads to lower porosity in the center of the bed.

Benenati and Brosilow (1962) have shown that the bed porosity in a packed cylindrical bed varies from unity at the wall to about 39% in the interior of large beds. The horizontal variation of the bed porosity should be more pronounced in a two dimensional bed geometry due to the effect of the wall edges. Disturbances generated in the lower region of 2D packed beds are propagated more easily towards the vessel-wall. Moreover particles are not allowed to move or dislocate in the L_2 direction. Particles pressed against the wall can reach failure and slip upwards (or downwards) on the vessel wall. As particles slip, changes in the pore geometry occur in the upper region of the bed. This is reflected in Fig. 4.3b as a change in bed surface. For lower bed heights, changes in the pore geometry are confined to the top layer of the bed. As the bed height increases, these changes disturb the particle arrangement in the upper central region. As a result, the anisotropy of the packed bed increases even for quasi spherical particles such as millet.

As shown in Chapter 5, the propagation of these disturbances in the upper region of the bed depends on how the bed reaches failure. The Ergun

equation cannot describe the air-particle interactions in a 2D packed bed due to the slip volumetric deformations occurring in the porous material before its total failure.

In 2D deep beds, the pressure drop fluctuations were large beyond minimum fluidization. For 2D beds of millet at H_o = 0.30 m and wheat at H_o = 0.25 m, a vigorously pulsating motion of the bed surface was observed just after the minimum fluidization, followed by an increase of pressure drop. The pressure drop characteristic curve for millet at H_o = 0.30 m is shown in Figure 4.5. A similar curve was also obtained for wheat at H_o = 0.25 m. The experiments for beds of millet at H_o = 0.30 m had to be interrupted at Re = 113 due to the intense pulsating motion of the bed surface.

Geldart et al. (1978) have analyzed the effect of a small column diameter on the fluidization behavior of coarse particles. Their results show an increase of the pressure drop with the air flow rate after the minimum fluidization point, similarly to the results reported here. Following Geldart et al. (1978), this behavior is characteristic of fluidized beds with low D_c / d_p ($D_c / d_p < 100$) and height high enough to assure the development of solids slugs at the top of the bed, while the bottom is barely fluidized. The increase of the pressure drop is due to the additional force required to form and accelerate these slugs.

Zenz (Geldart et al., 1978) has developed an empirical correlation to estimate the minimum bed height ($H_{min,s}$) below which slugging cannot occur in beds fluidized by ambient air. Defining solids slugs in a two dimensional column as large bubbles with width equal to L_1, Zenz's

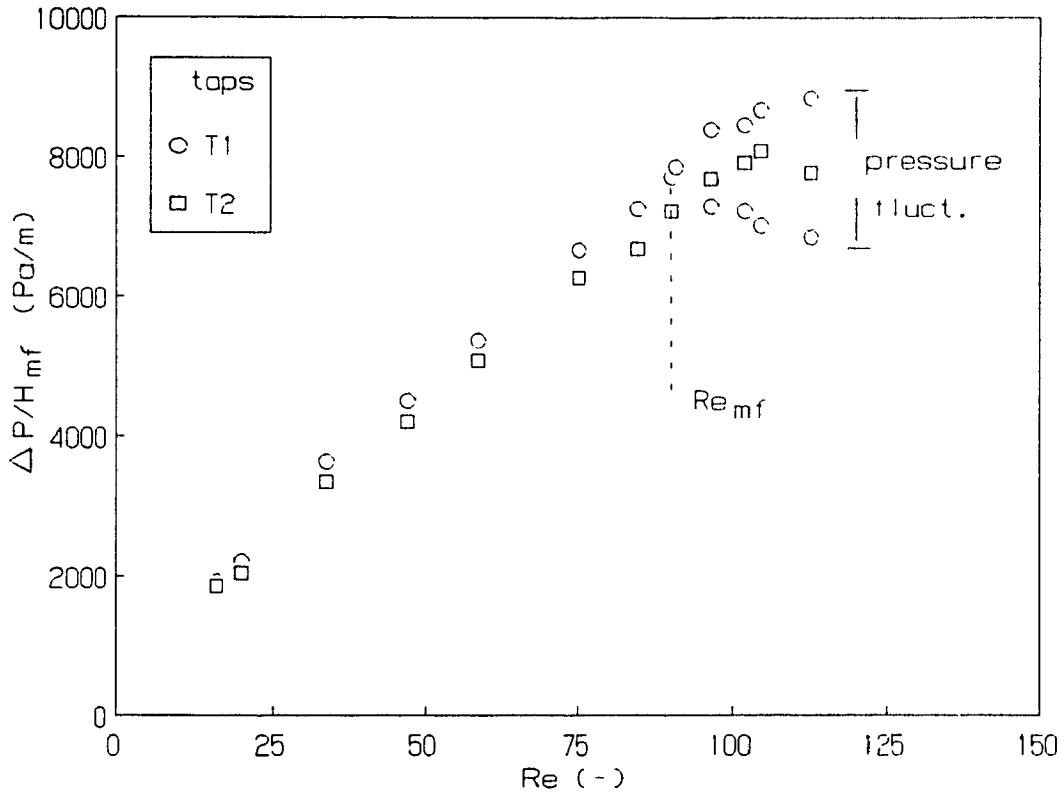

FIGURE 4.5 - Pressure Drop Characteristic Curve for 2D-Packed Bed of Millet at H_o = 0.30 m and RH = 60%.
T1- pressure drop measured by the annulus static tap. T2- pressure drop measured by the spout static tap.
SD = 3% for T1 data or T2 data.

correlation can be extrapolated to the 2D-bed column as:

$$H_{min,s} = 1.9\, L_1/(\rho_s d_p \phi)^{0.3} \qquad (4.4)$$

with all dimensions expressed in the MKS system of units.

Taking L_1 = 0.20 m in eq. (4.4), the estimated values of $H_{min,s}$ for linseed, millet and wheat are respectively: 0.33 m; 0.28 m and 0.24 m. The two last values agree very well with the experimental data obtained here for millet and wheat. The vigorously pulsating motion of the bed surface and the large pressure fluctuations in deep beds are now explained by the formation of solids slugs. However, there is no reason to suppose that solids slugs occur in beds of linseed at H_o = 0.20 m. Wide channels developed inside the bed of linseed are the apparent cause for the large pressure fluctuations observed in such beds.

From eq. (4.4), it can be seen that $H_{min,s}/L_1$ is close to 2 for particles of sub-group D_1 (linseed and sesame seed). $H_{min,s}/L_1$ is between 1.6 to 1.2 for particles of sub-group D_2, and close to 1 for very coarse particles, such as wheat and glass beads.

Geldart et al. (1978) have proposed the following correlation for $H_{min,s}$:

$$H_{min,s} = 0.365\, D_c^{1.235}/(V_G - V_{mf})^{1.37} \qquad (4.5).$$

All dimensions in eq. (4.5) are expressed in the MKS system of units.

Eq. (4.5) and eq. (4.4) are used together to estimate the minimum superficial slugging velocity (V_G), with $D_c = L_1$. The estimated values for V_G are respectively 0.88 m/s, 0.96 m/s and 1.41 m/s for linseed, millet and wheat. As pointed out, for deep beds of millet at Re = 113 (V

= 0.84 m/s) the pulsating motion of the bed surface becomes intense enough to stop further experiments with high air flow rates. This indicates that V_G in a 2D bed of millet is close to 0.84 m/s, which is lower than the predicted value obtained by eqs. (4.4) and (4.5).

Based on the above results, it can be seen that the development of solids slugs in the top of the bed is the mechanism of instability occurring in 2D deep fluidized beds of coarse particles. This mechanism is the same as one reported in cylindrical fluidized beds of coarse particles with $H_o > H_{min,s}$. However, the air flow distribution in 2D deep fluidized beds of coarse particles seems to be quite different from those reported in cylindrical fluidized beds of coarse particles, as inferred from the difference between the experimental and predicted values of V_G.

4.2.3 Effect of Air Relative Humidity:

The fluidization properties obtained in beds of linseed, millet and wheat fluidized by air with RH = 30% are shown in Table 4.8. H_o was equal to 0.17 m for linseed and wheat. Two values of H_o were used (0.15 m and 0.17 m) for millet. T_b was in the range of 19°C to 20°C.

Based on Table 4.8, the mean bed porosity and the minimum fluidization velocity decrease as the bed height increases.

A comparison among Table 4.8 and Tables 4.5, 4.6 and 4.7 shows that the decrease of the air relative humidity from 60% to 30% results in increasing the minimum fluidization velocity and the mean bed porosity.

The fluidization regime in 2D beds of wheat, millet and linseed using air with RH= 30% was more stable than that obtained with RH= 60%. Disturbances generated in the upper region of the packed bed moved

towards the center region of the bed. There was no particle slip on the vessel wall. Bubbles developed on both sides of the bed. For 2D beds of millet, the particles on the free bed surface moved up and down at minimum fluidization. Small bubbles were seen on the lateral vessel-wall and in the lower region of the bed near the bottom. For 2D beds of wheat, flat large bubbles start at 8 to 10 cm from the bottom of the bed. For 2D beds of linseed, channels were apparent inside the bed; however, they did not become wide as they did using air with RH= 60%.

The pressure drop characteristic curves for 2D beds of linseed, millet and wheat with RH = 30% are presented respectively in Figures 4.6a, 4.6b and 4.6c. The corresponding pressure drop characteristic curves obtained with RH = 60% are also plotted in these figures. A comparison between these curves shows that the reduction of RH from 60% to 30% causes a decrease in the pressure drop at the same Re number. This decrease in the pressure drop is 86% for 2D beds of linseed at Re = 35; 76% for 2D beds of millet at Re = 65; and 49% for beds of wheat at Re = 135. The decrease in pressure drop calculated by the Ergun equation (eq. A.9) due to the variation of air properties and the mean bed porosity is only 25% for all the three particles. These results show that the variation of the air properties and the mean bed porosity alone is not enough to explain the decrease in the pressure drop which occurred with the reduction of the air relative humidity. Moreover, as shown in Figs. 4.6b and c, the pressure drop characteristic curves become non-linear with Re as the air relative humidity is reduced from 60% to 30%.

Change in the air-particle-wall interactions must occur with the decrease of the air relative humidity. As already known, using air with

TABLE 4.8

MINIMUM FLUIDIZATION PROPERTIES FOR LINSEED, MILLET AND WHEAT AT RH = 30%.

PARTICLE	H_0 (m)	H (m)	ϵ_{mf} (-)	Re_{mf} (-)	$\Delta P_{mf}/H_{mf}$ (Pa/m)
LINSEED	0.17	0.185	0.436	99	5833 (6309)
MILLET	0.15	0.160	0.432	169	7336 (7336)
	0.17	0.175	0.412	157	7595 (7594)
WHEAT	0.17	0.183	0.437	332	6940 (7016)

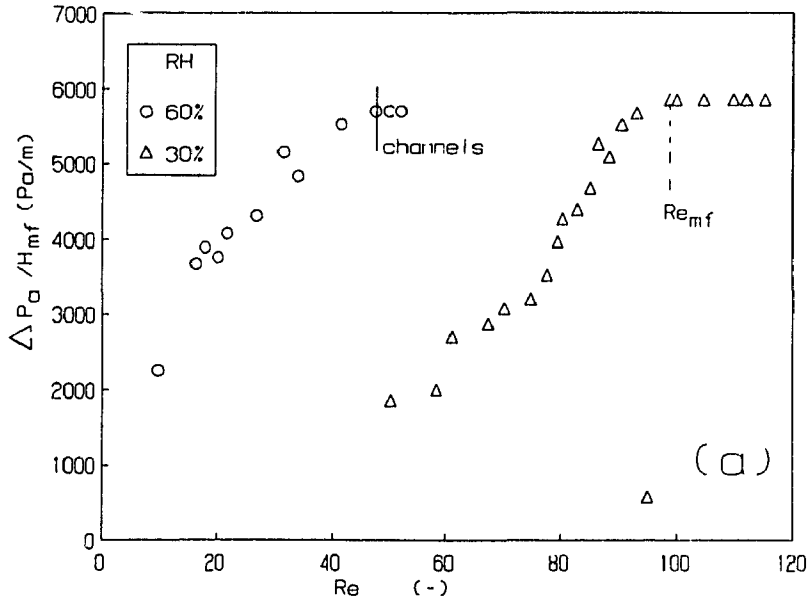

FIGURE 4.6 - Effect of Air Relative Humidity on Pressure Drop Characteristic Curves for 2D-Packed Beds of: (a) Linseed. Pressure drop measured by the annulus static tap. SD = 4% for data at RH=60% and 3.5% for data at RH=30%.

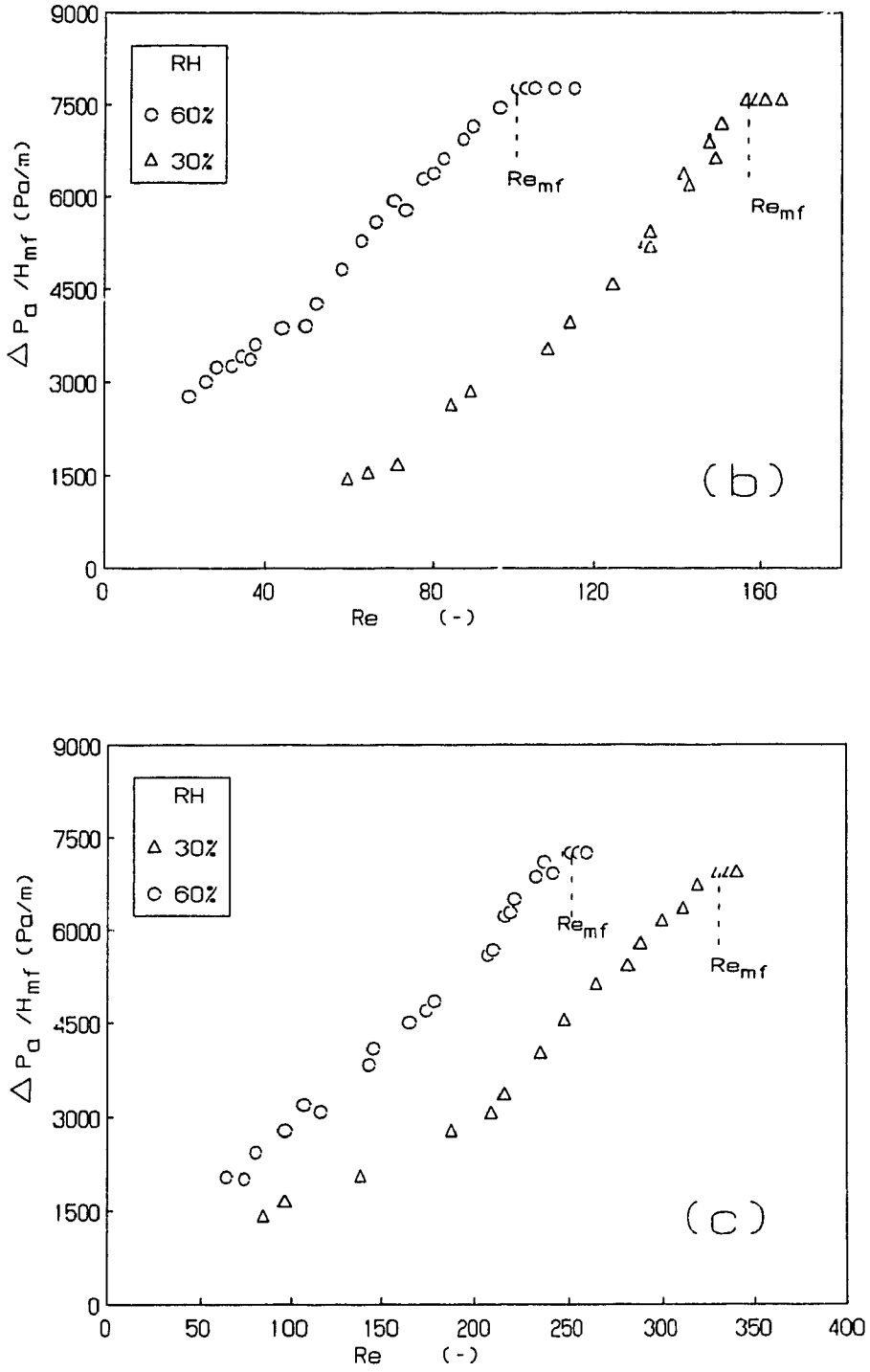

FIGURE 4.6 (cont.) - Effect of Air Relative Humidity on Pressure Drop Characteristic Curves for 2D-Packed Beds of: (b) Millet and (c) Wheat.
Pressure drop measured by the annulus static tap.
SD = 3.5% for millet at RH=60% and 4.5% at RH=30%.
SD = 4.5% for wheat at RH=60% and 3.4% at RH=30%.

low relative humidity, electrostatic forces developed inside the bed can interfere in the dynamics of the packed-fluidized beds. An analysis of this effect is presented in Appendix B.

Based on the results obtained here and those from Appendix B, the following conclusions can be drawn regarding the effect of air relative humidity on the dynamics of the 2D-packed beds of coarse particles presented here:

(i) Using air with RH = 60%, static charges are rapidly dissipated There is no significant amount of charge accumulated on wall or particle surface. The particle-wall adhesion force is negligible. The effect of the wall on the dynamics of the packed-fluidized beds is related to the growth of disturbances in the upper region of the 2D packed bed. These disturbances are due to deformations of the pore structure occurring in two different points inside the bed: (1) near the vessel wall where particles slip upwards or downwards; (2) centrally where gradients of porosity become significant. The extension of these deformations (i. e. the degree of anisotropy in the 2D packed bed) depends on the bed height.

(ii) Using air with RH = 30%, the particle-wall adhesion becomes important due to the static charge accumulated on the vessel-wall and on the particle surface. The effect of the wall on the bed dynamics is now to induce static charges on the particle surface by direct contact. As a result, the bed porosity in regions near the vessel-wall is decreased (dense packing). The particle-wall adhesion force prevents the slip of individual particle on the lateral vessel-wall. The bed failure is characterized by arrangement and slip of groups of particles. Deformations of the pore structure occur in the center upper part of the

bed due to the gradient of the bed porosity. The fluidization of the 2D packed beds using air with RH = 30% is more stable than using air with RH = 60% due to the no slip of particles on the vessel wall. This explains the general trends observed during the experiments using air with low relative humidity.

(iii) Beds of linseed present stronger electrostatic forces than beds of millet and wheat due possibly to the linseed surface characteristics. Particle agglomeration occurs in 2D fluidized beds of linseed with RH = 30%. Particle agglomeration may occur in 2D fluidized beds of millet with RH = 30%. However, for beds of large and rough particles, such as wheat, particle agglomeration is not expected to occur.

4.2.4 Effect of Particle Size Distribution:

As is well known, when using particles with a wide size distribution, particle segregation can occur in fluidized beds. Experiments carried out in 2D beds of millet-linseed mixtures at RH = 60% and H_o = 0.17 m have shown that segregation occurs in such beds.

Photographs taken before and after bed preparation show that linseed particles have migrated preferentially to the center region of the bed, while millet particles have concentrated in the vessel-wall region. Moreover, in the center of the bed, linseed particles are oriented with their highest dimensions almost parallel to the vertical axis of the column.

The pressure drop measurements obtained simultaneously at the center (or spout) tap and at the annulus tap showed that the horizontal pressure

drop variation increased from M#1 to M#3. For all the 2D beds of linseed-millet mixtures, this variation was always lower than that obtained for millet, as shown in Table 4.9.

The pressure drop characteristic curves for the three millet-linseed mixtures are presented in Fig. 4.7.

Wide channels were observed in 2D fluidized beds of M#1 with large pressure fluctuations at minimum fluidization. This behavior, as described earlier, was characteristic of 2D beds of linseed. The pressure drop characteristic curve for M#1 (Fig. 4.7) was very similar to the one for linseed at H_o = 0.15 m (Fig. 4.6a for RH = 60%).

For M#3, fluidization was characterized by large bubbles at the wall (wall slugs). The pressure drop characteristics were similar to the ones for 2D transitional beds of millet.

Based on Table 4.9, the segregation in beds of millet-linseed mixtures tended to reduce the vessel-wall effect. The concentration and orientation of linseed particles in the center region of the bed increased the bed porosity in this region. The lateral variation of the bed porosity was decreased. However, due to the shape of linseed particles, channels were formed easier than bubbles.

Beds of rice fluidized by air with RH = 60%, at H_o = 0.17 m, presented similar behavior. Disturbances developed inside the bed before fluidization degenerated into channels. For the pressure drop curves, the mean value of $(\Delta P_a - \Delta P_s)/\Delta P_a$ was 3.5%, lower than millet or wheat. Segregation of rice particles occurs due to the high amount of broken grains observed in the samples used here.

These results elucidate the effect of particle shape on fluidization

TABLE 4.9

COMPARISON OF THE FLUIDIZATION CHARACTERISTICS IN 2D-BEDS OF MILLET-LINSEED MIXTURES AT RH = 60%

MATERIAL	CONC. millet (%)	H_o (m)	ϵ_{mf} (-)	Re_{mf} (-)	$[\Delta P_a - \Delta P_s]/\Delta P_a$ mean value (%)	T_b (°C)
LINSEED	0	0.15	0.416	46	3.7	28
M #1	33	0.17	0.409	63	1.6	24
M #2	53	0.17	0.421	85	2.2	24
M #3	72	0.17	0.405	98	4.6	26
MILLET	100	0.17	0.393	104	6.5	24

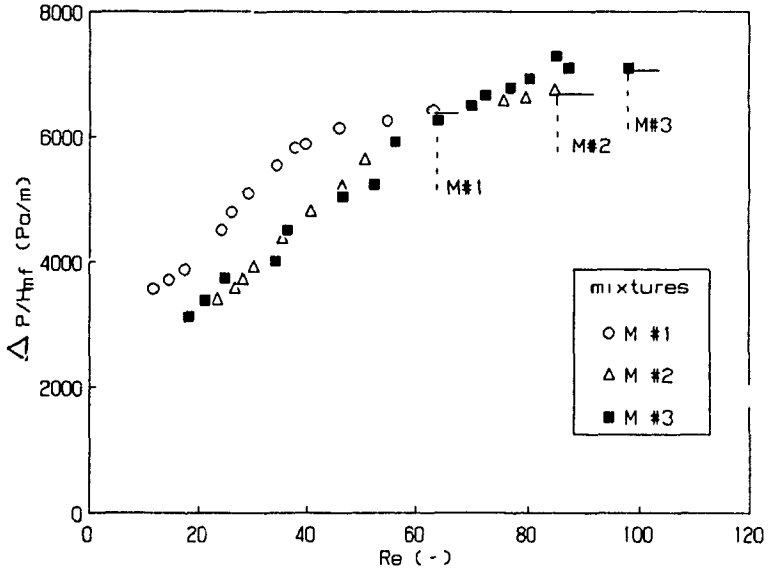

FIGURE 4.7 - Pressure Drop Characteristic Curves for 2D-Packed Beds of Millet-Linseed Mixtures at RH = 60% and H_o = 0.17 m.
Pressure drop data - mean value between the pressure drop measured by the spout and annulus static taps.
SD = 3% for M#1, and 4% for M#2 and M#3.

regime in 2D beds. For particles with low sphericity, channels occur due to the particle orientation.

4.3 Conclusions

Based on the results presented, the following conclusions can be drawn regarding the fluidization of 2D-packed beds of coarse particles:

(i) - Pressure Drop and Minimum Fluidization Characteristics:

The minimum fluidization properties depend upon the static bed height, the air relative humidity and the air-particle properties. Such a dependence is the result of particle-wall and particle-particle interactions occurring in the packed bed before fluidization.

For air with high relative humidity, the effect of the vessel-wall is to disturb the random particle arrangement in 2D-packed beds. For low column width/ particle size ratio, gradients of bed porosity develop inside the bed. This results in deformations of the porous material. The extent of these deformations depends upon the bed height. The Ergun equation cannot be used to describe the pressure drop characteristic curves for 2D-packed beds fluidized by air with high relative humidity except for shallow beds of coarse particles.

For low air relative humidity, the effect of the plexiglas vessel-wall is to generate electrostatic charges on particle surface in contact with the wall. Adhesion of particles on the wall decreases the bed porosity at the vessel boundary and prevents particle slip on the lateral wall. Electrostatic attraction between particles also develops due to breaking and making of particle contacts. Particle agglomeration can

affect the air-particle interaction forces. Hence again, the Ergun equation cannot be applied to describe the pressure drop characteristic curves in 2D-packed beds at low relative humidity.

(ii) - The mechanism of instability:

The mechanism of instability which prevents stable operation at high bed heights is identified as the development of solids slugs on the top bed surface while the bed bottom is barely fluidized. The minimum bed height at which this mechanism occurs is a function of the column dimensions and air-particle properties. An empirical correlation based on results in the literature has been used to predict the minimum bed height at which solids slugs occur in 2D fluidized beds.

CHAPTER 5

FLOW MODEL FOR TWO DIMENSIONAL BEDS OF COARSE PARTICLES

5.1 Introduction

It has been shown in Chapter 4 that the flow characteristics in a two dimensional bed of coarse particles depend on the slip deformations occurring in the bed before fluidization. These deformations are due to the anisotropy of the pore-solid structure caused by wall disturbances on the packing arrangement. A wall should be understood here as any boundary with a surface condition different from that of the bulk of the porous material such as the spout-annulus interface or the container wall.

Therefore, the mass, momentum, and energy balances for the particulate solid phase must be included in the basic equations of fluid flow in a 2D bed geometry. The approach used in this work to describe the solid phase stress tensor is based on conventional soil mechanics theory (Bridgwater, 1984). The stress in the solid phase is defined through an effective solid stress tensor which represents the strain response of the dry solid skeleton and the pore fluid structure (pore fluid pressure). In such an approach, the empirical parameters normally obtained for the characterization of the solid phase (such as the wall-factor, the solid bulk viscosity, etc.) acquire here real physical meanings. This allows a more general description of the air-solid flow characteristics in 2D packed beds as well as 2DSBs.

The objectives of this chapter are the following:

(i) to analyze the deformation mechanisms of the solid matrix and the pore structure for an anisotropic porous material;

(ii) to define the physical parameters that can be used to describe the relationship between these deformations and the air flow characteristics in a 2D packed bed of coarse particles;

(iii) to obtain basic equations to describe the flow characteristics in the annular region of a 2DSB.

Katsube and Carroll's (1987) theory and also Rowe's (1971) dilatancy model for granular flow are analyzed in the first part of this chapter. Based on this analysis, the mass, momentum and energy equations are developed including the specific parameters for the pore-solid deformations. The equations obtained are used to describe the pressure drop characteristic curves presented in Chap. 4 and to derive the failure criteria for the spout formation.

5.2 Katsube and Carroll's (1987) Modified Mixture Theory

Katsube and Carroll's (1987) theory combines coherently the soil mechanical theory with the dynamics of fluid flow through a porous medium. These authors have divided the porous material into micro and macro structures. In the macro structure, the properties of the porous material are continuous in space and time. This represents the continuous porous medium. In the micro structure, the properties of the porous material are discrete. The dry solid matrix as well the pore structure can deform, distinctly altering their geometry. The static deformations occurring in the micro structure during an infinitesimal time define the local average stress-strain properties of the continuous porous element. Moreover, in Katsube and Carroll's (1987) theory, the effective solid stress tensor is identified with the deformation mechanisms occurring in

the porous material. The anisotropy of the material is correlated with measurable parameters (such as the volume of fluid increase due to compression of the porous material) used in soil mechanics. Katsube and Carroll's model is used in this work to obtain the basic conceptual equations for fluid flow through an anisotropic medium.

5.2.1 Basic Assumptions

A schematic representation of Katsube and Carroll's physical model is shown in Figure 5.1. Their assumptions can be summarized as follows:

(1) A porous medium is a mixture of two distinct constituents: a homogeneous porous solid material and a homogeneous porous fluid material. The porous solid material is composed of the dry solid skeleton and fluid pores (i. e. empty voids corresponding to the space occupied by the fluid). The porous fluid material is formed by the empty fluid skeleton plus solid pores (i. e. empty voids corresponding to the space occupied by the solid). Both constituents are continuous media occupying the same point in the mixture at any given time.

(2) A local point in the medium is defined as an elementary volume of the porous material large enough to contain all details of the microstructure and small enough to allow the volume-average response of this element to be the local response of the medium.

(3) The local infinitesimal strain components are defined by the volume-average of the outer boundary displacements of the element. This assures definitions of the infinitesimal strain components for the dry solid matrix, the empty fluid skeleton as well as the fluid and solid pore spaces. The local strain rates components are the volume-average of

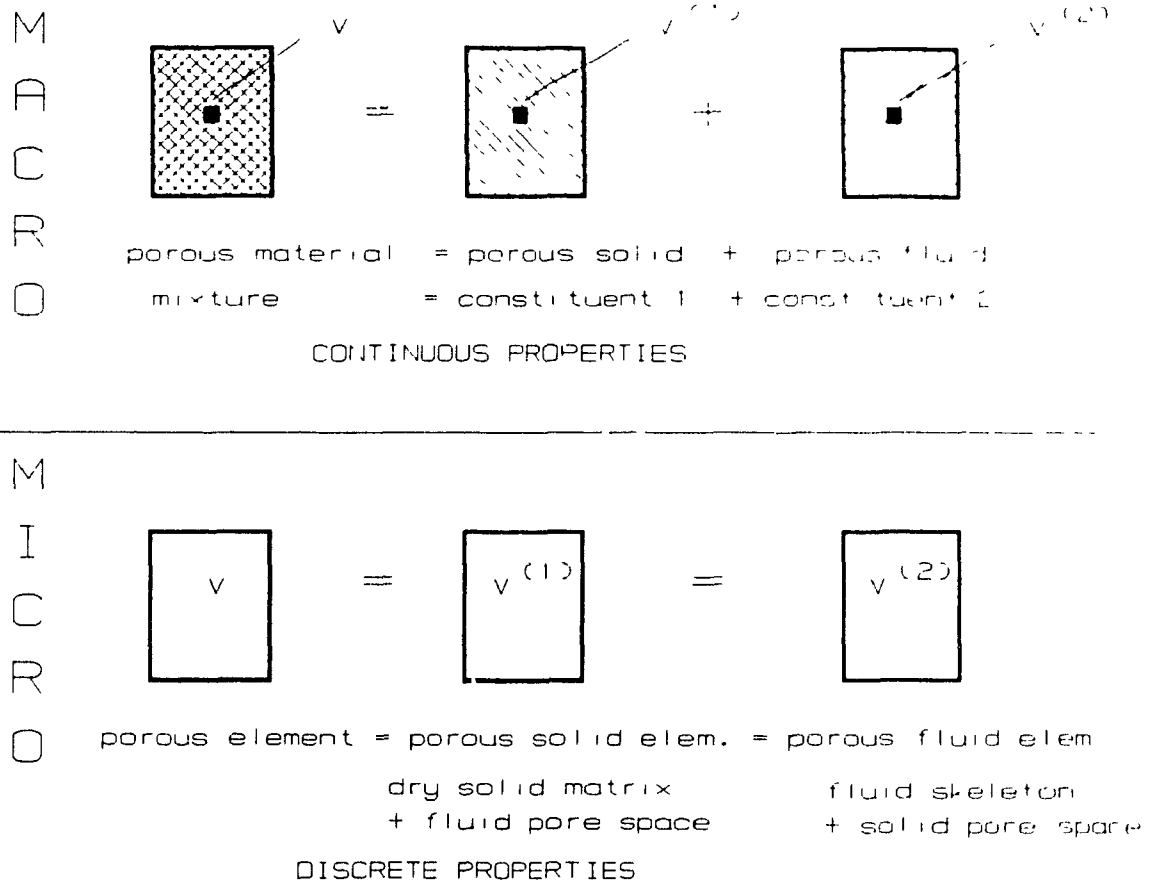

FIGURE 5.1 - Schematic Representation of the Physical Model of Katsube and Carroll's theory (1987).

the outer boundary surface velocities of the elementary point. The local stress components are the volume-average of the forces acting on the surface boundary of the elementary volumetric point.

(4) The porous material is fully saturated with fluid. Pores are interconnected and randomly distributed in location but not necessarily in orientation. This means that the porous medium can be anisotropic.

(5) The volumetric porosity is equal to the "areal" (related to transversal area) porosity even after infinitesimal deformations of the porous element.

(6) The applied stresses can be divided into static and dynamic components. The dynamic component of the porous solid element is always zero. The static component of the porous fluid element is reduced to the hydrostatic fluid pressure. The dynamic component of the porous fluid element is related to the viscous fluid flow.

(7) The interacting force between the two constituents is the resistive force for diffusion applied on the porous fluid by the porous solid. The interacting momentum between the two constituents is due to the pointwise shear stress distribution on the pore wall boundaries.

Based on the above assumptions, any force imposed on the surface of the porous material can be divided into two uncoupled systems of stress related to: (a) static deformations of the porous solid element under the effect of the hydrostatic pore fluid pressure; (b) dynamic or viscous deformation rates due to fluid flow through the pores.

5.2.2 Deformation Mechanisms in a Porous Material Saturated with a Fluid

The relevant points for this work concerning the deformation

mechanisms in a porous material element proposed by Katsube and Carroll's (1987) theory are discussed here.

Any static system of stress applied on the porous element can be reduced into a set of normal stresses (named principal stresses, σ_1, σ_2, and σ_3) acting on a set of mutually perpendicular planes (named principal planes). This reduces the stress-strain analysis to two specific cases:

(i) the hydrostatic stresses associated with the volumetric deformations given by the mean principal stress or the consolidated stress σ_3 ;

(ii) the non-hydrostatic stresses associated with the deviatoric stress given by ($\sigma_1 - \sigma_3$). Note that the intermediate principal stress is commonly equal to either the major principal stress or to the minor principal stress; otherwise it is irrelevant with respect to the slip deformation.

The following nomenclature is used here: superscript 1 refers to the porous solid element, and 2 to the porous fluid element. The superscript p represents pores, s - dry solid matrix, and f - fluid. The double repeated subscript denotes summation over the three directions (= trace of the deformation tensor).

For an isotropic porous sample subjected to a confining hydrostatic stress, the deformation mechanisms can be identified as:

(1) Deformations of the porous solid element:

$$e^{(1)}_{mm} = (1-\epsilon)\, e^{s}_{mm} + \epsilon\, e^{p(1)}_{mm} =$$

$$e^{s}_{mm} + e^{*(1)}_{mm} \qquad (5.1),$$

where:

e^{s}_{mm} - infinitesimal volumetric deformation of the dry solid matrix, related to the solid compaction;

$e^{p(1)}_{mm}$ - infinitesimal volumetric deformation of the fluid pore space;

$e^{*(1)}_{mm} = \epsilon\ (e^{p(1)}_{mm} - e^{s}_{mm})$ - infinitesimal change in porosity;

ϵ porosity of the porous element before deformation.

(2) Deformations of the porous fluid element:

$$e^{(2)}_{mm} = \epsilon e^{f}_{mm} + (1-\epsilon)e^{p(2)}_{mm} = e^{f}_{mm} + e^{*(2)}_{mm} \qquad (5.2),$$

where:

e^{f}_{mm} - infinitesimal volumetric deformation of the fluid skeleton, related to the fluid compaction;

$e^{p(2)}_{mm}$ - infinitesimal volumetric deformation of the solid pore space;

$e^{*(2)}_{mm} = (1-\epsilon)(e^{p(2)}_{mm} - e^{f}_{mm})$ - infinitesimal change in porosity.

Since fluid pores in the porous solid element is the space occupied by the fluid, and solid pores in the porous fluid element is the space occupied by the solid, the following equation holds:

$$(1-\epsilon)e^{*(1)}_{mm} = -\epsilon e^{*(2)}_{mm} \qquad (5.3).$$

A non-hydrostatic stress state, associated with the compressive deviatoric stress, results in a non-volumetric deformation of the porous solid element. For this case, eq. (5.1) is replaced by:

$$e^{(1)}_{ij} = e^{e}_{ij} + e^{*(1)}_{ij} \qquad (5.4),$$

where:

$e^{*(1)}_{ij} = \epsilon\ (e^{p(1)}_{ij} - e^{s}_{ij})$.

Comparing eq. (5.4) with eq. (5.1), it is seen that the deviatoric stress is responsible for different straining of the fluid pore space and the dry solid matrix. This means that changes in the relative orientation of the pore geometry can occur internally in the microstructure of the porous solid element. As a result, anisotropy is generated in the element compressed by a deviatoric stress.

Carroll and Katsube (1983) have demonstrated that the effective solid stress can be related to the change in the relative pore geometry, $e^{*(1)}_{ij}$. The effective solid stress, as used in soil mechanics, is the difference between the confining stress imposed on the porous material and the pore fluid pressure, i. e.:

$$\sigma^{e}_{ij} = \sigma_{ij} + P_f \delta_{ij} \qquad (5.5),$$

with:

σ^{e}_{ij} - the components of the effective solid stress;

σ_{ij} - the components of the applied confining stress;

δ_{ij} - the Kronecker delta;

P_f - fluid pressure.

Following the tensor notation, the compressive normal stress is

negative. In soil mechanics the compressive normal stress is taken as positive; this explains the difference in sign of eq. (5.5) when compared with the equation normally used in soil mechanics literature.

From eqs. (5.5) and (5.4), it can be deduced that the effective solid stress is only related to the relative change in pore geometry ($e^{*(1)}_{ij}$), and it does not describe the overall deformation of the anisotropic porous solid material ($e^{(1)}_{ij}$).

An anisotropic porous material can exhibit different types of anisotropy: intrinsic, structural or both. Intrinsic anisotropy is due to the dry solid matrix properties and it is a strong function of the particle shape and porosity. Structural anisotropy is due to the pore structure, and it depends also on such external factors as the container geometry, the stress path until failure, the initial packing arrangement, etc. Different degrees of anisotropy can be obtained in the porous material depending on the orientation of the dry solid matrix and the pore structure axes of symmetry.

The anisotropy in the porous material can be quantified by the effective solid stress components and by the increase in the mass of fluid in the porous solid element. The increase in the mass of fluid in the porous solid element per unit of porous solid volume is given by:

$$\Delta m = \epsilon \rho_f (e^{(1)}_{mm} - e^{(2)}_{mm}) =$$

$$\epsilon \rho_f (e^{p(1)}_{mm} - e^{f}_{mm}) \qquad (5.6).$$

Eq. (5.6) shows that fluid is expelled from the solid porous element

due to the difference between the volumetric deformation of the porous solid element and of the porous fluid element. Moreover, the mechanism responsible for the increase (or decrease) of fluid mass in the porous solid element is the different straining between the fluid pore space and the fluid compaction. Note that for an anisotropic porous material, fluid compaction is distinct from the contraction of the fluid pore space in the porous solid element.

5.2.3 Mass, Energy and Momentum Balances for a Porous Material

Following Katsube and Carroll's (1987) theory, the mass, momentum and energy balances for each constituent can be obtained from the mixture theory as shown in Table 5.1.

In Table 5.1, bold characters are used to represent the vector and tensor variables. The subscripts or superscripts 1 and 2 refer respectively to the porous solid and porous fluid constituents, $\mathbf{u}$ and $\mathbf{v}$ are the local velocities of the porous solid and porous fluid element respectively. The material derivative of any variable is given by the point notation as $\dot{\mathbf{u}}$ and $\dot{\mathbf{v}}$. The substantive derivative for any specific variable taking due account of the velocity of the porous solid element is given by the notation $d(\text{variable})/dt\ |_{\mathbf{u}}$.

The total interaction force between the two constituents, $\mathbf{f}^t$, corresponds to: (a) the resistive diffusion force, $\mathbf{f}$, exerted on the fluid by the solid; (b) the interacting momentum, Ω, between the two constituents due to the pointwise shear stress distribution on the pore wall boundaries. As a result, $\mathbf{f}^t$ in eqs. (5.9) and (5.10) (see Table 5.1) can be replaced by:

TABLE 5.1

MASS, MOMENTUM AND ENERGY EQUATIONS FOR AN ELEMENT OF A POROUS MATERIAL

(based on Katsube and Carroll's Modified Mixture Theory, 1987)

---

1 - Continuity Equations

1.a - for the porous solid:

$$\partial \rho_1 / \partial t + \mathrm{div}(\rho_1 \mathbf{u}) = 0 \quad , \quad \text{with} \rho_1 = (1-\epsilon)\rho_s \tag{5.7}$$

1.b - for the porous fluid:

$$\partial \rho_2 / \partial t + \mathrm{div}(\rho_2 \mathbf{v}) = 0 \quad , \quad \text{with} \rho_2 = \epsilon \rho_f \tag{5.8}$$

---

2 - Momentum Balances

2.a - for the porous solid:

$$\mathrm{div}\, \sigma - \mathbf{f}^t = \rho_1 (\mathbf{u} - \mathbf{b}^{(1)}) \tag{5.9}$$

2.b - for the porous fluid:

$$\mathrm{div}\, \pi + \mathbf{f}^t = \rho_2 (\mathbf{v} - \mathbf{b}^{(2)}) \tag{5.10}$$

---

3 - Mechanical Energy Balance for the Mixture:

$$(\rho_1 + \rho_2)\, dE/dt\,|_u = (\mathbf{u} - \mathbf{v}).\, \mathbf{f}^t + (\sigma : \nabla \mathbf{u}) + (\pi : \nabla \mathbf{v}) \tag{5.11}$$

$\mathbf{b}^{(1)}$ and $\mathbf{b}^{(2)}$ are the body forces per unit mass and taken equal to $\mathbf{g}$.

$$\mathbf{f}^{*} = \mathbf{f} - \mathbf{div}\,\Omega \qquad (5.12),$$

with **f** and Ω functions of (**u** - **v**) and **curl** (**u** - **v**).

The local average stresses for each constituent are divided into two parts: the static or deformation stress components and the dynamic or viscous stress components as follows:

$$\sigma_{ij} = \sigma^{D}_{ij} + \sigma^{V}_{ij} \quad \text{and} \qquad \pi_{ij} = \pi^{D}_{ij} + \pi^{V}_{ij} \qquad (5.13),$$

where the static stresses are given as:

$$\sigma^{D}_{ij} = (1 - \epsilon)\,\sigma^{s}_{ij} \quad \text{and} \qquad \pi^{D}_{ij} = \epsilon\, P_f \delta_{ij}$$

and the viscous or dynamic stresses are given as:

$$\sigma^{V}_{ij} = 0 \quad \text{and} \qquad \pi^{V}_{ij} = \epsilon\,(\pi^{f}_{ij} + P_f \delta_{ij})$$

with P_f representing the pore fluid pressure and σ^{s} the average stresses of the dry solid matrix;

π^{f} is the fluid viscous stress;

superscripts D and V represent the deformation or static stress and the viscous or dynamic stress components.

The objective here is to analyze the response of the solid porous material saturated with fluid when fluid flow through it. The porous solid stress tensor is replaced by the effective solid stress tensor as described in eq. (5.5).

The momentum balance for the porous solid and porous fluid materials can be obtained by the combination of eqs (5.10), (5.9) and (5.5) as:

$$-\text{div}\,\sigma^{e} = -\,\text{grad}(P_f) + (1-\epsilon)(\rho_s - \rho_f)g + \text{div}\,\pi^{V} + (-\beta_2 v - \beta_1 u) \qquad (5.14),$$

where:

$$\text{div}\,\pi^{V} - \rho_2 v = \text{grad}\,(\epsilon P_f) - f^{t} \qquad (5.15).$$

The continuity equation for the effective porous solid element is taken as a function of the mass of fluid "increase" in the porous solid element. From eqs. (5.6), (5.7) and (5.8), the following relation can be obtained:

$$dm/dt\,|_u + \Delta\, m\,\text{div}\,u = \text{div}\,(\epsilon\rho_f(u-v)) \qquad (5.16).$$

From eq. (5.16), it can be seen that the substantive derivative of the mass of fluid expelled from the solid matrix is related to the angle between the particle velocity (**u**) and the gradient of the mass of fluid expelled. If the degree of anisotropy is changed (this means that there is orientation of pores and particles), the substantive derivative of Δ m quantify this change. As shown later, Rowe's model for granular flow is based on this variable.

In this work, equations (5.14), (5.15) and (5.16) can be simplified as follows, assuming a loosely packed bed fluidized by an incompressible fluid :

$$-\text{div}\,\sigma^{e} = -\,\text{grad}(P_f) + (1-\epsilon)(\rho_s - \rho_f)g \qquad (5.17),$$

$$-\text{grad}\,(\epsilon P_f) = -f \qquad (5.18),$$

$$\partial\,\epsilon\,/\partial t + \text{div}(\epsilon(v-u)) = 0 \qquad (5.19).$$

Note that the gradients of porous fluid velocity are neglected in these equations. From eq. (5.17) and (5.18), it can be seen that the only force responsible for the fluid motion and the porous material deformations is the pore fluid pressure.

Elastic deformations are infinitesimal when compared to the magnitude of the main fluid flow velocity. The porous solid element can be assumed stationary, and eq. (5.19) is reduced to the mass balance in the porous fluid element. The variation of porosity with time is infinitesimal (elastic deformations) which results in the porosity gradient also being infinitesimal (eq. (5.19)). Such considerations reduce eq. (5.18) to Darcy's law.

In the range of non-Darcy flow, the Ergun equation (Ergun, 1952) can be appropriately used for the pressure drop characteristics in a loose "homogeneous" packed bed of coarse particles. Following Bridgwater (1984), the Ergun equation can be written as:

$$\Delta P/H = 72\, f_1\, V/\cos^2\lambda + 1.75\, f_2\, V^2 \qquad (5.20),$$

with:

$$f_1 = [(1-\epsilon)^2\, \mu_f / (d_p^2\, \phi^2 \epsilon^3)]$$

$$f_2 = [(1-\epsilon)\, \rho_f / (d_p\, \phi\, \epsilon^3)]$$

$\lambda/2$ representing the angle between the symmetric axis of the pore structure and the applied pressure gradient. The angle λ varies from 46 to 51 degrees ($150 < 72/\cos^2\lambda < 180$).

The first term on the right hand side of eq. (5.20) represents the viscous effect of the fluid flows through the porous material. This term

is one predicted by Darcy's law for an anisotropic porous material in the range of elastic deformations. The second term on the right hand side of eq. (5.20) represents the kinetic energy lost by the fluid as it flows through the porous medium. This term is related to the non-Darcy flow, and the non-elastic deformations of the porous material.

Non-elastic deformations become significant at high fluid flow rate where the expansion of the fluid occur. Particles can be dislocated and changes in pore geometry can disturb the fluid flow direction. Porosity gradients cannot be neglected, nor can the spatial variation of the mass of fluid expelled from the porous material. Eq. (5.20) can be applied in the range of non-Darcy flow.

In order to analyze the non-elastic deformations in the porous material, it is necessary to define the criterion of failure in the porous material.

5.3 Failure Criteria for the Porous Solid Material

5.3.1 Mohr-Coulomb Criterion

The Mohr-Coulomb criterion for rupture of granular material assumes that failures occur along a plane in a material by a critical combination of the normal and the shear stresses acting on these plane. For a non cohesive material, the Mohr-Coulomb equation can be written as:

$$|\tau_s| = (-\sigma_s^e) \tan \Theta_c \qquad (5.21),$$

or regarding the principal stress planes:

$$\sigma_1^e / \sigma_3^e = \tan^2 (45° + \Theta_c/2) \qquad (5.22),$$

Θ_c - the Coulomb angle of shearing resistance at the critical state, subscript s - the slip or failure plane (see Figure 5.2).

The critical state is defined as the one in which no volume change (or porosity change) occurs in the porous solid material during shearing. Eq. (5.21) predicts a straight line for the failure envelope locus as shown in Figure 5.2. Points below this failure envelope line are characterized by the elastic stress-strain relation. Points above the failure envelope are characterized by plastic deformations. Eq. (5.22) is obtained from the Mohr-Coulomb circle of stress presented in Figure 5.2.

The Mohr-Coulomb criterion establishes the plane of failure in a porous material (see Rowe, 1971). The intermediate stress does not play a role in the rupture of the material. There are three important cases in which eqs. (5.21) and (5.22) can be applied without restrictions regarding the intermediate stress. The first one is the plane strain condition in which the degree of freedom for particle motion is reduced to two directions (major and minor stress directions). Changes in pore geometry occur in these two directions. The intermediate principal strain component is assumed to be zero at failure. Such a case is typical of the two dimensional geometry. As shown later, the state of the solid stress in a 2DSB is given by the plane strain.

Two Mohr-Coulomb circles are necessary to represent the state of stress in a porous element in a three dimensional analysis. The first circle passes through the minor and the intermediate principal stresses, while the second one joins the intermediate and the major principal stresses. However, if the intermediate principal stress is equal to the minor or to the major principal stresses, the stress analysis is reduced

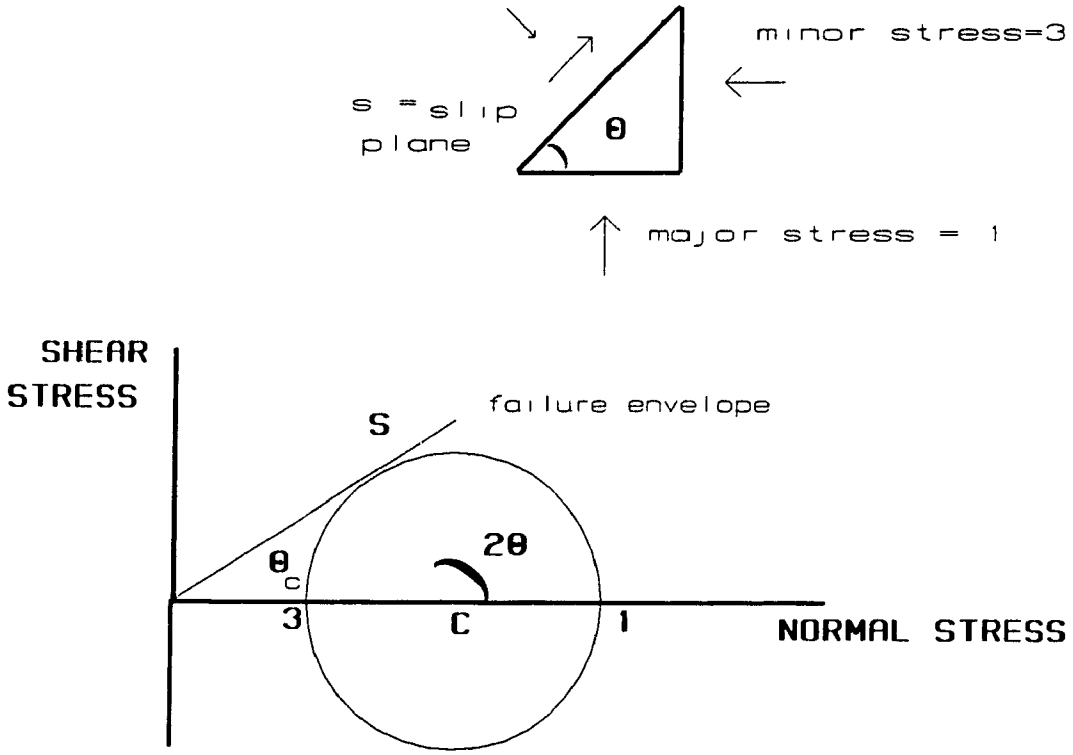

FIGURE 5.2 - Mohr-Coulomb Failure Envelope.

to one Mohr-Coulomb circle. Such a case is typical in a CSB as shown by McNab and Bridgwater (1974).

Two different types of failure can be identified in the Mohr-Coulomb circle depending on the value and direction of the shear and normal stresses acting on the failure plane. In active failure, the slip planes make an angle of $45°+ \Theta_c/2$ with the major principal plane. Based on Fig. 5.3, active failure is characterized by horizontal extension of the porous element. In passive failure, the slip planes make an angle of $45° - \Theta_c/2$ with the minor principal plane. Based on the system of coordinates presented in Fig. 5.3, passive failure is described by horizontal compression of the porous element.

Eq. (5.21) holds at the critical state when $e^{*(1)}_{mm}$ = constant ($\dot{e}^{*(1)}_{mm} = 0$). If changes in bed porosity occur before the failure point (i. e. gradient of porosity develops inside the material), the Mohr-Coulomb equation cannot be applied. Dense porous materials at low shear stress dilate before failure. The failure envelope for these materials is curved at low value of shear stress. Plastic or slip deformations occur in the porous element, and the critical state is reached beyond the failure point. Such a case represents spout formation in spouted beds. During the development of the spout cavity, the porous material is "remolding" before and beyond the point of maximum spout pressure drop. Particles slip inside the cavity and they rearrange into a new configuration at the spout-annulus interface. It is necessary to obtain a new failure criterion which takes into account plastic deformations in the pore and the particle structures before the critical state is reached.

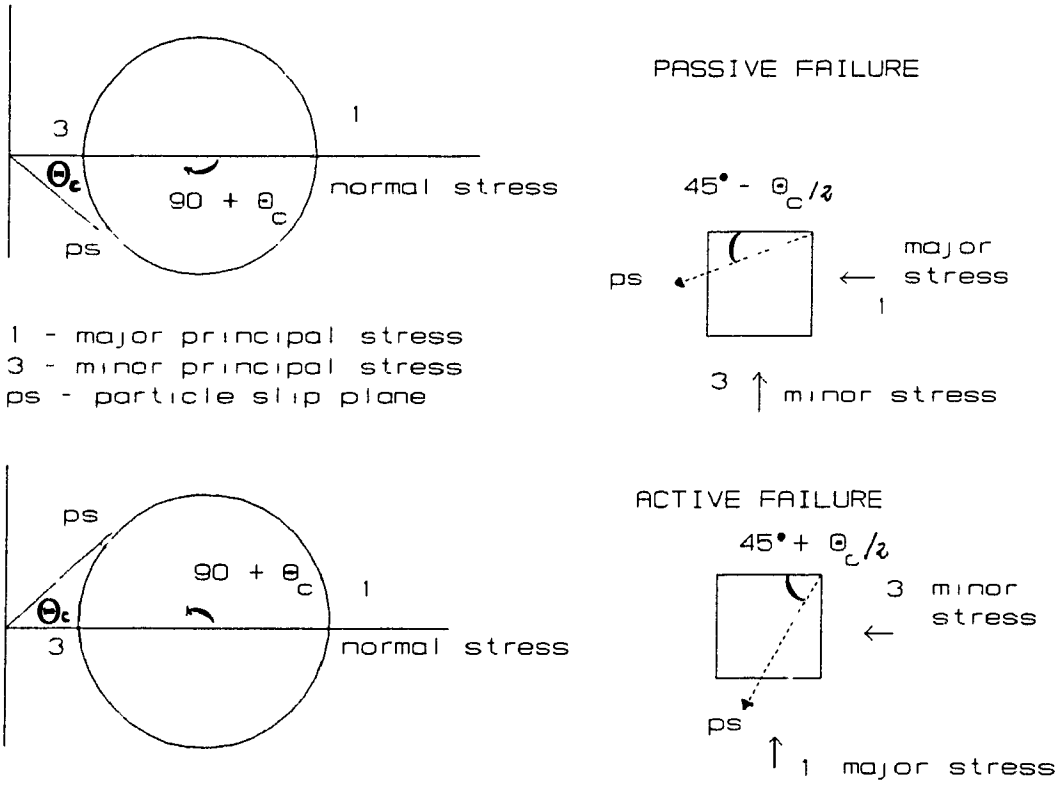

FIGURE 5.3 - Schematic Representation of the Active and Passive States of Failure in a Porous Material.

5.3.2 Rowe's (1971) Dilatancy Model

Rowe (1971) has developed a semi-empirical flow model for granular materials taking into account non-elastic deformations which occur in the pore structure before the critical state is reached.

Rowe's (1971) model is based on a state of pseudo equilibrium ("quasi-stationary" condition) in which the principal axes of the effective solid tensor coincide with the principal strain rates. The sliding of groups of particles is the only mechanism responsible for the slip strain rate in the porous solid element. Elastic deformations are neglected as soon as particles begin to slip. Interaction forces between the porous solid and the porous fluid elements are given by gradients of porosity and fluid pressure. The volumetric deformation rates are correlated to the variation of the mass of fluid "increase" in the porous solid element. A more detailed description of the assumptions of Rowe's model is given in Appendix C.

Rowe (1971) has shown that there is a minimum energy increment ratio (energy supplied by external forces/ total work done by internal forces) which defines the mean particle slip direction. In dense packing, for example, particles form locked groups. Each group slides against another (in a specific mean direction) before forming new groups. On the other hand, slip occurs at a number of different directions simultaneously for loose packing. The pore structure is continuously rearranged. Loose and dense packings require different rates of energy to deform. Such a difference is given by the different angles of particle slip. Rowe's stress dilatancy relation is described by:

$$(\sigma_1^e/\sigma_3^e) = \tan^2(45°+\Theta_f/2)\ D \qquad (5.23),$$

for $\sigma_2^e = \sigma_3^e$ or

for $\sigma_3^e < \sigma_2^e$ (plane strain)

$$(\sigma_1^e/\sigma_3^e) = \tan^2(45°+\Theta_f/2)\ /\ D^* \qquad (5.24),$$

for $\sigma_2^e = \sigma_1^e$

where:

σ_1^e - the effective major principal stress;

σ_2^e - the effective intermediate principal stress;

σ_3^e - the effective minor principal stress;

$D = -(\dot{e}_{3s} + \dot{e}_{2s})/(\dot{e}_{1s})$;

$D^* = (\dot{e}_{1s} + \dot{e}_{2s})/(-\dot{e}_{3s})$;

$\dot{e}_{ns}$ - the plastic or slip strain rates, with subscript n=1 representing the major principal stress direction, n=2 the intermediate and n=3 the minor principal stress direction;

Θ_f - the failure angle related to the particle slip direction, varying between the particle frictional angle (dense packing) to the Coulomb angle of shearing resistance at the critical state (loose packing).

The sign convention used by Rowe (1971) in eq. (5.23) and (5.24) is positive for the compressive stress and compressive strain rate. The sign convention adopted here is the opposite, i. e., negative for both compressive stress and compressive strain rate. Since eqs. (5.23) and (5.24) are presented as ratios between stress and strain rate, the sign convention becomes immaterial in this case.

In Appendix C Rowe's (1971) model is described following the continuum approach. The parameter D is shown to be related to the variation of the mass of fluid increase in the porous element for an infinitesimal increase of the compressive principal stress. For $D < 1.0$, the porous solid element is compacted ("negative dilatancy" occurs). Fluid is expelled from the porous solid element, and the pore fluid pressure is reduced. The actual major effective stress is corrected by the factor $1/D$. For $D > 1.0$, the porous solid element expands ("positive dilatancy" occurs). The fluid enters the porous solid element, the pore fluid pressure increases and the actual major effective stress is reduced by the factor $1/D$.

In eq. (5.24) the behavior is quite different due to the stress applied. In this case, the porous solid element is compressed in two directions. For $D^* < 1.0$, solid is expelled from the porous fluid element. The minor effective stress is increased by the factor $1/D^*$ due to expansion of the fluid. For $D^* > 1.0$, solid enters the porous fluid element, and the minor effective stress is decreased due to the compaction of fluid.

Eqs. (5.23) and (5.24) reduce to eq. (5.22) for $D = 1$ or $D^* = 1$ at the critical state. Therefore, the parameter D or D^* corrects the Mohr-Coulomb failure criterion for the case in which dilatancy occurs during the stress path.

Rowe (1971) showed that the parameter D is expressed by two specific angles in the plane strain condition as:

$$D = \tan\alpha \tan(45^\circ - \Theta_f/2) \qquad (5.25),$$

where:

α represents the angle between the mean direction of particle slip and the major principal plane when dilatancy of the porous material occurs;

Θ_f as defined before is the failure angle of the porous material.

Eq. (5.25) can be used with the Mohr-Coulomb circle of stress to determine a mean value of D for a 2D packed bed in which plastic deformations occur before fluidization.

5.4 Pressure Drop Correlation in a Two Dimensional Packed Bed

The following modified form of the Ergun equation is proposed in order to analyze the effect of the slip deformations of the air-particle material on the pressure drop characteristic curve in a 2D packed bed of coarse particles:

$$\Delta P/H = [\,72\,(1-\epsilon)/(\cos^2\lambda \mathrm{Re}) + a\,](1-\epsilon)\,\mu_f^2\,\mathrm{Re}^2/(\rho_f (d_p \phi \epsilon)^3) \qquad (5.26),$$

where:

λ is defined in eq. (5.20) following Bridgwater (1984);

$[72/\cos^2\lambda\,](1-\epsilon)/\mathrm{Re}$ is the frictional drag coefficient in a packed bed (resulting from viscous interaction air-particle forces). This is related to the elastic deformations of the pore-particle structure (Mutsers and Rietema, 1977);

a is the form drag coefficient in a packed bed (resulting from fluid inertia effects). This coefficient is related to the non-elastic deformations of the pore-particle structure following this work (see

Appendix C);

Re is the Reynolds number as defined earlier.

Ergun (1952) assumed a to be a constant value equals to 1.75 (see eq. (A.9)). In this work, it is assumed that a is a function of the slip deformations occurring in a 2D packed bed before fluidization. The value of a depends on the parameter D (or D^*) as defined by Rowe's model.

The angle λ includes also the wall effect due to the packing arrangement.

Assuming the plane strain condition for a 2D packed bed of coarse particles, eq. (5.23) can be applied in the range of non-elastic deformations. Since the parameter D varies during the stress path, a mean value, $\bar{D}$, is defined as a characteristic of a 2D packed bed. This mean value is obtained through the analysis of stress distribution in the packed bed at failure.

The experimental data obtained in 2D beds of wheat fluidized by air with RH = 30% were used in the following analysis. The steps adopted in this analysis were as follows:

(a) The determination of the empirical parameters λ and a in eq. (5.26). The pressure drop versus the air superficial velocity data were correlated by a multiple regression analysis;

(b) The particle slip planes at failure were determined based on the motion of particles just beyond fluidization of the bed. These particle slip planes characterize the stress configuration of the 2D bed at failure;

(c) Based on (b), the types of failure and the zones of plastic deformation were determined. The slip deformation mechanism was analyzed

to identify the relationship among $\bar{D}$, λ and a.

(d) The correlations obtained in (c) were extended for the other particles analyzed in Chap. 4.

The results obtained in step (a) are:

λ = 63° (SD = 1.5°) and a = 0.844 (SD = 0.02).

(The statistical parameters and empirical coefficients of the regression pressure drop versus air superficial velocity curve for wheat for RH = 30% can be seen in Appendix E).

The results of step (b) are presented in Figure 5.4. The analysis of these results can be summarized as follows:

In the upper region of the bed, particles tend to slip down on planes inclined $45° + \theta_c/2$ from the major principal plane. This direction defines the region RI in Fig. 5.4. The solid matrix is compacted in the lower region of the bed. A reversal in the particle slip direction occurs in this region. Such a reversal seems to be due to the two dimensional bed geometry used in which slip deformations in the z direction are not possible. Particles are forced to dislocate in the x direction as the fluid pressure increases. Variation of the pore fluid pressure in the x direction becomes significant in this region. Particles are compacted near the vessel wall in the lower region. Note that the frictional angle between particle-wall is increased due to electrostatic effects, and slip does not occur along the lateral wall (Chap. 4). Fluid is expelled towards the top of the bed, as shown by the dashed lines in Fig. 5.4. Slip deformations occur in specific zones as shown in Fig. 5.4. An

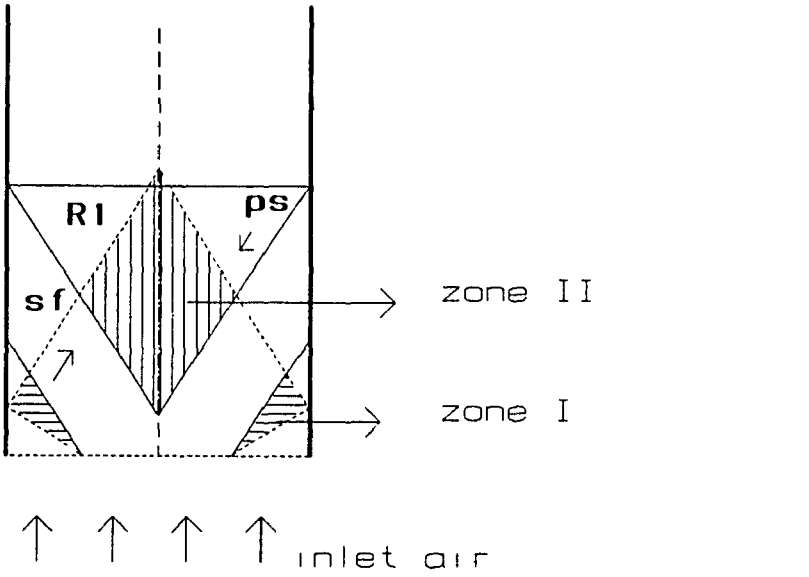

ps - plane of particle slip (top)

sf - plane of fluid flow (main direction)
RI - Rankine region 1 (top surface)

FIGURE 5.4 - Configuration of the Particle Slip Planes in a 2D Packed Bed of Wheat at Failure.
H_o = 0.17 m, RH = 30%.

element of the porous solid material in zone I (Fig. 5.4) can rotate due to the reversal of particle slip direction, and this element can deform plastically due to different compaction of the dry solid matrix near the wall vessel. An element of the porous solid material in zone II (Fig. 5.4) can deform plastically due to the change in pore geometry. This change occurs when the flow of fluid expelled from zone I reaches this region. As a result, plastic or slip deformations occur in a 2D packed bed before fluidization. These deformations are due to the change in the failure angle of the air-particle material.

Assuming that the overall relative rotation between fluid and particle in a 2D bed is negligible. the change in the particle-pore orientation in zone II is due to the pore fluid pressure gradient developed. This pore fluid pressure gradient is related to the new orientation of the pore structure in zone I. From the Mohr-Coulomb stress circle shown in Fig. 5.5, the pore geometry in the lower region changes from A' to A. The pore structure in the upper region of the bed changes from B' to B (see the Mohr-Coulomb circle in Figure 5.5) as the mass of fluid expelled reaches zone II.

The following equation is obtained from the overall force balance over zone I and II:

$$\sigma^{e}_{1II}/D_{II} = \tan^{2}(45^{\circ} + \Theta_{c}/2)\, \sigma^{e}_{1I}/D_{I} \qquad (5.27),$$

From eq. (5.27), $\bar{D}$ can be defined as:

$$\bar{D} = D_{II} / D_{I} \qquad (5.28),$$

where : D_{II} and D_{I} represent the mean value of D in zones I and II

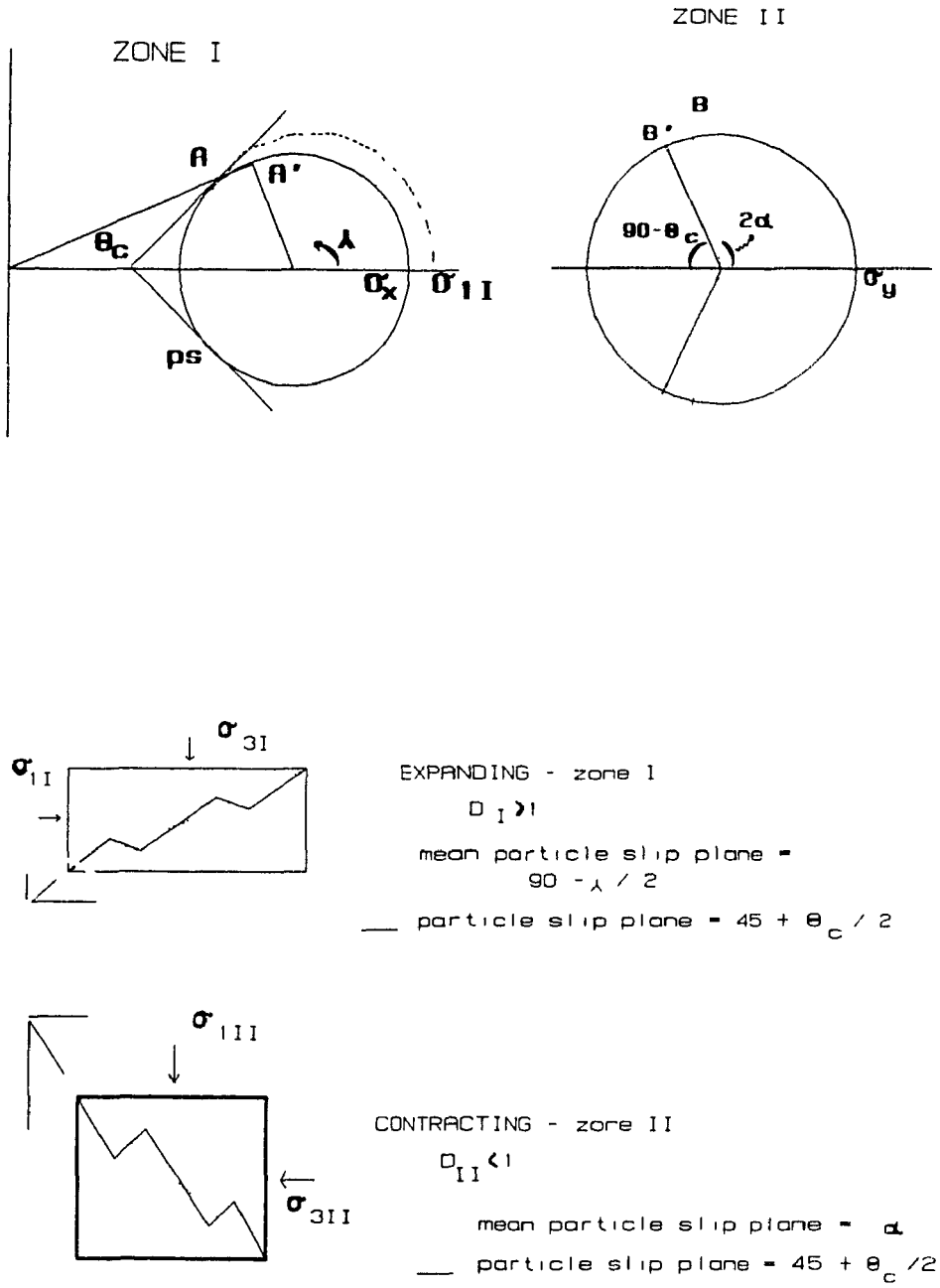

FIGURE 5.5 - Mohr-Coulomb Circle of Stress for Wheat in a 2D Packed Bed. H_o = 0.17 m and RH = 30%.

respectively. Note that $\bar{D}$ is the mean overall slip deformation ratio of a given 2D packed bed of particles, and it is related to the overall effective solid stress developed in this porous material.

From eq. (5.25), D_I and D_{II} can be given by:

$$D_I = \tan(90° - \lambda/2) \tan(45 - \theta_c/2) \qquad (5.29a),$$

$$D_{II} = \tan\alpha \tan(45 - \theta_c/2) \qquad (5.29b).$$

For $\bar{D} = 1.0$, the volumetric slip deformation of the porous material is zero. Point A (see Fig. 5.5) tends to A' and B to B'. This means:

$$\lambda = 90° - \theta_c \text{ , and}$$

$$2\alpha = 90° + \theta_c$$

Such a condition is obtained in packed beds of linseed where the electrostatic effect is high (Chap. 4). Compaction of the particles in the bottom of the bed is possibly constrained by electrostatic charges.

For $\bar{D} < 1.0$, the porous material contracts and the following conditions hold for the case analyzed in Fig. 5.5:

(a) $D_{II} < 1.0$, the porous material contracts in zone II (upper center of the bed). From Fig. 5.5, this means that:

$$2\alpha < 90° + \theta_c$$

(b) $D_I > 1.0$, the porous material dilates in zone I (lower region of the bed). From Fig. 5.5, it can be seen that :

$$\lambda < 90° - \theta_c.$$

Such conditions are obtained in beds of wheat, barley and rice.

For $\bar{D} > 1.0$, the porous material dilates and:

$\lambda > 90° - \Theta_c$, and

$2\alpha > 90° + \Theta_c$.

Based on eqs (5.29a and b) and on the Mohr-Coulomb circle in Fig. 5.5, $\bar{D}$ can be written as:

$$\bar{D} = \tan \alpha \tan \lambda/2 = 1 - \cos(\alpha + \lambda/2)/(\cos \alpha \cos \lambda/2) \quad (5.30),$$

where:

$$2\alpha = 180° - \lambda - 3(90° - \lambda - \Theta_c) \quad (5.31).$$

In eq. (5.30), it is assumed that there is no relative rotation between particle and fluid.

To obtain the relationship between a and $\bar{D}$ it is necessary to determine the Coulomb failure angle for wheat at the critical state. The value of this angle is in the range of 23.9 to 24.8 degrees (Lobnes et al., 1987). Assuming a value of 24° for the Coulomb failure angle, $\bar{D}$ calculated from eq. (5.30) is 0.843 (SD = 9%), which is virtually identical to the value of a obtained by the regression analysis.

The above result shows that the overall mean parameter $\bar{D}$ defined by eq. (5.28) is the drag coefficient related to the inertial fluid flow effects in packed beds of wheat. Moreover, this coefficient is a strong function of non-elastic deformations occurring in a 2D packed bed and, as

a result, a function of the porosity gradient.

The last step (d) is to extend these results of wheat to other particles. The experimental data obtained with packed beds of millet, linseed and barley and rice for RH = 30% were analyzed in the same way as those presented here for wheat. The values of the empirical constants in eq. (5.30) were determined by setting $\bar{D} = a$. These results are presented in Table 5.2.

(The statistical parameters and empirical coefficients of the regression pressure drop versus air superficial velocity curve for rice, millet, linseed and barley are presented in Appendix E).

TABLE 5.2

EXPERIMENTAL VALUES FOR THE PARAMETERS IN EQ. (5.30)

PARTICLE :	MILLET	BARLEY	LINSEED	RICE
λ (degrees)	63.0	69.5	38.9	65.2
α (degrees) from eq. (5.30)	65.0	44.5	70.1	50.1
Θ_c (degrees) from eq. (5.31)	31.5	13.0	51.0	20.0
$\bar{D} = a$ (-)	1.315	0.682	0.972	0.765

Note: SD = 1.5 degrees.

In the case of millet, $\bar{D} > 1$, and the porous material dilates before failure is reached. The bed configuration of millet at failure is different from that of the bed of wheat as presented in Fig. 5.4. In the upper region of the bed, particles slip up in the center, while in the region near the wall, the particle slip is restrained by the change in pore geometry. This result explains the continuous motion of the bed surface (particles move up and fall down) observed during the fluidization experiments in beds of millet. Moreover, fluidization starts at the bottom of the column in 2D beds of millet while it starts at the top of the column in 2D beds of wheat.

In the case of linseed $\bar{D}$ is close to 1. This means that the failure angle is close to the Coulomb angle at the critical state. The low sphericity of linseed particles and the electrostatic cohesion of particles explain the high value obtained for the failure angle. As pointed out in Chap. 4, the fluidization of 2D packed bed of linseed were characterized by channels. The channeling regime should be a result of the high Coulomb failure angle.

In the case of barley and rice, $\bar{D}$ is lower than that for wheat. Particle segregation explains the low value of the Coulomb failure angle. Rice presented a large amount of broken grains while barley was composed of two species of grains with different sizes.

There are no data in the literature to compare the Coulomb failure angle for millet, barley, linseed and rice. However, the ranges of these values obtained here are comparable to those obtained in triaxial compression tests for sand (22° - 30°), glass beads (22° - d_p = 3 mm),

soybeans (26.2°), corn (21.3°) (see Rowe, 1971 and Lobnes et al., 1987).

Eqs. (5.26) and (5.30) are well suited to predict the overall flow characteristics in the annular region of 2DSBs or 2DSFBs. Further data are needed to correlate the angle λ with bed dimensions and particle properties.

5.5 Conclusions

The main conclusions of these analyses can be summarized as follows:

(1) The deformations which occur in a 2D packed bed of coarse particles can be classified as elastic and plastic deformations. The plastic deformations result from anisotropy of the porous material due to the geometry of the container vessel;

(2) The lateral vessel wall on the 2D fluidized bed reverses the particle slip direction at the bottom. Different types of failure (active and passive) occur in the upper and lower regions of the 2D packed bed. The pore structure deforms following specific directions dictated by the reversal of the principal stresses. Zones of stress discontinuity develop inside the porous material, and plastic or slip deformations occur in these zones as the fluid flow rate is increased.

(3) Two physical parameters were obtained to describe the influence of the slip deformations on the air flow characteristics in a 2D packed bed. Based on the stress distribution at failure in 2D beds of wheat, these parameters have been related to the frictional angle of the porous material.

(4) A modified form of the Ergun equation was obtained to describe

the pressure drop in 2D packed beds characterized by slip deformations before fluidization.

(5) The modified form of the Ergun equation was applied to the experimental data for the determination of the failure angle of the porous material in a 2D packed bed. The results showed a good agreement between the range of the Coulomb failure angle obtained here and that reported in the soil mechanics literature.

CHAPTER 6

MECHANISMS OF SPOUT TERMINATION IN TWO DIMENSIONAL BEDS

6.1 Spout Formation

Spout formation and stability of a 2DSB are analyzed in this chapter regarding: nozzle dimensions; air relative humidity; and particle properties.

Wheat and molecular sieve particles were used for the first two steps. Both particles belong to the true Geldart group D and present similar properties except for the particle sphericity which is lower for wheat than for molecular sieve (see Tables 4.2 and 4.3 for details).

The two nozzles used in this work are specified as follows:

NOZZLE	A_N (m^2)	L_N (m)	height inside bed (m)
N1	0.015 x 0.015	0.015	0.007
N2	0.015 x 0.030	0.030	0.007

Two values for the air relative humidity were used: RH = 30% and RH = 60%. The inlet air temperature was 20°C for RH = 30%, and 27°C for RH = 60%. The effects of particle properties on spout stability were analyzed by fixing the range of air relative humidity and nozzle dimensions.

The experimental determination of the maximum spoutable bed height was based on the following criteria:

(i) $V_{ms} = V_{mf}$ at $H_{ms} = H_{max}$;

(ii) Changes of the shape of bed surface, from a parabolic concave to a convex shape.

The characterization of the spout termination mechanisms was based on visual observations of bed behavior and spout formation. The mean bed porosity at minimum spouting was calculated by measurements of the bed height and spout dimensions just before the onset of spouting.

6.1.1 Effect of Nozzle Width

Air with RH = 60% was used in these experiments. The static bed height was varied from 0.10 m to a little over the maximum spoutable bed height. During each experiment, changes of bed height and of the spout cavity dimensions were registered.

Two distinct spout pressure drop versus the air superficial velocity curves have been obtained for each nozzle, as shown in Figure 6.1. The mean experimental points in this figure are joined by a dashed smooth curve without any statistical analysis. The mean standard deviation values based on replicate data (SD) are listed in the figure caption.

Point A in Fig. 6.1 represents the maximum spouting pressure drop. At point B, the internal cavity breaks for the first time the top of the bed surface. At point C, the spout is formed. The fountain, the annulus and the spout regions are each well defined. At point D, the spout collapses completely. By definition, point D is the minimum spouting point.

The effects of nozzle width on the SB dynamics can be summarized as follows (see Fig. 6.1):

(i) The spouting pressure drop increases as the nozzle width increases. As shown in Fig. 6.1, it is higher for L_N = 0.03 m (N2) than it is for L_N = 0.15 m (N1). For wheat at H_o = 0.10 m, the maximum

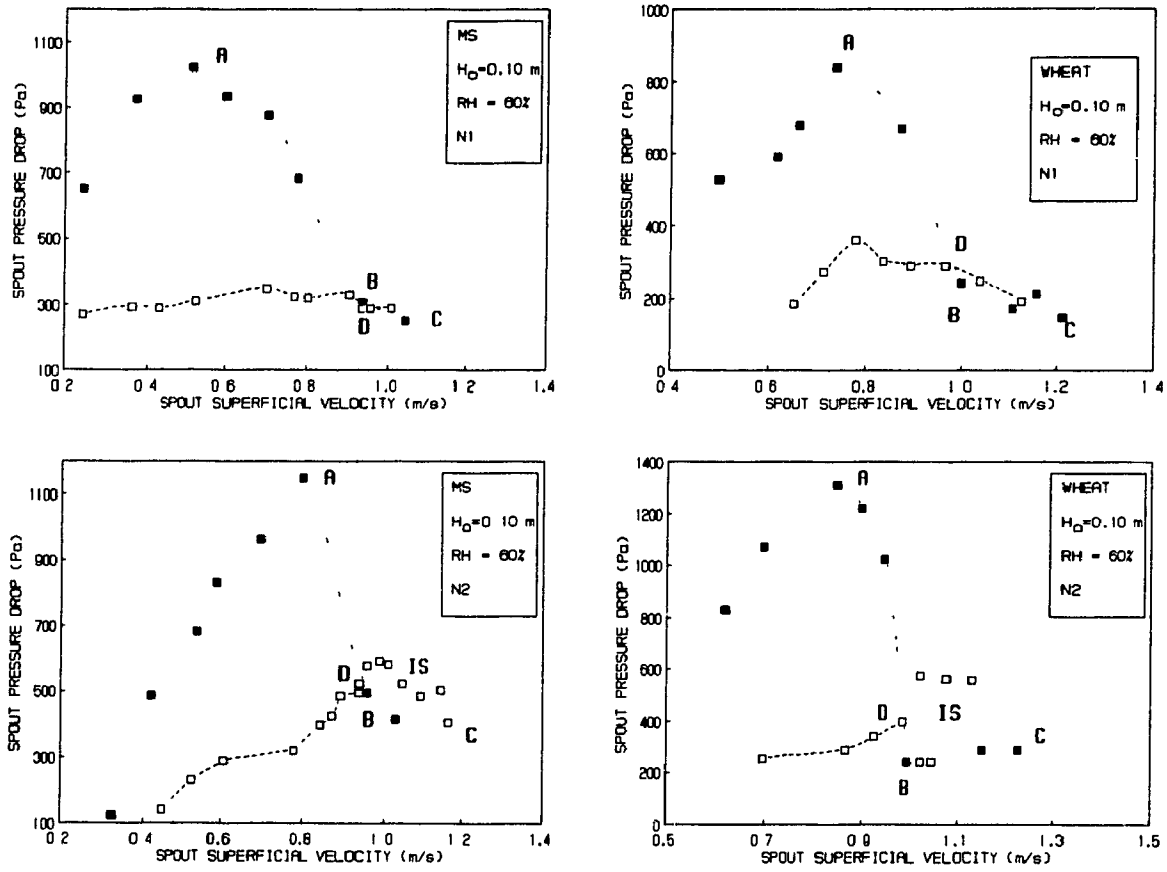

FIGURE 6.1 - Effect of Nozzle Width on Spouting Pressure Drop Curves for 2DSBs of Molecular Sieve and Wheat.
Full symbols = increasing air velocity; empty symbols = decreasing air velocity.
Point A = maximum spouting pressure drop; point B = spout formation; point C = stable spouting; point D = spout collapse. IS: unstable or incoherent spouting.
SD for molecular sieve = 5% (for both nozzles). SD for wheat = 4% (for both nozzles).

pressure drop was about 56% higher; while for molecular sieve it was only about 12%;

(ii) The spout formation is characterized by solids circulation inside the internal cavity for small nozzle widths (N1 type nozzle). Solids circulation develops just after point A (Fig. 6.1). From point A to B, the cavity grows laterally and vertically. At point B, it reaches the top of the bed surface. The bed height and the shape of bed surface change according to the cavity growth. Figure 6.2 presents a schematic representation of changes occurring in such beds before the onset of spouting;

(iii) The spout formation is characterized by an empty cavity for high nozzle widths (N2 type nozzle). At point A, a dense compact arch is developed above the cavity. This arch is broken suddenly and the spout appears at the top of the bed surface. The transition between point A and B is less smooth than that observed with N1 type nozzle. The pressure drop decreases rapidly beyond point A, as shown in Fig. 6.1 for N2 type nozzle. Just before point B, particles move up and down inside the cavity; however there is no solids circulation around or inside the cavity (see Fig. 6.2);

(iv) An unstable spouting regime (incoherent spouting) occurs beyond point B for N2 type nozzle. This regime is characterized by flat waves or ripples moving inside the spout region, and pressure fluctuations at the onset of spouting (see Fig. 6.1);

(v) The minimum spouting air superficial velocity is in the same range for both nozzles as shown in Fig. 6.1 (point D).

Different mechanisms of spout termination were observed for each

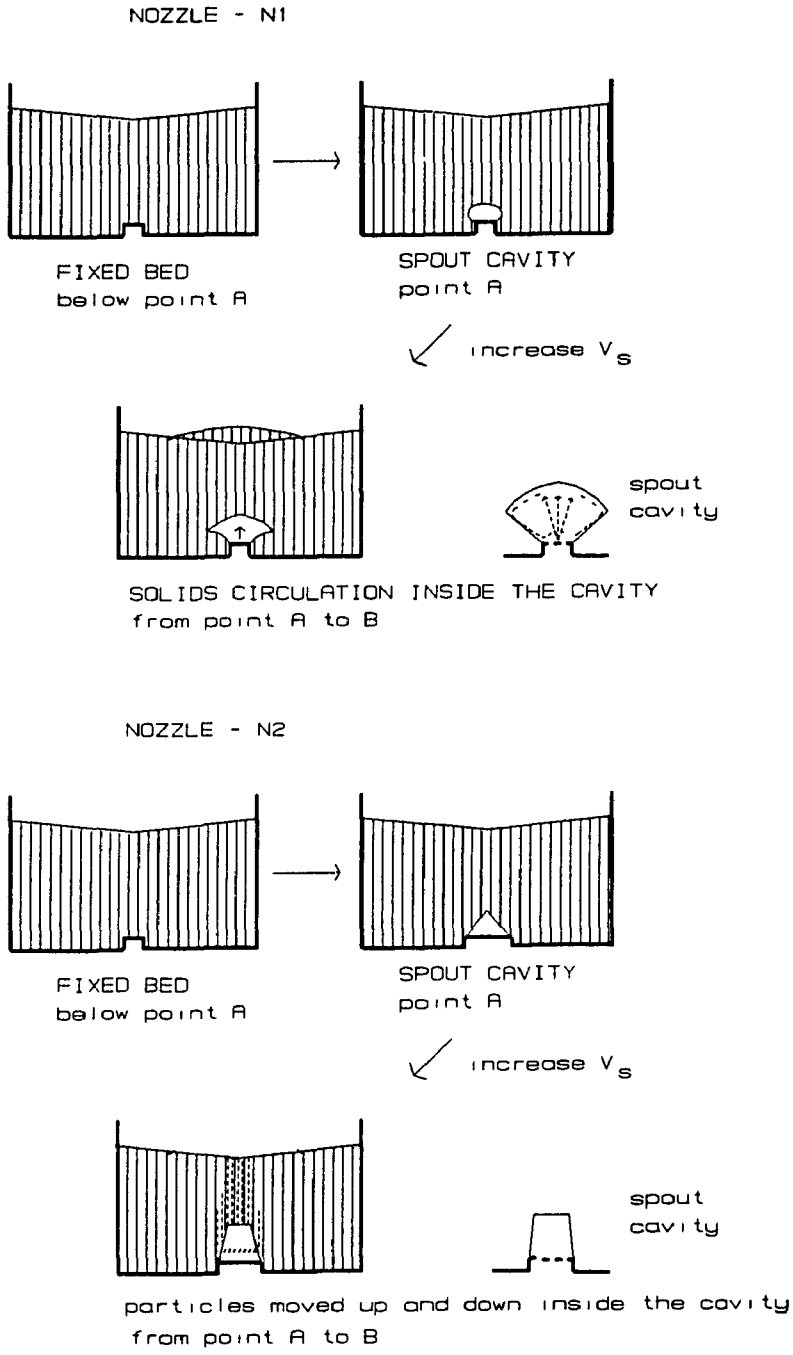

FIGURE 6.2 - Schematic Representation of Spout Formation in a 2DSB as a Function of the Nozzle Dimensions.

nozzle at $H_{ms} = H_{max}$. The spout cavity broke into bubbles in the lower region of the bed in 2DSBs fitted with N2 type nozzle. The top of the annulus surface was fluidized (mainly near the vessel wall) in 2DSBs fitted with N1 type nozzle. Moreover, H_{max} decreased as L_N increased.

For small nozzle widths (N1 type nozzle), a stable spout regime was observed at relatively high superficial velocities ($V_s > 1.2\ V_{mf}$), for $H_{max} < H_{ms} < H_{min,s}$. The spouting pressure drop decreased rapidly and reached negative values as shown by Ojalvo's (1989) results (curve 1 of Fig. 2.3b). At $H_{ms} = H_{min,s}$ the spout could not develop even at high flow rates due to the large bubbles (solids slugs) developed at the top of the annulus surface.

6.1.2 Effect of Air Relative Humidity

Typical spouting pressure drop versus air superficial velocity curves for 2DSBs using air with low relative humidity (RH = 30%) are presented in Figure 6.3. A comparison with Fig. 6.1 shows that a decrease of RH results in an increase of V_{ms}. Moreover, a high air flow rate is required for spout formation (points A and B in Fig. 6.3). For example, for 2DSBs of molecular sieve at H_o = 0.10 m with N1 type nozzle and RH = 60%, V_s = 0.52 m/s (=1.8×10^{-3} kg/s) at point A; while for RH = 30%, V_s = 1.08 m/s (= 3.8×10^{-3} kg/s), i. e., about twice as great.

These results are in agreement with those presented in Appendix B and Chap. 4 for 2D-fluidized beds. As shown in Chap. 4, the minimum fluidization velocity increases as RH decreases due to the electrostatic interactions between particle and vessel wall, and between particle-particle. The electrostatic adhesion force between the dry particles and

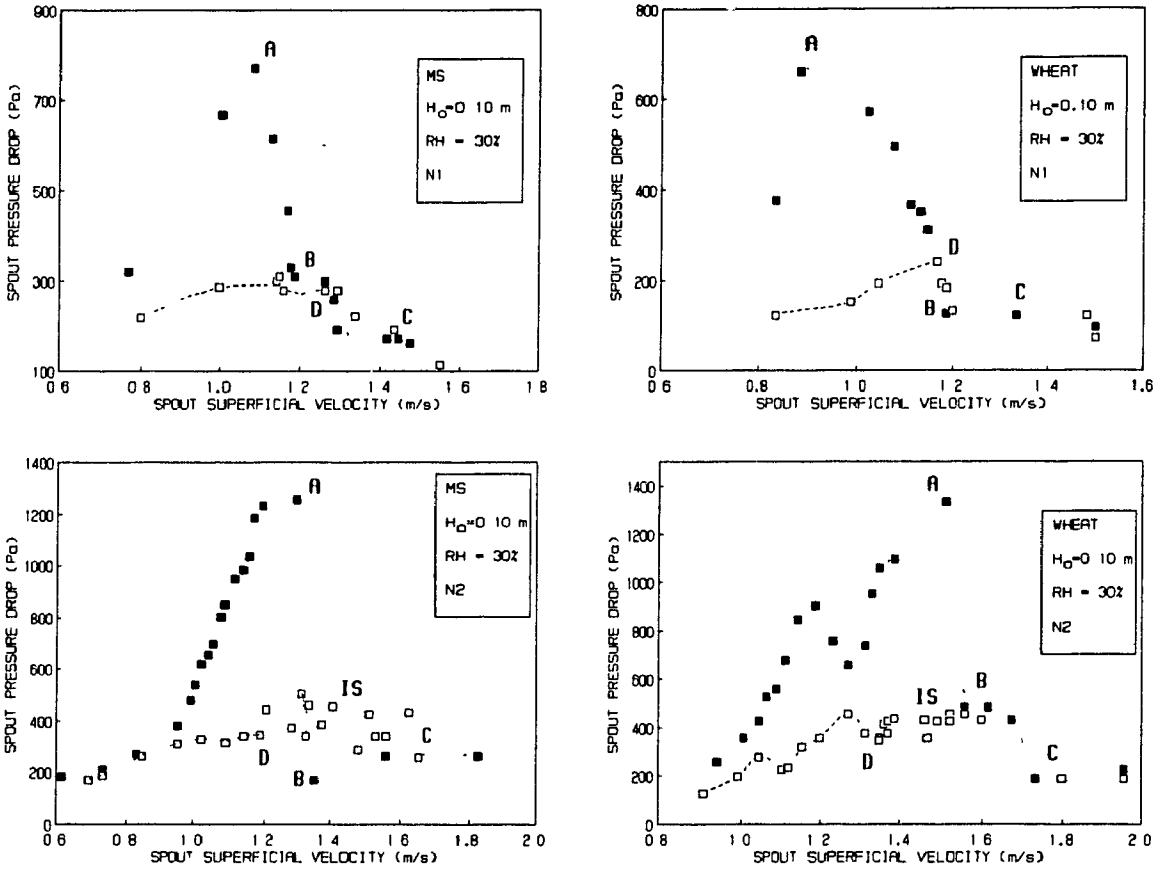

FIGURE 6.3 - Spouting Pressure Drop Characteristic Curves for 2DSBs of Molecular Sieve and Wheat with RH = 30%.
Full symbols = increasing air velocity; empty symbols = decreasing air velocity.
Point A = maximum spouting pressure drop; point B = spout formation; point C = stable spout; point D = spout collapse. IS: unstable or incoherent spouting.
SD for molecular sieve = 6% (N1 type nozzle) and 3% (N2 type nozzle). SD for wheat = 3% (N1 type nozzle) = 5% (N2 type nozzle). (SD-standard deviation for data replication).

vessel wall retards the onset of spouting in 2DSBs using air at RH = 30%. The bed porosity also increases similarly to the increase observed in 2D-fluidized beds (Chap. 4).

The mechanisms of spout formation in beds spouted with air at RH = 30% are similar to those at RH = 60%. However, for N2 type nozzle at RH = 30 %, the superficial velocity at point B (Fig. 6.3) is higher than that at point D (Fig. 6.3). As the air velocity is increased a compact arch forms above the spout cavity and the particles adhere to the vessel. The pressure drop rises again as shown in Fig. 6.3. A higher air flow rate is necessary to break this compact and cohesive arch. As seen in Fig. 6.3, for 2DSBs of wheat the cavity broke the bed surface at V_s = 1.56 m/s (point B), while the spout collapsed at V_s = 1.34 m/s (point D).

These data were replicated twice more through experiments carried out consecutively in the same vessels. The results obtained for wheat at H_o = 0.10 m are presented in Figure 6.4. The mean standard deviation of data replication is 6% when all data are included. From Fig. 6.4 it can be seen that consecutive experiments carried out with the same spouted bed of particles do not increase the amount of static charges. The saturation of static charges is a possible explanation for this result, as discussed in Appendix B.

For N1 type nozzle the effect of wall-particle adhesion on spout formation was lower possibly due to the solids circulation inside and around the cavity. The intensive motion of particles distributed the amount of static charges in a large particle-wall area. This means that the particle-wall adhesion force per unit area of the wall decreases compared with that in beds with N2 type nozzle. As a conclusion, for

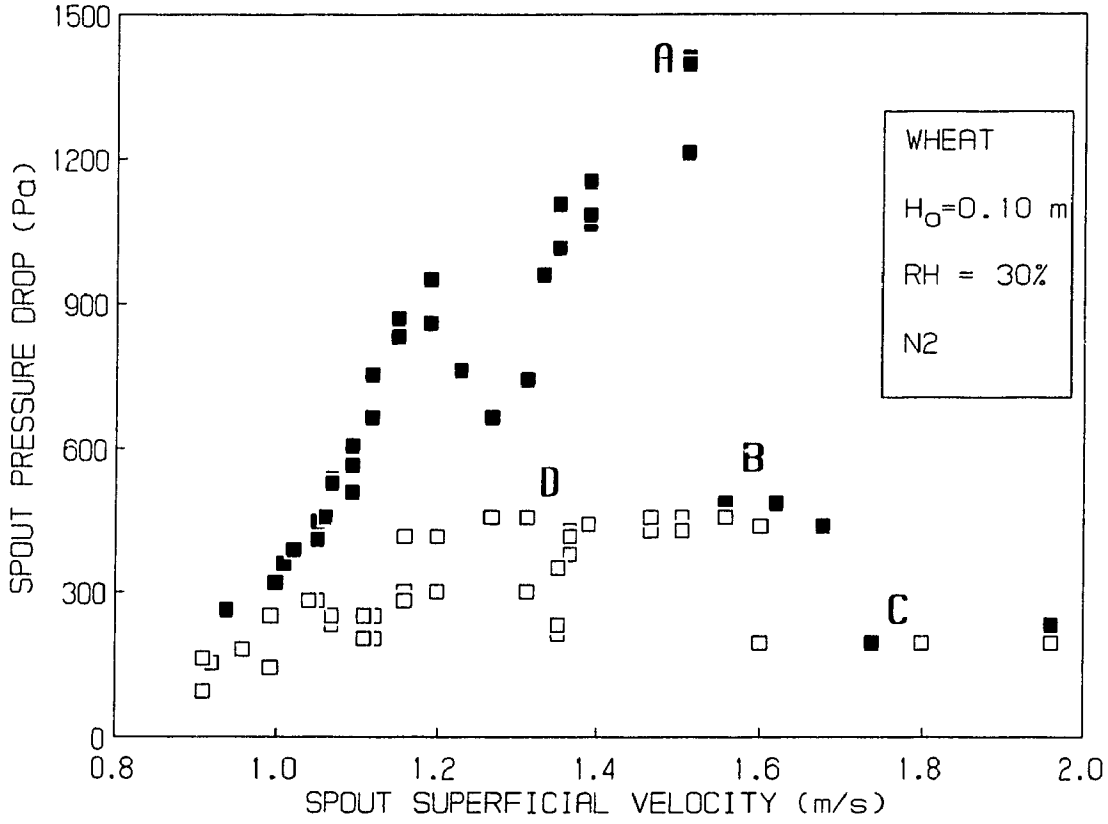

FIGURE 6.4 - Spouting Pressure Drop Characteristic Curves for 2DSBs of Wheat - Data Replication.
N2 type nozzle; RH = 30%.
(Nomenclature and symbols - see Fig. 6.3).

small nozzle widths (N1 type nozzle), the particle-wall adhesion force does not affect significantly the spouting pressure drop curves. The increase of bed porosity is the main effect of lower air humidity; this is evident from the low values obtained for the maximum spouting pressure drop in beds with N1 type nozzle and RH = 30% (see Figs. 6.3 and 6.1).

6.1.3 Effect of Particle Properties:

The experiments with the other particles, used in this work, were carried out in 2DSBs fitted with N1 type nozzle using air with RH = 30%.

The spout formation and the spouting pressure drop characteristics obtained for glass beads, barley and millet were found to be similar to those obtained for wheat and molecular sieve using the same nozzle and air relative humidity.

However, for particles with low sphericity e.g. linseed and plastic pellets, solids circulation around the cavity disappeared due to strong particle orientation effects. As shown in Figure 6.5, as soon as the cavity is formed and starts to grow, the particles orient themselves in a manner that blocks lateral air flow from the cavity to the annulus. A compact arch develops. The shape of the cavity changes and becomes similar to that observed in 2DSBs with N2 type nozzle. Similar behavior was also observed in 2DSBs of rice at RH = 60% and with N1 type nozzle.

The spouting pressure drop versus air superficial velocity curves for plastic pellets and barley at H_o = 0.10 m; and for molecular sieve and linseed at H_o = 0.17 m are shown in Figure 6.6. It can be seen from this figure that pressure fluctuations are apparent in the bed of plastic pellets and linseed beyond point B. This behavior characterizes the

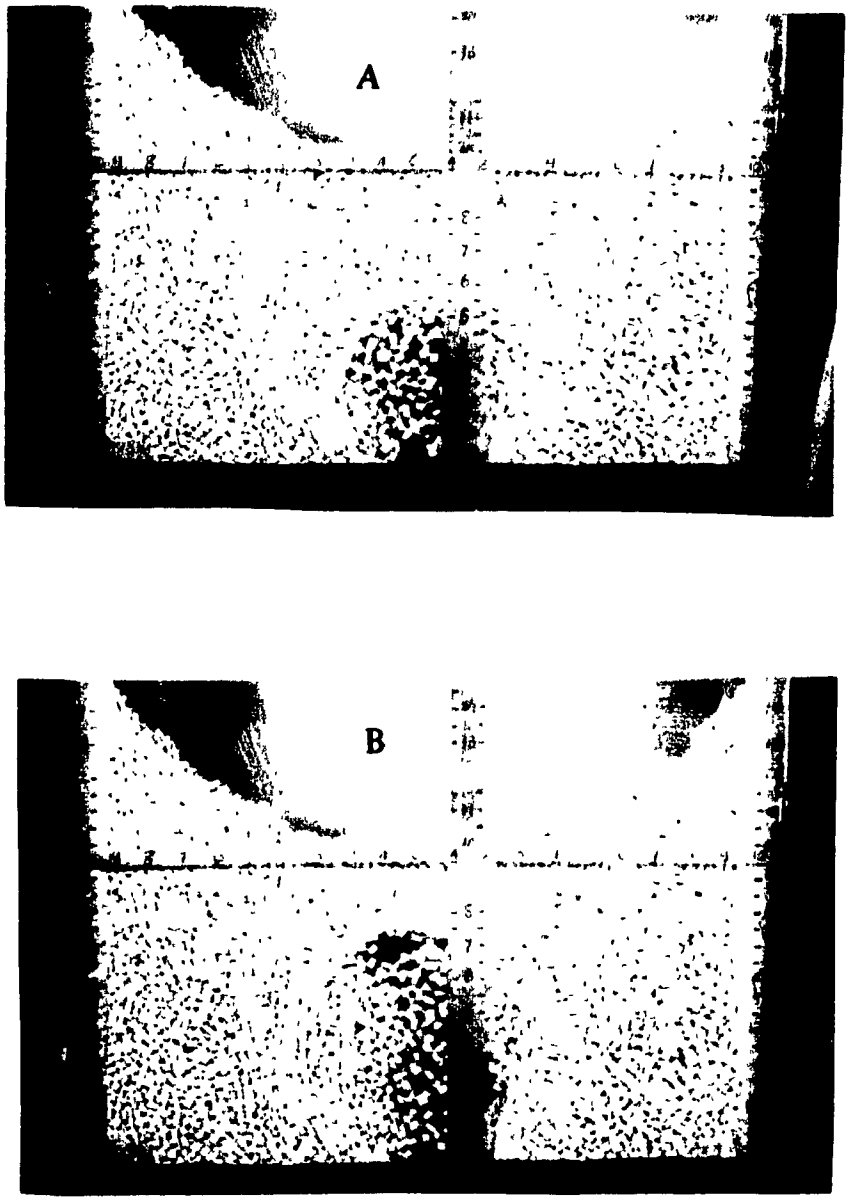

FIGURE 6.5 - Spout Formation in Beds of Particles with low Sphericity. Particle: plastic pellets, L_N = 0.015 m, RH = 30%. (a) = formation of internal cavity; (b) change of cavity shape before the onset of spouting.

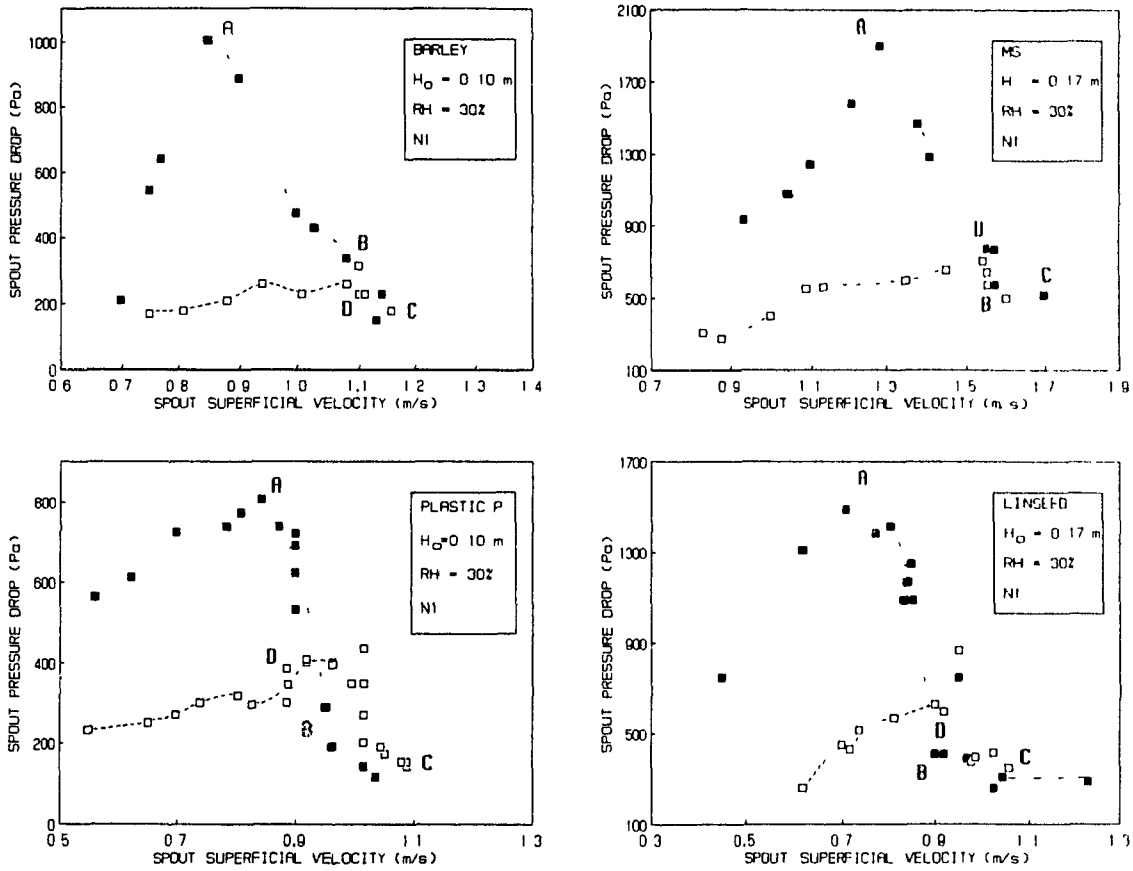

FIGURE 6.6 - Effect of Particle Properties on Spouting Pressure Drop Curves for 2DSBs: N_1 type nozzle; RH = 30%.
Full symbols = increasing air velocity. Empty symbols = decreasing air velocity.
Point A = maximum spouting pressure drop; point B = spout formation; point C: stable spouting; point D = spout collapse.
(SD is between 3% to 6%).

incoherent spouting regime reported in 2DSBs of nozzle N2 (see Figs. 6.1 and 6.3).

It was observed that the bed surface was broken at different points at the onset of spouting for 2DSBs of spherical and non-spherical (with a sphericity higher than 0.85) particles (e.g. glass beads, millet, barley). The spout was not stable but oscillated around the central axis of the column. This instability occurring in spouted beds between point B and C (Fig. 6.6) is related to the growth of the spout cavity.

The configuration of a 2DSB of millet at H_o = 0.15 m before and after the onset of spouting (V_s = 0.9 V_{ms} and V_s = 1.05 V_{ms}) is shown in Figure 6.7. As can be seen in Fig. 6.7a, there is a change in the particle slip direction along the spout cavity. This represents different types of failure in the annulus and the spout-annulus interface regions as shown later in Chap.7. The pore-particle material deforms plastically in the upper center region of the bed as the spout cavity grows. Basically, two weak points are developed in the top of bed surface before the onset of spouting. These points are represented in Fig 6.7a by the intercept of the dashed lines with the bed surface. A periodic oscillation of spout is observed around these two points (Fig. 6.7b). Particles slip on the bed surface from the vessel wall towards the central core, and the spout-annulus interface loses its stability in the upper region of the bed, as shown in Fig. 6.7b.

6.2 Maximum Spoutable Bed Height

Based on the experimental results of this study, the 2DSB air-particle systems used can be divided into two groups as follows. Group #1

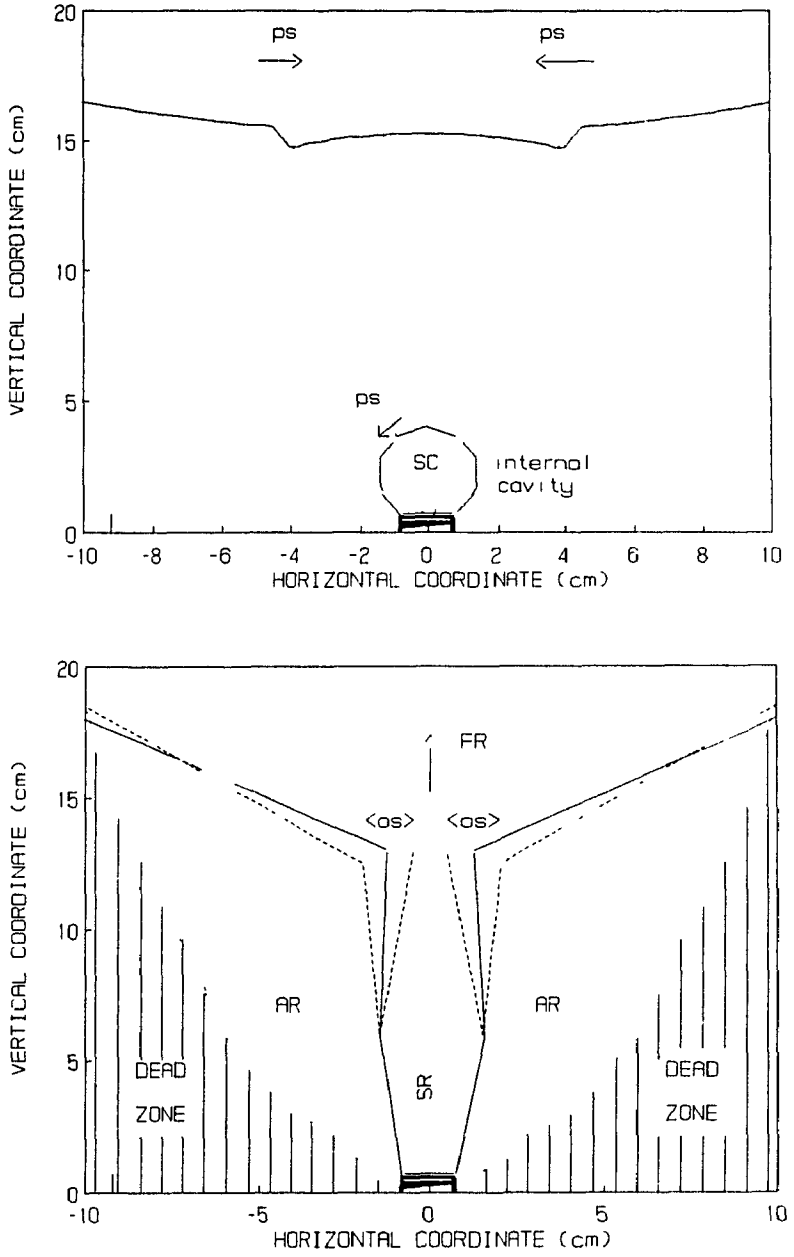

FIGURE 6.7 - Spouted Bed Configuration before and after the Spout Formation for Millet at H_o = 0.15 m.
(a) Bed configuration before the spout formation (V_s = 0.9 V_{ms}. SC = solids circulation inside the internal cavity; ps = particle slip. Dashed lines = region where plastic deformations occur.
(b) Bed Configuration at the minimum spouting (V_s = 1.05 V_{ms}). AR = annulus region with particle circulation; SR = spout region; FR = fountain region; os = region of spout oscillation.

is characterized by 2DSB systems where the incoherent spouting regime is observed beyond point B (see Figs. 6.1 and 6.3). Group #2 is characterized by 2DSB systems where periodic oscillations of the spout around the central axis of the column are observed after the onset of spouting.

The experimental values of H_{max} / L_1 are presented in Table 6.1 as a function of the dimensionless parameter A_{2D}. This dimensionless parameter A_{2D} represents the ratio of the minimum inlet energy required to sustain the spout to the frictional energy lost across the spout at $H_{ms} = H_{max}$ (see Chap. 2). This parameter is defined by eq. (2.7) for 2DSBs, and this characterizes the fluid-particle properties.

The maximum experimental standard error estimated for H_{max} was 6%. The minimum fluidization velocity was obtained from the experimental data and equations developed in Chaps. 4 and 5. The terminal fall particle velocity (V_T) was calculated using the correlations presented in Appendix A. The mean bed porosity was determined based on the spout dimensions and bed height at the onset of spouting for beds at $H_{ms} = H_{max}$ The maximum error estimated for A_{2D} varied from 6% (spherical or quasi-spherical particle) to 12% (very flat particles).

The 2DSBs of wheat and molecular sieve fitted with N2 type nozzle at RH = 30% represent the transition between Group #1 and #2. The predicted value of $(L_1/L_N)_{min}$ (see eq. (2.6)) for these two 2DSB systems is 5.0 (wheat) and 7.8 (molecular sieve). These results confirm the transitional behavior of these two 2DSB systems regarding the spout termination mechanism ($L_1/L_N = 6.7$). However, eq. (2.6) cannot predict the transition for particles with low sphericity such as rice, linseed

TABLE 6.1

MAXIMUM SPOUTABLE BED HEIGHT IN 2DSBs AS FUNCTION OF PARTICLE CHARACTERISTICS

Particle	RH (%)	L_N (m)	ϵ_{ms} (-)	A_{2D} (-)	H_{max}/L_1 (-)
		GROUP # 1			
linseed	30	0.015	0.420	0.010	0.795
plastic	30	0.015	0.414	0.026	0.575
rice	60	0.015	0.455	0.030	0.780
ms	60	0.030	0.383	0.031	0.825
wheat	30	0.030	0.452	0.035	0.553
		GROUP #2			
ms	30	0.030	0.395	0.044	0.515
wheat	60	0.015	0.394	0.047	0.510
millet	30	0.015	0.414	0.053	0.775
barley	30	0.015	0.425	0.056	0.798
wheat	30	0.015	0.420	0.062	0.880
ms	60	0.015	0.383	0.063	0.877
ms	30	0.015	0.413	0.099	0.901

Note: L_1 = 0.20 m, L_2 = 0.015 m. Bed porosity at H_{ms} = H_{max}

and plastic pellet.

Based on the results shown in Table 6.1, it can be seen that:

(i) H_{max} / L_1 is less than 1 for all 2DSBs analyzed. The maximum obtained value of H_{max} was 0.18 m (2DSB of molecular sieve fitted with N1 type nozzle at RH = 30%). It is important to note that a stable spouting regime could be achieved at $H_{ms} > H_{max}$ (but less than $H_{min,s}$) for high air flow rates ($V_g > V_{mf}$) in 2DSB systems of Group #2;

(ii) There is a progressive increase of H_{max} / L_1 with increasing A_{2D} for 2DSBs systems of Group #2. The ranges of the relevant dimensionless parameters to determine H_{max} (see eq. (2.7)) are: $3.5 < L_N / d_p < 9.0$; $0.044 < A_{2D} < 0.10$; $0.5 < L_2 / L_N < 1.0$. Moreover, the particle sphericity varies from 0.90 to 1.00.

(iii) There is no apparent relationship between H_{max} / L_1 and A_{2D} for 2DSBs systems of Group #1. For this group, A_{2D} is always lower ($0.010 < A_{2D} < 0.044$). The particle sphericity varies from 0.56 to 1.00.

It is important to point out that the electrostatic and wall effects are included implicitly in the dimensionless parameter A_{2D} through the appropriate minimum fluidization velocity. The values of A_{2D} obtained for each group are consistent with the mechanisms of spout formation and termination described earlier. Group #1 is characterized by low values of A_{2D} (low jet inlet momentum) with slugging or choking of spout as the possible mechanism for spout termination. Group #2 is characterized by higher values of A_{2D} ($A_{2D} > 0.044$) with fluidization of the annulus top as the main mechanism for spout termination. As shown later, there is a transitional region ($0.044 < A_{2D} < 0.094$) in which the spout mechanism changes from the choking of spout to the fluidization of the annulus top.

Although, in this transitional region, H_{max} is characterized by the choking of spout mechanism, the oscillating spouting regime can be achieved for $H_{max} < H_{ms} < H_{min,s}$

Table 6.2 presents three sets of data for H_{max} obtained from Ojalvo (1989) who used soybean as the model particle (d_p = 6 mm, sphericity = 0.98, solid density = 1190 kg/m^3). The value of H_{max} was determined based on his pressure drop characteristic curves ($V_{ms} = V_{mf}$ at $H_{ms} = H_{max}$). The mean bed porosity was calculated based on his data on bed expansion.

The Ergun equation (1952) was used to determine V_{mf}. As shown in Chap. 4, the Ergun equation cannot be used to predict the full pressure drop curve in 2D fluidized beds; however, for large particles (true Geldart group D particles) fluidized by air at RH = 60%, this equation estimates V_{mf} reasonably well. (See Table 4.7). The standard errors for H_{max} and A_{2D} obtained from Ojalvo's data are in the same range as those presented here.

Unfortunately, owing to insufficient information about particle properties, bed

TABLE 6.2

MAXIMUM SPOUTABLE BED HEIGHT IN 2DSBs OF SOYBEAN
(from Ojalvo, 1989)

Particle: Soybean

Group	L_1 (m)	L_N (m)	A_{2D} (-)	H_{max}/L_1 (-)
#1	2x0.119	2x0.013	0.042	0.771
#2	2x0.168	2x0.003	0.193	0.851
#2	2x0.146	2x0.003	0.194	0.848

Note: L_2 = 0.20 m.

expansion, and even an appropriate definition of H_{max}, Volpicelli et al.'s (1967) and Anderson et al.'s (1984) data could not be included in the present analysis.

Using the experimental data presented in Table 6.1 and 6.2, the following forms of correlations for H_{max} were tested:

$$H_{max}/L_1 = (L_2/L_N)^{c1} \ (L_N/d_p)^{c2} \ (L_1/L_N)^{c3} \ A_{2D}^{c4} \qquad (6.1)$$

and

$$(H_{max}/L_1) \ A_{2D} = a_o + a_1 \ A_{2D} + a_2/A_{2D} \qquad (6.2);$$

where $c1$, $c2$, $c3$, $c4$, a_o, a_1, and a_2 are constants to be fitted empirically.

Eq. (6.1) is based on the McNab and Bridgwater equation (see Epstein and Grace, 1984) while eq. (6.2) is based on the Littman and Morgan (1982) equation. As shown in Appendix A, the McNab and Bridgwater equation predicts H_{max} reasonably well for CSBs of non-spherical particles with low values of A. The Littman et al. equation predicts H_{max} better for CSBs of large particles (high values of A).

The iterative multiple STATPAK regression program was used for the data analysis. The obtained results show that, for 2DSB systems of Group #2, the best correlation (eq. 6.3) for H_{max} is based on eq. (6.2) with H_{max}/L_1 as a function of A_{2D} only :

$$H_{max} / L_1 = 0.605 + 6.206\times10^{-2}/A_{2D} - 2.913\times10^{-3}/A_{2D}^2$$

$$\text{for } A_{2D} > 0.044 \qquad (6.3).$$

The standard deviation of eq. (6.3) is 0.048, the average deviation

is 4.3%, and the correlation coefficient squared is 0.997.

Although the experimental data are too limited to generalize eq. (6.3), it appears to be consistent with the mechanism of spout termination observed in 2DSB systems of Group #2. From Littman et al.'s assumptions (see Appendix A), the basic geometric parameters to predict H_{max} in CSBs of coarse particles (in which the fluidization of the annulus top is the spout termination mechanism) are given in terms of A_c/A_N. This ratio is reduced to L_1/L_N in a 2DSB (L_2 is a common parameter for both areas). However, as pointed out earlier, the effect of vessel-wall (and consequently L_2) is included implicitly in A_{2D} through the minimum fluidization velocity.

The experimental data are compared with eq. (6.3) in Figure 6.8b. This curve, when compared with one obtained by Morgan and Littman (1982) for CSBs of coarse particles, shows the same trend for high values of A_{2D} (or A). However, as A_{2D} decreases the shape of the curve becomes different from the one proposed by Morgan and Littman (1982) due to the negative sign obtained for the last term on the right side of eq. (6.3). From Fig. 6.8b, it is observed that there is a maximum in the H_{max}/L_1 vs. A_{2D} curve at $A_{2D} = 0.094$. For $A_{2D} < 0.094$, H_{max}/L_1 increases with A_{2D}. For $A_{2D} > 0.094$, H_{max}/L_1 decreases with A_{2D} until a constant value ($= 0.605$) is reached. There are no available data to confirm this asymptotic value.

For a given 2DSB system of Group #2, H_{max} / L_1 increases rapidly with increasing d_p for $0.044 < A_{2D} < 0.094$ as shown in Figure 6.9a. At $A_{2D} = 0.094$, H_{max} / L_1 reaches the maximum value. Beyond this peak, H_{max} / L_1 decreases slowly with the increase of d_p.

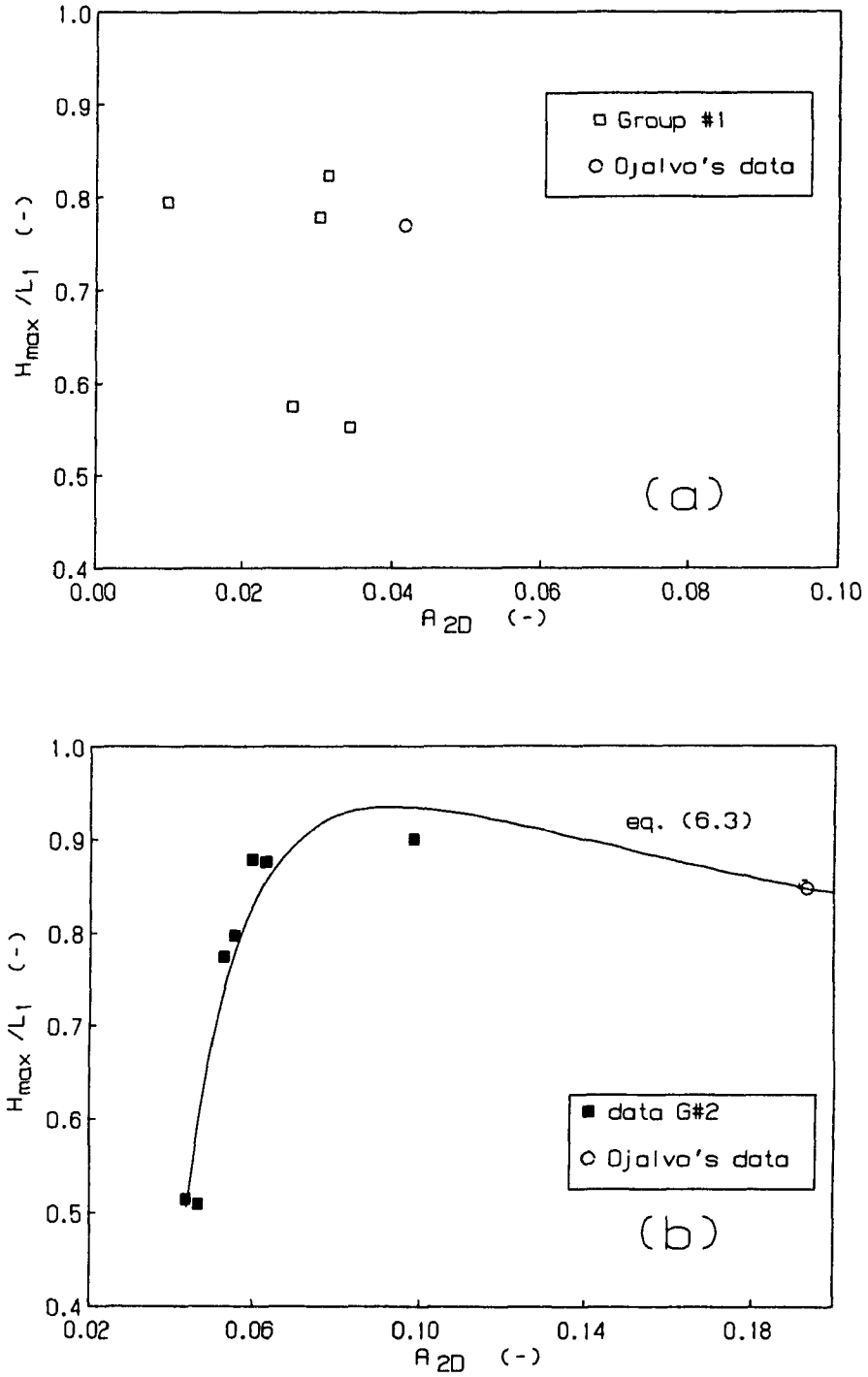

FIGURE 6.8 - Maximum Spoutable Bed Height in 2DSBs of Coarse Particles. H_{max} / L_1 versus A_{2D} .

(a) Group #1; (b) Group #2.

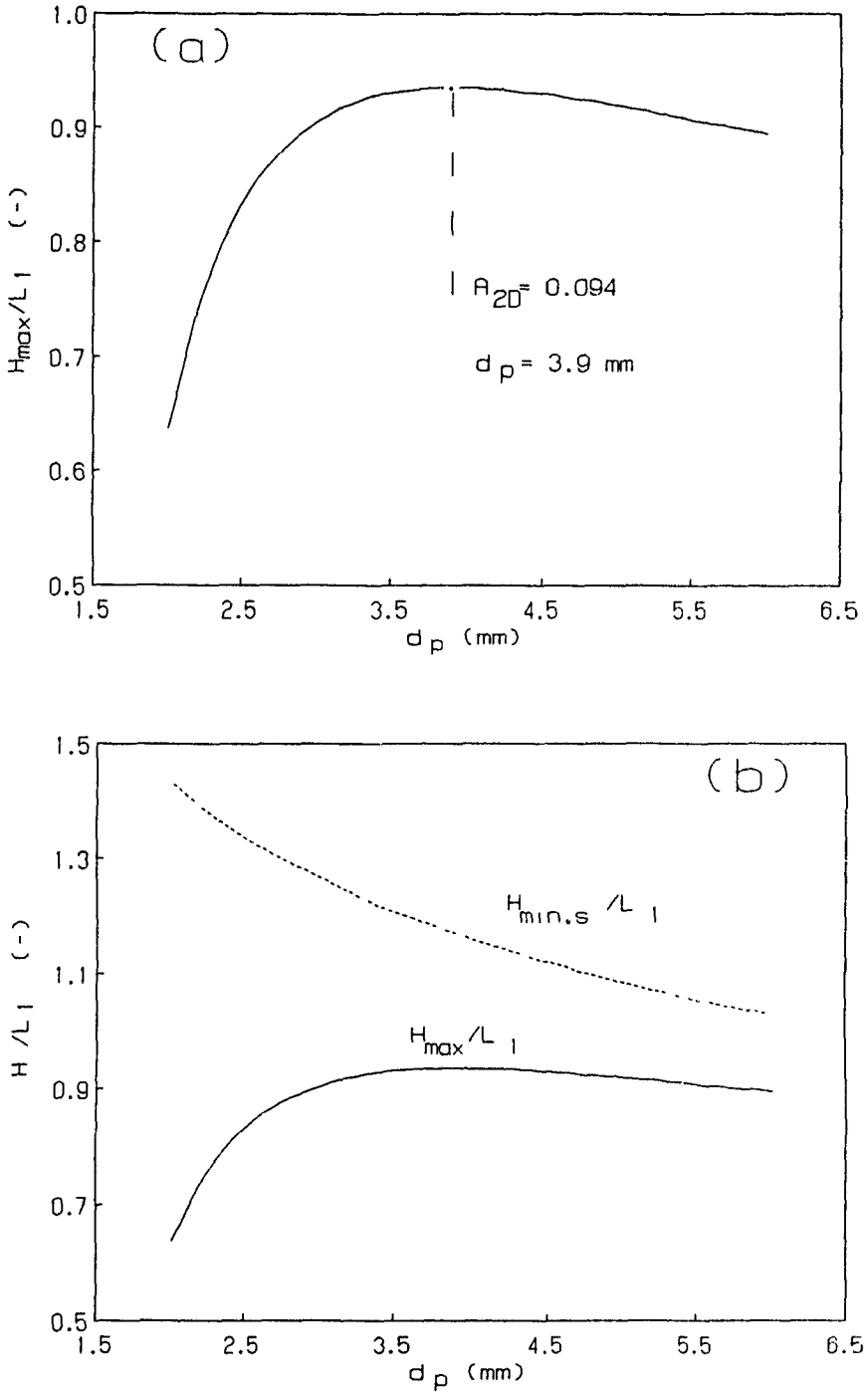

FIGURE 6.9 - Effect of Particle Diameter on Maximum Spoutable Bed Heights for 2DSB Systems of Group #2.
(a) H_{max}/L_1 vs. d_p - (curve predicted by eq. (6.3) with millet as the model particle and N1 type nozzle).
(b) Comparison between $H_{min,s}/L_1$ and H_{max}/L_1 for the same 2DSB systems used in (a).
Note: $H_{min,s}/L_1$ vs. d_p curve predicted by eq. (4.4).

As noted in Chap. 2, H_{max} decreases with increasing d_p for the fluidization of the annulus top mechanism (Chap. 2). Such a condition only occurs in 2DSB systems of Group #2 at $A_{2D} > 0.094$. From the results presented in Fig. 6.9a, it seems reasonable to suppose that for $0.044 < A_{2D} < 0.094$ the spout termination mechanism changes from choking of the spout to fluidization of the annulus. In Fig. 6.9b, the H_{max}/L_1 vs. d_p curve obtained for 2DSBs of millet is compared with the $H_{min,s}/L_1$ vs. d_p curve predicted by eq. (4.4). It was shown that as the particle diameter increases (and so A_{2D}) the values of H_{max}/L_1 approach those of $H_{min,s}/L_1$. This also indicates that fluidization (followed by slugging) should occur in the top of the bed as A_{2D} increases.

Morgan and Littman (1982) proposed a sudden transition for these two mechanisms. The results presented here show that, at least for 2DSBs, this transition is not sudden but it occurs in the range of A_{2D} between 0.044 and 0.094. In this transitional region, $V_{ms} = V_{mf}$ at $H_{ms} = H_{max}$, however the stable spouting regime can also be achieved for $H_{max} < H_{ms} < H_{min,s}$. As mentioned in the earlier section, for this range of H_{ms} between H_{max} and $H_{min,s}$, the spouting pressure drop decreases rapidly with the increase of V_s and a high superficial air velocity is necessary to maintain the spout. This transitional spout termination mechanism is the growth of instability mechanism defined by Volpicelli et al. (1967).

Eq. (6.3) can be used to elucidate the different spout pressure drop curves presented in Fig. 2.3. In Table 6.3 are shown the predicted values of H_{max}/L_1 and the calculated values of H_{ms}/H_{max} for each set of data in Fig. 2.3. For curve 2 (Fig. 2.3b), $H_{ms} < H_{max}$ and A_{2D} is much higher than 0.094. This leads to a different spouting drop curve from the one

TABLE 6.3

PREDICTED MAXIMUM SPOUTABLE BED HEIGHT FOR DATA IN FIG. 2.3

DATA (source)	A_{2D} (-)	H_{max}/L_1 (-) Eq. (6.3)	H_{ms}/H_{max} (-)
Fig. 2.3a	0.220	0.83	1.02
Fig. 2.3b			
curve 1	0.595	0.70	1.22
curve 2	0.825	0.68	0.74

reported in this work, and eq. (6.3) should be tested in this range of A_{2D}. For curve 1 (Fig. 2.3b), $H_{ms} > H_{max}$; this can explain the negative values of spout pressure drop reported by Ojalvo (1989). From eq. (4.4), $H_{min,s}$ is estimated to be 0.25 m which yields $H_{max} < H_{ms} < H_{min,s}$. This result is in agreement with the data presented here for 2DSBs of Group #2. For the spouting pressure drop curve presented in Fig. 2.3a, $A_{2D} >$ 0.094 (but closer to the values of A_{2D} reported in this work), the experimental H_{ms} is approximately equal to the calculated H_{max} . The minimum spouting velocity obtained from the pressure drop curve in Fig. 2.3a is 1.04 m/s (24 l/s); V_{mf} estimated by the Ergun equation is 1.06 m/s. This suggests that eq. (6.3), which predicts well values of H_{max} for $0.044 < A_{2D} < 0.2$ (see Fig. 6.8b), might be applicable to even higher value of A_{2D}.

For 2DSB systems of Group #1, data could be fitted by neither eq. (6.1) nor eq (6.2). As shown in Table 6.1 and Fig. 6.8a, high values of H_{max}/L_1 are obtained for RH = 60%; these values are very close due probably to the small range of A_{2D} . For RH = 30%, H_{max}/L_1 has the

tendency of increasing with decreasing A_{2D}. More data are necessary to develop a correlation for H_{max} in the range of $A_{2D} < 0.044$.

6.3 Conclusions

The mechanisms of spout termination identified in a 2DSB are two: fluidization of the annulus top and choking of spout. The dimensionless parameter A_{2D}, defined in this work, can be used to describe the transition between these two mechanisms.

For $A_{2D} < 0.044$, choking of the spout is the main mechanism of spout termination. Low particle sphericity, large nozzle width and small particle diameter may reduce A_{2D} to values lower than 0.044. The spout is formed by the growth of an internal cavity without solids circulation. An unstable (or incoherent) spouting regime with high pressure fluctuations and waves inside the spout characterizes the onset of spouting. The decrease of air relative humidity affects significantly the spout formation as well as the maximum spoutable bed height.

The transition between these two spout termination mechanisms occurs in the range $0.044 < A_{2D} < 0.094$. An oscillating spouting regime with a periodic motion of the spout around the central axis of the column characterizes the onset of spouting over this range of A_{2D}. For $A_{2D} > 0.094$, the fluidization of the annulus top is the main spout termination mechanism. For $A_{2D} > 0.044$, solids circulation inside and around the spout cavity is a typical characteristic of spout formation.

Equation (6.3) is proposed to predict H_{max} in a 2DSB for $A_{2D} > 0.044$. For $A_{2D} < 0.044$, data obtained are insufficient to correlate the effects of bed and nozzle dimensions and air humidity on H_{max} with accuracy.

CHAPTER 7

AERODYNAMICS IN TWO DIMENSIONAL SPOUTED BEDS

The objectives of this chapter are two: (i) to obtain general equations to predict the minimum spouting conditions in a two dimensional spouted bed (2DSB) as function of fluid-particle properties, bed height and vessel dimensions; (ii) to describe the solids flow characteristics for a given 2DSB near the minimum spouting condition.

In the first part of this Chapter, the minimum spouting pressure drop and the minimum spouting superficial velocity are correlated with the dimensionless parameters obtained in Appendix D and Chap. 2.

In the second part, the solids flow rates in the annular region are determined as function of air-particle characteristics, vessel dimensions, spout width and air superficial velocity.

7.1 Minimum Spouting Condition in a Two Dimensional Spouted Bed

7.1.1 Minimum Spouting Pressure Drop

Based on Table 2.1 and Appendix A, the minimum spouting pressure drop in a 2DSB should be a function of the following dimensionless groups:

$$Y^* = f(X^*_{2D}, A_{2D}, L_N/L_1) \tag{7.1}$$

where: $Y^* = 1 - \Delta P_{ms} / \Delta P_{mf}$;

$X^*_{2D} = 1/(1 + H_{ms}/L_1)$;

$Y^* = 1$ at $X^*_{2D} = 1$;

A_{2D} defined by eq. (2.7);

H_{ms} - the mean bed height at minimum spouting;

L_N and L_1 - the nozzle and bed widths;

ΔP_{ms} - the minimum spouting pressure drop;

ΔP_{mf} - the minimum fluidization pressure drop.

The dimensionless parameters A_{2D} and L_N/L_1 were suggested by Morgan and Littman (1980) to characterize the fluid-particle spouted bed system (Chap. 2). The dimensionless groups Y^* and X^*_{2D} are related to the effective normal solid stresses as shown in Appendix D.

Eq. (7.1) is supposed to apply in a 2D vessel geometry where slip deformations are reduced to the x horizontal and y vertical directions. This allows the assumption of plane strain condition for the failure criterion in the spout-annulus interface. Based on this assumption, the overall momentum balance for the porous material in the spout-annulus region was developed in Appendix D. A summary of the main conclusions obtained from this study is presented below:

1 - An inversion of the principal stress direction occurs just beyond the maximum spouting pressure drop in 2DSBs of Group #2. Plastic or slip deformations are the basic mechanisms of solids circulation around and inside the spout cavity. Passive failure of the spout region (center region of the bed) characterizes the onset of spouting for 2DSB systems of Group #2.

2 - Active failure of the annulus region (spout-annulus interface) characterizes the onset of spouting for 2DSB systems of Group #1.

3 - At the minimum spouting, there is a point in the spout-annulus region ($x = L_o/2$) where the solid shear stress becomes zero. This point is at the center upper spout region for passive failure, while it is in the annulus region (between the wall and the spout-annulus interface) for active failure. The horizontal and vertical effective solid stresses are the principal stresses at this point. (The horizontal effective solid stress is the major principal stress for passive failure, while the vertical effective solid stress is the major principal stress for active failure).

4 - The dimensionless parameter Y^* is a function of the overall vertical effective solid stress at $x = L_o/2$. X^*_{2D} is supposed to be a function of the overall horizontal effective solid stress.

5 - The relationship between Y^* and X^*_{2D} depends on the spout-annulus interface wall failure. This relationship is given by:

(i) Group #1 ($A_{2D} < 0.044$):

$$Y^* = a_1 + a_2 X^{*\,1/n}_{2D} \qquad \text{(D.11)};$$

(ii) Group #2 ($A_{2D} > 0.044$):

$$Y^* = a_1 + a_2 X^{*\,n}_{2D} \qquad \text{(D.12)},$$

where:

a_1, a_2 are dimensionless parameters which depend on the solid-fluid system and the bed dimensions; a_1 is a function of the fraction of the effective bed weight supported by the vessel wall, the spout width and the location of L_o; a_2 is a function of the plastic deformations of the

spout-annulus interface as well as the column dimensions. The parameter a_1 is a negative number in eq. (D.11) and a positive number in eq. (D.12);

$n = \tan^2 (45 + \Theta_c/2)$.

Θ_c is the Coulomb failure angle as defined in Chap. 5.

A comparison between eqs. (D.11) and (D.12) shows that the exponential coefficient of X^*_{2D} inverts from n to 1/n as the spout termination mechanism changes from the fluidization of the annulus top (Group #2) to choking of the spout (Group #1). This result is due to the change in the failure state in the spout-annulus interface region.

In order to determine the values of the empirical constants a_1 and a_2 in eqs. (D.11) and (D.12), the values of Y^* and X^*_{2D} were calculated from the measurements of the minimum spouting pressure drop and the minimum spouting bed height for air-particle systems used in this step. These values of Y^* and X^*_{2D} are presented in Tables 7.1 to 7.6 for the different 2DSB systems used. Values in the range of $H_{max} < H_{ms} < H_{min,s}$ were also included in this analysis. The Coulomb failure angles were obtained from the literature or from the fluidization experiments as described in Chap. 5 (see also Table 7.9 and Appendix E).

The STATPAK multiple regression program was used to specify a_1 and a_2 for each 2DSB air-particle system. These empirical constants as well as the statistical parameters for the regression curves obtained are presented in Tables 7.7 and 7.8. (The point $X^*_{2D} = 1$; $Y^* = 1$ was also included).

The experimental data for the minimum spouting pressure drop agree well with the theoretical curves proposed by eqs. (D.11) and (D.12) as

TABLE 7.1

MINIMUM SPOUTING PRESSURE DROP FOR A 2DSB OF WHEAT

(RH = 30%, L_N = 0.015 m, Group #2)

A_{2D} = 0.060 ϵ_{ms} = 0.420 H_{max}/L_1 = 0.85

H_o (m)	ΔP_{ms} (Pa)	H_{ms}/L_1 (-)	Y^* (-)	X^*_{2D} (-)
0.10	245	0.522	0.612	0.657
0.17	554	0.888	0.523	0.530
0.20	721	1.060	0.489	0.485
0.24	892	1.254	0.472	0.444

TABLE 7.2

MINIMUM SPOUTING PRESSURE DROP FOR A 2DSB OF BARLEY

(RH = 30%, L_N = 0.015 m, Group #2)

A_{2D} = 0.055 ϵ_{ms} = 0.419 H_{max}/L_1 = 0.77

H_o (m)	ΔP_{ms} (Pa)	H_{ms}/L_1 (-)	Y^* (-)	X^*_{2D} (-)
0.10	235	0.518	0.657	0.658
0.15	458	0.777	0.582	0.556
0.17	578	0.866	0.540	0.536
0.18	617	0.917	0.539	0.522
0.20	764	1.019	0.492	0.495

TABLE 7.3

MINIMUM SPOUTING PRESSURE DROP FOR A 2DSB OF MILLET

(RH = 30%, L_N = 0.015 m, Group #2)

A_{2D} = 0.054 $\quad \epsilon_{ms}$ = 0.416 $\quad H_{max}/L_1$ = 0.75

H_o (m)	ΔP_{ms} (Pa)	H_{ms}/L_1 (-)	Y^* (-)	X^*_{2D} (-)
0.10(*)	383	0.549	0.421	0.646
0.15	684	0.775	0.343	0.563
0.17	784	0.885	0.350	0.530
0.20	1029	1.041	0.287	0.490

(*) A_{2D} = 0.0600, bed porosity = 0.448.

TABLE 7.4

MINIMUM SPOUTING PRESSURE DROP FOR A 2DSB OF LINSEED

(RH = 30%, L_N = 0.015 m, Group #1)

A_{2D} = 0.011 $\quad \epsilon_{ms}$ = 0.427 $\quad H_{max}/L_1 > 0.79$

H_o (m)	ΔP_{ms} (Pa)	H_{ms}/L_1 (-)	Y^* (-)	X^*_{2D} (-)
0.10	144	0.530	0.750	0.653
0.15	314	0.795	0.659	0.557
0.17	412	0.923	0.612	0.520

TABLE 7.5

MINIMUM SPOUTING PRESSURE DROP FOR A 2DSB OF RICE

(RH = 60%, L_N = 0.015 m, Group #1)

A_{2D} = 0.030 ϵ_{ms} = 0.456 H_{max}/L_1 = 0.78

H_o (m)	ΔP_{ms} (Pa)	H_{ms}/L_1 (-)	Y^* (-)	X^*_{2D} (-)
0.10	314	0.520	0.523	0.658
0.15	637	0.780	0.395	0.562
0.17	853	0.900	0.296	0.526
0.18	897	0.941	0.305	0.515

TABLE 7.6

MINIMUM SPOUTING PRESSURE DROP FOR A 2DSB OF MOLECULAR SIEVE

(RH = 30%, L_N = 0.015 m, Group #2)

A_{2D} = 0.103 ϵ_{ms} = 0.420 H_{max}/L_1 = 0.93

H_o (m)	ΔP_{ms} (Pa)	H_{ms}/L_1 (-)	Y^* (-)	X^*_{2D} (-)
0.10	304	0.543	0.526	0.648
0.17	652	0.901	0.444	0.526

(RH = 60%, L_N = 0.015 m, Group #2)

A_{2D} = 0.065 ϵ_{ms} = 0.390 H_{max}/L_1 = 0.87

0.10	313	0.527	0.521	0.655
0.17	640	0.876	0.464	0.533

TABLE 7.7

EMPIRICAL CONSTANTS AND STATISTICAL PARAMETERS OF Y^* VERSUS X^*_{2D} REGRESSION CURVES

(L_N = 0.015 m)

PARTICLE	a_1 (-)	a_2 (-)	n (-)	SD (-)	R^2 (-)	mean deviation (%)	RH (%)
GROUP #2 - eq. (D.12):							
wheat	0.382	0.618	2.37	0.004	0.999	0.4	30
barley	0.271	0.732	1.58	0.014	0.994	1.9	30
millet	0.225	0.777	3.19	0.017	0.997	3.0	30
ms	0.369	0.630	3.23	0.010	0.998	1.2	30-60
GROUP #1 - eq. (D.11):							
linseed	-3.88	4.89	7.97	0.006	0.992	0.6	30
rice	-1.53	2.52	2.04	0.017	0.997	3.2	60

Note: R^2 - the multiple correlation coefficient squared of regression.

TABLE 7.8

EMPIRICAL CONSTANTS AND STATISTICAL PARAMETERS OF Y^* VERSUS X^*_{2D} REGRESSION CURVES

Group #2 -eq. (D.12), L_N = 0.030 m

PARTICLE	a_1 (-)	a_2 (-)	n (-)	SD (-)	R^2 (-)	mean deviation (%)	RH (%)
wheat	0.174	0.826	2.37	0.006	0.999	0.9	30
ms	0.174	0.826	3.23	0.026	0.994	4.0	30

shown by the standard deviation and the multiple correlation coefficient for the Y^* vs. X^*_{2D} curves obtained. Even the highest mean deviation (4.0%) for 2DSBs of molecular sieve fitted by nozzle N2 is low compared with the experimental error predicted for pressure drop curves (Chap. 3). Moreover, as expected from the analysis presented in Appendix D, a_1 is negative for 2DSB systems of Group #1.

The effect of the particle characteristics on the minimum spouting pressure drop in a 2DSB is seen in Figure 7.1. Note that the nozzle dimensions (N1 type nozzle) and the air properties are the same for the curves in Fig. 7.1. The dashed lines in Fig. 7.1b represent values predicted for the minimum pressure drop at $H_{ms} > H_{min,s}$. Stable spouting regime is not reached for $H_{ms} > H_{min,s}$.

The minimum spouting pressure drop ratio tends to an asymptotic value as the bed height increases for Group #2 (Fig. 7.1 curves for barley, wheat, and millet). This asymptotic value is given by $1- a_1$ in eq. (D.12). The minimum pressure drop also increases as the bed height increases for Group #1 (linseed in Fig. 7.1). The minimum pressure drop for Group #1 can reach higher values than those for Group #2 at high bed height (Fig. 7.1c). These results are also in agreement with the literature of CSBs (Chap. 2).

The effect of the air humidity on Y^* is of no significance for 2DSB systems of molecular sieve. The Y^* versus X^*_{2D} data presented in Table 7.6 for molecular sieve were fitted by the same regression curve (SD = 0.010, R^2 = 0.998 and a mean deviation of 1.2%.). This can be explained by the reduction of the bed porosity as RH increases. Both the minimum fluidization pressure drop and the minimum spouting pressure drop are

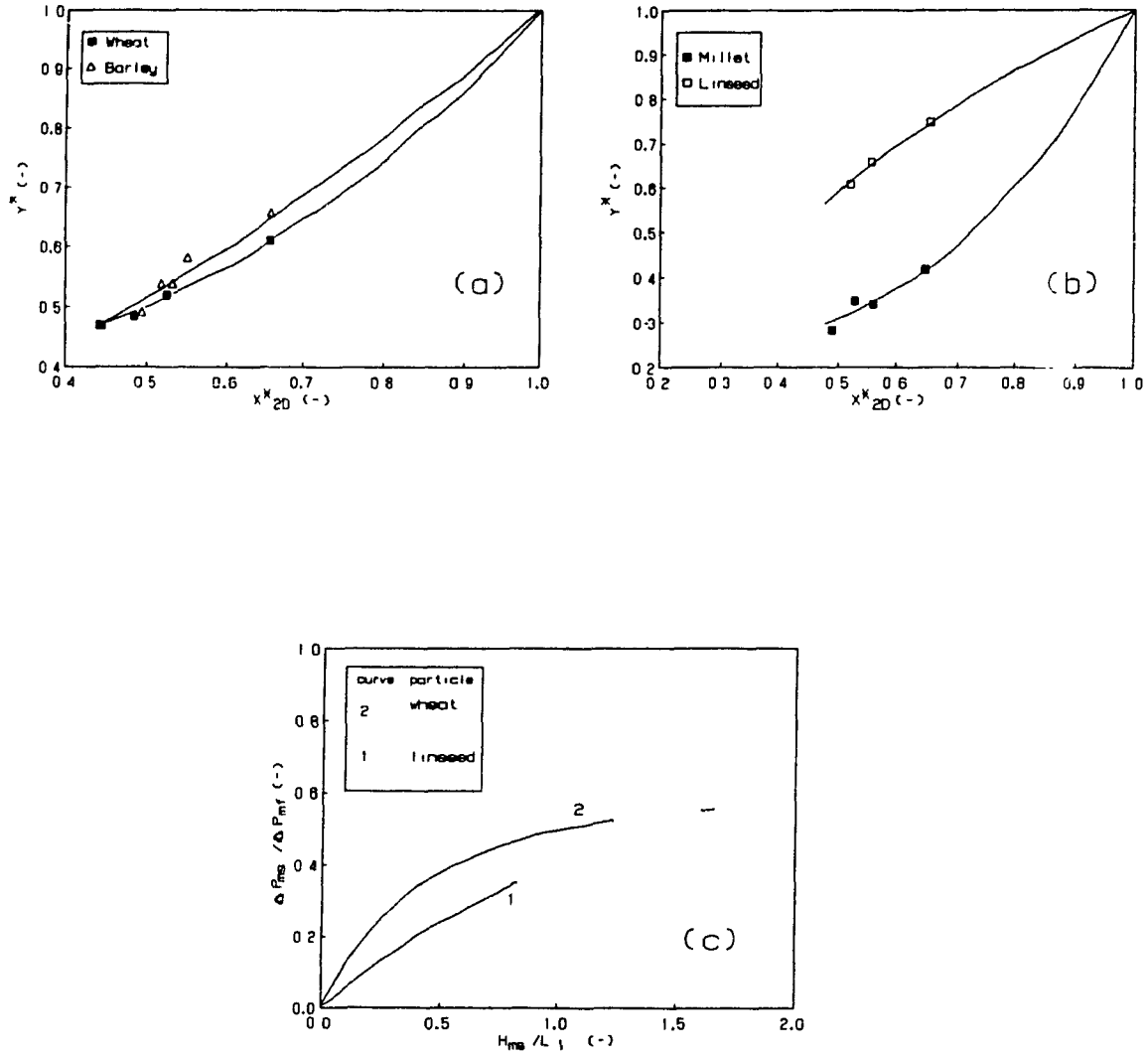

FIGURE 7.1 - Effect of Particle Characteristics on Minimum Spouting Pressure Drop Curves for 2DSBs with L_N = 0.015 m and RH = 30%.

(a), (b) Y^* versus X^*_{2D} Curves;
(c) Minimum spouting pressure drop ratio versus bed height ratio.
(see Table 7.7 for more details).

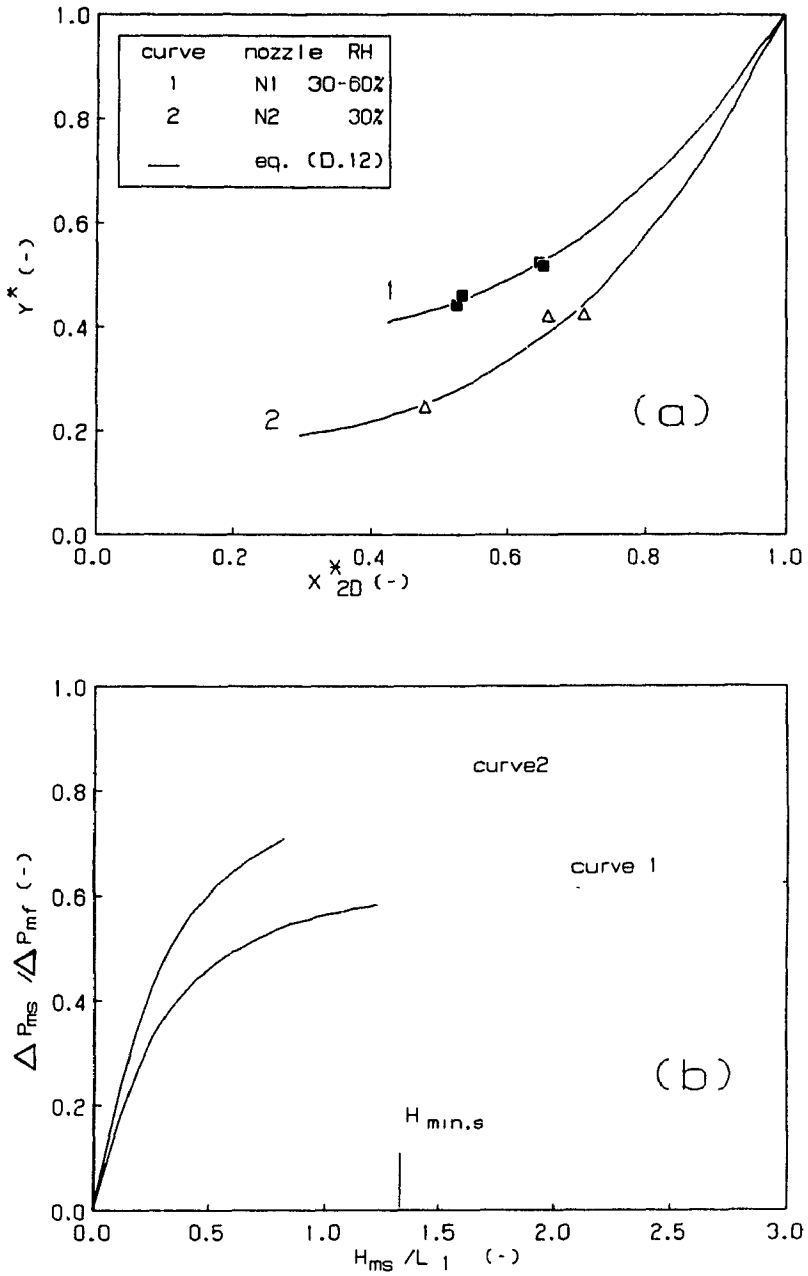

FIGURE 7.2 - Effect of the Nozzle Width on Minimum Spouting Pressure Drop Curves for 2DSBs of Molecular Sieve.

(a) Y^* versus X^*_{2D} curves;
(b) Minimum spouting pressure drop ratio versus bed height ratio curves.
(see Tables 7.7 and 7.8 for more details).

affected by this reduction in the same way, and Y^* is not altered as RH changes from 30% to 60%.

The effect of the nozzle width on the minimum spouting pressure drop is shown in Figure 7.2 for 2DSBs of molecular sieve. (see also Tables 7.7 and 7.8). The minimum spouting pressure drop increases with the increase of the nozzle width. The asymptotic value of the minimum spouting pressure drop is higher for larger values of L_N. As shown in Tables 7.7 and 7.8, a_1 decreases for increasing values of L_N.

The Y^* versus X^*_{2D} curves are not affected by the variation of A_{2D} because of changes in the bed porosity as shown in Tables 7.3 and 7.6. Therefore, A_{2D} is not an adequate dimensionless parameter to characterize the 2DSB air-particle systems in the minimum spouting pressure drop correlation. This parameter is only used to determine the change in spout termination mechanisms.

The parameter a_2 is equal to $1-a_1$ based on eq. (7.1). The parameter a_1 is a function of the $L_o/2$ location, the mean spout width, and the vessel wall-particle interaction forces (Appendix D). The minimum spouting condition in a 2DSB of coarse particles is characterized by dead zones near the vessel wall (Fig. 6.7). Particles do not slip on the vessel wall but slip on particles at the dead zone boundary. Therefore, the parameter a_1 depends on the particle-particle slip angle at the dead zone boundary instead of the particle-vessel wall frictional angle. The location of $L_o/2$ depends on the failure state of the spout-annulus interface. The mean spout width is a function of the nozzle width, the bed height, the column width, and particle properties (Littman and Morgan, 1989). Shallow and deep SBs present different spout shapes. As a

result, a_1 can be correlated as follows:

$$a_1 = f(d_p \phi , L_N , L_1 \Theta_c)$$

The dimensionless groups used for determining the parameter a_1 are presented in Table 7.9. From Tables 7.7, 7.8 and 7.9, the following correlations were obtained for a_1:

(i) Group #2

(a) non-spherical particles (wheat and barley):

$$a_1 = (d_p \phi / L_N) \tan (45° + \Theta_c/2) \qquad (7.2a),$$

(b) spherical (ms) and quasi-spherical (millet, $\phi >$ 0.95) particles:

$$a_1 = (d_p \phi / L_N) \tan (90° - \Theta_c) \qquad (7.2b),$$

(ii) Group #1:

(a) for rice:

$$a_1 = -(d_p \phi / L_N) \tan (45° - \Theta_c/2)\ L_1/L_N \qquad (7.3a),$$

(b) for linseed:

$$a_1 = -(d_p \phi / L_N) \tan (45° + \Theta_c/2)\ L_1/L_N \qquad (7.3b),$$

Eq. (7.2) shows how the particle sphericity affects the failure state of the annular region in 2DSBs of Group #2. For non-spherical particles such as wheat and barley, the dependence of a_1 on the Coulomb failure angle is given by tan $(45° + \Theta_c/2)$. For spherical or quasi-spherical particles it is given by tan $(90° - \Theta_c)$. This difference

TABLE 7.9

DIMENSIONLESS PARAMETERS FOR a_1 CORRELATION

Reference: eqs. (D.11) and (D.12).

PARTICLE	$d_p\phi/L_N$ (-)	L_1/L_N (-)	Θ_c (°)	tan (45 - Θ_c/2) (-)
wheat	0.238 0.119	13.333 6.667	24.0 [a]	0.649
ms	0.228 0.114	13.333 6.667	31.8 [b]	0.556
barley	0.215	13.333	13.0 [c]	0.795
millet	0.144	13.333	31.5 [c]	0.560
linseed	0.095	13.333	51.0 [c]	0.354
rice	0.163	13.333	20.0 [c]	0.700

(a) - Lobnes et al., 1987.
(b) - based on eq. (5.26) and on data of the minimum fluidization velocity (see Appendix E).
(c) - based on eqs. (5.26) and (5.31) as shown in Chap. 5.

between failure in packed beds of non-spherical (such as wheat) and quasi-spherical (millet) particles was already discussed in Chap. 5.

For Group #1, the dependence of a_1 on the Coulomb failure angle is given by tan (45° - Θ_c/2) for rice and tan (45° + Θ_c/2) for linseed. This difference is related to the shallow and deep bed conditions. In the range of H_{ms} used here, the beds of rice can be considered deep 2DSBs, while the beds of linseed are shallow 2DSBs.

The measurements of the dead zone volume show that non-spherical particles for Group #2 slip in the upper annulus region near the vessel wall boundary at an angle of $45° + \theta_c/2$ from the x plane (see Fig. 7.3a), while rice-particles slip at an angle of $45 - \theta_c/2$ from the x plane (see Fig. 7.3b). The dead zone volume for 2DSBs of linseed-particles differs from those obtained for Group #2 and from that obtained for rice as shown in Fig. 7.3c. This configuration for 2DSBs of linseed represents a shallow spouted bed condition. For 2DSBs of linseed, the spout width enlarges at the top of the bed.

The minimum spouting pressure drop for the 2DSB air-particle systems used here matches extremely well the theoretical values predicted by eqs. (D.11), (D.12), with a_1 given by eq. (7.2) and (7.3). It is shown in Figure 7.4 where the theoretical values for the minimum spouting pressure drop are compared with those obtained experimentally. The mean deviation and the standard deviation between the experimental data and the theoretical values of the minimum spouting pressure drop are 2.8% and 18.5 Pa respectively.

In order to analyze the applicability of eqs. (D.11), (D.12), (7.2) and (7.3) in other 2DSB columns, the minimum spouting pressure drop data obtained from the published literature are presented in Table 7.10. Additional spouting experiments were also carried out in a 2DSB column with 0.50 m x 0.04 m of cross sectional area. The minimum spouting pressure drop reported for this 2DSB column are listed in Table 7.10. The Coulomb failure angles for glass beads, corn and soybean are 22°, 21.3° and 26.2° respectively (Rowe, 1971 and Lobnes et al., 1987). The Coulomb failure angle for sesame seed was calculated from the pressure drop

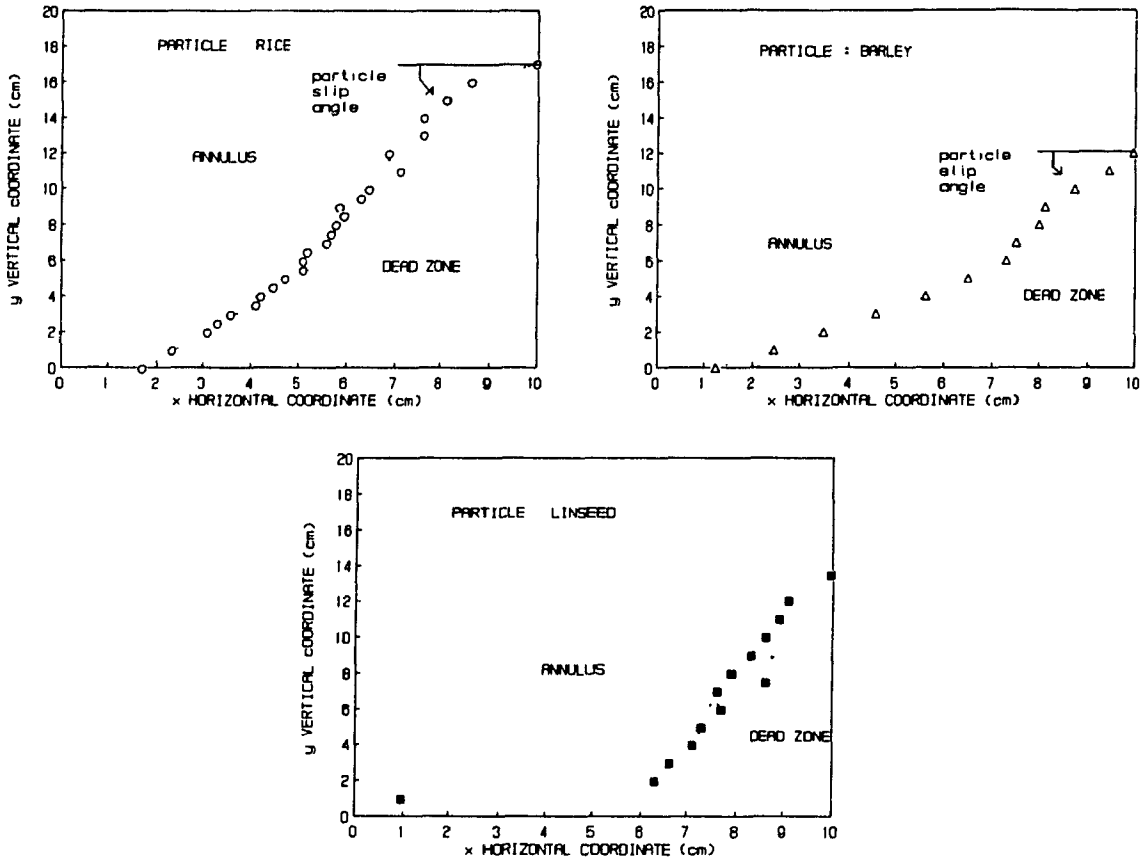

FIGURE 7.3 - Dead Zone Extent in a 2DSB of: (a) Barley; (b) Rice; (c) Linseed.
H_0 = 0.17 m.

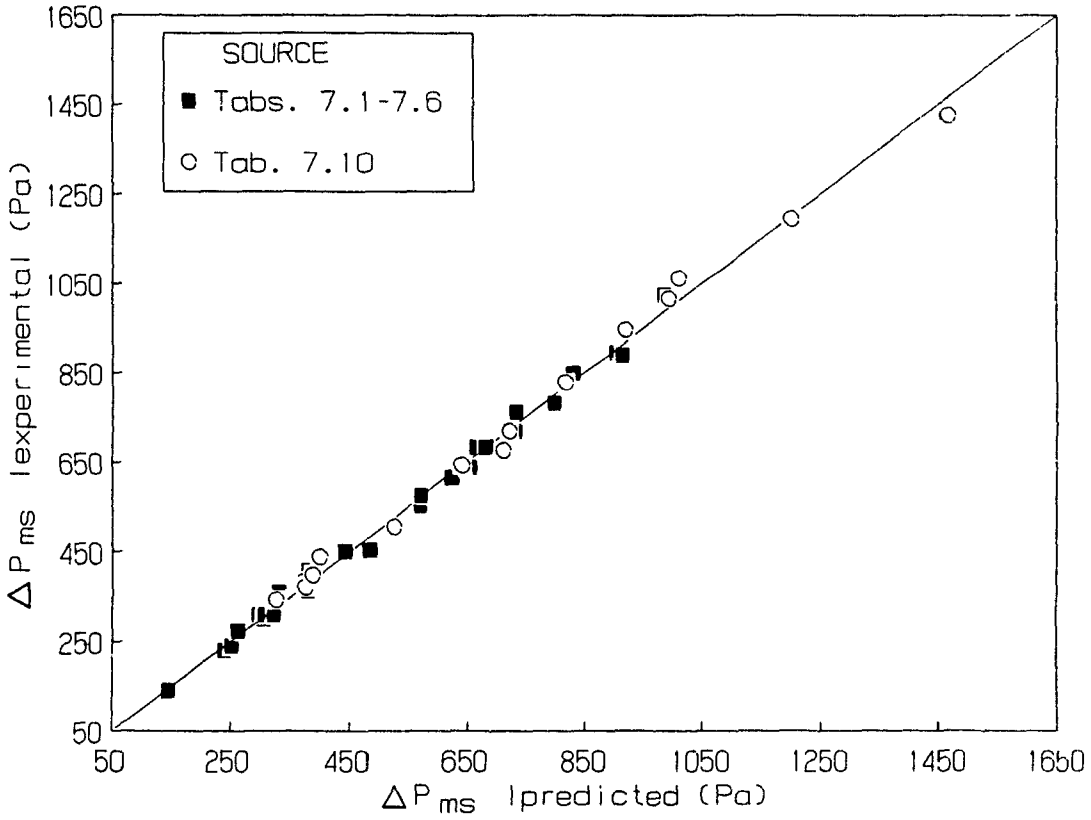

FIGURE 7.4 - Comparison between The Predicted and The Experimental Values of The Minimum Spouting Pressure Drop for 2DSBs.
Reference: eqs. (D.11), (D.12), (7.2) and (7.3).
$0.01 < A_{2D} < 0.10$.

TABLE 7.10

EXPERIMENTAL AND PREDICTED VALUES FOR THE MINIMUM SPOUTING PRESSURE DROP IN 2DSBs OF COARSE PARTICLES

PARTICLE	H_o (m)	$\Delta P_{ms\|exp}$ (Pa)	$\Delta P_{ms\|pred}$ (Pa)	mean deviation (%)	NOTES
	SOURCE: this work				
	L_1 = 0.20 m; L_N = 0.015 m: L_2 = 0.015m.				
Glass	0.10	401	390	2.8	A_{2D}= 0.065.
	0.15	678	712	4.9	
Sesame seed	0.17	387	374	3.3	A_{2D}= 0.013.
	L_1 = 0.50 m; L_N = 0.01 m; L_2 = 0.04 m.				
Millet	0.15	411	402	2.3	A_{2D}= 0.076.
Wheat	0.15	373	376	0.8	A_{2D}= 0.084. shallow bed
Soybean	0.15	348	327	6.0	A_{2D} > 0.05. shallow bed
	SOURCE: Anderson (1984) - L_1 = 2x0.05 m ; L_N = 2x0.01 m.				
Wheat	0.12	645	644	0.2	A_{2D}= 0.042
	0.15	830	822	1.0	
	0.18	1020	998	2.1	
Corn	0.12	509	526	3.3	A_{2D}> 0.03
	0.16	723	723	0.0	
	0.20	949	918	3.3	
	0.22	1066	1015	4.8	
	SOURCE; Ojalvo (1989)				
Soybean	0.18 included angle = 60°	1200	1203	0.1	L_N=2x13 mm. L_1=2x0.12 m. A_{2D}=0.042.
	0.18 included angle = 70°	1430	1470	6.1	L_N=2x7 mm. L_1=2x0.13 m. A_{2D}=0.076.

versus the air flow rate curves in the packed bed (Chap.5) as being 25.2°.

The predicted and experimental values of the minimum pressure drop presented in Table 7.10 are also plotted in Fig. 7.4. The predicted values agree well with the experimental data available. The mean deviation obtained was 3.3% for $0.01 < A_{2D} < 0.15$.

For Anderson's (1984) and Ojalvo's (1989) column designs, X^{*}_{2D} was calculated based on the half column width (see Table 1.1).

The results obtained show that:

1 - Shallow 2DSBs of Group #2 are characterized by:

(1.a) non-spherical particles:

$$a_1 = (d_p \phi / L_N) \tan (45° - \Theta_c/2) \qquad (7.4a),$$

(1.b) spherical or quasi-spherical particles:

$$a_1 = (d_p \phi / L_N) \tan (90° + \Theta_c) \qquad (7.4b).$$

2 - In Ojalvo's (1989) design (conical Half-2DSB), the included angle influences significantly the particle slip in the annular region Particle slip on the wall follows the direction imposed by the slant wall surface. This results in different aerodynamic behaviors As shown in Table 7.10, eq. (D.12) can predict well the minimum spouting pressure drop for the included angle close to 60°, with a_1 given by eq (7.4). For the nozzle width equal to or less than one particle diameter, $A_{2D} > 0.18$, eq. (D.12) predicts a value 20% higher than the experimental one However, for this case, soybean-particles seem to be confined by the slant wall in a such a way that the internal solids circulation may be

prevented during the spout formation. If this is true, eq. (D.12) cannot be applied for this latter case.

Morgan and Littman (1980) reported Y^* versus X^* curves for CSBs of wheat as a function of D_i. Based on their results, the inversion of the Y^* versus X^* occurs at D_i = 50.8 mm. The value of A calculated from this data set for wheat (D_i = 50.8 mm) is 0.013, which represents the transition of the spout termination mechanism in CSBs (Chap. 2). This result is in agreement with those reported here for a 2DSB.

A comparison between Fig 1 (Morgan and Littman, 1980) and Fig. 7.1 shows that the shape of the Y^* versus X^* curves for A > 0.013 is similar to the Y^* versus X^*_{2D} curves obtained for 2DSBs of particles of Group #1 (A_{2D} < 0.04). This mean that coarse particles in a CSB (characterized by the fluidization of the annulus top spout termination mechanism) behave similarly to small particles in a 2DSB (characterized by the choking of spout termination mechanism). Such an apparent disparity can be explained by taking into consideration the type of spout-annulus interface failure.

The basic difference between the spouting formation in a CSB and a 2DSB is the degree of freedom for the particle slip deformation. In a CSB of coarse particles, the volumetric deformation of the porous material element in the annular region can occur in the three different directions x, y and z. In a 2DSB of coarse particles, the volumetric deformation of the porous material occurs in the horizontal x direction and the vertical y direction. As a result, in a CSB of coarse particles the spout-annulus interface failure is active, with the intermediate effective stress equal to the major vertical effective stress (McNab and Bridgwater, 1974). As mentioned before, the active state of the spout-annulus interface failure

occurs in 2DSBs systems of Group #1. This explains why the Y^* versus X^* curves obtained by Morgan and Littman (1980) in a CSB of wheat with A > 0.013 are similar in shape with those obtained here for rice and linseed. Although the Y^* and X^* curves are similar, eq. (D.11) cannot be used to describe the minimum spouting pressure drop in a CSB due to the plane strain failure condition used in a 2D geometry.

In conclusion, it is seen that the inclusion of the momentum balance of the solid phase is fundamental to understand and describe the aerodynamics in spouted beds. The type of spout-annulus interface failure results in different correlations for the minimum spouting pressure drop As shown, the minimum spouting pressure drop is a function only of the Coulomb failure angle of the porous material, the particle size, the column dimensions and the nozzle width.

7.1.2 Minimum Spouting Velocity

7.1.2.1 Minimum Spouting Velocity Equation

The minimum spouting velocity for the 2DSB systems used here is close to the minimum fluidization velocity at $H_{ms} > 0.15$ m Any attempt to correlate these experimental data should be based on the pressure drop gradient at the spout-annulus interface.

Based on the analysis developed in Chap. 5 for 2D packed beds, the minimum spouting air superficial velocity can be correlated to the overall pressure drop in the spout-annulus interface region as follows:

$$\Delta P_{ms} / H_{ms} = (72/ \cos^2 \lambda) f_1 V_{ms} + \bar{D} f_2 V_{ms}^2 \qquad (7.5),$$

where:

ΔP_{ms} - the minimum spouting pressure drop;

H_{ms} - the mean annulus bed height at minimum spouting;

$\lambda /2$ - the angle between the direction of fluid flow inside the pores (channels) and the symmetric axis of the pore structure;

$\bar{D}$ - the overall slip principal strain rate ratio;

f_1 and f_2 - parameters defined in eq. (5. 20);

V_{ms} - the minimum spouting superficial velocity.

By analogy with eq. (5.28), the overall parameter D for the annular spout region is given by:

$$\bar{D} = D_{|annulus} / D_{|ms} \qquad (7.6),$$

where:

$D_{|annulus}$ is the overall slip strain rate ratio in the annulus-wall region. $D_{|annulus} = \tan \alpha \tan (45° - \Theta_c/2)$;

$D_{|ms}$ is the overall slip principal strain rate ratio in the spout-annulus interface at minimum spouting = $\tan (90° - \lambda /2) \tan (45° - \Theta_c/2)$.

α , λ and Θ_c as specified in eq. (5.28).

The justification for applying eq. (7.5) globally to a 2DSB is based on the definition of the overall parameter $\bar{D}$ which takes into account the slip deformation rates in the annulus-wall and the annulus-spout interface regions (see Appendix D for more details). Moreover, any variation of porosity occuring in these regions is expressed through the value of parameter $\bar{D}$ (see Appendix C).

In order to determine $\bar{D}$, the following assumptions are made:

(a) The maximum value for $D_{|ms}$ (= 2.0) is reached at $H_{ms} = H_{max}$. As shown in Appendix D, the porous material in the spout-annulus interface

region tends to expand. The spout necks in the upper region of the bed (see Fig. 6.7);

(b) $D_{|annulus}$ is constant for each 2DSB system at the minimum spouting. This means that the slip deformations of the porous material in the annulus-wall region of the spouted bed do not depend (straightly) on the value of H_{ms}, but on the deep and the shallow 2DSB conditions. The value of $D_{|annulus}$ is determined by setting: (i) $Y^* = 1$ and $X^*_{2D} = 1$ in eq. (D.9a) or (D.9b) in Appendix D; and, (ii) $\overline{D} = 1$ in eq. (7.6).

Based on the assumption (a), the following correlations can be obtained through eqs. (D.8) and (D.10) in Appendix D:

1 - Group #1 :

$$D_{|ms} = 2(X^*_{2D|Hmax} / X^*_{2D})^{(n-1)/n} \qquad (7.7a),$$

2 - Group #2 :

$$D_{|ms} = 2(X^*_{2D|Hmax} / X^*_{2D})^{(n-1)} \qquad (7.7b),$$

where:

$X^*_{2D|Hmax} = X^*_{2D}$ at $H_{ms} = H_{max}$;

$n = \tan^2 (45 + \Theta_c/2)$.

Eqs. (7.7a) and (7.7b) show that the slip deformations of the porous material in the spout-annulus interface region depend on the bed height. $D_{|ms}$ is normally more than one.

Based on the assumption (b), $D_{|annulus}$ can be determined by setting $X^*_{2D} = 1$ in eqs. (7.7a and b). This results in the following correlations:

For Group #2:

$$\bar{D} = D_{|annulus} / D_{|ms} = (X^{*}_{2D})^{(n-1)} \qquad (7.8a),$$

For Group #1:

$$\bar{D} = D_{|annulus} / D_{|ms} = (X^{*}_{2D})^{(n-1)/n} \qquad (7.8b).$$

Eqs. (7.8a and b) determine the relationship between the overall slip deformation strain ratio and the geometric parameters of the 2D column. Note that $\bar{D}$ is a function of the bed height, the column width and the Coulomb failure angle only. For both groups, $\bar{D}$ is always less than 1. This indicates that the porous material contracts, and large volumes of dead zones are developed at the minimum spouting.

The minimum spouting superficial air velocity can be determined using eq. (7.5) as follows:

(i) Calculate H_{max} - eq. (6.3) for Group #2 ($\Lambda_{2D} > 0.04$);

(ii) Calculate the minimum spouting pressure drop in the spout-annulus interface region - eq. (D.11) or (D.12) with a_1 given by eqs. (7.2), (7.3) or (7.4);

(iii) Calculate λ - eq. (7.7), with:

$D_{|ms} = \tan (90° - \lambda/2) \tan (45° - \Theta_c/2)$

(iv) Calculate the overall value of $\bar{D}$ - eq. (7.8).

(v) Calculate the minimum spouting superficial velocity - eq. (7.5).

7.1.2.2 Theoretical Results For the Minimum Spouting Velocity

The analysis of the minimum spouting superficial air velocity is limited to Group #2 since there is no equation available to determine

H_{max} for Group #1.

Simulations of the minimum spouting velocity were carried out for the 2DSBs systems used here following the above sequence of steps and equations proposed here. The first result obtained from this simulation was the minimum spouting velocity at $H_{ms} = H_{max}$. It is close to the minimum fluidization velocity, with a mean value of 1.09 V_{mf} for the 2DSB systems of Group #2 used. The maximum value reported is 1.3 V_{mf} for a shallow 2DSBs for which eq. (6.3) was not tested. Note that the only condition imposed to solve eq. (7.5) is $D_{|ms} = 2$ (maximum value possible for D following Rowe theory, 1971) at $H_{ms} = H_{max}$. There is no restriction regarding the minimum spouting velocity at $H_{ms} = H_{max}$. The fact that V_{ms} is approximately equal to V_{mf} at H_{max} is independent of the imposed conditions; this corroborates the equations proposed here.

(a) Effect of Nozzle Width

The minimum spouting superficial velocity vs. the bed height curves for 2DSBs of wheat with different nozzle designs (L_N = 0.010 m, 0.015 m and 0.030 m) are plotted in Figure 7.5. An increase in L_N increases V_{ms} for a fixed bed height. On increasing L_N the minimum spouting pressure drop is increased (as already shown in Fig. 7.2), therefore increasing V_{ms}. Moreover, the maximum spoutable bed height decreases as L_N increases ($X^*_{2D|Hmax}$ increases), therefore it reduces the value of λ . Such an effect also contributes to an increase V_{ms} at a fixed bed height (see eq. (7.5)).

(b) Effect of Bed Height

The effect of shallow and deep bed conditions on the minimum spouting superficial velocity is presented in Figure 7.5b. A deep 2DSB is

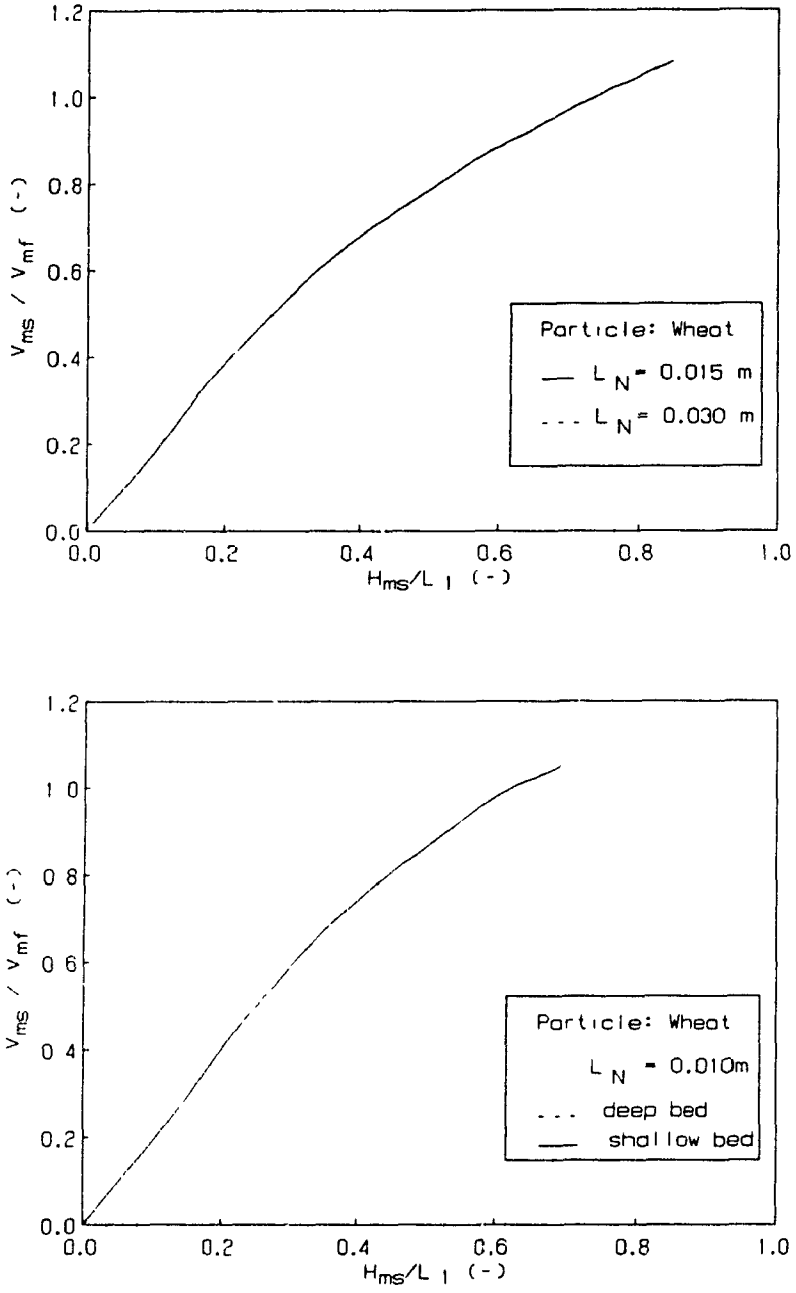

FIGURE 7.5 - Effect of Nozzle Width and Bed Dimensions on Minimum Spouting Velocity for 2DSBs of Wheat Particles.
Results obtained from eq. (7.5).
Deep beds - L_1 = 0.20 m; Shallow bed - L_1 = 0.50 m.

defined by the neck of the spout in the upper region. A shallow 2DSB is characterized by the large spout width at the top of the bed. Note that shallow or deep beds are related to the column width, bed height, nozzle width and particles properties. For non-spherical particles of Group #2, such as wheat, it was observed that for $\lambda = 45^{\circ} + \Theta_c/2$ the spout tends to expand at the top surface. Assuming that the limit between shallow and deep beds is given by the above value of λ, the bed height for this transition can be determined by eq. (7.7). For 2DBSs of wheat with L_1 = 0.20 m and L_N = 0.015 m, the value of H_{ms} for this transition is 0.05 m, while for L_N = 0.030 m it is 0.01 m. For the 2DSB column with L_1 = 0.50 m and L_N = 0.01 m, the transition should occur at H_{ms} = 0.165 m ; this is in agreement with the results presented in Table 7.10. Returning to Fig.7.5b, it is seen that the minimum spouting velocity is comparatively greater in a shallow 2DSB than in a deep bed. The minimum spouting pressure drop also increases; this is probably related to the increase in the spout width. Littman and Morgan (1983) have also reported this difference between shallow and deep CSBs.

(c) Effect of Particle Properties

The effect of particle properties on the minimum spouting velocity can be seen in Fig. 7.6. For spherical or quasi spherical particles, an increase in the particle diameter causes a decrease in the minimum spouting velocity ratio (V_{ms}/ V_{mf}) (see Fig. 7.6a). This result is due to an increase of the maximum spoutable bed height as d_p rises. Note that the Coulomb failure angle for molecular sieve and millet is approximately the same.

The effect of particle sphericity and the Coulomb failure angle on

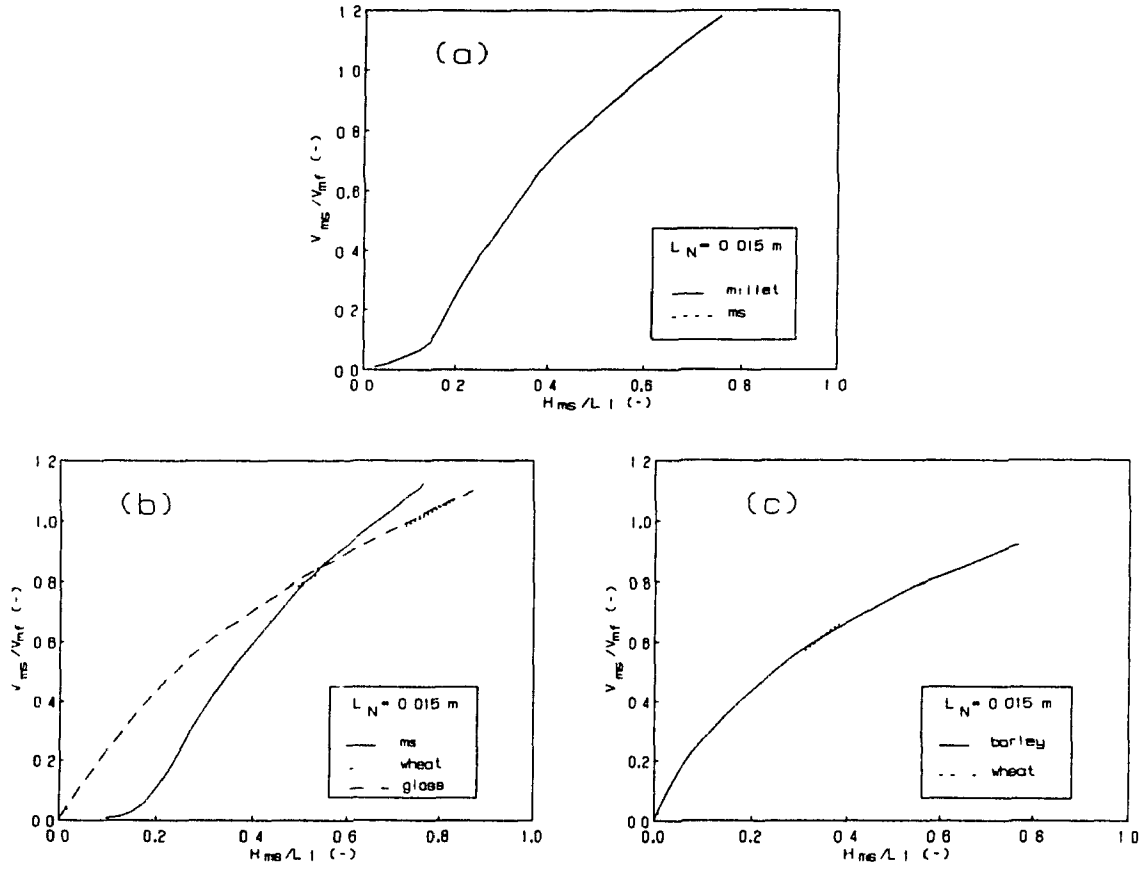

FIGURE 7.6 - Effect of Particle Properties on Minimum Spouting Velocity of 2DSBs of Group #2 Particles.
- Results obtained from eq. (7.5) for deep 2DSBs.

V_{ms}/V_{mf} can be analyzed using Figures 7.6b and 7.6c for Group #2. Glass beads, wheat, molecular sieve and barley all have approximately the same particle size (3.0 mm < d_p ϕ < 3.6 mm). Glass beads and molecular sieve are spherical particles. Wheat is a non-spherical particle with a low sphericity (= 0.91). Molecular sieve presents the highest Coulomb failure (= 31.8°), while barley presents the lowest one (= 13°). The Coulomb angle for wheat and glass beads is in the same range (24° for wheat and 22° for glass).

From Fig. 7.6b it is seen that the V_{ms}/V_{mf} vs. H_{ms}/L_1 curves are approximately the same for particles with the same (or approximately the same) Coulomb failure angle. Increasing the Coulomb failure angle resulted in significant changes of the V_{ms}/V_{mf} vs. H_{ms}/L_1 curve. Moreover, at high bed heights, V_{ms}/V_{mf} is low for particles with lower Coulomb failure angle. At low bed heights, this ratio is lower for particles with higher Coulomb failure angle. Similar trends are also observed for barley and wheat in Fig. 7.6c.

The above results are very interesting and they may explain the controversy in the SB literature regarding the effect of particle sphericity on the minimum spouting velocity. As it is shown, the particle sphericity is not a significant parameter in V_{ms}/V_{mf} ratio for particles of the same size. This is in agreement with Mathur and Gishler's correlation for V_{ms} (see Mathur and Epstein, 1974). However, the dependence of V_{ms} on H_{ms} varies with the Coulomb failure angle. Although the effect of particle sphericity is emphasized in Littman and Morgan's (1983) correlation, these authors have shown that V_{ms} varies with H_{ms}^{k}, k being dependent on the air-particle properties. This is in agreement with

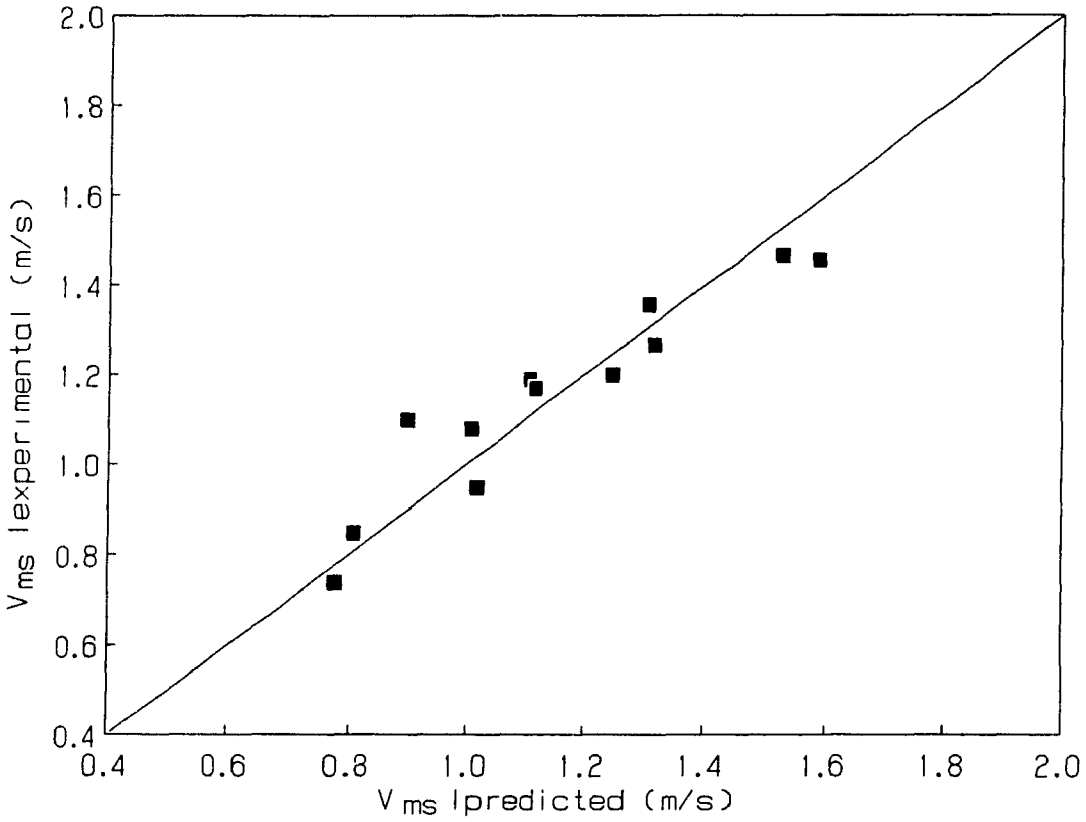

FIGURE 7.7 - Comparison of the Experimental and Predicted Values of the Minimum Spouting Velocity.
Reference: eq. (7.5).

the results presented here.

The minimum spouting velocity obtained solving eq. (7.5) is compared to the experimental values for each air-particle system used in this work. This comparison is shown in Figure 7.7. The mean deviation of the experimental and predicted values of V_{ms} is 6.5%, which is in the range of the experimental error (Table 3.6).

In conclusion, equations were obtained to describe the minimum spouting condition in a 2DSB. These equations were used for 2DSB systems of Group #2. The results predicted from these equations for the minimum spouting pressure drop and the minimum spouting velocity are in good agreement with the experimental results.

7.2 Granular Flow Characteristics in a Two Dimensional Spouted Bed

7.2.1 Vertical Particle Velocity

The vertical particle velocities were measured according to the procedure described in Chap. 3. Data obtained here were for beds with N1 type nozzle (L_N = 0.015 m), spouted by air with RH = 30%, except for rice for which the air relative humidity was maintained in the range of 60%. Barley, glass bead, rice, sesame seed, wheat, and millet were used as model particles. The effect of bed height was analyzed only for beds of millet.

The condition for each vertical particle velocity measurement is presented in Table 7.11. The spout width, L_s (y) , was obtained by direct measurements and photographs. The mean integrated value (L_s) is shown in Table 7.11. The percentage volume of the dead zone (in relation to the total volume of the annulus) was determined by direct measurements of the

TABLE 7.11

EXPERIMENTAL CONDITIONS FOR VERTICAL PARTICLE VELOCITY DATA

PARTICLE	V_s (m/s)	V_s/V_{ms} (-)	L_s (cm) (*)	V_{jDZ}/V_{ja} (%) (*)	H_o (m)	H_f (m)
barley	1.38	1.16	2.7	33	0.15	0.11
glass bead	1.60	1.18	2.1	50	0.10	0.03
	1.70	1.25	2.5	43	0.10	0.08
rice	1.21	1.01	2.4	47	0.15	0.09
sesame seed	0.70	1.37	1.8	41	0.17	0.18
wheat	1.65	1.20	2.6	41	0.17	0.11
millet	1.16	1.22	2.5	45	0.10	0.22
	1.01	1.06	2.0	45	0.10	0.16
	0.92	1.00 +	2.2	66	0.10	0.06
	1.28	1.11	2.4	45	0.15	0.15
	1.15	1.00 +	2.3	62	0.15	0.07
	1.20	1.04	2.4	44	0.17	0.13

(*) - integrated values.
Note: the standard error for spout width and dead zone extent varies with the particle diameter (0.2 cm to 0.4 cm).

dead zone extent. For V_s close to V_{ms}, the spout oscillated around its axis in the upper region of the bed, and the data presented here are average values as discussed in Chap. 3 (see Fig. 3.5 for details).

The variation of the dead zone volume with the spouting air superficial velocity is shown in Fig. 7.8 for glass beads at H_o = 0.10 m. At low air superficial velocities the dead zones were larger and the solids circulation was restricted to the annular region near the spout-annulus interface. As the spouting air superficial velocity increased, the volume of the dead zone decreased in the upper region of the bed. At V_s close to V_{ms}, the dead zone interface changed continuously due to oscillation of the spout. Curve AB in Fig. 7.8b represents the dead zone boundary when the spout oscillates towards the right hand side of the bed. Curve BC is the dead zone boundary when the spout is on the left hand side of the bed. Assuming the dead zone boundary as one particle path, it is seen that the particle can move outwards (from spout to annulus) in the upper region of the annulus. This represents the passive state of the spout annulus interface failure (Appendix D).

For the particles used here, two typical zones of entrainment were observed at the spout-annulus interface for $V_s < 1.2\ V_{ms}$. The first one, located in the upper region of the bed, was similar to a vortex. The particles falling in the annulus were entrained rapidly into the spout. This region is illustrated in Figure 7.9a. Basically, the particle vortex was caused by oscillation of the spout. With increase of the spout air velocity, the spout-annulus interface became more stable and the volume of this zone was reduced, as shown in Fig. 7.9b.

The second zone of particle entrainment was located 1 to 2 cm above

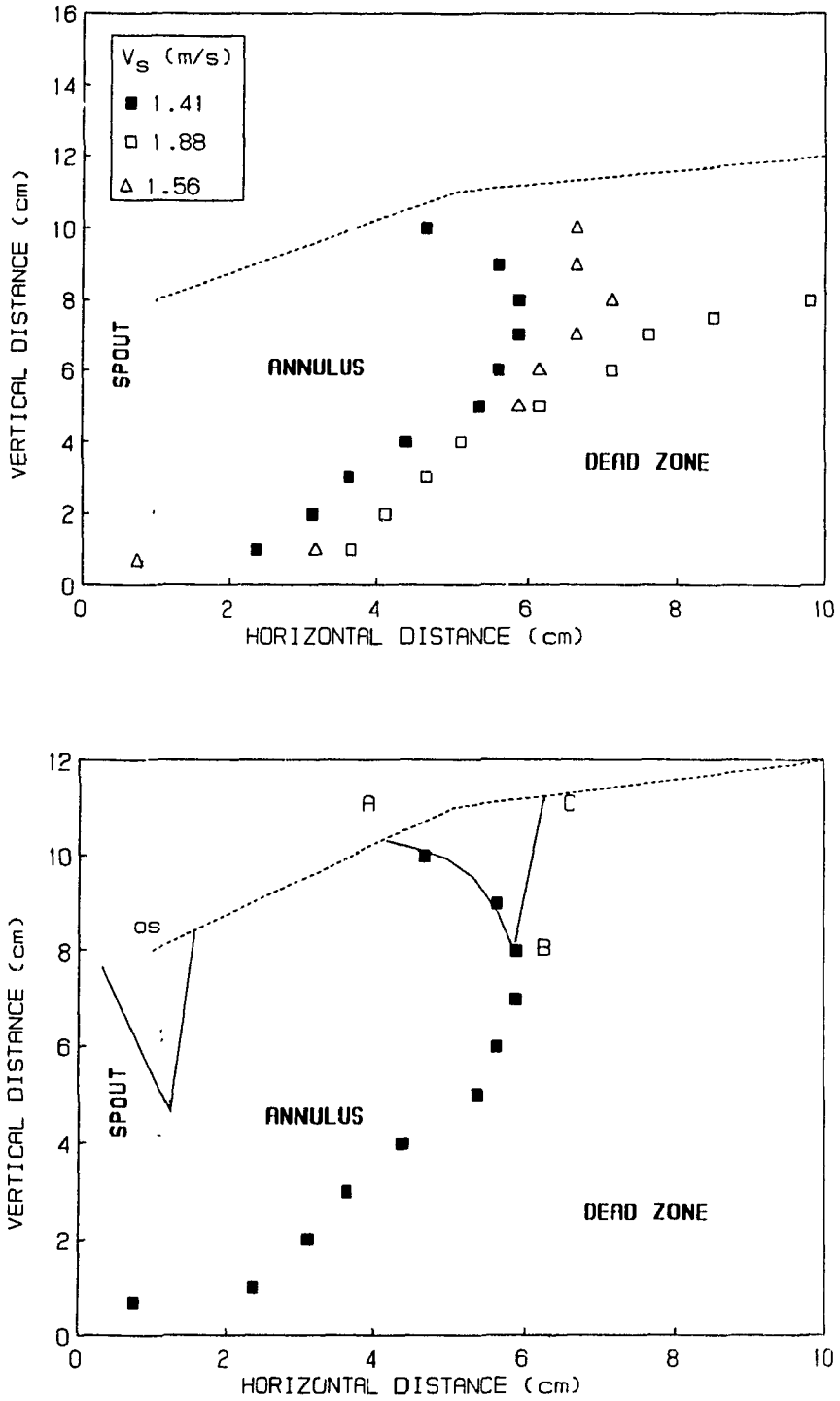

FIGURE 7.8 - Effect of Air Velocity on Dead Zone Volume for a 2DSB of Glass Beads.
Curves AB and BC represent the dead zone boundary.
os - region of spout oscillation.
Note - data were obtained by measurements on both sides of columns.

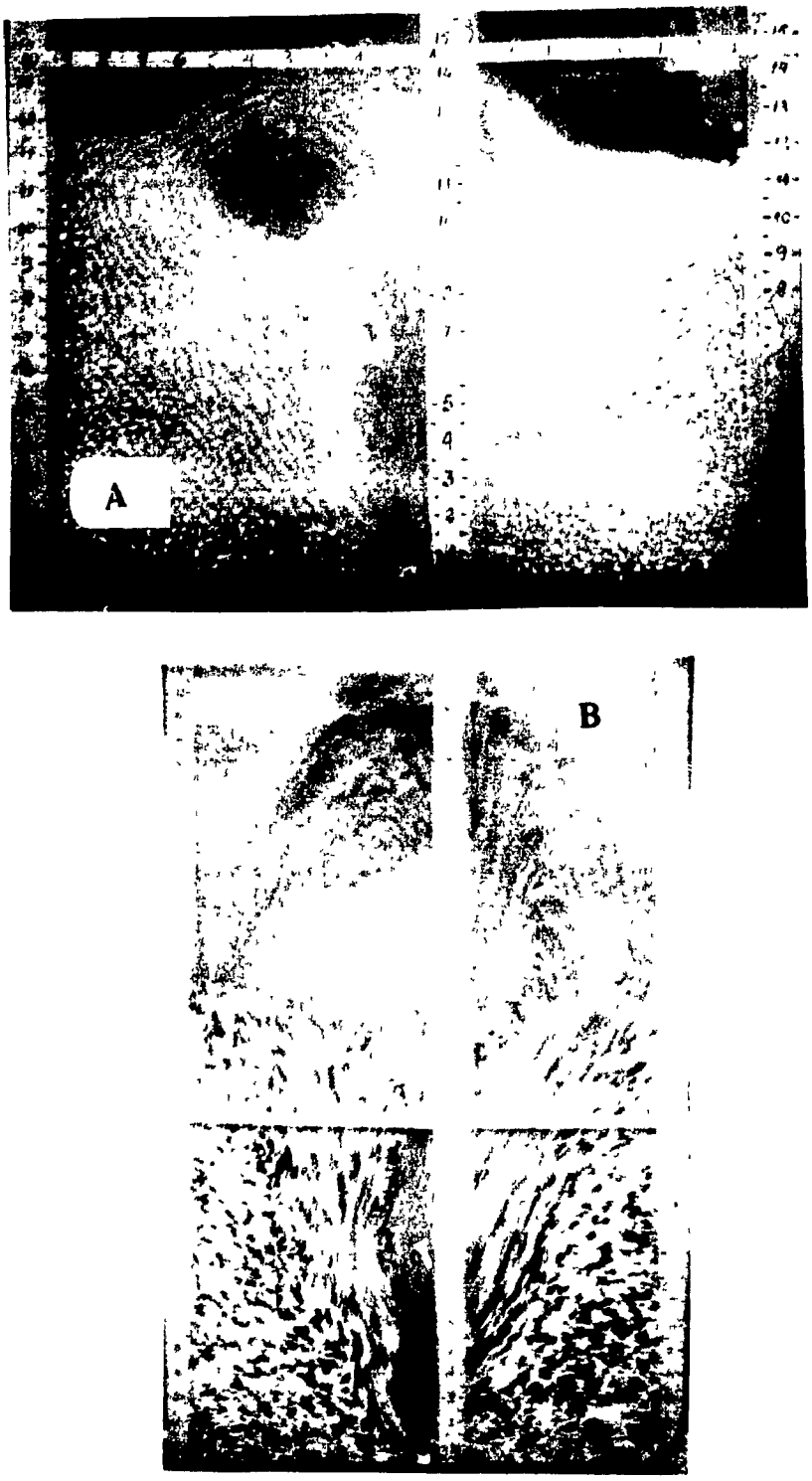

FIGURE 7.9 - Spouting Pattern in 2DSBs of Glass Bead and Millet-Linseed Mixture #3.
(a) Minimum spouting Condition, Particle: Glass Bead, H_o = 0.10 m.
(b) Stable Spouting Condition, Particle: Millet-Linseed Mixture #3, H_o = 0.17 m.

the nozzle. The measurements carried out here were restricted to this zone. As observed experimentally, in this zone, the vertical particle velocity decreased faster until vanishing at or close to the spout-annulus interface.

Data for the vertical particle velocity showed the same trends for the various particles used. At high value of X_i (X_i close to L_1), u_y was lower; as X_i decreased u_y increased passing through a maximum value at a specific X_i, and then decreased. Figure 3.5 represents a typical set of data as a u_y vs. X_i curve. The best fit for the vertical particle velocity profile was a polynomial of the form:

$$u_y = a_0 + a_1 X_i + a_2 X_i^2 + a_3 X_i^3 \qquad (7.9),$$

where a_0, a_1, a_2 and a_3 are functions of particle properties, bed height and spout air superficial velocity. The mean standard error of these curves was 0.93 cm/s and the correlation coefficient of regression ranged from 0.95 to 0.99.

The vertical particle velocity versus X_i curves obtained for millet and barley are presented in Figure 7.10. The effect of the air spouting velocity on the vertical particle velocity can be seen in Figs. 7.10a and b. On increasing V_s, the dead zone volume is reduced in the upper region of the bed (Fig. 7.8); this results in an increase of u_y at a fixed X_i in this region. This can be explained as a dead zone boundary moving with increasing of V_s. The peak of particle velocity moves to the center of the annulus region. The value of u_{ymax} also increases as V_s rises. This increase in u_{ymax} becomes less significant for higher bed heights (Fig.

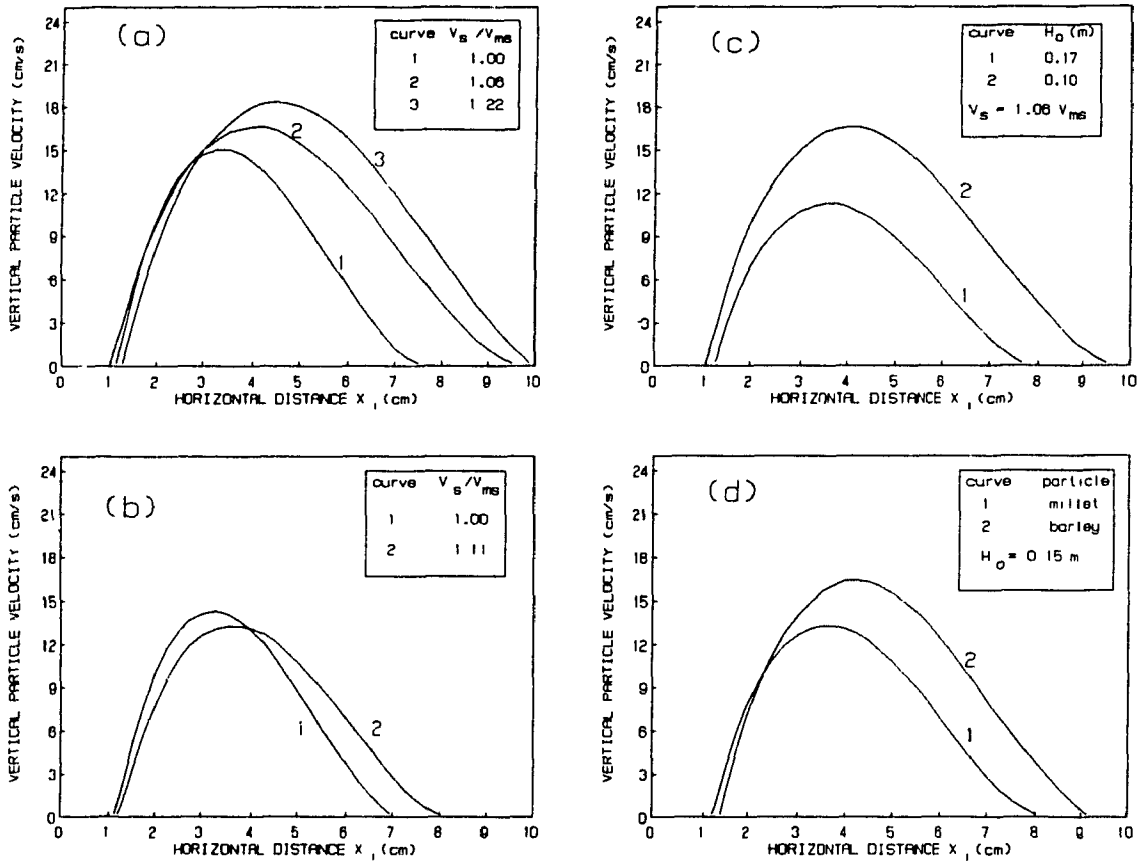

FIGURE 7.10 - Vertical Particle Velocity Curves for 2DSBs of Millet and Barley.
(a) and (b) Effect of spout air superficial velocity in beds of millet: (a) H_o = 0.10 m; (b) H_o = 0.15 m.
(c) Effect of bed height in beds of millet at the same annulus porosity (=0.409).
(d) Effect of particle properties (V_s = 1.15 V_{ms}).

7.10b) in which the bed porosity is lower. (The annular bed porosity is 0.45 for H_o = 0.10 m and 0.41 for H_o = 0.15 m).

The effect of bed height on the vertical particle velocity is shown in Fig. 7.10c for $V_{ms} < V_s < 1.2\ V_{ms}$. An increase of H_o decreases both u_y and u_{ymax}. The bed porosity is the same for these two 2DSBs of millet.

From the above results, it can be concluded that, for a given 2DSB system, the vertical particle velocity varies with the bed height, the annulus bed porosity and the air superficial velocity. The effect of these three variables on u_y can be described by the variation of u_{ymax} and by the reduction of the dead zone volume.

The effect of particle properties on the vertical particle velocity is shown in Figure 7.10d. The value of u_{ymax} and $(X_{iDZ} - L_s/2)$ depend on the particle characteristics, and they are higher for barley than for millet, at the same spouting conditions.

In order to quantify the above results, the vertical particle velocity profile was normalized following the dimensionless parameters:

$$x^*_i = (X_i - L_s/2)/(X_{iDZ} - L_s/2) \qquad (7.10a),$$

$$u^*_y = u_y / u_{ymax} \qquad (7.10b),$$

where x^*_i is greater than or equal to zero; u_{ymax} and $(X_{iDZ} - L_s/2)$ are obtained from the regression u_y versus X_i curves.

The normalized vertical particle velocity, u^*_y, vs. the normalized horizontal distance, x^*_i, data are plotted in Figure 7.11 for all air-particle systems specified in Table 7.11. As it can be seen, the

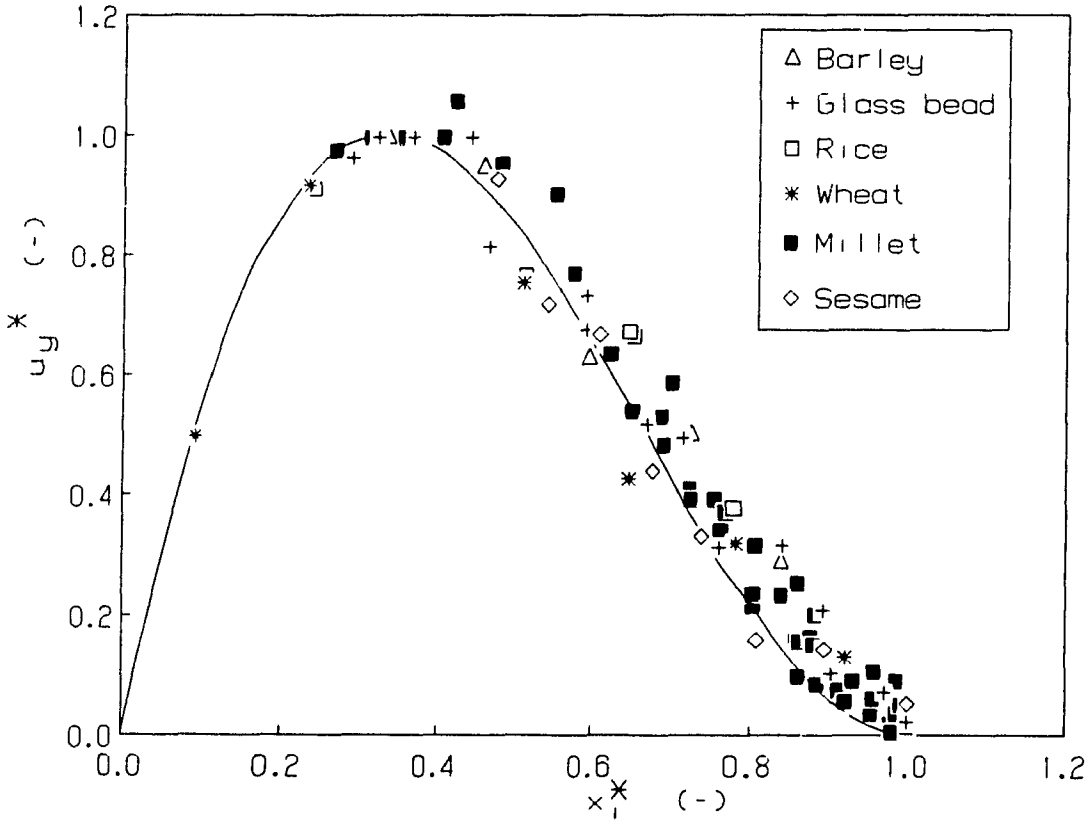

FIGURE 7.11 - Particle Vertical Velocity Profile for a 2DSB of Coarse Particles.
Full line represents eq. (7.11).

normalized data can be fitted well by:

$$u_y^* = 6.9\, x_i^* (1-x^*_i)^2 \qquad (7.11).$$

The standard deviation of the regression curve (SD) is 0.10 and the correlation coefficient squared of the regression, R^2, is 0.99.

Eq. (7.11) shows that the solids motion in the annulus region of a 2DSB is similar for all particles independently of the particle characteristics. The normalized particle velocity is zero at $x_i^* = 1$ and maximum (= 1) at $x_i^* = 1/(6.9\ (1 - x_i^*)^2\ )$. Although changes can occur in u_{ymax} and $(X_{iDZ} - L_s/2)$, the nature of the vertical particle velocity profile remains unchanged.

7.2.2 Solids Circulation Rates

Solids circulation rates (M_p) were determined using eq. (7.11) and the experimental values of u_{ymax} and $(X_{iDZ} - L_s/2)$ for the data sets presented in Table 7.11. The effective cross sectional annular area was based on the annular porosity in the effective region of particle circulation. This porosity was calculated using a simple mass balance in the annular region considering the volume of the dead zone. The porosity in the dead zone was determined by bed height measurements in the regions close to the vessel-wall, before the onset of spouting. The values of the solids circulation rates as well as the values of the basic variables used in this calculation are presented in Table 7.12.

From Table 7.12, it can be concluded that with increasing V_s, the solids circulation rates always increase due to enlargement of the annular effective area, due to an increase of u_{ymax} or even due to

TABLE 7.12

SOLIDS CIRCULATION RATES FOR 2DSBs OF COARSE PARTICLES

PARTICLE	H_o (m)	V_s/V_{ms} (-)	ϵ_{aeff} (-)	u_{ymax} (cm/s)	$(X_{IDZ} - L_s/2)$ (cm)	M_p (kg/hr)
millet	0.10	1.22	0.461	18.3	8.7	751
		1.06		16.6	8.7	649
		1.00 +		15.0	6.7	435
	0.15	1.11	0.421	13.3	6.7	448
		1.00 +		14.3	6.0	414
	0.17	1.04	0.424	11.3	6.6	369
glass bead	0.10	1.25	0.443	10.0	8.0	730
		1.18		9.1	6 6	544
barley	0.15	1.16	0.439	16.4	7.9	658
rice	0.15	1.01	0.471	13.7	7.4	496
sesame seed	0.17	1.36	0.410	8.6	7.6	248
wheat	0.17	1.20	0.433	18.3	7.3	594

coupled effects. Enlargement of the annular effective area means a dislocation of the u_{ymax} point towards the vessel wall. As a consequence, more particles reach failure and circulate.

There are two equations to estimate the solids circulation rates in SBs of coarse particles based on Chap. 2 and Appendix A. Chatterjee's (1970) empirical correlation predicts the solids circulation rates in CSBs as a function of the particle diameter, the solid density and the V_s/V_{ms} ratio. Chatterjee's correlation is presented in Appendix A.

The second correlation presented here was developed by Day (1986) based on the solid-fluid momentum balance in the spout region. As shown in Appendix A, Day's simplified equation for the solids circulation rates near the minimum spouting is a function of the porosity in the spout region, the air-particle properties, and the pressure drop at the top of the annulus region. Moreover, Day's simplified equation can be modified for a 2DSB near the minimum spouting condition as follows:

$$M_p = L_2\, L_s\, \rho_s \{ (1-\epsilon_s)(\rho_s - \rho_f)(g\, H_o/\rho_s)(\epsilon_s - \epsilon_{mf})\, C_o \}^{1/2} \qquad (7.12),$$

where:

$$C_o = (1 - Y^*) + M_o$$

$$M_o = \rho_f \{ (L_1/L_s)^2\, V_{ms}^2 - \epsilon_{mf}\, v_{ms}^2 \} / ((1-\epsilon_{mf})(\rho_s - \rho_f)\, g\, H_o)$$

$$v_{ms} = (A_c\, V_{ms} - A_{aeff}\, V_{ae}) / (L_s\, L_2\, \epsilon_{mf})$$

$$V_{ae} = (1 - (1 - H_o/H_{max})^3)\, V_{mf}\, f(\epsilon_{aeff})$$

$$A_{aeff} = 2\,(X_{iDZ} - L_s/2)\, L_2$$

$$\epsilon_{s} = \{(H_f/H_o) + 0.937\ \epsilon_{mf}\ C_o\}/\{(H_f/H_o) + 0.937\ C_o\}$$

Y^* - calculated by eq. (D.11) for Group #1 and eq. (D.12) for Group #2;

$f(\epsilon_{aeff})$ is an empirical function which should correct the value of V_{ae} due to the porosity variation in the annular region of 2DSBs. Note that V_{ae} is calculated based on the mean bed porosity at minimum fluidization.

The predicted values of the solids circulation rates given by Chatterjee's correlation (eq. A.8) and by the modified Day equation (eq. (7.12)) are presented in Table 7.13 for the 2DSB air-particle system used here. Chatterjee's correlation predicts solids circulation rates much higher than the experimental values obtained here. This suggests that Chatterjee's correlation is valid only for CSB geometry. Note that the cross sectional area of a cylindrical bed with $D_c = L_1$ is about 10 times more than the cross sectional area of the 2DSB used in this work. This can explain the high values of M_p obtained by eq. (A.8). Moreover, eq. (A.8) predicts the highest solid circulation rates for sesame seed, which is against the trends observed in this experimental work in a 2DSB (Table 7.12). This shows that eq. (A.8) cannot predict the solids circulation rates in 2DSBs, even correcting the cross sectional area for 2D geometry.

Day's modified correlation can predict reasonably well the solids circulation rates obtained in 2DSBs of coarse particles near the minimum spouting condition when $f(\epsilon_{aeff}) = 1$ and $\epsilon_{mf} = \epsilon_{ms}$. Eq. (7.12) takes into account the cross sectional area of the 2DSB column as well as the dead zone extent. Moreover, in this eq. (7.12), the minimum spouting pressure drop is the one obtained in a 2DSB design.

TABLE 7.13

PREDICTED VALUES OF THE SOLIDS CIRCULATION RATES

PARTICLE	H_o (m)	V_s / V_{ms} (-)	M_p (kg/hr) eq. (A.8)	M_p (kg/hr) eq. (7.12) (*)
millet	0.10	1.22	1254	
		1.06	1090	
		1.00	1028	376
	0.15	1.11	1141	
		1.00	1028	487
	0.17	1.04	1069	550
glass beads	0.10	1.25	1250	
		1.18	1180	780
barley	0.15	1.16	1324	519
rice	0.15	1.01	1105	517
sesame seed	0.17	1.36	2591	
wheat	0.17	1.20	1449	513

(*) - $f(\epsilon_{aeff}) = 1$ and $\epsilon_{mf} = \epsilon_{ms}$.

7.3 Conclusions

The basic conclusions from this chapter can be summarized as follows:

1 - Equations describing the overall fluid flow characteristics at the minimum spouting conditions in a 2DSB of coarse particles were developed based on the failure state of the spout-annulus interface region. These equations can be used to design and simulate the aerodynamics in a 2DSB. The variables required for this simulation are: (a) the air-particle properties: particle size, air and solid densities, air viscosity, bed porosity at the minimum fluidization, and Coulomb failure angle of the porous material; (b) the column and nozzle dimensions.

2 - The minimum spouting pressure drop equation developed here for 2DSBs predicts the experimental data obtained in this work and those from the literature with a mean deviation of 3.3 %.

3 - The minimum spouting superficial velocity equations developed in this work for 2DSBs predicts the experimental data with a mean deviation of 6.5%.

4 - It was shown that the basic differences in aerodynamics between a 2DSB and a CSB of coarse particles are those regarding the type of spout-annulus interface failure. The plane strain condition holds in a 2DSB design while the intermediate effective solid stress plays a role in the failure criterion for a CSB. Moreover, passive failure occurs in the spout-annulus interface wall in a 2DSB of Group #2 while active failure occurs in the spout wall in a CSB. All these result in different

correlations for scale-up and design of a 2DSB.

5 - It was shown that the minimum spouting velocity depends on the bed height in an exponential form with the Coulomb failure angle. Particles with different sphericity can presents the same minimum spouting velocity vs. bed height curves if the particle size and the Coulomb failure angle are approximately the same. These results can explain some controversy in the SB literature regarding the effect of air-particle properties on the minimum spouting velocity.

6 - An easy and practical technique to measure the solids circulation rates was developed in this work.

7 - Solids circulation rates calculated based on the vertical particle velocity near the minimum spouting condition compared reasonably well with a modified equation obtained from Day's (1986) model. This equation together with the aerodynamic equations proposed here can be used to predict solids circulation rates in a 2DSB of coarse particles near the minimum spouting condition.

CHAPTER 8

FLOW REGIMES IN A TWO DIMENSIONAL SPOUT-FLUIDIZED BED

8.1 Introduction

The effect of additional aeration of the annular region of a 2DSB on the minimum spouting condition, the fluid flow regimes and the solids circulation rates is examined in this chapter.

Additional air was injected in the flat base of a 2DSB fitted with N1 type nozzle following the procedure described in Chap. 3. Millet was chosen as the model particle for this study. The measured variables for the fluid flow characterization were the same as those selected for the pure spouting studies. The air humidity was equal to 30%.

Some remarks about the nomenclature used in this chapter are in order. A 2DSB with supplementary aeration of the annular region is termed a two dimensional spout-fluidized bed (2DSFB). The annular superficial velocity, V_a, is the inlet annular volumetric flow rate to the cross sectional area of the column. The subscript msf denotes the minimum spouting condition. The minimum spouting velocity, V_{msf} , and the spouting superficial velocity, V_s, are defined in terms of the ratio of inlet spouting volumetric flow rate to the cross sectional area of the column.

8.2 Minimum Spouting Condition in a 2D Spout-Fluidized Bed

Typical pressure drop vs. spouting air superficial velocity curves in 2DSFBs are presented in Figure 8.1. These curves are similar to those for pure spouting when the values of V_a are low (V_a < 0.60 m/s), as seen

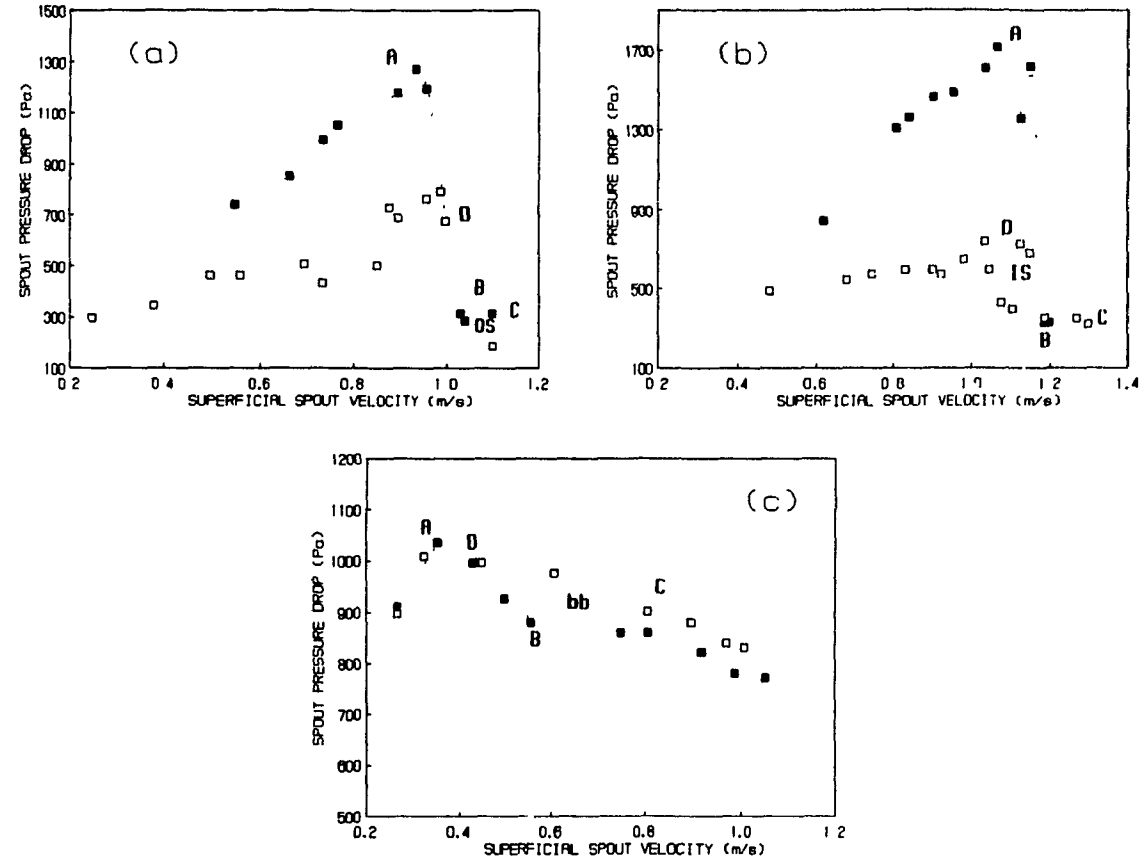

FIGURE 8.1 - Spouting Pressure Drop Characteristic Curves for a 2DSFB of Coarse Particles.
Particle: Millet. H_o = 0.15 m. RH = 30%, d_p = 2.21 mm.
(a) V_a = 0.0 m/s; (b) V_a = 0.29 m/s; (c) V_a = 1.08 m/s.
Point A - maximum spouting pressure drop; Point C - Stable Spouting regime; Point D - spout collapse.
OS - oscillating spout regime; bb - bubbling or incoherent spout regime.
Full symbols - increasing spouting air velocity; empty symbols - decreasing spouting air velocity.

in Figs. 8.1a and b. The peak of pressure drop becomes less apparent as V_a increases. For V_a close to V_{mf}, these curves are similar to those obtained in 2D fluidized beds (Fig. 8.1c).

The minimum spouting condition in a 2DSFB is defined by the collapse of the spout (point D in Fig. 8.1). The stable spouting condition is reached at $V_a > 1.2\ V_{msf}$ (point C in Fig. 8.1). Note that the pressure drop required for stable spouting is lower than the minimum spouting pressure drop.

The minimum spouting pressure drop increases with the increase in V_a while the minimum spouting velocity decreases with the increase in V_a for a fixed bed height and a given air-particle system. The relationship between the minimum spouting pressure drop (or the minimum spouting velocity) and the inlet annular air flow rate depends on the bed height and the aerodynamic regime attained at the onset of spouting (Vukovic et al., 1984).

The mechanism of spout formation observed at low values of V_a is likely to be similar to the one described for pure spouting (Chap. 6). This mechanism changes as V_a increases. The spout cavity degenerates into flat bubbles or waves which move towards the top of the bed for a characteristic value of V_a, viz. V_{amax}. This value depends on the bed height and the air-particle system properties. Vukovic et al. (1984) defined V_{amax} as the inlet annular superficial velocity required to just fluidize the top of the annulus in a conventional spout-fluidized bed. (Vukovic et al. worked with spherical particles with d_p = 1.8 mm spouted by ambient air in a CSFB column with D_c/D_i = 4.7 and D_i = 1.5 cm). As shown later V_{amax} defined in this work is higher than that defined by

Vukovic et al.

The effect of bed height on the minimum spouting pressure drop and the superficial velocity for 2DSFBs is shown in Figure 8.2. The dimensionless parameter ADI in this figure is defined as:

$$ADI = \Delta P_{msf}/\Delta P_{mf} - \Delta P_{ms}/\Delta P_{mf} \qquad (8.1).$$

This parameter ADI represents the additional increase in the minimum spouting pressure drop for a given V_a compared to the minimum spouting pressure drop for the pure spouting ($V_a = 0$). As shown in Fig. 8.2a, the ADI vs. V_a/V_{mf} curves depend on H_o and V_{amax}. The values of V_{amax} were estimated based on the experimental observations of the spout formation mechanisms. V_{amax} is close to zero at $H_o = 0.17$ m.

The maximum spoutable bed height (H_{max}) for 2DSBs of millet is 0.15 m (eq. (6.3) with $A_{2D} = 0.0537$).

The ADI vs. V_a/V_{mf} curve is discontinuous for $H_o < H_{max}$, as shown in Fig. 8.2a for 2DSFBs of millet with $H_o = 0.10$ m. For $V_a < V_{amax}$, ADI increases rapidly with V_a/V_{mf}. For $V_a > V_{amax}$, ADI increases more slowly with the increase of V_a/V_{mf}. At $V_a = V_{amax}$, there is a discontinuity in the ADI vs. V_a/V_{mf} curve. Passos et al. (1988) obtained a similar result for a 2DSFB of glass beads at $H_o = 0.10$ m. Such a result shows that two different fluid flow regimes can be attained at the onset of spouting in 2DSFBs for $H_o < H_{max}$, depending on the value of V_{amax}.

The ADI vs. V_a/V_{mf} curve is typically non-linear for $H_o > H_{max}$ as can be seen in Figure 8.2a for 2DSFBs of millet at $H_o = 0.17$ m. The dashed line in this figure is a parabolic regression curve for the experimental data for $H_o = 0.17$ m. This result indicates that there is

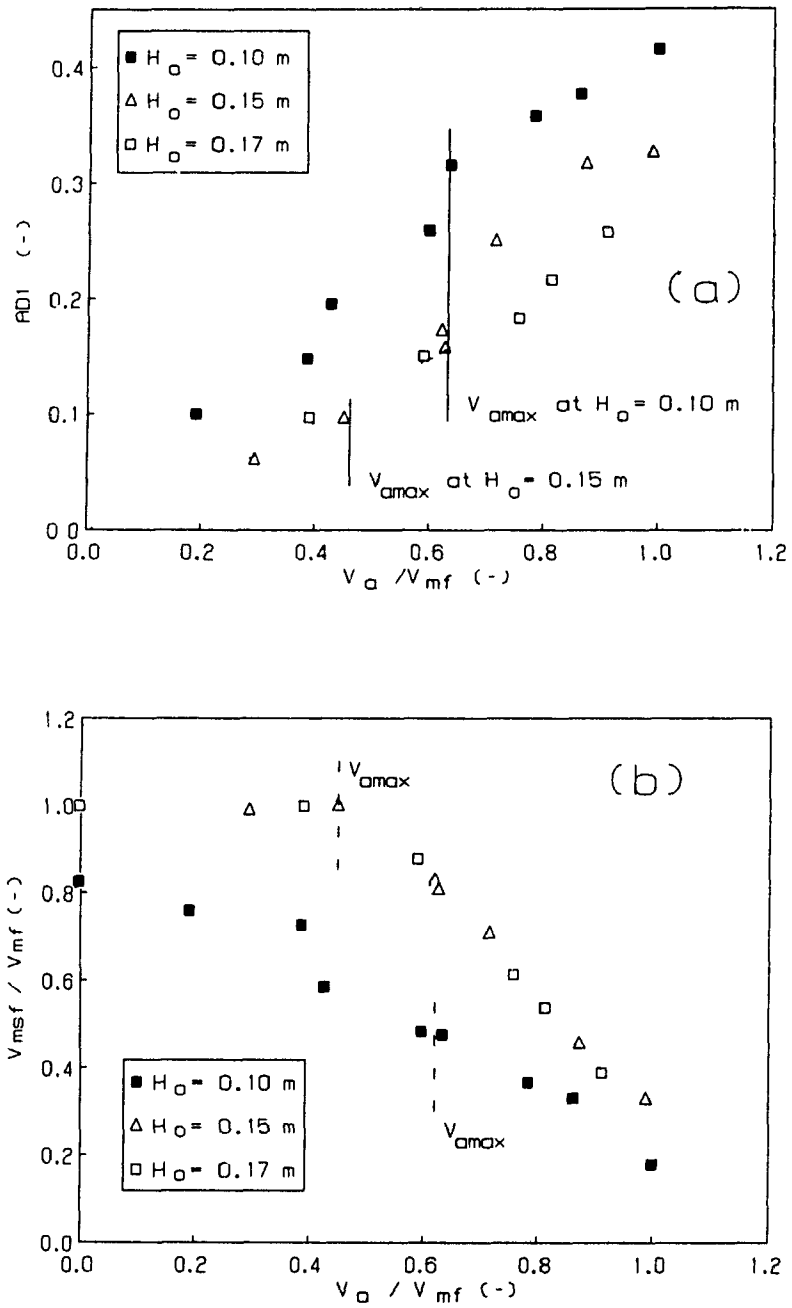

FIGURE 8.2 - Effect of Bed Height on Minimum Spouting Pressure Drop and Minimum Spouting Velocity in a 2DSFB of Coarse Particles. Particle = millet. RH = 30%. Dashed line - regression curve for data at H_o = 0.17 m (R^2 = 0.99 and SD = 0.01).

only one fluid flow regime at the onset of spouting in 2DSFBs for $H_o > H_{max}$ with $V_a < V_{mf}$

The V_{msf}/V_{mf} vs. V_a/V_{mf} data are plotted in Fig. 8.2b. The variation of V_{msf} with V_a depends on the value of V_{amax}. Different trends are observed for $V_a < V_{amax}$ and for $V_a > V_{max}$. This confirms the existence of two different flow regimes at the minimum spouting in a 2DSFB for $H_o < H_{max}$.

The relationship between V_{msf}/V_{mf} and V_a/V_{mf} is linear for $V_a > V_{amax}$ (see Fig. 8.2b for H_o = 0.15 m and 0.17 m). The following equation holds at the minimum spouting for these data :

$$V_{msf} = V_G - V_a \qquad (8.2),$$

where: V_G is the minimum slugging air superficial velocity predicted by eq. (4.5) with $H_{min,s} = H_{ms}$. The values of V_G obtained by eq. (8.2) are compared to those predicted by eq. (4.5) in Table 8.1.

Eq. (8.2) shows that slugs in the top of the bed surface characterizes the minimum spouting condition for $V_a > V_{amax}$ provided $H_o > H_{max}$. This explains the pulsating motion of the spout-annulus region observed in beds of millet at H_o = 0.17 m.

Vukovic et al. (1984) postulated the minimum spouting velocity in a CSFB at $H_o > H_{max}$ as $V_{msf} = V_{mf} - V_a$. Such a condition cannot hold true for a 2DSFB. As observed experimentally, the shape of the bed surface changed (from a parabolic shape to a horizontal line) at $V_a = V_{mf} - V_a$; however the spout (or internal jet) was not developed at this point. Flat bubbles or ripples moved through the jet region towards the top of the

TABLE 8.1

PREDICTED AND EXPERIMENTAL VALUES OF THE MINIMUM SLUGGING VELOCITY

Particle: Millet

H_o (m)	H_{ms} (m)	V_G/V_{mf} (-) (exp.)*	V_G/V_{mf} (-) (pred.)**
0.15	0.152	1.40 SD = 0.06 MD = 4%	1.41
0.17	0.176	1.38 SD = 0.06 MD = 3%	1.35

* - mean value calculated from eq. (8.2) using the experimental data presented in Fig. 8.2b. SD and MD are the standard and the mean deviation of data from the mean value.

** - value predicted by eq. (4.5) with $H_{min,s} = H_{ms}$.

bed. There was no continuous motion of particles in the annulus region. These experimental observations justify the use of eq. (8.2) for calculation of the minimum spouting velocity in 2DSFBs at $H_o > H_{max}$. Moreover, this result shows that V_{amax} should be higher than that obtained by Vukovic et al. (1984).

8.3 Flow Regime Maps

The flow regimes observed for a 2DSFB of millet spouted by air were

mapped following Vukovic et al.'s (1984) flow regime map (see Chap. 2). A schematic representation of the spout formation and the physical appearance of the various flow regimes in a 2DSFB is shown in Figure 8.3. The regime maps are presented in Figures 8.4 and 8.5 for H_o = 0.10 m and H_o =0.15 m.

The five flow regimes identified in Figs. 8.4 and 8.5 can be described as following :

(1) Fixed bed - characterized by the formation of the spout cavity with $0 < V_a < V_{msf}$.

The mechanism of spout formation is similar to that observed in the pure spouting regime for values of V_a less than V_{amax} . Intensive solids circulation around the spout cavity characterizes the onset of spouting over this range of V_a as shown in Fig. 8.3.

The mechanism of spout formation for $V_a > V_{amax}$ is characterized by flat bubbles moving from the spout cavity to the top of the bed (Fig. 8.3). These bubbles travel towards the bed surface as ripples. Solids circulation was not observed inside or around the spout cavity.

(2) Transitional spouting regime may be identified as:

(a) Oscillating spouting - characterized by oscillation of the spout around the central axis of the column as shown in Fig. 8.3. This regime is observed in 2DSFBs at the minimum spouting condition for $V_a < V_{amax}$. This transitional regime also occurs in 2DSBs systems of Group #2 beyond the minimum spouting (Chap. 6). This regime represents the transition between the fixed bed and the spout with aeration regimes.

(b) Incoherent spouting - characterized by a bubbling jet. Bubbles or ripples move inside the spout breaking discontinuously at the bed

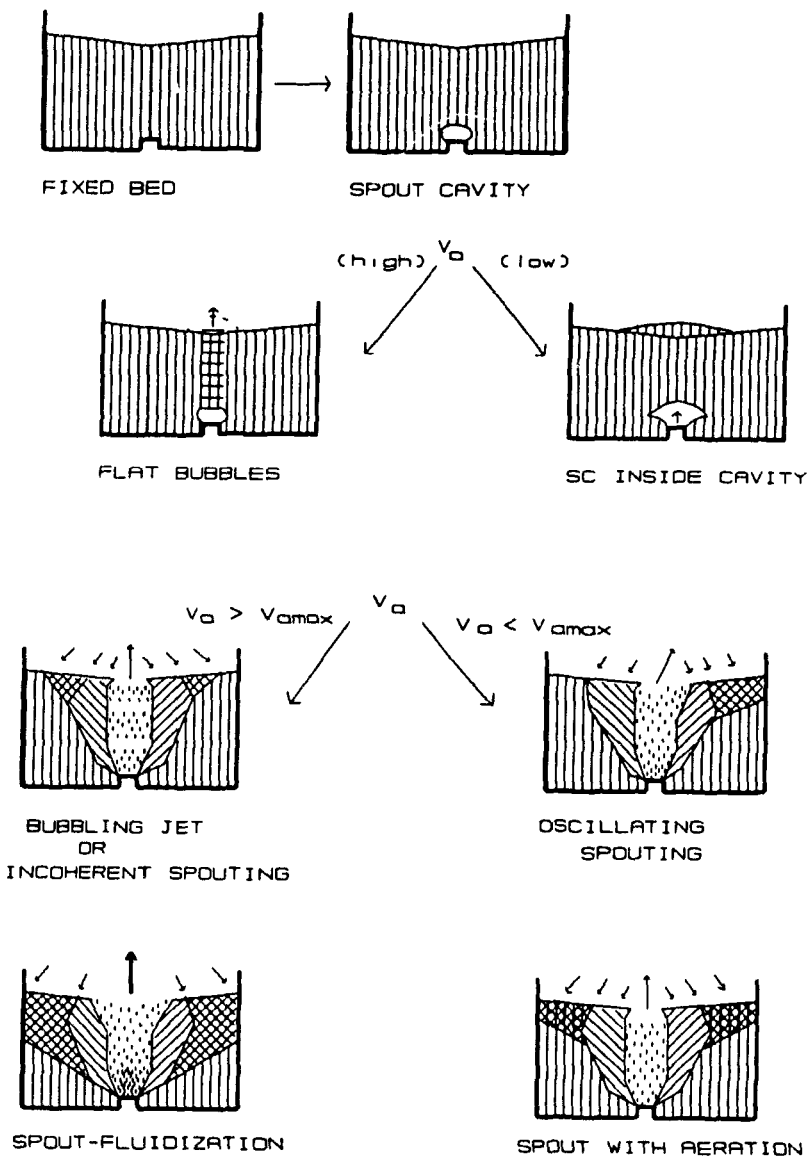

FIGURE 8.3 - Physical Appearance of the Flow Regimes in a 2DSFB of coarse Particles.
SC - solid circulation.

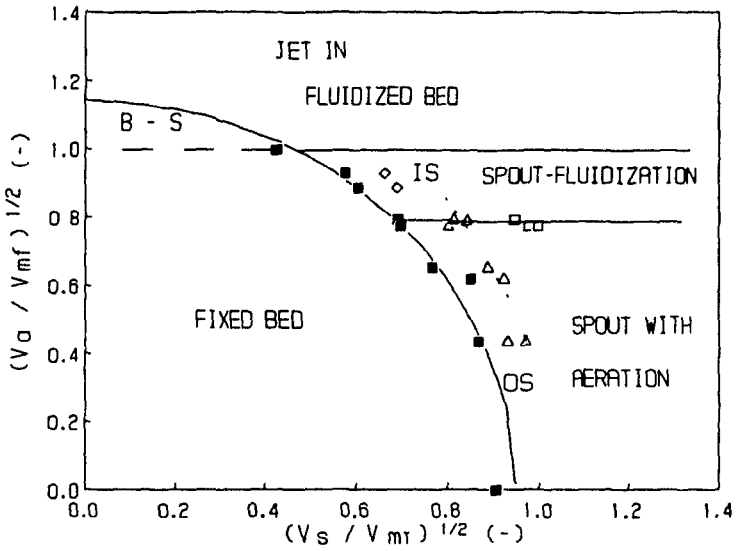

FIGURE 8.4 - Flow Regime Map for a 2DSFB of Millet at H_o = 0.10 m. (see Fig. 8.5 for nomenclature).

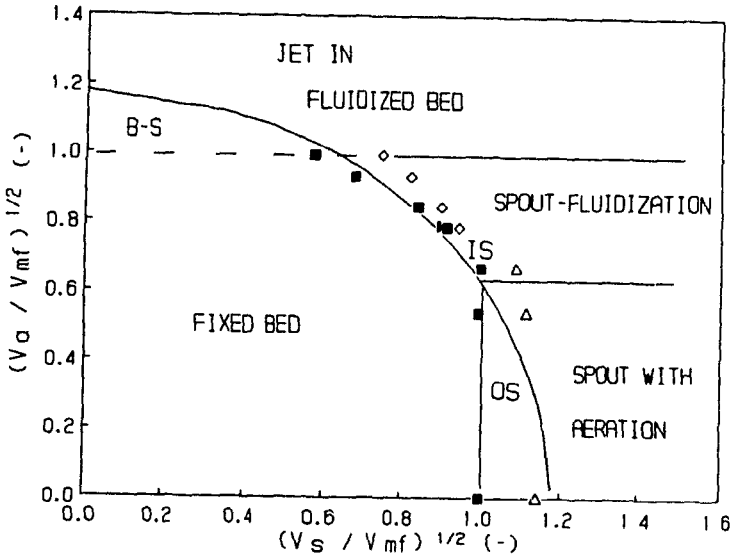

FIGURE 8.5 - Flow Regime Map for a 2DSFB of Millet at H_o = 0.15 m.
OS - oscillating transitional spouting regime,
IS - incoherent transitional spouting regime.
B-S - bubbles and slugs.

surface. A well-defined spout appears at the top of the bed which collapses periodically following the pulsating motion of the bubbles. This regime separates the fixed bed and the spout-fluidization regimes; it is observed for $V_a > V_{amax}$. Such a regime is similar to the one described for 2DSBs systems of Group #1 (Chapter 6).

(3) Spout with aeration regime. This is similar to the pure spouting regime with additional aeration of the annular region. This regime occurs for $V_a < V_{amax}$, $H_o < H_{max}$ and $V_a > V_{msf}$. In this regime, the spout enlarges some distance above the nozzle and then necks at the top of the bed. The fountain can reach high heights (up to 0.30 m) as the spout superficial velocity increases beyond the minimum spouting velocity.

(4) Spout-fluidization regime. This regime is characterized by bubbles or slugs inside the spout region (see Fig. 8.3), resulting in a pulsating motion of the particles inside in the upper region of the bed. In this regime, the spout periodically discharges bubbles near the bed surface. The annular solids flow shows a pulsating motion at the top and a more continuous motion lower in the bed. The annular superficial velocity is higher than V_{amax}. Bubbles begin to form at the bottom of the bed as V_a approaches V_{mf}.

(5) Jet in Fluidized Beds. This regime is characterized by the formation and growth of bubbles in the annular region. The spout is essentially an internal jet. The solids circulation is not cyclic as it is in pure spouting. This regime occurs at high values of the inlet annular flow rate ($V_a > V_{mf}$).

An increase of H_o results in a decrease of V_{amax} as shown in Figs. 8.4 and 8.5. This means that the spout with aeration regime tends

disappear as H_o becomes greater than H_{max}. This was indeed observed experimentally in a 2DSFB of millet at H_o = 0.17 m. These results are in agreement with those obtained by Vukovic et al. (1984) in a CSFB.

8.4 Solids Circulation Rates

The solids circulation rates in a 2DSFB were determined following the same procedure as that described in Chap. 7 for 2DSBs. The vertical particle velocities were measured at different values of V_a for V_a/V_{mf} between 0.84 and 1.11. These measurements were carried out at two bed heights, H_o = 0.15 m and 0.17 m. Table 8.2 presents the experimental conditions for these measurements. The spout and the fountain regions were each well defined. The values of the fountain height (H_f) were in the same range for all the vertical particle velocity measurements.

The volume of the dead zone decreases by about 30% when the spout-fluidization regime is achieved (Table 8.2). Thus the bed hold-up per unit floor space increases by the introduction of air in the annular region of a 2DSFB.

The experimental values of the solids circulation rate (M_p), the mean porosity in the effective annular region of the bed where particles move (ϵ_{aeff}), the maximum vertical particle velocity (u_{ymax}), and the width of the effective annular region ($X_{iDZ} - L_{s/2}$) are presented in Table 8.3. (L_s is the integrated value of L_s (y)).

Data for the solids circulation rates presented in Table 8.3 can be analyzed as follows:

(a) The solids circulation rates decrease with the increase of H_o for a given total inlet flow rate. This is shown by comparing data (2) to

TABLE 8.2

EXPERIMENTAL CONDITIONS FOR VERTICAL PARTICLE VELOCITY DATA

V_s (m/s)	V_s/V_{mf} (-)	V_a/V_{mf} (-)	L_s (cm)	V_{jDZ}/V_{ja} (%)	H_o (m)	H_f (m)	Flow Regime
1.20	1.04	0.0	2.4	44	0.17	0.13	PS
1.22	1.06	0.39	2.7	33	0.17	0.20	SF
0.97	0.84	0.76	3.0	31	0.17	0.12	SF
0.99	0.86	0.81	2.9	30	0.17	0.10	SF
1.15	1.00	0.0	2.3	62	0.15	0.07	PS
1.28	1.11	0.0	2.4	45	0.15	0.15	PS
1.19	1.09	0.45	2.2	38	0.15	0.16	SWA/SF
0.97	0.91	0.63	2.0	38	0.15	0.08	SF
0.97	0.89	0.87	2.5	36	0.15	0.11	SF

Note: PS - pure spouting; SF - spout-fluidization; SWA - spouting with aeration. Mean bed porosity = 0.40 (H_o = 0.15 m) = 0.415 (H_o = 0.17 m).

TABLE 8.3

SOLIDS CIRCULATION RATES IN A 2DSFB OF MILLET

V_s/V_{mf} (-)	V_a/V_{mf} (-)	ϵ_{aeff} (-)	u_{ymax} (cm/s)	$(X_{iDZ} - L_s/2)$ (cm)	M_p (kg/hr)
		H_o = 0.17 m			
1.04	0.0	0.424	11.3	6.6	369 (1)
1.06	0.39	0.417	10.5	8.6	284 (2)
0.84	0.76	0.417	15.2	8.5	402 (3)
0.86	0.81	0.417	13.7	8.6	410 (4)
		H_o = 0.15 m			
1.00	0.0	0.421	14.3	6.0	414 (5)
1.11	0.0	0.421	13.3	6.7	448 (6)
1.09	0.45	0.410	10.0	8.1	374 (7)
0.91	0.63	0.401	18.2	8.1	433 (8)
0.89	0.87	0.413	19.2	8.7	465 (9)

data (7), and data (4) to data (9);

(b) For a given V_a/V_{msf} ratio and H_o, M_p tends to decrease on adding annular gas at low values of V_a (V_a < 0.5 m/s). This is seen by the comparison between data (1) and (2), and data (5) and (7). On increasing V_a (into the range of spout-fluidization regime), M_p increases, as seen by the comparison between data (5) and (8);

(c) In order to maintain the fountain height as the same as that in pure spouting, the total inlet air flow rate must increase. This causes an increase in the solids circulation rates for values of V_a/V_{mf} > 0.45.

As shown, the solids circulation rates tend to decrease with increase of V_a at low values of V_a/V_{mf} (V_a < 0.5 m/s). Sutanto et al. (1984) reported similar results in a CSFB of coarse particles at low bed heights (H_o/D_c < 2). These authors postulated that such results are due to the spout-to-annulus air crossflow.

To analyze the spout-to-annulus crossflow in a 2DSFB, the overall air flow rate in the annular region was estimated by eq. (5.26) as follows:

(a) the pressure drop in eq. (5.26) was the one measured by the annular static tap (T1) at each specific value of V_a;

(b) the mean porosity and the bed height were those measured in the annular region;

(c) the values of λ and a (= $\bar{D}$) in eq. (5.26) are assumed to be equal to those obtained in the fluidization experiments. Note that $\bar{D}$ is a function of the plastic deformations occurring in the annulus region. The assumption for $\bar{D}$ is a rough estimation of the $\bar{D}$ value, and this should be refined when more data become available;

(d) the air superficial velocity calculated by eq. (5.26) is an estimated value of the total air superficial velocity in the annulus region at a given value of V_s.

The fraction of the inlet spouting flow rate which flows from the spout region to the annulus, AD2, was obtained as: (total flow rate in the annulus region - inlet annular flow rate) / (inlet spouting flow rate). The mean values of AD2 over $0.85 < V_s/V_{mf} < 1.11$ are plotted in Figure 8.6a as a function of V_s/V_{mf} for 2DSFBs of millet at H_o = 0.15 m. The fraction of the total inlet air flow which percolates through the annulus (i. e. annulus aeration) vs. V_s/V_{mf} is plotted in Fig. 8.6b for the same 2DSFBs of millet.

The parameter AD2 decreases slightly with V_s/V_{mf} for the spout with aeration regime. At $V_s = V_{smax}$ (V_s = 0.45 V_{mf}), AD2 increases to values of about 30%. This means that the amount of air crossflow from the spout to the annulus increases significantly. The annular air flow rate rises to 50% of the total inlet flow rate (Note that it is only 23% of the total inlet flow rate for pure spouting, as shown in Fig. 8.6b). This characterizes the transition between the spout-with-aeration and the spout-fluidization regimes. Beyond $V_s = V_{smax}$, AD2 decreases nearly linearly with the increase of V_s/V_{mf}. The annulus aeration is maintained in the range of 50%. Negative values of AD2 were obtained at V_s close to V_{mf} indicating a net air inflow from the annulus into the spout.

As shown in Fig. 8.6a the spout-to-annulus crossflow is high at V_s/V_{mf} = 0.45 ($V_s = V_{smax}$). This increase in the air crossflow should reduce the vertical particle velocity at the top of the annulus. As observed earlier, the solids flow shows a pulsating motion at the top of

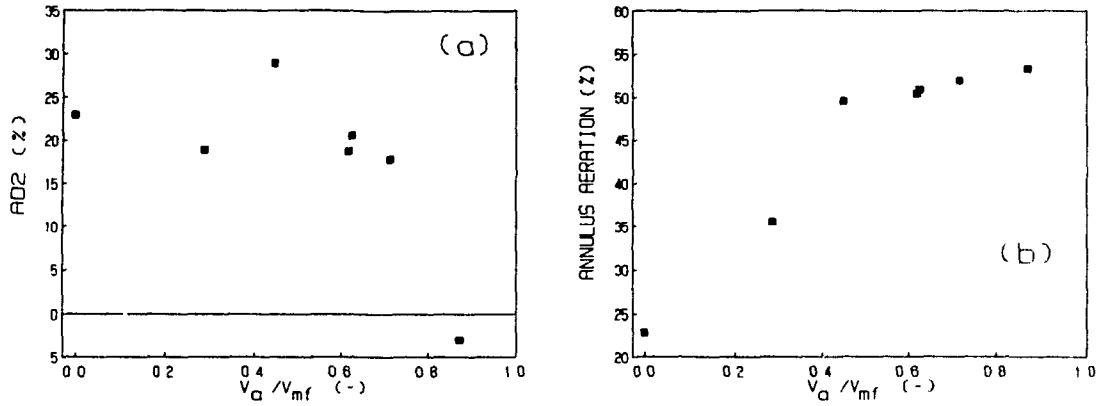

FIGURE 8.6 - Overall Annular Flow Rate versus V_a/V_{mf} of a 2DSFB.
Particle: millet. H_o = 0.15 m.
(a) AD2 (%) vs. V_a/V_{mf};
(b) Annulus Aeration (%) vs. V_a/V_{mf} .

the bed. This reduction of the particle velocity and the decrease of the dead zone volume cause a decrease of the solids circulation rate at V_a/V_{mf} = 0.45. However, at V_a/V_{mf} = 0.87, the air flows from the annulus to the spout region. This should result an acceleration of the annular particle velocity which explains the increase in the solids circulation rates as observed in Table 8.3.

In conclusion, these results show that the solids circulation rates can be controlled by the introduction of additional fluid in the annulus region of a 2DSB. Moreover, the annular air flow rate increases

significantly and the volume of the dead zone is reduced for the spout-fluidization regime. This implies a greater potential for the use of 2DSFBs in particulate drying operations. Improvement in the annulus aeration rate represents an increase in the heat and mass transfer rates in the annular region. The drying capacity of a 2DSFB must therefore be greater than that of an equivalent 2DSB. The inlet annulus flow rate is an additional parameter which can be used to control the solids circulation rates and the drying efficiency in a 2DSFB.

8.5 Conclusions

From this preliminary study on the aerodynamics of a 2DSFB the following conclusions are drawn:

(1) Five flow regimes are identified and mapped for 2DSFBs as functions of the annular fluid flow rate, the spouting fluid flow rate and the bed height.

(2) The introduction of air in the annular base of a 2DSB results in an increase in the volume of air flowing through the annulus; and a decrease in the volume of the dead zone. The solids circulation rates can be increased or decreased (compared with those in pure spouting) by a variation of the inlet annular flow rate.

(3) For the spout-fluidization regime, the annular air flow rate is about twice that obtained for pure spouting. The solids circulation rates can reach the same values as those obtained for pure spouting by increasing the inlet annular flow rate. Moreover, the processing capacity of the bed per unit floor space is increased up to 30% over that obtained by pure spouting.

CHAPTER 9

CONCLUSIONS

9.1 Conclusions

Reliable measurements were made for the flow characterization of two dimensional spouted and spout-fluidized beds of coarse particles. Ten different particle types were used as the spout solid phase with the column width to particle dimension ratio varied between 56 and 150. Two different nozzles were used to inject air into the 2D column. The nozzle width to particle dimension ratio ranged from 4 to 23. The ambient air used to spout the solid phase was maintained at two different levels of relative humidity (30% and 60%). The inlet superficial air velocity was varied from 0.10 to 2.5 m/s. The static bed height was varied from 0.10 m to values beyond the maximum spoutable bed height (up to 0.25 m).

The conclusions presented at the end of each chapter of this thesis are summarized as:

(1) It was found that the fluid flow characteristics in a 2D packed bed of coarse particles depend on the particle-wall (vessel wall) interactions as well as the fluid particle properties. The unmodified Ergun equation cannot be applied to predict the pressure drop versus fluid superficial velocity curves in a 2D packed bed of coarse particles.

(2) The fluid flow characteristics of a 2DSB of coarse particles also depend on the type of failure of the spout-annulus interface. The commonly used equations for predicting the minimum spouting pressure drop and the minimum spouting velocity in a CSB cannot be applied to a 2DSB.

(3) A new approach to describe the effect of the particle-wall interactions on the dynamics of fluid flow through a porous medium was developed. In this approach, the particle-wall interactions are correlated to the anisotropy of the porous material. A "wall boundary" is understood as the specific region in the porous medium where the pore-particle arrangement differs from that in the bulk of the porous material. As the fluid flows through the porous medium, particles and pores deform differently in these regions. Plastic or slip deformations occur in these wall boundary regions, and the mean direction of fluid flow is changed. Mass and momentum balances for the porous medium together with Rowe's (1971) dilatancy model were used to describe the overall flow characteristics in 2D packed and spouted beds.

(4) The effect of air relative humidity on the aerodynamics of a 2D packed bed was analyzed as a change in the particle-wall interaction forces. The particles become well ordered in the wall boundary region when ambient high air humidity is used to fluidize a 2D packed bed. Particles tend to slip upwards (or downwards) on wall as the fluid flow rate increases. The electrostatic particle-wall adhesion force generated when air with low humidity is used prevents particle slip on the wall and improves the homogeneity of a 2D packed or fluidized bed.

(5) A new correlation for the pressure drop versus fluid superficial velocity in a 2D packed bed was proposed. This correlation was applied to determine the Coulomb failure angle for the porous materials used in this work. The results obtained were in good agreement when compared with the range of Coulomb failure angles reported in the literature. Moreover,

the theoretical values obtained for the overall slip deformation rates could be used to explain the experimental findings of bubble formation and the type of fluidization regime developed in 2D packed bed of coarse particles.

(6) The mechanisms of spout termination in a 2DSB were found to be the same as those reported in a CSB. The instability growth mechanism proposed in the literature as being one characteristic of a two dimensional geometry is in reality a transitional mechanism between the fluidization of the annulus top and the choking of spout mechanisms.

(7) Basic equations for scaling-up a 2DSB of coarse particles were proposed. They are as follows:

(i) An empirical correlation to predict the maximum spoutable bed height in 2DSBs of coarse particles characterized by the fluidization of the annulus top as the main mechanism of spout termination was proposed. This correlation was based on the experimental data obtained in this study and those reported in published literature. This correlation fitted the available data for the maximum spoutable bed height with an error of 4%.

(ii) General equations to predict the minimum spouting pressure drop and the minimum spouting velocity in 2DSBs of coarse particles were proposed. These equations were based on the overall momentum balance in the spout-annulus wall interface region and the overall plastic deformation rates of the spout and annulus regions. These equations were used for 2DSBs of different scales and the results were found to be satisfactory. The mean errors for the minimum spouting pressure drop and the minimum spouting superficial velocity were estimated to be 3% and 6%.

(8) The solids flow characteristics in the annular region of the 2DSB were studied by vertical particle velocity measurements, by measuring the dead zone volume, by measuring the annulus bed porosity and the spout width. A similar dimensionless particle velocity profile was obtained for all the particles used in this work.

(9) A modified equation based on Day's (1986) model was shown to predict reasonably well the solids circulation rates in a 2DSB of coarse particles near minimum spouting.

(10) Five different flow regimes were identified, mapped and described for a 2DSFB of coarse particles. A comparative analysis of the flow characteristics in a 2DSB and a 2DSFB showed that improvement in the annulus aeration and in the volumetric bed capacity can be obtained in the spout-fluidization regime.

9.2 Recommendations for Future Works

Some important area for future research are:

(1) Experimental studies on the aerodynamics of 2DSB should be designed to improve the maximum spoutable bed height correlation obtained in this work.

(2) A more complete study should be conducted on the dynamics of 2DSFBs of coarse particles.

(3) A comparative analysis of the aerodynamic conditions in a 2DSB and those in a similar CSB can be performed now in greater depth. The scale-up equations obtained here can be used to simulate the aerodynamics of a 2DSB. The equations presented in Appendix A can be used to simulate the aerodynamics of a similar CSB.

(4) The potential application for 2DSFB dryers seems to be towards the drying of materials with high moisture content due to the high aeration of the annular region obtained here. Future works in this area should include:

(i) experimental determination of the heat and mass transfer rates in a 2DSB and 2DSFB;

(ii) experimental studies of drying particles with high moisture content in a 2DSFB.

9.3 Contributions to Knowledge

(1) A new approach to investigate the dynamics in packed and spouted beds was developed based on the effective solid stress and plastic deformations of the porous medium. This approach allowed the examination of the particle-wall interaction effects (such as variations of porosity due to the wall boundary) on the overall flow characteristics of spouted and packed beds.

(2) Simple correlations for scaling-up a two dimensional spouted bed were proposed in terms of physically meaningful dimensionless groups.

(3) A new correlation between the pressure drop versus superficial air velocity curves in packed beds was proposed. This correlation allowed the analysis of the type of fluidization regime according to the dilatancy (positive or negative) of the porous material.

(4) The type of spout-annulus interface failure was shown to be the fundamental difference between CSBs and 2DSBs of coarse particles. This also explained the basic differences between the aerodynamics of the two types of spouted beds.

(5) A consistent theoretical and experimental study of the dynamics of a 2DSB of coarse particles was presented. This allowed the elucidation of some questions in the literature on 2DSBs such as: the mechanisms of spout termination; the effect of vessel wall boundaries; the oscillating motion of the spout-annulus interface; and scale-up problems.

NOMENCLATURE

A	parameter defined in eq. (2.2)
A_a	annulus cross sectional area
A_{aeff}	effective annulus cross sectional area
A_c	column cross sectional area
A_{2D}	parameter defined in eq. (2.7)
A_N	nozzle cross sectional area
Ar	Archimedes number ($= g\, d_p^3\, \rho_f (\rho_s - \rho_f)/\mu_f^2$)
A^*	parameter defined in eq. (A.3)
ADI	dimensionless parameter defined in eq. (8.1)
AD2	dimensionless parameter = (total flow rate in the annulus region - inlet annular flow rate)/(inlet spouting flow rate)
C_o	parameter defined in eq. (2.9)
C^*	parameter defined in eq. (A.4)
D, D^*	Rowe's dilatancy parameter defined in eq. (5.23), (5.24)
$\overline{D}$	Rowe's dilatancy parameter for 2D beds (overall mean value)
$D_{\|ms}$	Rowe's dilatancy parameter for 2D spouted bed in the spout-annulus interface region
$D_{\|annulus}$	Rowe's dilatancy parameter for 2D spouted bed in the annulus-vessel wall region
D_c	column diameter
D_i	nozzle diameter
$D_{i(eq)}$	equivalent-area nozzle diameter in 2DSBs
E	internal energy of a porous material element per unit mass
$\dot{E}$	rate of internal energy variation of a porous material element
$\dot{E}_1$	rate of internal energy variation of a porous solid material with fluid inside the pores

H	bed height
H_{dz}	height of the dead zone
H_f	fountain height
H_{max}	maximum spoutable bed height
H_{mf}	expanded bed height at the minimum fluidization measured from the pressure tap height to the top of the bed
$H_{min,s}$	minimum bed height in which solids slugs can occur
H_{ms}	bed height at the minimum spouting in spouted beds
H_{msf}	bed height at the minimum spouting in spout-fluidized beds
H_o	static bed height
H_s	height of the spout cavity
H^*	minimum bed height required for one dimensional fluid flow regime (see eq. A.4)
L	length
L_1	column width
L_2	column thickness
L_{dz}	width of the dead zone
L_N	nozzle width
$L_o/2$	horizontal distance from the center of a 2DSB column at the point at which the solid shear stresses become zero
$L_s(y)$	spout width
L_s	integrated value of spout width (from $y = 0$ to $y = H$)
M_p	solids circulation rate
M_o	parameter defined in eq. (A.7)
P	pressure
P_f	pore pressure
ΔP	pressure drop

ΔP_a annulus pressure drop (measured by the annulus static pressure tap)

ΔP_{mf} minimum fluidization pressure drop

ΔP_{ms} minimum spouting pressure drop in spouted beds

ΔP_{msf} minimum spouting pressure drop in spout-fluidized beds

ΔP_s spout pressure drop (measured by the spout static pressure tap)

Re particle Reynolds number

$(=\rho_f d_p \phi V/\mu_f)$

Re_{mf} minimum fluidization particle Reynolds number

$(=\rho_f d_p \phi V_{mf}/\mu_f)$

Re_{ms} minimum spouting particle Reynolds number

$(=\rho_f d_p \phi V_{ms}/\mu_f)$

Re_T terminal particle Reynolds number

$(=\rho_f d_p g(\phi) V_T/\mu_f)$

RH relative air humidity

R^2 correlation coefficient squared of regression

S_p particle surface area

SD standard deviation

T_b bed temperature

V superficial fluid velocity

V_a inlet annulus superficial fluid velocity based on A_c

V_{ae} effective annulus superficial fluid velocity based on A_a (CSBs) or on A_{aeff} (2DSBs)

V_{amax} inlet annulus superficial fluid velocity in which changes in spout-formation occur

V_G minimum superficial fluid velocity at slugging regime

V_{mb} minimum bubbling superficial fluid velocity

V_{mf} minimum fluidization superficial fluid velocity

V_{ms} minimum spouting superficial fluid velocity in spouted beds

V_{msf} minimum spouting superficial fluid velocity in spout-fluidized beds

V_p particle volume

V_s inlet spout superficial fluid velocity (based on A_c)

V_T terminal fall velocity of a spherical particle

V_{DZ} dead zone volume

X^* parameter defined in eq. (A.3)

$X^*_{2D} = 1/(1 + H_{ms}/L_1)$

$X^*_{2D|max} = 1/(1 + H_{max}/L_1)$

X_i horizontal distance from the center of the column to the point at which the tracer particle fell back into the annulus

X_{Vi} volumetric concentration of the ith component in mixture

Y^* dimensionless pressure drop defined in eq. (7.1) and (A.3)

a constants

a form drag coefficient in a 2D packed bed of particles

b $= V_{ms}/V_{mf}$ at h = 1

b body force per unit mass

c constants

d_p volume-equivalent particle diameter

d_{ps} mean particle size from standard sieve analysis

d_s spout diameter

d_{sms} average spout diameter at the minimum spouting

e_{ij} strain component (i - direction of unit area vector, j - direction of the strain deformation)

$\dot{e}_{ij}$ strain component rate

f	interacting force between fluid and solid per unit volume
g,$\underline{g}$	acceleration due to gravity
$g(\phi)$	function defined in eq. (A.2)
g	plastic potential defined in Appendix D
h	dimensionless height (= H / H_{max})
m	moisture content, dry basis
Δm	mass of fluid increase in the porous solid element per unit of solid porous volume
n	number of data replication in Chap. 3
n	= $\tan^2(45^\circ + \theta_c/2)$ in Chap. 7 and Appendix D
p	any measured variable in eq. (3.1)
t	time
u	interstitial solid velocity
u_y	vertical particle velocity (in the annulus region)
$\bar{u}_y$	mean vertical particle velocity (in the annulus region)
u_{ymax}	maximum vertical particle velocity (in the annulus region)
u_y^*	dimensionless vertical particle velocity defined in eq. (7.10b)
v	interstitial fluid velocity
x	horizontal coordinate
x_1^*	dimensionless horizontal distance defined in eq. (7.10a)
y	vertical coordinate
θ_c	Coulomb angle of shearing resistance at critical state for a porous material
θ_f	failure angle for a porous material
θ_i	frictional angle between particle-particle
Ω	interaction moment between fluid and solid per unit volume
α	angle between mean particle slip plane and major principal plane

γ effective weight of a bed of particles defined in Appendix D

γ^* effective dimensionless weight of a bed of particles defined in Appendix D

ϵ bed porosity

ϵ_a annulus porosity

ϵ_{aeff} annulus porosity in the effective region of the annulus

ϵ_{aH} annulus porosity at the top of the bed

ϵ_{mf} minimum fluidization bed porosity

ϵ_{ms} minimum spouting bed porosity in spouted beds

ϵ_{msf} minimum spouting bed porosity in spout-fluidized beds

ϵ_o bed porosity at static conditions

ϵ_s spout porosity

θ included angle in a spouted bed

$\lambda/2$ angle between the applied pressure gradient and the symmetric axis of the pore-particle structure

μ_f fluid viscosity

π fluid stress tensor

ρ_b solid bulk density

ρ_f fluid density

ρ_s solid density

ρ_w water density

σ solid stress tensor

σ^e effective solid stress tensor

τ solid shear stress

ϕ particle sphericity

REFERENCES

Abrahamsen, A. R. and D. Geldart, "Behavior of Gas-Fluidized Beds of Fine Particles. Part I. Homogeneous Expansion". *Powder Technol.* 26 (1980): 35-46.

Anderson, K., G. S. V. Raghavan, and A. S. Mujumdar, "Characteristics of Asymmetric Two-Dimensional Slot Spouted Beds for Grains". *Drying' 84*, A. S. Mujumdar, ed., Hemisphere McGraw-Hill, New York, 1984, 205-209.

Baxter, J. F and R. H. Hahn, Jr., eds. *1982 Agricultural Engineers Yearbook*. American Society of Agricultural Engineers, Michigan, 1982.

Becker, H. A., "An Investigation of Laws governing the Spouting of Coarse Particles." *Chem. Eng. Science* 13 (1961): 245-262.

Becker, H. A., "A Study of Diffusion in Solids of Arbitrary Shape, with Application to the Drying of Wheat Kernel." *J. Applied Polymer Science* 1 (1959): 212-226.

Benenati, R. F. and C. B. Brosilow, "Void Fraction Distribution in Beds of Spheres". *AIChE J.* 8 (1962): 359-361.

Botterill, J. S. M., Y. Teoman and K. R. Yuregir, "The effect of Operating Temperature on the Velocity of Minimum Fluidization Bed Voidage and General Behaviour". *Powder Technol.* 31 (1982): 101-110.

Bridgwater J., "Fundamental Properties of Powders - Part 2. Behavior of Powders in a Condensed State." *Handbook of Powder Science and Technology*, M. E. Fayed and L. Otten, eds., Van Nostrand Reinhold Co., New York, 1984, 169-180.

Carroll, M. M., and N. Katsube, "The Role of Terzaghi Effective Stress in

Linearly Elastic Deformation." *ASME J. of Energy Resources Technol.* 105 (1983): 509-511.

Chandnani, P. P. and N. Epstein, "Gas Spouting of Fine Particles". Proceedings of 34th Can. Chem. Eng. Conference, Quebec, 1984, 452-455.

Chatterjee, A., "Effect of Particle Diameter and Apparent Particle Density on Internal Solid Circulation Rate in Air-Spouted Beds". *Ind. Eng. Chem. Des. Develop.* 9 (1970): 531-536.

Clift, R., "Measuring the Size of Particle in Gases." Proceedings of 37th Can. Chem. Eng. Conf., Can. Society for Chem. Eng., ed., Montreal, Quebec, 1987, 101-103.

Day, J-Y, "Spout Voidage Distribution and Particle Circulation Rates in Spouted Beds." Ph.D. Thesis, Rensselaer Polytechnic Institute, Troy, New York, 1986.

Donadono S. and L. Massimilla, "Mechanism of Momentum and Heat Transfer between Gas Jets and Fluidized Beds". *Fluidization*, J. F. Davidson and D. L. Keairns, eds., Cambridge Univ. Press, Cambridge, 1978, 375.

Dumitrescu, C. , "The Hydrodynamical Aspects of a Spouted Bed Modified by Introduction of an Additional Flow." Proceedings on 7th Int. Cong. Chem. Eng. (CHISA 81), J3.23, Praha, Czechoslovakia, 1981.

Epstein, N. and J. R. Grace, "Spouting of Particulate Solids." *Handbook of Powder Science and Technology*, M. E. Fayed and L. Otten, eds., Van Nostrand Reinhold Co., New York, 1984, 507-536.

Epstein, N. and P. P. Chandnani, "Gas Spouting Characteristics of Fine Particles." *Chem. Eng. Science.* 42 (1987): 2977-2981.

Epstein, N., C. J. Lim and K. B. Mathur, "Data and Models for Flow Distribution and Pressure Drop in Spouted Beds." *Can. J. Chem. Eng.* 56

(1978): 436-447.

Ergun, S., "Fluid Flow through Packed Columns." *Chem. Eng. Prog.* 48 (1952): 89-94.

Filla, M., L. Massimilla and S. Vacarro, "Jets in Fluidized Beds and Spouts: A Comparison of Experimental Behavior and Models". *Can. J. Chem. Eng.* 61 (1983): 370-376.

Geldart, D., "Types of Gas Fluidization." *Powder Technol.* 7 (1973): 285-292.

Geldart, D., J. M. Hurt, and P. H. Wadia, "Slugging in Beds of Large Particles." *AIChE Symposium Series* 74: 176 (1978): 60-66.

Grace, J. R. and C. J. Lim, "Permanent Jet Formation in Beds of Particulate Solids." *Can. J. Chem. Eng.* 65 (1987): 160-162.

Grbavcic, Z. B., D. V. Vukovic, F. K. Zdanski and H. Littman, "Fluid Flow Pattern, Minimum Spouting Velocity and Pressure Drop in Spouted Beds." *Can. J. Chem. Eng.* 54 (1976): 33-42.

Hadzismajlovic, D. Z., Z. B. Grbavcic, D. V. Vukovic and H. Littman, "The Mechanics of Spout-Fluid Beds at the Minimum Spout-Fluid Flowrate". *Can. J. Chem. Eng.*, 61 (1983): 343-348.

Heil, C., and M. Tels, "Pressure Distribution in Spout-Fluid Bed Reactors." *Can. J. Chem. Eng.*, 61 (1983): 331-342.

Himmelblau, D. M. *Process Analysis by Statistical Methods.* Sterling Swift Swift Co., Austin, 1970.

Kalwar, M. I., V. G. S. Raghavan, and A. S. Mujumdar, "Static Vertical Pressure of Grains on Slots (air-entry) in a Two Dimensional Nonaerated Spouted Bed Grain Dryer." *Drying'86*, A. S. Mujumdar, ed., Hemisphere

McGraw-Hill, New York, 1986.

Katsube, N., and M. M. Carroll, "The Modified Mixture Theory for Fluid-Filled Porous Materials: Theory and Application." *ASME J. of Applied Mechanics,* 54 (1987): 35-46.

Littman, H. and M. H. Morgan, "The Measurement, Prediction and Correlation of the Minimum Spouting Velocity, Pressure Drop, Maximum Spoutable Height and Spout Diameter in Spouted Beds of Coarse Particles." *Transport Processes in Fluidized Beds*, L. K. Doraiswamy and A. S. Mujumdar, eds., Elsevier, Amsterdam, 1988, 287-315.

Littman, H., and M. H. Morgan III, "A New Spouting Regime in Beds of Coarse Particles Deeper than the Maximum Spoutable Height." *Can. J. Chem. Eng.* 64 (1986): 505-508.

Littman, H. , and M. H. Morgan III, "A General Correlation for the Minimum Spouting Velocity." *Can. J. Chem. Eng.* 61 (1983): 269-273.

Littman, H., M. H. Morgan III, D.V. Vukovic, F. K. Zdanski, and Z. B. Grbavcic, "Prediction of the Maximum Spoutable Height and the Average Spout to Inlet Tube Diameter Ratio in Spouted Beds of Spherical Particles." *Can. J. Chem. Eng.* 57 (1979): 684-687.

Littman, H., M. H. Morgan III, P. V. Narayanan, S. J. Kim, J-Y Day, and G. M. Lazarek, "An Axisymmetric Model of Flow in the Annulus of a Spouted Bed of Coarse Particles. Model, Experimental Verification and Residence Time Distribution." *Can. J. Chem. Eng.* 63 (1985): 188-194.

Lobnes, R. A., J. C. Liu, and W. H. Bokhoven, "Experimental Determination of K_o Stress Ratios in Grain." Proceedings on 34th Can. Chem. Eng. Conf., Montreal, 1987, 231-237.

Mathur, K. B., and N. Epstein, *Spouted Beds*, Academic Press, New York,

1974.

Massimilla, L., G. Donsi and N. Migliaccio, "The Dispersion of Gas Jets in Two-Dimensional Fluidized Beds of Coarse Solids." *AIChE Symposium Series* 77 (1981): 17-27.

McNab, G. S., "Prediction of Spout Diameter." *Brit. Chem. Eng. Proc. Tech.* 17 (1972): 532.

McNab, G. S. and J. Bridgwater, "The Application of Soil Mechanics to Spouted Bed Design." *Can. J. Chem. Eng.* 52 (1974): 162-169.

Morgan III, M. H., and H. Littman, "Predicting the Maximum Spoutable Height in Spouted Beds of Irregularly Shaped Particles." *Ind. Eng. Chem. Fundam.* 21 (1982): 23-26.

Morgan III, M. H., and H. Littman, "General Relationships for the Minimum Spouting Pressure Drop Ratio, $\Delta P_{ms}/\Delta P_{mf}$, and the Spout-Annular Annular Condition in a Spouted Bed." *Fluidization*, J. R. Grace, and J. M. Matsen, eds., Plenum Press, New York, 1980, 287-296.

Morgan III, M. H., H. Littman and J. Y. Day, "A Generalized Axial Pressure Model for Spout and Spout-Fluid Bed Systems at Minimum Spouting." Proceedings of Fluidization VI, J. R. Grace and L. W. Schmilt, eds., Engineering Foundation, New York, 1989, 261-268.

Morgan III, M. H., J. Y. Day and H. Littman, "Spout Voidage Distribution, Stability and Particle Circulation Rates in Spouted Beds of Coarse Particles - I. Theory." *Chem. Eng. Science.* 40 (1985): 1367-1377.

Mujumdar, A. S., "Spouted Bed Technology - a Brief Review." *Drying'84*. A. S. Mujumdar, ed., Hemisphere McGraw-Hill, New York, 1984, 151-157.

Mutsers, S. M. P., and K. Rietema, "The Effect of Interparticle Forces on

the Expansion of a Homogeneous Gas-Fluidized Bed." *Powder Technol.* 18 (1977): 239-248.

Nagarkatti, A. and A. Chatterjee, "Pressure and Flow Characteristics of a Gas Phase Spout-Fluid Bed and the Minimum Spout-Fluid Condition." *Can. J. Chem. Eng.*, 52 (1974): 185-195.

Ojalvo, J. R. O., "Rectangular Spouted Bed." , Master Thesis, Universidade Federal de Sao Carlos, Sao Carlos, Sao Paulo, 1989.

Ojalvo, J. R. O and J. C. Gubulin, "Slot Two Dimensional Spouted Beds: Effect of Bed Geometry on Solids Circulation." Proceedings of XVI Symposium in Porous Media (ENEMP), vol. 2: 469-477, Oct., Rio de Janeiro, 1988.

Passos, M. L., A. S. Mujumdar, and V. G. S. Raghavan, "Spouted and Spout-Fluidized Beds for Grain Drying." *Drying Technol.* , 7 (1989): 663-696.

Passos, M. L., A. S. Mujumdar, and V. G. S. Raghavan, Spouting and Spout-fluidization of Dry-Wet Particles in a Two Dimensional Bed, paper paper presented in 6th Int. Drying Symposium (IDS'88), Sept., France (1988).

Passos, M. L., A. S. Mujumdar and G. S. V. Raghavan, "Pressure Drop in Slotted Spouted Beds of Grains: Comparison of Data with Models." *Powder Technol.* 52 (1987a): 131-137.

Passos, M. L., A. S. Mujumdar and V. G. S. Raghavan, "Spouted Beds for Drying: Principles and Design Considerations." *Advances in Drying*, vol. 4, A. S. Mujumdar, ed., Hemisphere Publishing Corp., New York, 1987b, 359-398.

Passos, M. L., A. S. Mujumdar and V. G. S. Raghavan, " Aerodynamics and

Solids Circulation Rates in Two Dimensional Spouted Bed." Proceedings 12th Annual Powder & Bulk Solids, Rosemont, Illinois, 1987c, 117-133.

Patrose, B. and H. S. Caram, "The Mechanics of Particle Motion in a Grid Jet." AIChE Meeting, San Francisco, California, 1984.

Perry, R. H. and C. H. Chilton, ed. *Chemical Engineers' Handbook*. 5th ed., McGraw-Hill Kogakusha, Ltd., Tokyo, 1973.

Povrenovic, D. S., D. E. Hadzismajlovic, Z. B. Grbavcic, V. Vukovic and H. Littman, "Minimum Fluid Flowrate, Pressure Drop and Stability of a Conical Spouted Bed." Proceedings of 9th Int. Cong. of Chem. Eng. (CHISA 87), E9.27, 1987.

Rovero, G., C. M. H. Brereton, N. Epstein, J. R. Grace, L. Casaiegno and N. Piccinini, "Gas Flow Distribution in Conical-Base Spouted Beds." *Can. J. Chem. Eng.* 61 (1983): 289-296.

Rowe, P. W., "Theoretical Meaning and Observed Values of Deformation Parameters for Soil." Stress Strain Behavior of Soils, Roscoe Memorial Symposium, Cambridge, 1971, 148-193.

Saxena, S. C, and V. L. Ganzha, "Heat Transfer to Immersed Surfaces in Gas-Fluidized Beds of Large Particles and Power Characterization." *Powder Technol.* 39 (1984): 119-208.

Stanek, V., and J. Szekely, "Three-Dimensional Flow of Fluids through Nonuniform Packed Beds." *AIChE J.* 20 (1974): 974-980.

Sutanto, W., N. Epstein and J. R. Grace, "Hydrodynamics of Spout-Fluid Beds." Proceedings of 8th Int. Cong. Chem. Eng. (CHISA 84), G6.5: 254, Praha, Czechoslovakia, 1984; *Powder Technol.* 44 (1985): 205-212.

Szekely, J. and J. J. Poveromo, "Flow Maldistribution in Packed Beds: Comparison of Measurements with Predictions." *AIChE J.* 21 (1975): 769-

775.

Verlaan, T. D., "The Performance of a Two Dimensional Spouted Bed Grain Dryer.", Internal Report, Dep. of Agricultural Engineering, Macdonald College of McGill University, April, 1984.

Volpicelli, G., G. Raso , and L. Massimilla, "Gas and Solid Flow in Bidimensional Spouted Beds." Proceedings Eindhoven Fluidization Symposium, 1967, Netherlands Univ. Press, Amsterdam, 1967, 123-133.

Vukovic, D. V., D. E. Hadzismajlovic, Z. B. Grbacvic, R. V. Garic and H. Littman, "Flow Regimes for Spout-Fluid Beds." *Can. J. Chem. Eng.* 62 (1984): 825-829.

Vukovic, D. V., Z. B. Grbavcic, D. E. Hadzismajlovic, R. V. Garic and H. Littman, "The Maximum Spoutable Bed Height in a Spout-Fluid Bed." Proceedings on 9th Int. Cong. of Chem. Eng. (CHISA 87), E9.27, 1987.

Wu, S. W. M., C. J. Lim and N. Epstein, "Hydrodynamics of Spouted Beds at Elevated Temperatures." *Chem. Eng. Comm.* 62 (1987): 251-268.

Yang, W. C. and D. L. Keairns, "Solid Entrainment Ratio into Gas and Gas-Solid, Two-Phase Jets in a Fluidized Bed." *Powder Technol.* 33 (1982): 89-94.

Yang, W. C., D. L. Keairns and D. K. McLain, "Gas Mixing in a Jetting Fluidized Bed." *AIChE Symposium Series* 80 (1984): 32-41.

APPENDIX A

BASIC CORRELATIONS FOR THE DYNAMICS OF SPOUTED BEDS

A.1 Littman et al.'s Semi-Empirical Aerodynamic Model

Littman et al.'s semi-empirical aerodynamic model for CSBs of coarse particles (Littman and Morgan, 1988) is summarized as following:

A.1.1 Maximum Spoutable Bed Height:

(a) Spherical Particles

$$H_{max} D_i / D_c^2 = 0.218 + 5.00 \times 10^{-3} / A \; ; \qquad A > 0.02 \qquad (A.1)$$

(b) Non-Spherical Particles

$$H_{max} D_i / D_c^2 = 0.218 + 5.13 \times 10^{-3} / A + 2.54 \times 10^{-5} / A^2 \; ; \qquad A > 0.014 \qquad (A.2)$$

with:

$$A = Re_{mf} Re_T (d_p / D_i) / Ar$$

$$Re_{mf} = \rho_f d_p \phi V_{mf} / \mu_f$$

$$Re_T = \rho_f d_p g(\phi) V_T / \mu_f$$

$$g(\phi) = 1.0 \quad \text{for} \quad \phi = 1.0$$

$$g(\phi) = 5\phi^3 - 7.57\phi^2 + 4.09\phi - 0.516 \quad \text{for} \quad \phi < 1.0$$

A.1.2 Minimum Spouting Pressure Drop:

$$\Delta P_{ms} / \Delta P_{mf} = 1 - Y^* \; ; \quad h < 1 \qquad (A.3)$$

with:

$$Y^{*2} + [2(X^*-0.2) - 1.8 + (3.24/A^*]Y^* + [(X^*-2)(X^*-0.2)-3.24/A^*] = 0$$

$$X^* = 1/(H/D_c + 1)$$

$$A^* = 7.18\,[A-D_i/D_c] + 1.07$$

A.1.3 Minimum Spouting Velocity:

$$V_{ms}/V_{mf} = 42.86(1-\epsilon_{aH})[\{1+ 3.111\times10^{-4}(\epsilon_{aH}\phi)^3 Ar\, C^*/(1-\epsilon_{aH})\}^{1/2} - 1]/Re_{mf} \quad (A.4)$$

with:

$$C^* = 1 - Y^* - (H/D_c)\,X^{*2}\{[\,2Y^* + (X^* - 2) + (X^* - 0.2) - 3.24/A^*\,]/$$

$$[2Y^* + 2(X^*-0.2) - 1.8 + 3.24/A^*\,]\}$$

$$H/D_c > H^*/D_c$$

H^*/D_c	1.282	1.204	1.132	1.664	1.000	0.940	0.884	0.831	0.780
A^*	-2.0	-1.5	-1.0	-0.5	0	0.5	1.0	1.5	2.0

A.2 McNab and Bridgwater's Correlation

McNab and Brigwater's (Epstein and Grace, 1984) correlation for H_{max} is given by:

$$H_{max}\,D_i/D_c^2 = (D_i/d_p)(D_c/D_i)^{2/3}\,568b^2\,[(1+ 3.59\times10^{-5}Ar)^{1/2} - 1]^2/Ar \quad (A.5)$$

with:

$$b = (V_{ms}/V_{mf})_{h=1} = 1.11;$$

V_{ms} given by the Mathur and Gishler equation (Mathur and Epstein, 1974);

$\phi\ \epsilon_{mf}^3 = 1/14$ and $(1-\epsilon_{mf})/\phi^2\epsilon_{mf}^3 = 11$.

A comparison among eqs. (A.1) or (A.2), (A.5) and experimental data from literature (Littman et al., 1979 and Morgan and Littman, 1982) is shown in Figure A.1. Table A.1 presents the standard and the average deviation from the predicted and experimental data for each equation.

Eq. (A.1) predicts better H_{max} for CSBs of spherical coarse particles spouted by air or water at ambient conditions.

It is important to point out that the experimental data used in Fig. A.1b are based on 21 points from Malek and Lu (Morgan and Littman, 1982) and 4 points from Mathur and Gishler (Morgan and Littman, 1982). These data have a considerable scatter due to the different approaches used to determine H_{max}. However, as shown in Table A.1, Littman et al.'s correlation predicts better H_{max} at high A (A> 0.05), while eq. (A.5) predicts better H_{max} at low A ($0.007 < A < 0.02$).

A comparison between eq. (A.5) and (A.2) shows that the basic difference is related to the coefficient of proportionality between the minimum frictional energy lost across the spout and the inlet kinetic energy carried out by the fluid, i. e.:

$$(\rho_s - \rho_f) g H_{max} = k' \rho_f V_N^2 = k'' \rho_f V_T V_{mf} (D_c/D_i)^2 \qquad (A.6a)$$

or:

$$H_{max} D_i / D_c^2 = k'' A \qquad (A.6b)$$

with k" the coefficient of proportionality, and equal to:

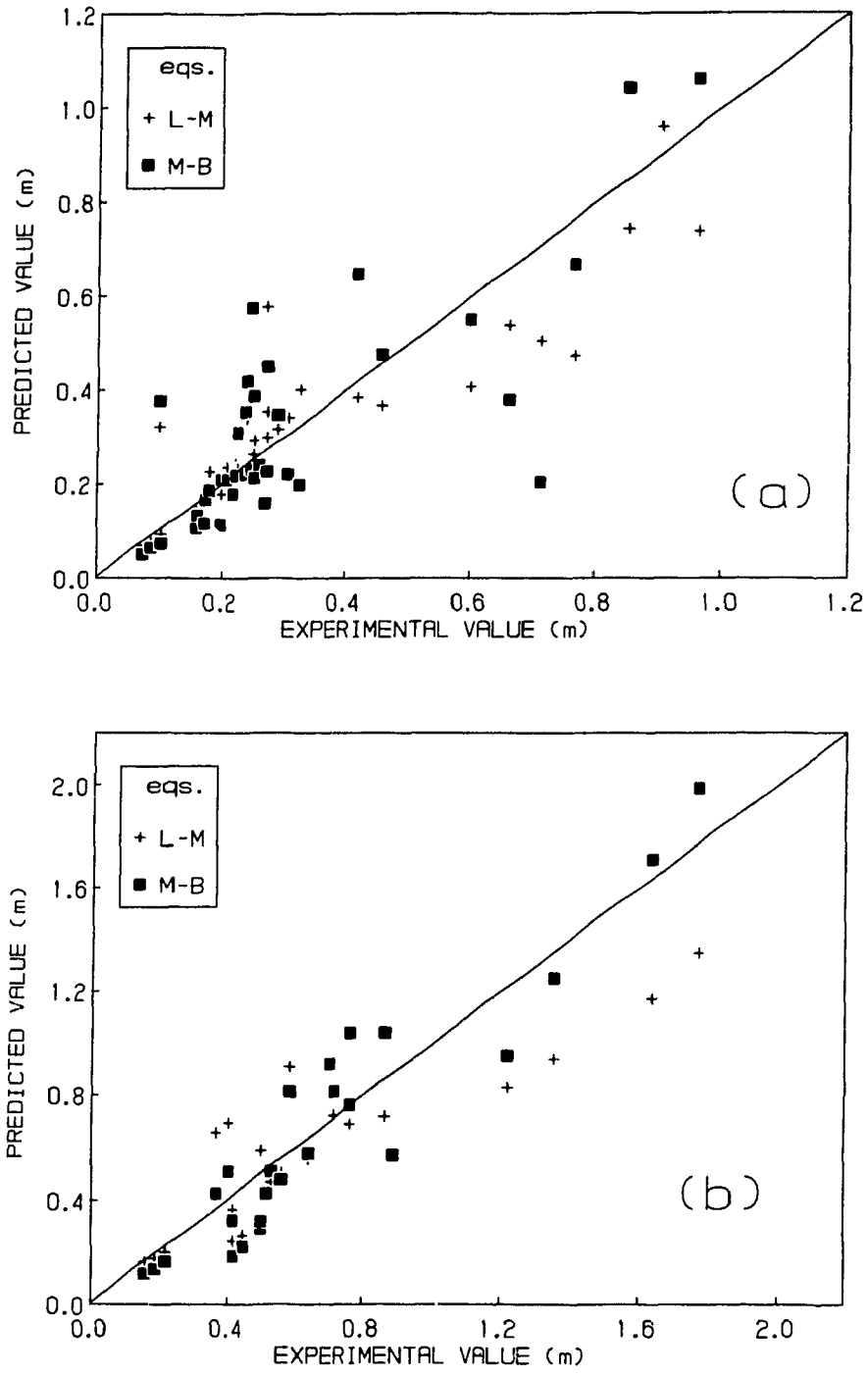

FIGURE A.1 - Maximum Spoutable Bed Heights for CSBs of Coarse Particles. (a) spherical particles: L-M = eq. (A.1), M-B = eq. (A.5); (b) non-spherical particles: L-M = eq.(A.2), M-B = eq.(A.5).

TABLE A.1

ANALYSIS OF DATA PRESENTED IN FIGURE A.1

PARTICLE	EQUATION	STANDARD DEVIATION (m)	AVERAGE DEVIATION (%)	NOTE
spherical (fig. A1a)	eq. (A.1)	0.112	25	fluid: air and water
	eq. (A.5)	0.161	36	exp. points = 38(*)
non-spherical (fig. A1b)	eq. (A.2)	0.252	35	fluid: air, A>0.014
	eq. (A.5)	0.191	24	exp. points = 25(**)
	eq. (A.2)	0.238	35	0.014 < A < 0.02
	eq. (A.5)	0.191	27	exp. points = 8
	eq. (A.2)	0.195	12	A > 0.05
	eq. (A.5)	0.206	22	exp. points = 7
(***)	eq. (A.5)	0.136	37	A<0.014 -9 points

(*) - see Littman et al. (1979).
(**) - see Morgan and Littman (1982).
(***) - data not presented in Fig. A.1.

$k'' = c' (D_i/d_p)^2 (D_i/D_c)^{(4/3)}$, for McNab and Bridgwater; and

$k'' = 0.218/A + 5.13 \times 10^{-3}/A^2 + 2.54 \times 10^{-5}/A^3$, for Littman et al.

with $c' = 0.555 (V_{ms} D_c^2/V_T D_i^2)_{h=1}$. Following Littman et al.'s assumptions c' must be a constant value. Comparing the two coefficients, it can be seen that McNab and Bridgwater's coefficient varies with D_c $(1/D_c^{1.333})$;

while Littman et al.'s coefficient is constant with D_c. On the other hand, for Littman et al., k" is a function of the particle sphericity, for McNab and Bridgwater, k" is constant with this parameter. Increasing the particle diameter, the two coefficient decreases. McNab and Bridgwater's coefficient is proportional to $1/d_p^2$. Littman et al.'s coefficient is not an explicit function of d_p, but a function of V_T V_{mf}; however for large particles their coefficient becomes proportional to $1/d_p$.

From Table A.1 and based on the above analysis, it can be concluded that for high values of A, k" is not a function of D_c. However, for low A close to the transition from fine to coarse particles, k" should be a function of column dimension.

A.3 Correlations for Solids Circulation Rate in Spouted Beds

A.3.1 Day's (1986) Simplified Equation for CSBs of Coarse Particles:

$$M_p(H) = (\pi/4)\, d_s^2 \rho_s \{(1-\epsilon_s(H))(\rho_s - \rho_f)(gH/\rho_s)(\epsilon_s(H) - \epsilon_{mf})\, C_o\}^{1/2} \qquad (A.7)$$

with:

$$C_o = \Delta P_{ms} / \Delta P_{mf} + M_o$$

$$M_o = \rho_f \{(D_c/d_{sms})^4 V_{ms}^2 - \epsilon_{mf}[v_s^2(H)]_{ms}\}/\{(1-\epsilon_{mf})(\rho_s - \rho_f)gH\}$$

$$[v_s(H)]_{ms} = \{A_c V_{ms} - A_a V_{ae}(H)\}/\{(\pi/4)\, d_s^2 \epsilon_{mf}\}$$

$$V_{ae}(H) = V_{mf}\,(1 - (1 - h)^3)$$

$$\epsilon_s(H) = \{(H_f/H) + 0.937\, \epsilon_{mf} C_o\}/\{(H_f/H) + 0.937\, C_o\}$$

A.3.2 Chatterjee's (1970) empirical correlation for CSBs:

$$M_p = 870\ (V_s/V_{ms})\ \rho_s^{-0.17} d_p^{0.27} \qquad (A.8)$$

A.4 Correlation for The Minimum Fluidization Velocity

The Ergun equation (1952):

$$\Delta P/H = 150\ f_1 V + 1.75\ f_2 V^2 \qquad (A.9),$$

where:

$$f_1 = \mu_f (1 - \epsilon)^2 / (d_p \phi)^2 \epsilon^3$$

$$f_2 = \rho_f (1 - \epsilon) / d_p \phi \epsilon^3 .$$

APPENDIX B

ELECTROSTATIC EFFECTS ON A TWO DIMENSIONAL FLUIDIZED BED

B.1 Introduction

Based on the review of Lowell and Rose-Innes (1980) on contact electrification, some important observations which are useful to elucidate the experimental data presented here are presented in Table B.1.

Ciborowski and Wlodarski (1962) have pointed out that the static charges generated in fluidized beds are due to the slip (or rubbing) of particles on particles or on vessel walls. Boland and Geldart (1971) analyzed the electrostatic effect in a 2D packed-fluidized bed of glass beads by the amount of static charge accumulated inside the bed. They found that the resistivity in a perspex-walled bed of glass beads (d_p= 0.7 mm to 0.8 mm) was reduced dramatically as the RH changed from 50% to 70%. For RH greater than or equal to 50%, the dissipation of the charges was rapid and the electrostatic effect was minimal. For low RH, the charges accumulated (on vessel-wall and particle surfaces) in such a way that they affected the dynamics of the packed-fluidized bed. The reduction of bed resistivity was related to the presence of surface layers of water on the particle and on the wall surfaces (see Table B.1).

The critical range of RH depends on the vessel and the particle materials; Table 4.8 and Figure 4.6 indicate that a significant change of the bed resistivity must occur for 30% < RH < 60%. Assuming slip-friction as the mechanism of charge transfer between plexiglas wall and the particles, the amount of charge transferred depends primarily on the

TABLE B.1

BRIEF REMARKS ABOUT ELECTROSTATIC CHARGES

(Based on Lowell and Rose-Innes' work, 1980)

---

(1) Charge transfer between two materials: depends on

(i) the properties of both materials (electrical conductivity and surface characteristics)

(ii) the type and duration of the contact.

(2) Charge build-up between two insulators:

(i) charges can build up by repeated contacts. Usually the rate of increase of charge decreases as contacts are repeated. After many contacts, the charges may saturate.

(ii) identical insulators charge only by rubbing.

(3) Effect of air relative humidity on charge transfer:

(i) superficial water layer adsorbed by same insulators can change the superficial conductivity of such materials.

(ii) the ionization of the surrounding atmosphere can cause partial neutralization of the charge on the insulator surface.

(4) Electrostatic forces resulting from charge transfer:

(i) electrostatic forces are weak for insulators; however they can become important when previously charged materials are brought together or when an extensive area is involved at contact.

(ii) if adhesion between surfaces is dictated by static electrification, it will influence the coefficient of friction between the two materials in contact.

---

contact area and particle surface characteristics.

B.2 Electrostatic Effects in a Two Dimensional Packed Bed

The wall-particle electrostatic force depends on the wall-particle contact area; it must be noted that the relation between the available vessel-wall superficial area to the bed volume is higher in a 2D column than it is in a cylindrical column. As a consequence, this type of force can become very important in a two dimensional geometry at low air relative humidities.

The effect of particle surface characteristics on the particle-wall electrostatic force can be examined qualitatively using the results in Tables 4.1, 4.2 and 4.3. Linseed is an oil seed with low capacity for water adsorption compared with millet and wheat. This implies that static charges should accumulate on the linseed surface more readily than on other particles. Moreover, linseed is a flat particle with a very smooth surface, while millet is a quasi-spherical particle with asperities on its surface. The available contact area for linseed is higher than that for millet. The amount of charge transferred between the plexiglas wall and linseed particles should be higher than for the plexiglas wall and millet particles. Wheat has a rough surface. However, it has a larger diameter. Rough surface area and high particle diameter act in opposite ways in regard to static charge transfer, and a comparison between wheat and millet or wheat and linseed becomes difficult. Based on Fig.4.6, it seems that the electrostatic effect in 2D beds of wheat is lower than that in 2D beds of linseed and millet.

In addition to particle-wall attraction, Ciborowski and Wlodarski

(1962) have shown that the attraction between particles can also become important in fluidized beds at low air relative humidity. They observed that agglomerates of particles were ejected by bubbles above the surface of the bed. From Table B.1, it is seen that static charges can be built up by repeated contacts of bodies. As a result, intensive mixing of the particles promoted by bubbles induces charges on the particle surfaces due to the making and breaking of particle contacts (Ciborowski and Wlodarski, 1962).

Since, in the experiments carried out here, bed preparation involves preliminary fluidization of the bed, it is necessary to verify the effect of charge build-up on the pressure drop characteristics. The following experiments were carried out to evaluate this effect:

(i) Experiments #1 and #2 consisted of consecutive fluidization of the same packed bed. Data #1 and #2 obtained from these experiments were used to check for a possible increase in charges with the renewal of particle and particle-wall contacts. The static bed height was equal to 0.17 m. These data are presented in Figures B.1 and B.2 for further analysis;

(ii) Experiment #3 consisted of fluidization of similar packed beds with different initial bed configurations. In this experiment the packed bed was prepared by spouting the particles before fluidization. The static bed height and the mean bed porosity were in the same range as in (i). Data #3, in Figs. B.1 and B.2, represent this experiment. These data were used to check if the previous history of the bed could influence the pressure drop characteristic curves in 2D-packed beds at low RH;

(iii) Experiment #4 consisted of changing the mean bed porosity. For

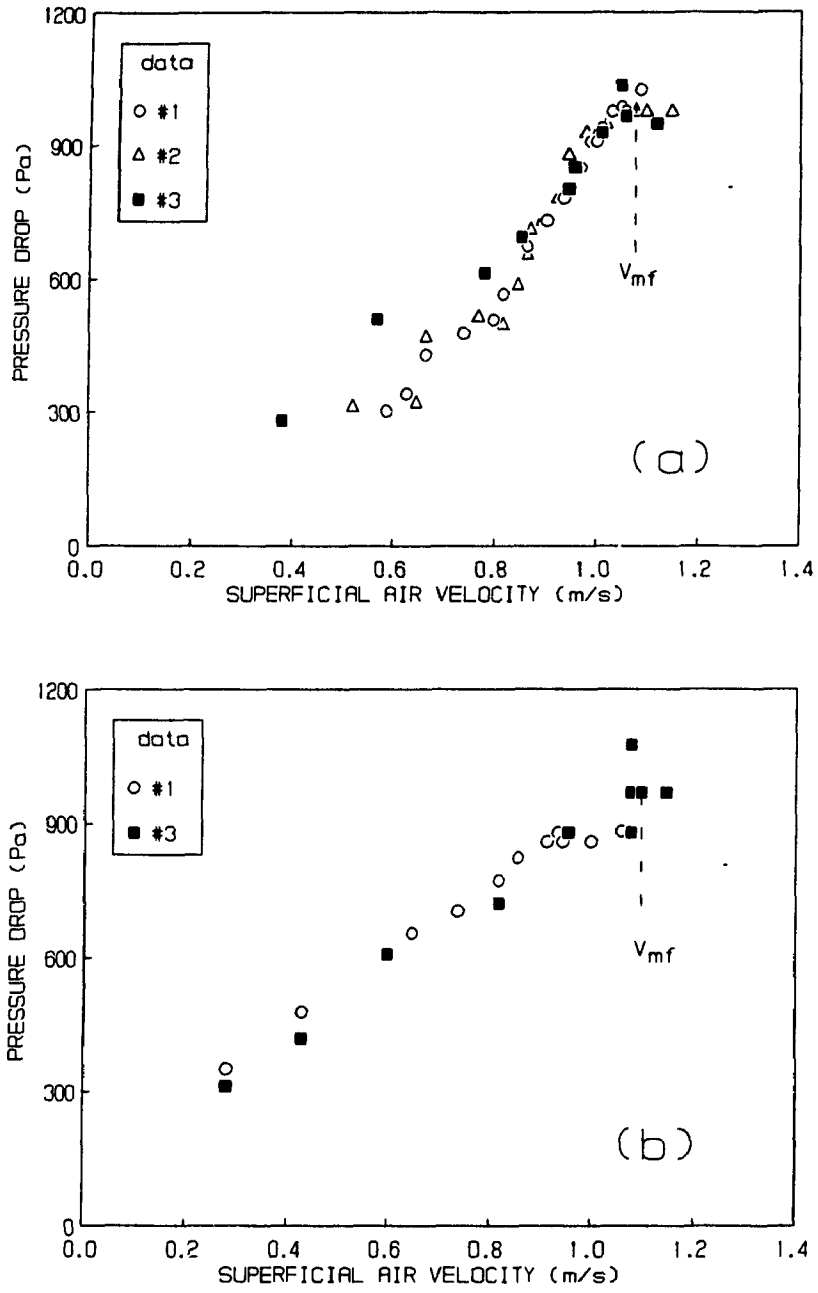

FIGURE B.1 - Effect of Static Charges on Pressure Drop Characteristic Curves for Packed Beds of: (a) Linseed; (b) Sesame seed. Data #1 and #2 represent consecutive experiments at the same initial conditions. Data #3 represent experiments in which the initial bed configuration has been changed. SD for linseed: = 3.4% (D#1 + D#2); = 18.6% (D#1 + D#2 + D#3). SD for sesame seed = 6.3% (D#1 + D#3).

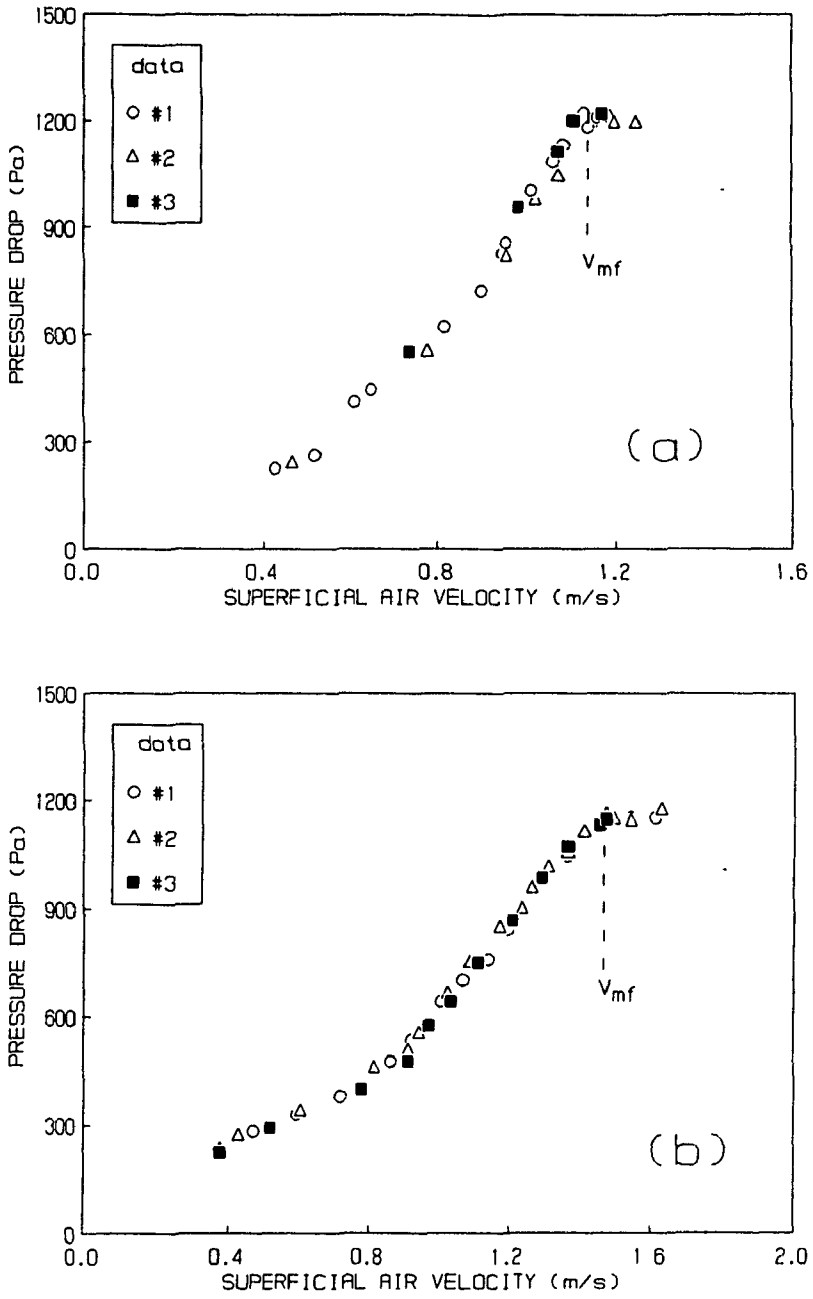

FIGURE B.2 - Effect of Static Charges on Pressure Drop Characteristic Curves for Packed Beds of: (a) Millet; (b) Wheat.
Data #1 and #2 represent consecutive experiments at the same initial conditions. Data #3 represent experiments in in which the initial bed configuration has been changed. SD for millet = 4.4% (D#1 + D#2 + D#3). SD for wheat = 3.4% (D#1 + D#2 + D#3).

millet, the static bed height was decreased from 0.17 m to 0.15 m. For wheat, the packed bed was compressed. The experimental results of this step are presented in Figure B.3.

Data obtained for sesame seed are also included in Fig. B.1 for comparison with the linseed data. Both particles belong to the same sub-group D_1 of particles (see Fig. 4.1). Sesame seed is a rough particle with more capacity for water absorption than linseed (see Table 4.3).

From Figs. B.1 and B.2, a comparison between data #1 and #2 shows that the pressure drop curves do not change in consecutive experiments. A probable explanation for this result is that the amount of static charge generated inside the bed reached its saturation level during the process of bed preparation (Table B.1).

For data #3, different types of particle contacts are achieved during the spouting bed preparation. In the spout and fountain regions, particles collide with each others. In the annulus region, particles slip against each other and against the vessel-wall. In the dead region, particles are pressed forming a dense packing. The packed bed prepared in this way can possibly retain memory of these differences through the different degrees of charging accumulated in each region. However, a comparison between data #1 and data #3 shows that only for linseed is the pressure drop curve affected significantly by the previous history of the bed. For millet and wheat, the pressure drop characteristic curves do not change significantly with different procedures of bed preparation.

For beds of linseed, different degrees of charge remain in memory for a short period (i. e. low flow rate). As the air flow rate is increased, the air-particle interaction force becomes large enough to

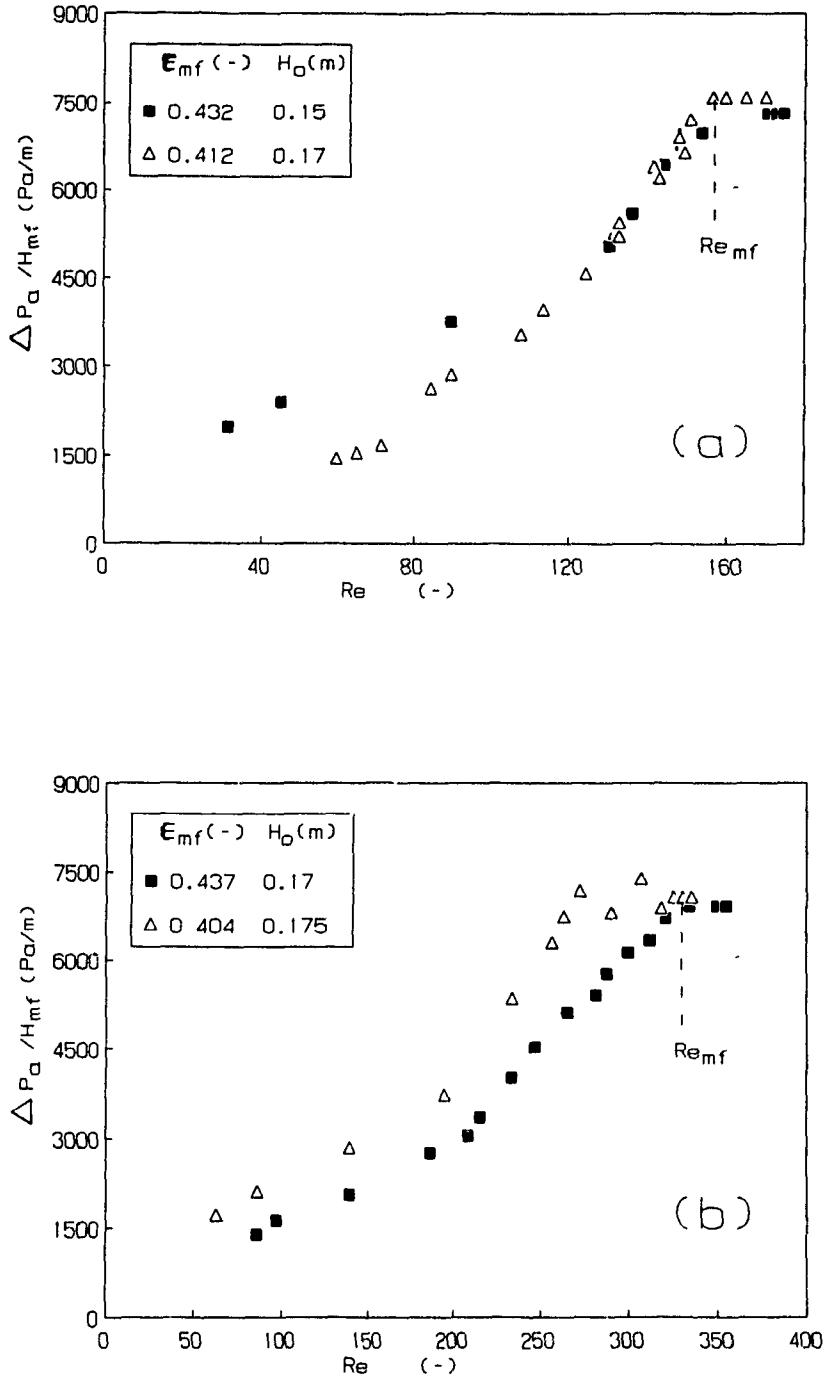

FIGURE B.3 - Effect of Static Charges on Pressure Drop Characteristic Curves at Different Bed Porosity for 2D-Packed Bed of: (a) Millet and (b) Wheat.

promote a new particle arrangement. (It was noted that at V = 0.96 m/s, the surface of the bed changed. This means that the particles are rearranged). Data #3 coincide with data #1 at high air flow rates (V > 0.86 m/s), as shown in Fig. B.1a.

The effects of bed porosity variation on the pressure drop curve for 2D beds of millet with low RH are shown in Fig. B.3a. Data #1 coincide with data #4 at high Re number. Such a behavior is similar to that described above for 2D beds of linseed. Based on interparticle contacts, an increase of bed porosity results in a decrease of electrostatic forces between particles. For high value of bed porosity (data #4 in Fig. B.3a), the solid skeleton can be compacted until the static attraction and repulsion between particles become significant. Beyond this point, any compression of the solid skeleton due to the increase of the air flow rate results in particle dislocation. Particle and pores are rearranged in a new configuration similar to the one obtained at low value of bed porosity. This explains why the same value of pressure drop/ bed height were obtained for data #1 and #4 at high Re.

Graham and Harvey (1965), and Boland and Geldart (1972) have noted that the degree of charging increases with mean particle size. A packed bed of large particles charges more readily than one of the same but smaller particles. This is attributed to the greater interparticle contact and lower bed porosity experienced as the particle size is increased. Although the effect of particle size is to increase the degree of charging in packed-fluidized beds, it seems improbable that the static forces generated are strong enough to agglomerate large particles, such as wheat, even at low bed porosity. It seems reasonable to suppose that

the electrostatic effect on 2D packed-fluidized beds of large particles (the true Geldart group D) is less significant regarding static forces between particles. As a result, the change in packed bed porosity for wheat should result in two different pressure drop characteristic curves, as shown in Fig. B.3b.

B.3 Conclusions

The following conclusions can be drawn concerning electrostatic effects on the dynamics of 2D-fluidized beds:

(1) Good data replication for 2D beds fluidized by air of low humidity is obtained by using the standard procedure of bed preparation;

(2) Static charge accumulation on the particle surface and on the vessel-wall surface is significant for 2D beds of particles fluidized by air of low relative humidity. For 2D beds of particles fluidized by air of high relative humidity, the static charges are dissipated rapidly, and the amount of charge accumulated inside the bed is too small to affect particle-air-wall interactions;

(3) The electrostatic forces developed in 2D beds of particles fluidized by air of low relative humidity are: adhesion between particles and vessel wall and attraction-repulsion between particles. These forces depend on the contact area between particle-particle and particle-wall, as well as the particle and wall surface characteristics.

(4) The particle-wall adhesion force prevents: (a) high values of porosity gradient at the vessel-wall boundary (observed in a 2D packed bed with RH= 60%); (b) individual particles slip on the lateral vessel wall boundary.

(5) The electrostatic attraction between particles causes particle agglomeration; the electrostatic repulsion between particles prevents compaction of the solid skeleton;

(6) For the particles analyzed here, linseed presents the strongest electrostatic interactions due to its surface properties. For a 2D-packed bed of linseed at RH = 30%, the pressure drop characteristic curves depend on the previous history of the bed;

(7) For particles belonging to the true Geldart's group D, such as wheat, the electrostatic forces between particles (attraction-repulsion) are negligible regarding the dynamics of the 2D packed bed.

ADDITIONAL REFERENCES

Boland. D and D. Geldart, "Electrostatic Charging in Gas Fluidised Beds". Proceedings of Int. Powder Technol. & Bulk Granular Solids Conf., Goldberg, A. S., Ed., Dorchester Harrogate, 1971, 243-249.

Ciborowski, J. and A. Wlodarski, "On Electrostatic Effects in Fluidized Beds". *Chem. Eng. Science* 17 (1962): 23-32.

Graham, W. and E. A. Harvey, "The Electrical Resistance of Fluidized Beds of Coke and Graphite". *Can. J. Chem. Eng.* 43 (1965): 146-149.

Lowell J. and A. C. Rose-Innes, "Contact Electrification". *Advances in Physics* 29 (1980): 947-1023.

APPENDIX C

A NEW DERIVATION OF ROWE'S DILATANCY EQUATIONS FOR FLOW IN A CONTINUOUS POROUS MEDIUM

C.1 Introduction

The basic objectives of this appendix are:

(a) to derive Rowe's dilatancy equations for a continuous porous material where a fluid flows through it;

(b) to understand the physical meaning of the dimensionless parameter D, through the continuum approach used in this work.

This theoretical study is deemed necessary because Rowe's model is used to describe the flow characteristics in a 2DSB of coarse particles.

C.2 Brief Review about Rowe's Dilatancy Model

Rowe (1971) summarized his earlier works (1962, 1964), presenting a complete model for solid flow in "quasi-static" porous material. His model describes the dilatancy observed experimentally in a dense porous material compressed axially at low stress levels until failure occurs.

The experimental results obtained during the axial compression of a dense and a loose porous material sample are shown schematically in Figure C.1. Such results are typical of the triaxial compression drained standard tests used in soil mechanics to determine the failure angle of the porous medium. In these tests, a cylindrical specimen of a given porous material contained by a rubber membrane is first subjected to a given cell pressure (hydrostatic stress). The cell pressure is then kept constant and the axial stress alone is altered by applying an end load to

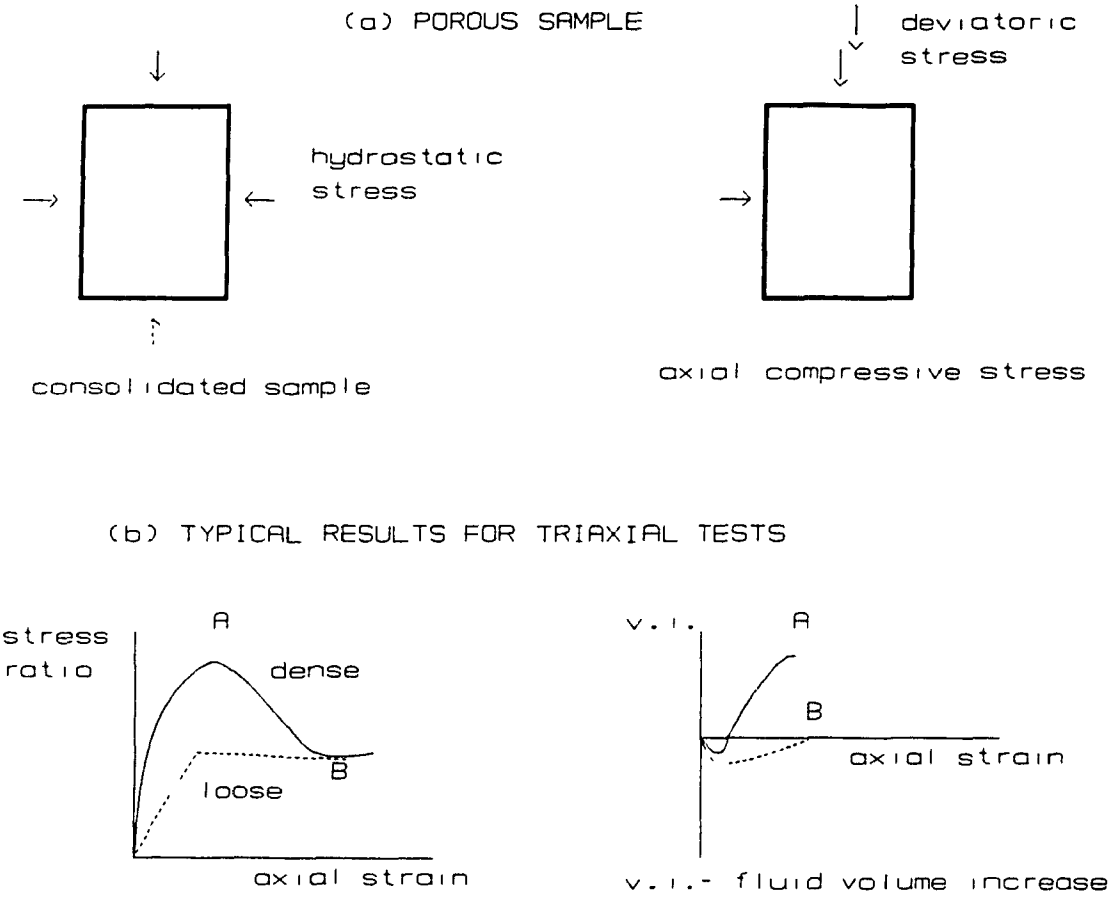

FIGURE C.1 - Schematic Representation of the Triaxial Compression Drained Test used in Soil Mechanics.
(a) Porous material sample. (b) Typical results for triaxial tests on dense and loose materials.
(Stress ratio = major / minor principal stresses).

the cylinder (Horne, 1965).

The measured variables during these tests are: the axial strain, the volume of fluid drained from the sample and the axial load (= major principal stress). The volume of fluid drained from the sample provides a measure of the volume change of the specimen. The stress ratio in Fig. C.1 is defined as the ratio between the major effective solid stress and the minor effective solid stress. The minor effective solid stress is equal to the intermediate effective solid stress (= cell pressure). The volume increase of the sample (v. i.) is the ratio between the volume change and the initial volume of the sample.

The stress ratio vs. the axial strain curve for a dense porous material rises to a maximum, decreasing for further increases in the axial load until the critical state is reached as shown in Fig. C.1. The stress ratio vs. the axial strain curve for a loose porous material does not an overshot; the stress increases until the critical state is reached. The non linear shape of these curves indicates a non-elastic stress-strain relationship. Points A and B in Fig. C.1 represent respectively the failure point and the critical state.

The volume increase for a loose porous sample is always negative while it becomes positive before failure for a dense porous sample. This indicates that a dense porous sample dilates when compressed at a low stress level.

Rowe (1964, 1971) assumed that a dense porous material can present different degrees of anisotropy as it is compressed axially, i. e., the relative geometry of pores changes continuously during the stress path until the critical state is reached. Slip or plastic deformations occur

in specific regions of the porous sample. In these zones, groups of particles slide against each other over a short distance and then rearrange into new groups with different contact points. Assuming a "quasi-static" condition in the porous sample and a minimum energy ratio (energy supplied to the sample / work done by the sample), Rowe obtained the failure angle (Θ_f) for dense and for loose porous media samples.

Although individual particles (or groups of particles) slip against each other following the slip plane ($45° + \Theta_f/2$ from the principal major plane), the mean direction of particle motion is affected by the rearrangement of the pore structure. As a result, the mean particle slip direction is given by the angle α as shown in Fig. C.2. This angle depends on the particle slip contacts along the principal planes of stress (see Rowe, 1971). These slip contacts change as the principal effective solid stress increases during the triaxial compressive test. From Fig. C.2, it can be seen that:

(a) for $\alpha < 45° + \Theta_f/2$, the porous material contracts;

(b) for $\alpha = 45° + \Theta_f/2$, there is no volumetric slip deformation of the porous sample;

(c) for $\alpha > 45° + \Theta_f/2$, the porous material dilates.

A dense porous sample contracts at the beginning of the compressive

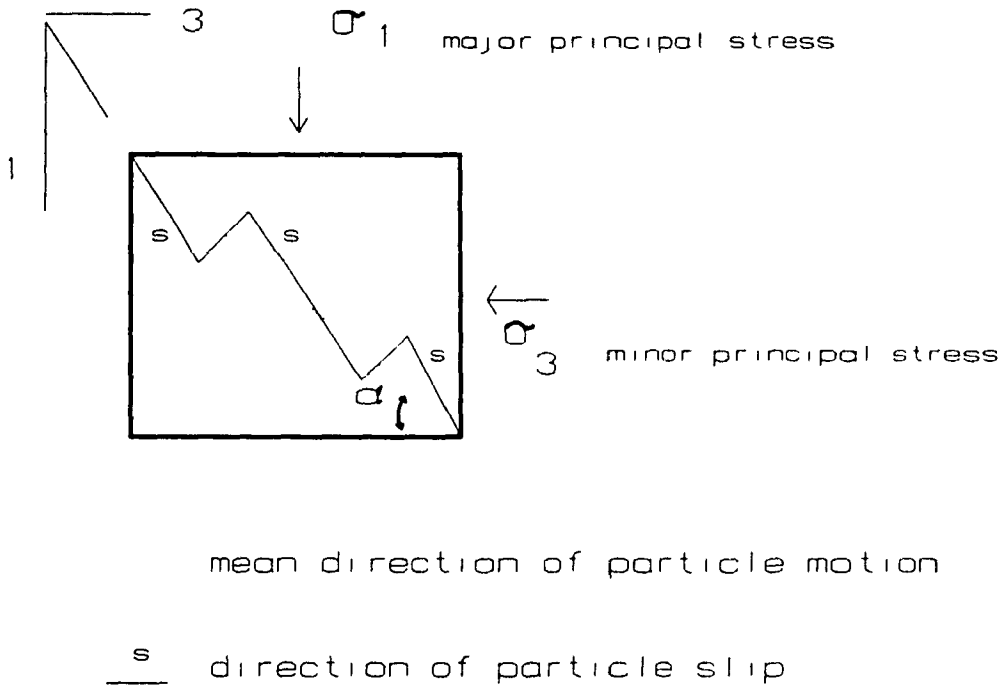

FIGURE C.2 - Schematic Representation of Rowe's Model.

triaxial test (v. i. is negative), as can be seen in Fig. C.1. Condition (a) represents the degree of anisotropy of this sample at the beginning of the test. As the axial stress increases, v. i. reaches a minimum value; and condition (b) describes the mean direction of particle slip. With further increase of the axial stress, v. i. becomes positive indicating the dilatancy of the sample. Condition (c) represents the mean direction of particle motion until failure occurs. This shows how the pores and particles are rearranged during a given stress path towards the critical state.

Rowe (1971) showed that the dimensionless parameter D, defined by eq. (5.23), is a function of the angle α as follows:

$$D = \tan\alpha \tan(45^\circ - \Theta_f/2) \qquad (5.25).$$

The parameter D is calculated experimentally from the v.i. vs. axial strain curves obtained during the triaxial drained tests as follows:

$$D = 1 - [d(v.i)/d(e_{1|s})]/(1 + v.i.) \qquad (C.1),$$

where:

$e_{1|s}$ is the axial strain taken as negative for compression;

$d(v.i)/d(e_{1|s}) = [d(v.i)/dt]/[\dot{e}_{1|s}]$ is the slope of the v. i. vs. axial strain curves between two infinitesimal increments of the axial strain;

$[d(v.i)/dt]/(1 + v.i) = \dot{e}_{mm|s}$ is the volumetric slip strain rate of the porous sample (negative for compression).

It can be seen from eq. (C.1) that D varies with the stress ratio. The maximum value of D for a given stress path is reached at failure (point A in Fig. C.1), and it depends on the initial condition of the

porous sample. Rowe (1964) has shown that the parameter D varies between 1 and 2 for a dense porous material. The maximum value for D, found experimentally, is 2.

Horne (1965) analyzed the slip deformation mechanism proposed by Rowe (1962, 1964) for different packing arrangements of the porous material. Horne's analysis supplies some fundamental bases for Rowe's dilatancy model. Moreover, Horne showed theoretically that D = 2 is the maximum value possible for this parameter.

C.3 Continuous Porous Medium Approach

The continuous porous medium approach was used in the present work. What follows are the theoretical considerations to adapt Rowe's dilatancy equations to a continuous porous material.

The mass and energy balance equations presented in Chap. 5 (Table 5.1) are used to derive Rowe's dilatancy equations for a continuous porous medium when fluid flow through it. The relative motion of the fluid and the solids as well as the fluid-particle interaction forces are taken into account in this derivation.

C.3.1 Effect of Fluid-Particle-Wall Interaction Forces on Deformations of a Porous Material

As discussed in Chap. 5, a porous medium can be seen as a mixture of two media: a porous fluid material and a porous solid material. Note that a porous solid material is supposed to be a homogeneous material composed of the dry solid matrix and pores (= empty spaces occupied by the fluid). The porous fluid material is formed by solid pores (= empty space occupied by the solid matrix) and fluid flowing around these solid pores.

The fluid pores can be understood as a number of passages with a characteristic angle in respect to the mean flow direction.

At low Reynolds numbers (in the range of Darcy flow), the viscous fluid-particle interacting force is predominant. The pressure gradient is proportional to the fluid velocity. The viscous interacting force tends to deform elastically the pore-particle structure (Mutsers and Rietema, 1977; Katsube and Carroll, 1987).

At high Reynolds numbers (in the range of non-Darcy flow), the fluid inertia interacting force is predominant. The pressure gradient becomes proportional to the square of the fluid velocity. Variations in the bed porosity can affect significantly the fluid pressure distribution inside the porous material. This phenomenon can be compared to the incompressible fluid flow through small orifices in turbulent flow regime (Bridgwater, 1984). The passages (or channels) for fluid flow enlarge in regions where the porosity is high. This results in a reduction of the interstitial fluid velocity and in an increase of the fluid pressure. On the other hand, the passages for fluid flow are reduced in regions where the porosity is low. This results in an increase of the interstitial fluid velocity and in a reduction of the fluid pressure.

Variations in pore fluid pressure leads to stress concentrations on the dry solid matrix. Pores and particles rearrange into new configurations redistributing these internal forces.

It is important to point out that gradients of porosity are generated inside a porous medium due to the effect of wall boundaries. The wall boundaries may be vessel walls or spout-annulus interface walls.

C.3.2 Energy Balance for a Porous Solid Material

The following assumptions can be made based on the previous analysis for the energy balance in an element of a porous material contained within fixed wall boundaries with fluid flow through it:

(a) There is a gradient of porosity in the porous element due to the effect of the fixed wall boundaries on particle packing;

(b) Variations on the fluid pressure occur inside the porous element at high Reynolds number (non-Darcy flow) due to the passage of fluid through regions of low and high porosity;

(c) Pores and particles rearrange into a new structure reacting to the forces on the solid porous element caused by fluid pressure variations;

(d) Increasing continuously the fluid velocity (in the range of non-Darcy flow) leads to a continuous rearrangement of the pore-particle structure. This continuous rearrangement of pores and particles occurs in the microstructure of the solid porous element, and it can be treated as infinitesimal strain rates as proposed in Katsube and Carroll's theory (Chap. 5).

(e) Elastic deformations of the porous solid element are neglected as soon as the pores and the particles start to rearrange;

(f) The dynamic part of the fluid stress tensor (see eq. (5.14)) is negligible when compared to the pressure gradient applied to the porous element;

(g) The fluid is incompressible.

It is important to point out that the pressure gradient is imposed on the porous element to cause fluid flow through it. In addition to this pressure gradient are variations in the fluid pressure due to the porosity gradient. These variations are assumed to occur in the

microstructure of the element generating the infinitesimal (plastic) deformations of the porous solid element.

Assumption (d) allows one to define a mean porosity, ϵ , and the fluid pressure, P_f, characteristic of the porous element. The fluid pressure includes static and dynamic pressures. The interacting moment between the porous solid and the porous fluid elements is considered to be zero from assumptions (c) and (d). As a result, the momentum equation for the porous element is given by eqs. (5.17) and (5.18). Eq. (5.16) represents the mass balance for this element.

The mechanical energy balance for the porous element can be written following eq. (5.11) as:

rate of internal energy variation in the porous element	=	rate of work done to the porous solid and porous fluid elements	+ rate of work done to the porous element through interacting force and moment

(C.2).

The first term on the right hand side of eq. (C.2) can be divided into:

(i) the rate of work done to the porous solid element through the stress imposed on the boundaries of this element:

$$\sigma_{ik} \dot{e}^{(1)}_{ki} \ ;$$

where:

σ_{ik} are the components of the stresses applied on the boundaries of the porous element;

$\dot{e}^{(1)}_{ki}$ are the infinitesimal strain rates of the porous solid element;

(ii) the rate of work necessary to push fluid into the pores of the porous solid element :

$$\epsilon \; P_f (\dot{e}^{(1)}_{mm} - \dot{e}^{(2)}_{mm}) ;$$

where:

ϵ is the porosity characteristic of the porous element;

P_f is the fluid pressure as defined earlier;

$\dot{e}^{(1)}_{mm}$ and $\dot{e}^{(2)}_{mm}$ are the volumetric deformation rates of the porous solid element and the porous fluid element respectively.

Considering the element on the plane where the solid shear stresses becomes zero, the rate of work given by (i) can be written as a function of the effective principal solid stresses as follows:

$$\sigma_{ik} \dot{e}^{(1)}_{ki} = \sigma^e_1 \dot{e}^{(1)}_1 + \sigma^e_2 \dot{e}^{(1)}_2 + \sigma^e_3 \dot{e}^{(1)}_3 - P_f \dot{e}^{(1)}_{mm} \qquad \text{(C.3)},$$

where:

the superscript e indicates the effective solid stress;

the subscripts 1, 2 and 3 indicate respectively the directions of the major, intermediate and minor principal effective stresses.

From eq. (5.16), the rate of work (ii) necessary to push fluid into the pores can be written as a function of the rate of fluid expelled from the solid porous element as:

$$\epsilon \; P_f (\dot{e}^{(1)}_{mm} - \dot{e}^{(2)}_{mm}) = P_f \{dm/dt \;|_u + \Delta \; m \; \dot{e}^{(1)}_{mm} - \rho_f \, \mathrm{grad}\epsilon \,.(u - v)\} / \rho_f \qquad \text{(C.4)};$$

where:

u and v are the solid and fluid velocities;

$dm/dt_{|u}$ is the rate of mass of fluid increase in the porous solid element per unit of volume of the porous solid element.

Note that eq. (C.4) defines an additional rate of work term due to the deformation of the porous solid element.

The rate of work done through the interacting force (second term in the right hand side of eq. (C.2)) is obtained from eq. (5.18) as:

$$f(u - v) = P_f (\mathbf{grad}\, \epsilon).(u - v) + \epsilon (\mathbf{grad}\, P_f).(u - v) \qquad (C.5).$$

Combining eqs. (C.3), (C.4) and (C.5), the mechanical energy balance for the porous material element is obtained as follows:

$$\sigma^e_1 \dot{e}^{(1)}_1 + \sigma^e_2 \dot{e}^{(1)}_2 + \sigma^e_3 \dot{e}^{(1)}_3 - \dot{e}^{(1)}_{mm} P_f (1 - \Delta m/\rho_f) +$$

$$P_f (dm/dt_{|u}/\rho_f) + \epsilon (\mathbf{grad}\, P_f).(u - v) = \dot{E} \qquad (C.6),$$

where:

$\dot{E}$ is the rate of internal energy variation for the porous material element.

The rate of work correlated to the porosity gradient vanishes in eq. (C.6) since it represents internal work exchanged between the porous solid and the porous fluid elements.

The last term on the left hand side of eq. (C.6) represents energy dissipation due to the relative fluid flow through the porous element.

For a two dimensional case where the plane strain condition is

assumed to be valid ($\dot{e}^{(1)}_{2|s} = 0$), the porous solid material is compressed in the direction of the major principal stress and it is extended in the direction of the minor principal stress. Considering the slip or plastic deformations of the pore-particle structure, the balance energy equation for the porous solid element filled with fluid can be obtained from eq. (C.6) as:

$$\sigma^{e}_{1}\dot{e}^{(1)}_{1|s} + \sigma^{e}_{3}\dot{e}^{(1)}_{3|s} - \dot{e}^{(1)}_{mm|s} P_f (1 - \Delta m/\rho_f) +$$

$$P_f (dm/dt_{|u}/\rho_f) = \dot{E}_1 \qquad (C.7),$$

where:

$\dot{E}_1$ is the rate of internal energy variation for the porous solid element filled with fluid;

the subscript s represents the slip or plastic strain rates.

Note that eq. (C.7) can also be obtained from the scalar product of u with each term of eq. (5.17). The rate of internal energy variation refers to the porous solid element and the fluid inside the pores.

The third term on the left hand side of eq. (C.7) can be obtained from the definition of Δm and the assumption of incompressible fluid flow as follows:

$$\dot{e}^{(1)}_{mm|s} P_f (1 - \Delta m/\rho_f) = \dot{e}^{(1)}_{mm|s} P_f (1 - d\epsilon/(1-\epsilon)) \qquad (C.8),$$

where ϵ is the mean porosity characteristic of the porous element and $d\epsilon$

is the variation of the porosity during an infinitesimal deformation of the pore-particle structure.

Note that $P_f (1 - \Delta m/\rho_f)$ is the corrected fluid pressure applied on the solid matrix after an infinitesimal deformation. The minor internal effective solid stress (internal reaction against the minor effective solid stress) can then given by:

$$\sigma_3^e = P_f(1 - \Delta m/\rho_f) \qquad (C.9).$$

The internal effective stress defined in eq. (C.9) refers to the internal force (reactive force against the applied force). The second term on the left hand side of eq. (C.7) is the part of the work done by the porous solid element filled with fluid to extend its boundaries, and this term is given by the internal reaction stress as defined in eq. (C.9).

Combining eqs. (C.7) and (C.8), the following equation is obtained:

$$\sigma_1^e /(-\sigma_3^e D) = \dot{E}_1 / (-\sigma_3^e \dot{e}_1^{(1)} + P_f\, dm/dt|_u/\rho_f) - 1 \qquad (C.10),$$

where:

$$D = 1 - [dm/dt|_u/\rho_f]/((1-\Delta m/\rho_f)\,\dot{e}_1^{(1)}).$$

C.3.3 The Dimensionless Parameter D

The parameter D obtained in eq. (C.10) is the same as the parameter

defined by Rowe (eq. (C.1)). The term $[dm/dt|_u/\rho_f]$ is the rate of volume increase of the porous element; it corresponds to d(v.i)/dt in eq.(C.1). For $dm/dt|_u < 0$, a mass of fluid is expelled from the porous solid element, i. e., the volume of the porous solid element decreases for the same initial mass of solid (the porous solid element contracts), and D in eq. (C.9) becomes less than 1. Moreover, additional work (done by the fluid) is required to expel fluid from the pores as shown in eq. (C.7).

For $dm/dt|_u > 0$, a mass of fluid enters the porous solid element, i. e., the volume of the porous solid element increases for the same initial mass of solid (the porous solid element dilates). Additional work is done by the porous solid element to extend its outer boundaries (see eq. (C.7)).

For $dm/dt|_u = 0$ and $\Delta m = 0$ (i.e. no variation of porosity), there is no additional work needed to push fluid into the pores. Such a condition represents a critical state of the porous material. There is no volumetric strain rates during the stress path. This is the case of fluidization of homogeneous beds of particles belonging to Geldart's group B. The fluidization of 2D beds of coarse particles is not homogeneous, dilatation and contraction of the porous solid material occur in different regions inside the packed bed as shown in Chapter 5. This requires an overall mean value of parameter D over the bed height as obtained in Chap. 5; however the slip or plastic deformation mechanism is the same as analyzed here.

Rearranging eq. (C.10) results in:

$$\sigma_1^e \dot{e}^{(1)}_1 / -(\sigma_1^e \dot{e}^{(1)}_1 - E_1) = \sigma_1^e / (-\sigma_3^e D) \qquad \text{(C.11)},$$

where:

$\sigma_1^e \dot{e}^{(1)}_1$ is the rate of energy supplied to the porous solid element;

$-(\sigma_1^e \dot{e}^{(1)}_1 - \dot{E}_1)$ is the rate of work done by the porous solid element.

Comparing eq. (C.11) with Rowe's (1971) energy balance equation, it can be seen that both equations are identical. As mentioned before, Rowe (1971) has shown that there is a minimum and a maximum value for the ratio between the rate of energy supplied to the porous element and the rate of work done by this element to extend its boundaries. The minimum value of this ratio is obtained at D = 1, where the Mohr-Coulomb failure criterion is applied. This represents a loose packing structure with the minimum energy ratio given by:

$$[\sigma_1^e \dot{e}^{(1)}_1 / -(\sigma^e_1 \dot{e}^{(1)}_1 - \dot{E}_1)]_{|min} = \tan^2 (45^\circ + \Theta_c/2) \qquad \text{(C.12)}.$$

The maximum value for the energy ratio defined in eq. (C.11) is given by the inter-particle friction angle (Rowe et al. 1964, 1971 and Horne, 1965). This angle represents the maximum possible value for particle slip. This condition is obtained at dense packings where particles slip against particles, and the energy ratio is given by:

$$[\sigma_1^e \dot{e}^{(1)}_1 / -(\sigma^e_1 \dot{e}^{(1)}_1 - \dot{E}_1)]_{|max} = \tan^2 (45^\circ + \Theta_i/2) \qquad \text{(C.13)}.$$

From eq.(C.12), the stress ratio for the plane strain condition is obtained as follows:

$$\sigma_1^e / (-\sigma_3^e) = D \tan^2(45^\circ + \Theta_c/2) \qquad \text{(C.14).}$$

The minor effective solid stress in eq. (C.14) is the internal extensive reaction of the porous element as defined in eq. (C.9). The negative sign, which comes naturally from the development of this equation, changes the internal reaction into the compressive applied effective solid stress as defined in Rowe's dilatancy equation (eq (5.23)).

A similar analysis as the one presented here can be developed for a three dimensional case where the intermediate principal effective solid stress plays a role in the failure criterion for a porous medium.

C.4 Conclusions

(i) Rowe's dilatancy model is consistent with the continuum approach used in this work and can be applied to describe the slip deformations of a porous material with fluid flow through it. Identical correlations for the stress ratio and for the dimensionless parameter D have been obtained through the mass and energy balance equations for a continuous porous material with fluid flows through it;

(ii) The gradients of porosity are responsible for variations in the fluid pressure in packed beds of coarse particles at high Reynolds numbers (non-Darcy flow). These variations in fluid pressure result in rearrangement of the pore-particle structure towards a stable

equilibrium. Increasing continuously the fluid velocity leads to continuous rearrangement of pores and particles similarly to the slip or plastic deformation mechanism proposed by Rowe (1971) for solids flow in a "quasi-static" porous medium.

(iii) The parameter D defined by Rowe's equations was shown to be related to the rate of the mass of fluid expelled from the porous solid element This a dynamic variable function of the porous material and the particle-wall interactions. The gradients of porosity are generated inside 2D packed beds of coarse particles due to the effect of the vessel wall boundaries on particle packing.

ADDITIONAL REFERENCES

Bridgwater, J. "Fluid Effects in Powder Mechanics." *Powder Technol.* 37 (1984): 245-254.

Horne, M. R., "The Behavior of an Assembly of Rotund, Rigid, Cohesionless Particles: I and II." *Proc. Roy. Soc.* A286 (1965): 62-97.

Rowe, P. W., L. Barden, and I. K. Lee, "Energy Components during Triaxial Cell and Direct Shear Tests." *Geotechique* 14 (1964): 247-261.

Rowe, P. W., "The Stress-Dilatancy Relation for Static Equilibrium of an Assembly of Particles in Contact." *Proc. Roy. Soc.* A269 (1962): 500.

APPENDIX D

THE EFFECTIVE SOLID STRESS ANALYSIS IN A TWO DIMENSIONAL SPOUTED BED

D.1 Introduction

The objectives of this appendix are:

(i) to describe the type of failure occurring in a 2DSB of particles belonging to Group #1 and Group #2;

(ii) to relate the dimensionless parameters Y^* and X^*_{2D} to the effective principal solid stresses.

As pointed out in Chap. 2, McNab and Bridgwater (1974) have analyzed the solid stress distribution in the annular region of a CSB. These authors assumed that the effects of height and radius on the dynamics of a deep CSB can be studied separately. This assumption was based on experimental evidence that the annular pressure drop gradient is almost constant with radius above the conical region. From their analysis, at a specific radial distance from the center of the bed, $r = r_o$, the vertical solid shear stress becomes zero. At this point, the radial normal effective stress is the minor principal stress, while the vertical normal effective stress is the major principal stress. (The angular normal effective stress is equal to the vertical normal effective stress). Below this point, the effective weight of the bed is supported by the vertical shear stress at the spout-annulus interface. Beyond this point, the effective weight of the bed is supported by the vertical shear stress at the vessel wall. The vertical failure of the annular packed bed

occurs between the spout radius and r_o.

McNab and Bridgwater (1974) used the Mohr-Coulomb criterion to describe failure in the annular region. As discussed in Chap. 5, this criterion is only valid at the critical state where the porosity variation is zero. From data presented in this work, it is apparent that the pore structure and the dry solid matrix are rearranged in a new configuration beyond the maximum spouting pressure drop point. Particles slip around the spout cavity and the bed surface is altered before and beyond the onset of spouting as shown in Fig. 6.2. These results demonstrate that plastic deformations characterize the spout formation in a 2DSB.

The analysis developed here is based on McNab and Bridgwater's result that there is a point in the annular region where the solid shear stress vanishes. Rowe's model (1971) is used to define the relationship between the principal effective solid stresses.

D.2 Failure in a Two Dimensional Spouted Bed

The following assumptions are made for the overall momentum in the annulus-spout region:

(i) Slip or plastic deformations occur in the porous material. Such deformations integrated over the bed height are related to the overall effective normal solid stresses following Rowe's model (1971).

(ii) The plane strain failure condition holds for 2D bed geometry. This means that deformations of the porous element in z direction are negliglible compared to those in x (horizontal) and y (vertical) direction;

(iii) The viscous fluid shear stress and the interacting moment between fluid and solid are neglected compared to the effect of the fluid pressure;

(iv) The variation of fluid pressure includes the effect of the static pressure as well as the dynamic pressure. The mean applied pressure gradient is in the y direction;

(v) The effective solid porous material is in equilibrium;

(vi) Porosity gradients generated during the spout formation are responsible by variations in the fluid pressure and in the effective normal solid stresses;

(vii) Different types of failure (active or passive) can occur in the spout-annulus interface.

Moreover, there is a mean location, $x = L_o/2$, in the annulus-spout region of a 2DSB where the solid shear stresses becomes zero. At this point, the vertical and horizontal normal effective stresses are the principal stresses. The location of L_o depends on the spout-annulus interface failure, and the vessel wall effects.

The momentum balance in the vertical direction for the element of the porous material can be derived with reference to the three specific control volumes as shown in Figure D.1. Eq. (5.17) was applied for each control volume. The equations obtained were integrated over the bed height (from 0 to H_{ms}). The final results are:

(a) Control Volume a:

$$-\bar{\sigma}^{s}_{yy|a}/\Delta P_{mf} = \bar{\gamma}^{*}_{a} + 2((\bar{\tau}^{w} - \bar{\tau}^{s})/\Delta P_{mf})\, H_{ms} / (L_1 - L_s) = 0 \qquad \text{(D.1a)},$$

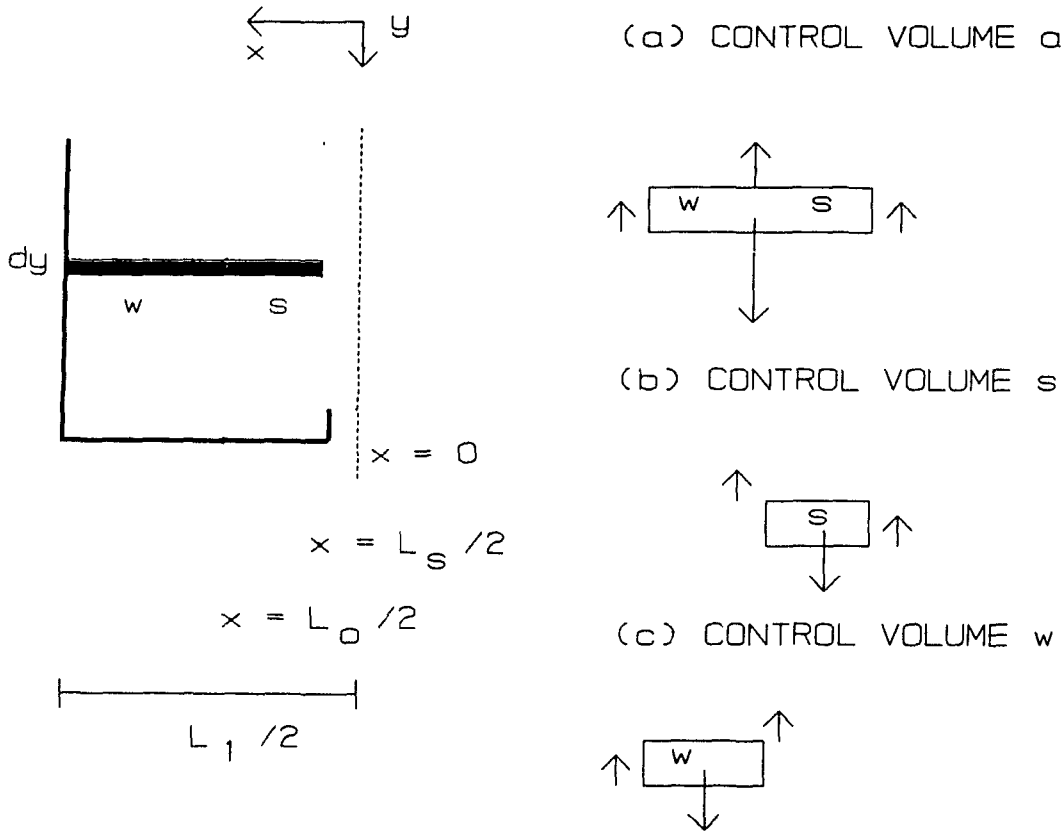

FIGURE D.1 - Schematic Representation of the Control Volumes for the Momentum Balance in the Annular Region of a 2DSB. Case #1: Active Failure.

(b) Control Volume w:

$$-\overline{\sigma}^{e}_{yy|w}/\Delta P_{mf} = \overline{\gamma}^{*}_{w} + 2(\overline{\tau}^{w}/\Delta P_{mf})\, H_{ms} / (L_1 - L_o) \qquad \text{(D.1b)},$$

(c) Control Volume s:

$$-\overline{\sigma}^{e}_{yy|s}/\Delta P_{mf} = \overline{\gamma}^{*}_{s} - 2(\overline{\tau}^{s}/\Delta P_{mf})\, H_{ms} / (L_o - L_s) \qquad \text{(D.1c)},$$

where the bar superscript represents the overall mean value of each variable (over the bed height); the subscripts a, w and s represent the control volumes shown in Fig. D.1;

$\overline{\gamma}^{*}$ is the dimensionless overall effective weight of each control volume region, and is given by $(1-\Delta P_f / \Delta P_{mf})$ with $\overline{\gamma}^{*}_{s} = Y^{*}$;

$\overline{\sigma}^{e}_{yy}$ is the overall variation of the vertical normal effective stress from y = 0 to y = H_{ms}. Note that the compressive normal stress is negative;

$\overline{\tau}^{w}$, $\overline{\tau}^{s}$ are the mean values of the shear stress at the vessel wall boundary and at the spout-annulus interface, respectively;

L_s is the mean value of the spout width;

L_o is the mean horizontal distance in which the solid shear stress vanishes.

From eqs. (D.1a) and (D.1c), the following condition yields active failure:

$$(-\overline{\sigma^{e}_{yy|s}}\ \Delta P_{mf})(L_o - L_s) + (-\overline{\sigma^{e}_{yy|w}} / \Delta P_{mf})(L_1 - L_o) = 0 \qquad \text{(D.2)}.$$

From McNab and Bridgwater's (1974) analysis, the failure in the spout-annulus region is active when $L_s < L_o < L_1$. This type of failure occurs in 2DSBs of Group #1, and in deep CSBs of coarse particles. The solid material moves downwards in the annulus region a until it reaches the spout. The vertical normal effective stress at $x = L_o/2$ is the major principal stress.

Using eqs. (D.2) and (D.1c), the overall major principal stress is determined at $x = L_o$ as:

$$-\overline{\sigma^{e}_{1}} / \Delta P_{mf} = Y^{*} + a_I \qquad \text{(D.3)},$$

where:

$$\overline{-\sigma}^{e}_{1} / \Delta P_{mf} = -\overline{\sigma^{e}_{yy|s}} / \Delta P_{mf} + \overline{\gamma^{*}_{s}}\,(L_1 - L_s)/(L_o - L_s);$$

$$a_I = -2(\overline{\tau^{w}}/\Delta P_{mf})\, H_{ms} / (L_o - L_s).$$

Note that a_I depends on the column dimensions, the particle properties and the particle-wall interactions; it is a function of the part of the bed weight supported by the vessel wall.

Equation (D.3) represents the active failure in the spout-annulus region.

For the passive failure, the spout formation is characterized by the

particle slip down in the apex of the spout cavity towards the annulus region in a 2DSB of Group #2. As shown in Figs. 6.2 and 6.7, the plane of particle slip is inclined at less than 45° from the x horizontal plane (apex of the spout cavity). Passive failure occurs in the annulus-spout interface, and $L_o/2 < L_s/2$ as shown in Figure D.2. This type of the annulus-spout wall failure occurs in 2DSBs of Group #2 due to the inversion of the principal stress direction (Chap. 5). At $x = L_o/2$, the horizontal normal effective stress is the major principal stress.

The control volume a is from $L_o/2$ to $L_1/2$ for the passive failure case. Note that $L_o/2$ should be close to the center of the column. The control volume w is from $L_s/2$ to $L_1/2$; while the control volume s is from $L_o/2$ to $L_s/2$. Following the same procedure described for the active case, the overall momentum balance for each region is given by:

(a) Control Volume w:

$$-\overline{\sigma}^{e}_{yy|w}/\Delta P_{mf} = \overline{\gamma}^{*}_{w} + 2((\overline{\tau}^{w} - \overline{\tau}^{s})/\Delta P_{mf})\, H_{ms} / (L_1 - L_s) = 0 \qquad \text{(D.4a)},$$

(b) Control Volume a:

$$-\overline{\sigma}^{e}_{yy|a}/\Delta P_{mf} = \overline{\gamma}^{*}_{a} + 2(\overline{\tau}^{w} / \Delta P_{mf})\, H_{ms} / (L_1 - L_o) \qquad \text{(D.4b)},$$

(c) Control Volume s:

$$-\overline{\sigma}^{e}_{yy|s}/\Delta P_{mf} = \overline{\gamma}^{*}_{s} + 2(\overline{\tau}^{s} /\Delta P_{mf})\, H_{ms} / (L_s - L_o) \qquad \text{(D.4c)},$$

From (D.4b) and (D.4c), the following condition is obtained:

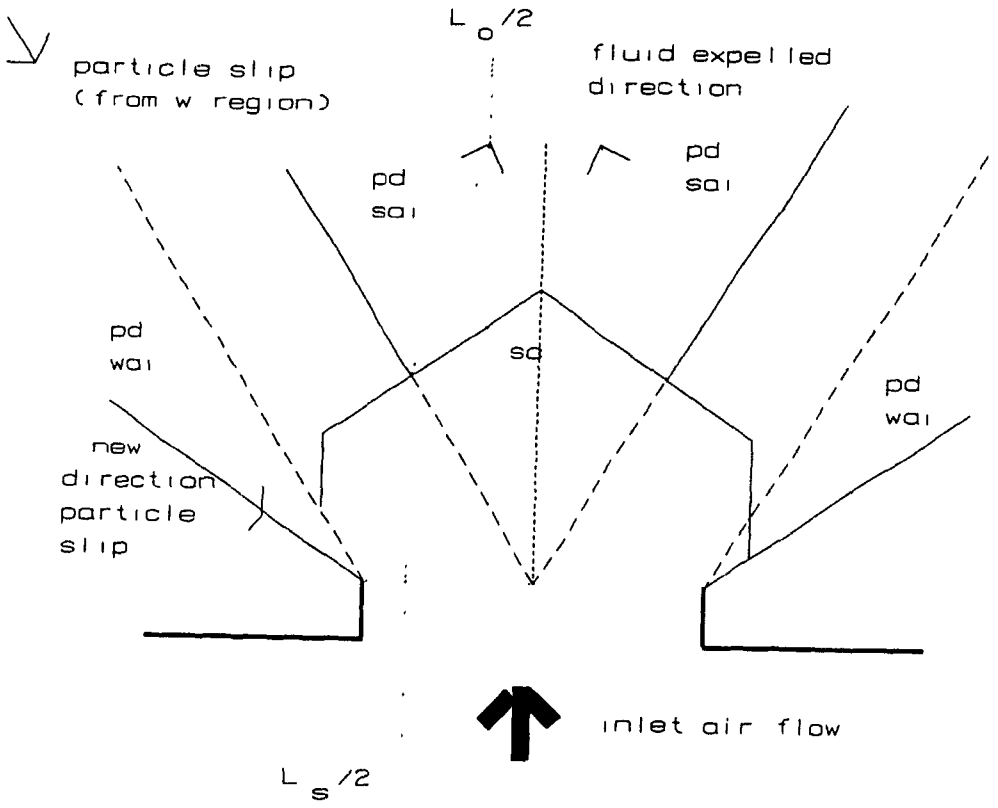

FIGURE D.2 - Plastic Deformations in the Spout-Annulus Interface Wall at the Onset of Spouting. Passive Failure ($D_{|m_s} > 1.0$). pd - plastic deformations; sc - solids circulation; sai - spout-annulus interface; wai - wall-annulus interface

$$(-\overline{\sigma}^{e}_{yy|s}/\ \Delta P_{mf})\ (L_s - L_o) - (-\overline{\sigma}^{e}_{yy|s}\ /\ \Delta P_{mf})\ (L_1 - L_o) = 0 \qquad (D.5).$$

The overall variation of the minor principal stress is obtained from eqs. (D.4c) and (D.5) as:

$$-\overline{\sigma}^{e}_{3}\ /\ \Delta P_{mf} = Y^{*} + a_{II} \qquad (D.6),$$

where:

$$\overline{-\sigma}^{e}_{3}\ /\ \Delta P_{mf} = -\overline{\sigma}^{e}_{yy|s}\ /\ \Delta P_{mf} - \overline{\gamma}^{*}_{w}\ (L_1 - L_s)/(L_s - L_o);$$

$$a_{II} = 2(\overline{\tau^{w}}\ /\ \Delta P_{mf})\ H_{ms}\ /\ (L_s - L_o).$$

Note that a_{II} is a negative quantity which depends on the column dimensions, the particle properties and the particle-wall frictional angle. Its value is related to the part of the bed weight supported by the wall boundaries.

The major principal stress for passive failure and the minor principal stress for active failure should be a function of X^{*}_{2D}. Eq. (5.23) describes the overall flow criterion for 2D packed beds with $\overline{D}$ defined as a mean value of the volumetric slip deformations of the pore-particle structure. The overall value of $\overline{D}$ is given by the slip strain rates in the $\underline{w}$ and $\underline{s}$ regions for a 2DSB. The minimum spouting pressure drop is related to the slip strain rates in the $\underline{s}$ region. The overall value of $\overline{D}$ in the $\underline{s}$ region can be defined as:

(i) Passive failure in $\underline{s}$ region ($x = L_o/2$):

$$D_{|ms} = -\dot{e}_{3s}/\dot{e}_{1s} = -\dot{e}_{yy|s}/\dot{e}_{xx|s} \qquad \text{(D.7a)},$$

(ii) Active failure in $\underline{s}$ region ($x = L_o/2$):

$$D_{|ms} = -\dot{e}_{3s}/\dot{e}_{1s} = -\dot{e}_{xx|s}/\dot{e}_{yy|s} \qquad \text{(D.7b)},$$

Eq. (D.7a) shows that a porous element in the $\underline{s}$ region is extended in the y direction and compressed in the x direction. Eq. (D.7b) shows that a porous element in the $\underline{s}$ region is extended in the x direction and compressed in the y direction. For $D_{|ms} > 1.0$, the porous material expands. In the passive case, pores expand due to the mass of fluid expelled from the $\underline{w}$ region (see Fig. D.2). At the minimum spouting, the spout necks in the upper region of the bed (Fig. 6.7). The shape of the center bed surface is parabolic just before the onset of spouting (Fig. 6.7). This indicates that the $\underline{s}$ region contracts in the x direction and expands in y direction. The slip strain rates are higher in the y direction with particles moving up at the center. The effective normal horizontal solid stress decreases (by $1/D_{|ms}$) due to the increase in the pore fluid pressure gradient in the x direction. Plastic deformations occur in the center upper part of the spout-annulus interface (Figure D.2). In the active case, the solid effective horizontal stress is increased by $D_{|ms}$ due to the contraction of the pores. Fluid is expelled from the $\underline{s}$ region.

Values of $D_{|ms} < 1.0$ are not possible in the passive failure case beyond the maximum pressure ($D_{|ms} < 1.0$ means that the porous material contracts in the $\underline{s}$ region). The porous material tends to dilate until the critical state is reached. $D_{|ms}$ must be > 1.0 for 2DSBs of Group #2 (see

Appendix C).

For a given 2DSB of particles, the slip deformations depend on H_{ms} and L_1 (see eqs. (D.3) and (D.6)). It is assumed that $\bar{D}$ is linearly related to $1/X^*_{2D}$ for passive failure and to X^*_{2D} for active failure. Based on this assumption, the overall variation of the effective horizontal normal stress at $x = L_o/2$ can be written as:

(i) Active failure:

$$\bar{\sigma}^e_3 / \Delta P_{mf} = a_{III} X^*_{2D} \qquad \text{(D.8a)},$$

(ii) Passive failure:

$$\bar{\sigma}^e_1 / \Delta P_{mf} = a_{IV} X^*_{2D} \qquad \text{(D.8b)},$$

where a_{III} and a_{IV} are constants for a given fluid-solid system spouted in a given column. These values do not depend on H_{ms}.

From eqs. (D.8b), (D.6) and (5.23), the relationship between Y^* and X^*_{2D} for Group #2 is given by:

$$\bar{\sigma}^e_1 / \bar{\sigma}^e_3 = a_{IV} X^*_{2D} / (Y^* + a_{II}) = \tan^2(45° + \Theta_f/2)\, D_{|ms} \qquad \text{(D.9a).}$$

From eqs. (D.8a), (D.3) and (5.23), the relationship between Y^* and X^*_{2D} for Group #1 is given by:

$$\bar{\sigma}^e_1 / \bar{\sigma}^e_3 = (Y^* + a_I) / (a_{III} X^*_{2D}) = \tan^2(45° + \Theta_f/2)\, D_{|ms} \qquad \text{(D.9b).}$$

Smith (Rowe, 1971) has shown that eq. (5.23) generates two sets of plastic potential curves for the plane strain given by:

$$g = (\sigma_3^e)^{(1/n)} / \sigma_1^e \qquad \text{for active failure,} \qquad \text{(D.10a),}$$

$$g = (\sigma_1^e)^n / \sigma_3^e \qquad \text{for passive failure,} \qquad \text{(D.10b),}$$

where $n = \tan^2 (45 + \Theta_c/2)$;

g is the plastic potential function defined by:

$$(dg/d\sigma_3^e) = D\ (dg/d\sigma_1^e).$$

Eqs. (D.10a and b) together with eqs. (D.9a and b) define the final form of the relationship between Y^* and X_{2D}^* as:

(i) Group #1 - active failure:

$$Y^* = a_1 + a_2 X_{2D}^{*\,1/n} \qquad \text{(D.11),}$$

(ii) Group #2 - passive failure:

$$Y^* = a_1 + a_2 X_{2D}^{*\,n} \qquad \text{(D.12),}$$

where:

a_1 and a_2 are parameters dependent on the fluid-particle system and the column dimensions; a_1 is related to the fraction of the effective bed weight supported by the vessel wall. The value of a_1 is negative for active failure and positive for passive failure. The parameter a_2 is

related to g and the proportionality parameter between the horizontal effective normal stress and X^*_{2D}. The sum of $a_1 + a_2$ must equal 1 when $Y^* = 1$ and $X^*_{2D} = 1$.

Eqs. (D.11) and (D.12) are used, in Chap. 7, to define the general equation for the minimum spouting pressure drop and the minimum spouting velocity in 2DSBs of Group #1 and Group #2 particles.

D.3 Conclusions

Based on the analysis of failure in a 2DSB of coarse particles, the following conclusions can be drawn:

(1) For a 2DSB systems of Group #1, active failure of the spout-annulus interface characterizes the onset of spouting. For a 2DSB systems belonging to Group #2, passive failure of the spout-annulus interface characterizes the onset of spouting. Note that active failure occurs at the inlet nozzle for systems of Group #2; however, due to the inversion of the principal stress direction passive failure characterizes the spout development.

(2) For a given 2DSB at the minimum spouting, Y^* is related to the overall vertical normal effective stress while X^*_{2D} is related to the overall horizontal effective stress.

(3) Eqs. (D.11) and (D.12) define the relationship between Y^* and X^*_{2D} for 2DSB systems in which plastic deformations occur beyond the maximum spouting pressure drop.

APPENDIX E

PRESSURE DROP CHARACTERISTIC CURVES IN 2D PACKED BEDS OF COARSE PARTICLES

E.1 Regression Curve:

$$\Delta P_s/H_{mf} = c_1 Re + c_2 Re^2 \qquad (E.1).$$

E.2 Experimental Results:

TABLE E.1

EMPIRICAL COEFFICIENTS FOR PRESSURE DROP VERSUS AIR SUPERFICIAL VELOCITY CURVES IN 2D PACKED BEDS

PARTICLE	c_1 (Pa/m)	c_2 (Pa/m)	SD (%)	R^2 (-)	note
wheat	8.378	0.036	5.0	0.98	(see Fig. B.2) *
barley	22.685	0.045	5.4	0.98	(see Fig. 3.4) *
rice	22.668	0.080	4.6	0.99	RH=60%, T_b= 25°C
linseed	43.732	0.153	5.1	0.98	bed not prepared *
		0.653	5.0	0.98	(see Fig. B.1)
millet	39.946		7.2	0.97	loose (see Fig. B.3) *
		0.309	6.0	0.98	dense (see Fig. B.2)

* - RH = 30%, T_b = 19°C ± 1°C

E.3 - Experimental Results for Molecular Sieve:

E.3.1 - Minimum Fluidization Velocity (RH = 30%, T_b = 19°C):

Number of data replication = 4

bed porosity = 0.395 - V_{mf} = 1.33 m/s ; $\Delta P_{mf}/H_{mf}$ = 7404 Pa/m

bed porosity = 0.413 - V_{mf} = 1.50 m/s ; $\Delta P_{mf}/H_{mf}$ = 7184 Pa/m

SD = 0.11 m/s; average deviation = 0.08 m/s

From these above experimental data and from eq. (5.26), the following parameters were determined:

$\lambda = 65.8°$ and $D = a = 0.361$.

Based on eq. (5.30), the value of α was calculated as being 29.1°. This value is lower when compared with those obtained for wheat, millet, barley, linseed and rice (Table 5.2); therefore eq. (5.31) cannot be applied for molecular sieve. Note that molecular sieve is the largest spherical particle used in this work (L_1/d_p = 58.5). The slip deformation mechanism including rearrangements in the pore-particle structure should be more difficult to occur in beds of very large spherical particles than it is in beds of non-spherical particles. As a result, relative rotation between particle and fluid elements may occur in 2D beds of molecular sieve. For a such case, eq. (5.31) is replaced by:

$$2\alpha = 2(90° - \Theta_c) - \lambda - (90° - \Theta_c - \lambda) = (90° - \Theta_c) \qquad \text{(E.2).}$$

Eq. (E.2) was used to estimate the Coulomb failure angle for molecular sieve (Θ_c = 31.8°). However, more data are necessary to be available for a specific analysis of this case.